Measurements of Pre-Clinical Liver Perfusion Using Arterial Spin Labelling MRI

Rajiv Ramasawmy, MPhys, MRes.

Submitted for the degree of

Doctor of Philosophy in Medical Physics

April 2015

Department of Medical Physics and Bioengineering

And

Centre for Advanced Biomedical Imaging, Division of Medicine

University College London

*"**It's still magic even if you know how it's done.**"*

Terry Pratchett - *A Hat Full of Sky (2004)*

Declaration

I, Rajiv Ramasawmy, confirm that the work presented in this thesis is my own, except where stated otherwise in the text. This work is based on research which has been conducted by me, during the time period from October 2010 to September 2014 at University College London.

Rajiv Ramasawmy

14th August 2015

Abstract

Magnetic Resonance Imaging (MRI) has been at the focus of medical research as its availability and fidelity has improved in the last thirty years. MRI offers both high spatial resolution and excellent soft tissue contrast compared to complimentary medical imaging techniques, without the need to expose patients to ionising radiation.

Novel MRI methods that utilise the intrinsic body water signal are still being developed and refined. Arterial Spin Labelling (ASL) MRI provides a non-invasive method to measure tissue perfusion, which has been extensively applied in the brain, and demonstrated pre-clinically in the heart and kidneys. However, there is currently no literature reporting the development and use pre-clinical liver ASL – possibly due to complex methodology and quantification necessary in small animals.

Clinical liver perfusion imaging is predominantly carried out using an injected Gadolinium-based contrast agent; this technique can be challenging to quantify, cannot be immediately re-administered and may have complications for patients with renal impairment. A methodology to measure liver perfusion without the need for a contrast agent would find utility in a number of different hepatic diseases; monitoring pathophysiology and therapy efficacy.

This research investigates the feasibility of a pre-clinical measure of liver perfusion using ASL and its potential application to a pre-clinical model of hepatic disease. We aim to apply the method to monitor novel therapy efficacy in pre-clinical disease models, to eventually translate both therapy and hepatic ASL into the clinical environment.

Acknowledgements

Despite declaring two pages back this work is my own, nothing could be further from the truth. I must thank a number of people for their relentless support, generous patience and unswerving friendships, without which the following thesis would just be 100 blank pages soaked in tears.

Firstly, Dr Simon Walker-Samuel, who literally pulled me through the mud. His drive, intuition and ultimately, his friendship has been the fulcrum of my PhD. He has pushed me to be proud of the work I have achieved and so thanks, Simon!

I would also be very far behind and, heaven forbid, even more disorganised without Dr Jack Wells joining the team and perennially bringing his enthusiasm. I would like to thank Professor Barbara Pedley and Professor Mark Lythgoe for allowing me to make a mess in their labs, and always willing to have a conversation when needed.

Everything I know is thanks to Dr Adrienne Campbell-Washburn. For some reason she never screamed at me to go away, but I'm so grateful that she instead, patiently explained it all. Dr Peter Johnson and I were thrown together, and I am so grateful to have him around as a long-standing collaborator and temporary yoga partner. Dr Manil Chouhan revolutionised my knowledge of the liver, and also gave me hope that I wasn't crazy to be interested in such an organ. I cannot put in to words what I owe to both Dr Thomas Roberts and Dr Niral Patel, who have been the most fantastic friends and sounding boards in the last few years.

A special mention must be passed to Isabel Christie, Holly Holmes, Rupy Ghatrora, Ozy Ismail, Miguel Goncalves, Ben Duffy, Katy Ordidge, Anthony Price, James O'Callaghan, Bernard Siow, Simon Richardson, Magda Sokolska, Adam Badar, Tammy Kalber, Daniel Stuckey and the whole CABI family for making the last few years so enjoyable.

I would like to thank my dear friends who have always been a phone call, a smile and a pub away: Valentin Hamy, Charlie Meyrick, Rory Toher, Mat Pannell, Chris Fiander, Nic Clarke, Paul Wahnon, Corrie Lencz, James Sayers, Dan & Terri Amos, Seb Weidt, Anne Faber, Anette Reisjo, Kieran Flew, Damian Hartley, Ben Leonard and Kyle Davison. I am indebted to Julie Desrousseaux, who was inspiring and encouraging throughout my PhD.

Finally, to my parents, my brother and my sister. You have always been the perfect blend of supportive, distracting and crazy. Mostly crazy.

Lots of love, Raj

Publications and Proceedings

S. Walker-Samuel, R. Ramasawmy, F. Torrealdea, M. Rega, V. Rajkumar, S.P. Johnson, S. Richardson, M. Gonçalves, H.G Parkes, E. Arstad, D.L. Thomas, R.B. Pedley, M.F. Lythgoe and X. Golay. In vivo imaging of glucose uptake and metabolism in tumors, *Nature Medicine*; 2013, 19, 1067–1072.

R. Ramasawmy, A.E. Campbell-Washburn, J.A. Wells, S.P. Johnson, R.B. Pedley, S. Walker-Samuel and M.F. Lythgoe. Hepatic arterial spin labelling MRI: an initial evaluation in mice. *NMR Biomed*; 2014, DOI: 10.1002/nbm.3251.

M. R. Gonçalves, S. Walker-Samuel, S. P. Johnson, R. Ramasawmy, R. B. Pedley and M. F. Lythgoe. Pulse Oximetry and Independent Component Analysis Separate Systemic from Tumor-specific Influences on Oxygen Spontaneous Fluctuations in Colorectal Carcinomas. *British Journal of Cancer*; 2015. *In print.*

S. Walker-Samuel, T.A. Roberts, R. Ramasawmy, S.P. Johnson, B. Siow, S. Richardson, M. Gonçalves, D. Pendsé, R.B. Pedley, M.F. Lythgoe. Technical feasibility of interstitial fluid flow measurement in tumours with EVAC MRI. *In submission*.

R. Ramasawmy, S.P. Johnson, T.A. Roberts, D.J. Stuckey, A.L. David, R.B. Pedley, M.F. Lythgoe, B. Siow, S. Walker-Samuel. Monitoring the growth of orthotopic tumour xenograft models: multi-modal imaging assessment with high-field MRI (9.4T), benchtop MRI (1T), ultrasound and bioluminescence. *In submission*.

S.P. Johnson, R. Ramasawmy, A.E. Campbell-Washburn, J.A. Wells, M. Robson, V. Rajkumar, M.F. Lythgoe, R.B. Pedley, S. Walker-Samuel. Hyper-acute changes in liver tumour perfusion measured noninvasively with arterial spin labelling. *In submission.*

Conference Proceedings

R. Ramasawmy, S. Walker-Samuel, A. Campbell, S.P. Johnson, J. Wells, R.B. Pedley and M.F. Lythgoe. Look-Locker Arterial Spin Labelling (ASL) of Liver Metastases. *Proc Intl Soc Mag Reson Med. 2012*; (20); P1520.

S.P. Johnson, R. Ramasawmy, A.E. Campbell-Washburn, M. Robson, V. Rajkumar, S. Walker-Samuel, M.F. Lythgoe and R.B. Pedley. Comparison of Arterial Spin Labelling and R2* as Predictive Response Biomarkers for Vascular Targeting Agents in Liver Metastases. *Proc Intl Soc Mag Reson Med*. 2013; (21); O506.

R. Ramasawmy, A.E. Campbell-Washburn, S.P. Johnson, J.A. Wells, R.B. Pedley, S. Walker-Samuel and M.F. Lythgoe. Multi-Slice Look-Locker FAIR for Hepatic Arterial Spin Labelling. *Proc Intl Soc Mag Reson Med*. 2013; (21); P2188.

M. Chouhan, R. Ramasawmy, A.E. Campbell-Washburn, A. Bainbridge, J.A. Wells, N. Davies, R. Mookerjee, S. Punwani, S.A. Taylor, S. Walker-Samuel and M.F. Lythgoe. Measurement of bulk liver perfusion: initial assessment of agreement between ASL and phase-contrast MRI at 9.4T. *Proc Intl Soc Mag Reson Med*. 2013; (21); P2190.

R. Ramasawmy, T.A. Roberts, B. Siow, S.P. Johnson, J.A. Wells, A. Bainbridge, R.B. Pedley, M.F. Lythgoe and S. Walker-Samuel. 1 Tesla Bench-top MRI of a Mouse Model of Colorectal Carcinoma Metastasis in the Liver: Comparison with 9.4 Tesla, *Proc Intl Soc Mag Reson Med*. 2014; (22); P1153

R. Ramasawmy, M. Chouhan, D.K. Dhar, A.E. Campbell-Washburn, J.A. Wells, R.B. Pedley, M. Malago, R. Mookerjee, S.A. Taylor, M. F. Lythgoe and S. Walker-Samuel. Monitoring of Rat Liver Regeneration following Portal Vein Ligation using MR Volumetry and Hepatic Arterial Spin Labelling, *Proc Intl Soc Mag Reson Med*. 2014; (22); eP3618.

R. Ramasawmy, A.E. Campbell-Washburn, S.P. Johnson, J.A. Wells, R.B. Pedley, S. Walker-Samuel and M.F. Lythgoe. Repeatability and Variability of Pre-Clinical Hepatic Arterial Spin Labelling, *Proc Intl Soc Mag Reson Med*. 2014; (22); P2725.

M.R. Goncalves, S. Walker-Samuel, R. Ramasawmy, S.P. Johnson, R.B. Pedley, and M.F. Lythgoe. Assessment of the response of colorectal tumours to imatinib mesylate therapy using carbogen and hypercapnia gas challenges. *Proc Intl Soc Mag Reson Med*. 2014; (22); O914.

Y. Zhu, R. Ramasawmy, S.P. Johnson, V. Taylor, R.B. Pedley, A. Berger, N. Chattopadhyay, D. Bradley, M.F. Lythgoe, and S. Walker-Samuel. Detection of Acute Response to Proteasome Inhibitor Treatment in Mouse Colorectal Tumour Models Using Amide Proton Transfer (APT) Magnetic Resonance Imaging. *Proc Intl Soc Mag Reson Med*. 2014; (22); O844.

R. Ramasawmy, T.A. Roberts, S.P. Johnson, D.J. Stuckey, A. David, R.B. Pedley, M.F. Lythgoe, B. Siow, S. Walker-Samuel. Multimodal Imaging of a Mouse Model of Colorectal Carcinoma Metastasis in the Liver. *Proc Intl Soc Mag Reson Med*. 2015; (23); P1094.

R. Ramasawmy, J.A. Wells, J.A. Meakin, M. Sokolska, A.E. Campbell-Washburn, S.P. Johnson, R.B. Pedley, M. F. Lythgoe & S. Walker-Samuel. Separation of arterial and portal blood

supply to mouse liver and tumour tissue using pseudo-Continuous Arterial Spin Labelling (pCASL). *Proc Intl Soc Mag Reson Med*. 2015; (23); O532.

H. Holmes, R. Ramasawmy, M. Da, N. Powell, M Cardoso, M Modat, S Ourselin, M.F. Lythgoe, B. Siow. Implementation of a high-throughput ex vivo brain atlas with “benchtop” 1T MRI: Comparison with 9.4T MRI. *Proc Intl Soc Mag Reson Med*. 2015; (23); eP3518.

J.O. Wingrove, D.J. Stuckey, V. Taylor, T.A. Roberts, R. Ramasawmy, B. Siow and M.F. Lythgoe. Assessment of Experimental Stroke Lesion Size Using 1T Benchtop MRI. *Proc Intl Soc Mag Reson Med*. 2015; (23); P2154.

A. d’Esposito, R. Ramasawmy, T.A. Roberts, S.P. Johnson, A. Desjardin, M.F. Lythgoe, S. Walker-Samuel. Three dimensional *in vivo* and *ex vivo* visualization of metastatic liver vasculature with Magnetic Resonance Imaging and Optical Projection Tomography. *Proc World Mol Congr* 2015.

Table of Contents

Contents

List of Figures

List of Tables

List of Abbreviations

2D	Two dimensional
3D	Three dimensional
ANOVA	Analysis of Variance
ASL	Arterial Spin Labelling
ATT	Arterial Transit Time
BS	Between Session
CASL	Continuous Arterial Spin Labelling
CT	X-ray Computed Tomography
CV	Coefficient of Variability
DA	Descending Aorta
DCE	Dynamic Contrast Enhancement
DL	Data-logger
ECG	Electrocardiagram
EPI	Echo Planar Imaging
FAIR	Flow-sensitive Alternating Inversion Recovery
FOV	Field of view
FSE	Fast Spin Echo
GE	Gradient Echo
HA	Hepatic Artery
IR	Inversion Recovery
IVC	Inferior Vena Cava
LL	Look-Locker
MRI	Magnetic Resonance Imaging
NMR	Nuclear Magnetic Resonance
PASL	Pulsed Arterial Spin Labelling
pCASL	Pseudo-Continuous Arterial Spin Labelling
PC-MRI	Phase contrast MRI
PE	Phase encoding
PENIR	Phase Encoded Noise-based Image Rejection

PV	Portal Vein
RC	Repeatability Coefficient
RF	Radiofrequency
RO	Read-out
SE	Spin Echo
SNR	Signal to noise ratio
SS	Slice Selection
TE	Echo time
TI	Inversion Time
TR	Repetition time
US	Ultrasound
WS	Within Session

Chapter 1

Context of Research

The aims of this thesis research is explore the potential of magnetic resonance imaging (MRI) to measure liver perfusion in mice, for application to pre-clinical models of human disease. Perfusion measurements can potentially inform on tissue function, disease progression and therapy efficacy.

This chapter reviews the existing literature on hepatic disease and dysfunction, covering the liver's anatomy and subsequent pathophysiology. A review of the different available techniques to measure liver perfusion and function will then be followed by an overview of MRI techniques, highlighting the requirement and potential application for a non-invasive measurement of liver perfusion using arterial spin labelling (ASL) MRI. The research in this thesis will be performed on rodents, thus a strong emphasis of this chapter will include pre-clinical literature.

1.1 Liver Anatomy and Physiology

1.1.1 Liver Dysfunction and Cirrhosis

The liver has a significant role in blood filtration, biosynthesis, immunity and metabolism; thus the deterioration of hepatic homeostasis is associated with a high morbidity rate (1). Liver disease is the fifth most common cause of UK deaths (2), approximately 8000 new patients are diagnosed with cirrhosis in the UK each year (3). Fibrosis and subsequent cirrhosis pathophysiology is due to hepatic inflammation leading to fibrogenesis (4). As cirrhosis develops, an increased deposition of collagenous fibres within the liver sinusoids cause the liver to 'stiffen' and become more resistant to flow, resulting in portal hypertension (5). Currently, there are no available therapies for cirrhosis, and thus the clinical focus is on early prevention and lifestyle adjustments to minimise the need for a liver transplant.

Anatomical ultrasound, X-ray computed tomography (CT) and magnetic resonance imaging (MRI) are insensitive to the initial stages of cirrhosis, however, there a number of blood serum markers that can stage fibrosis to cirrhosis (4). Palpation of the liver and invasive portal pressure measurements are commonplace to determine the onset of cirrhosis and portal hypertension (6); in addition to stiffness-sensitive techniques such as transient elastography using ultrasound (FibroScan) (7), and MR elastography (8). However, non-invasive and spatially informative MRI measurements using perfusion has potential benefits to be used in tandem with multi-parametric assessments.

1.1.2 Liver Cancer and Metastasis

Hepatocellular carcinoma (HCC), the most common form of primary liver cancer, is the 6th most prevalent cancer worldwide (9). Cirrhosis patients are at the most risk to developing primary tumours, in addition to patients exposed to infection from hepatitis and carcinogens. Though a raised presence of the carcinoembryonic antigen blood serum marker occurs in many tumour types (10), it is not exclusive and sufficiently sensitive to diagnose the presence of tumours. Imaging has a large role in diagnosing tumours; anatomical CT and MRI are commonplace, as well as more invasive techniques of liver biopsy and laparoscopy.

HCC is a well vascularised tumour and though anti-angiogenesis treatment has been trialled for treatment, resection of the affected lobe is the standard clinical procedure (9). Other successful clinical methods include percutaneous ablation, chemoembolization and liver transplantation. In order to guarantee a sufficient post-resection liver, techniques have

been developed which promote growth of non-cancerous lobes (11) which exploit the regenerative property of the liver.

However, it is more common for cancers to develop in the liver as a secondary tumour site; metastasis of cancerous cells is an aggressive and late stage of tumour development (12). Approximately 6 in 10,000 people are diagnosed with colorectal cancer in Britain each year (13); approximately 40% of these will develop liver metastases, which results in a low 5 year survival rate (14). Additionally, for patients with other distal primary tumours, liver metastasis is a major cause of cancer-related deaths. Similarly to HCC, routine clinical practice is for patients to undergo hepatectomy of the affected lobe. However, such surgery is not without complications, is liable to remission (15), and is limited if the disease is widespread. A body of cancer research has thus focussed on developing tumour-targeted therapies (16), in order to minimise highly invasive surgery. Measurements of tumour perfusion have the potential to inform on tumour malignancy and therapy efficacy.

1.1.3 Liver Anatomy

The primary function of the liver is the clearance of toxins and foreign bodies from the blood stream, and consequently, the liver has a unique 'dual' arterial and venous blood supply (Figure 1.1A). Venous blood from the intestines, pancreas and spleen enter the liver via the portal vein (PV), which delivers approximately 75% of the blood to the liver (17). The remaining blood is derived from the hepatic artery (HA), originating from the descending aorta at the celiac trunk, which supplies hepatocytes with oxygen-rich blood. Though the portal vein conducts partly deoxygenated blood, it provides 50% of the liver's oxygen, due to its relatively higher flow rate. This dual-supply works in tandem to produce a steady flow in healthy hepatic circulation: the hepatic artery will regulate changes in the portal flow. This process is known as the hepatic arterial buffer response (HABR)(18), there is no reciprocity of the portal vein however, as it cannot regulate the blood flow from other organs. The ratio of the arterial to total liver blood flow is known as the hepatic arterial perfusion index (HPI), which has been shown to increase in certain hepatic diseases (19).

The hepatic arterial buffer response is impaired in cirrhosis and cannot account for the reduced portal venous flow, resulting in an overall reduction in perfusion (20). Reduced portal perfusion has been characterised by Doppler ultrasound (21), contrast CT measurements (22), as well as recent clinical liver MRI measurements (23, 24). The typical oxygen saturation of arterial blood and portal venous blood is 95% and 70% respectively (25), which will lead to a significant T_2 and T_2* difference between the two blood supplies,

arterial blood and venous blood T_2 have been respectively measured at 40 and 5-7 ms at 9.4T (26). This difference has potential to give information on the respective supplies to the liver; the signal changes under different gas challenges have been explored to give 'functional' information (27). In addition, the disparity in relaxation times may potentially confound perfusion quantification, but may also lend to separating out the perfusion sources.

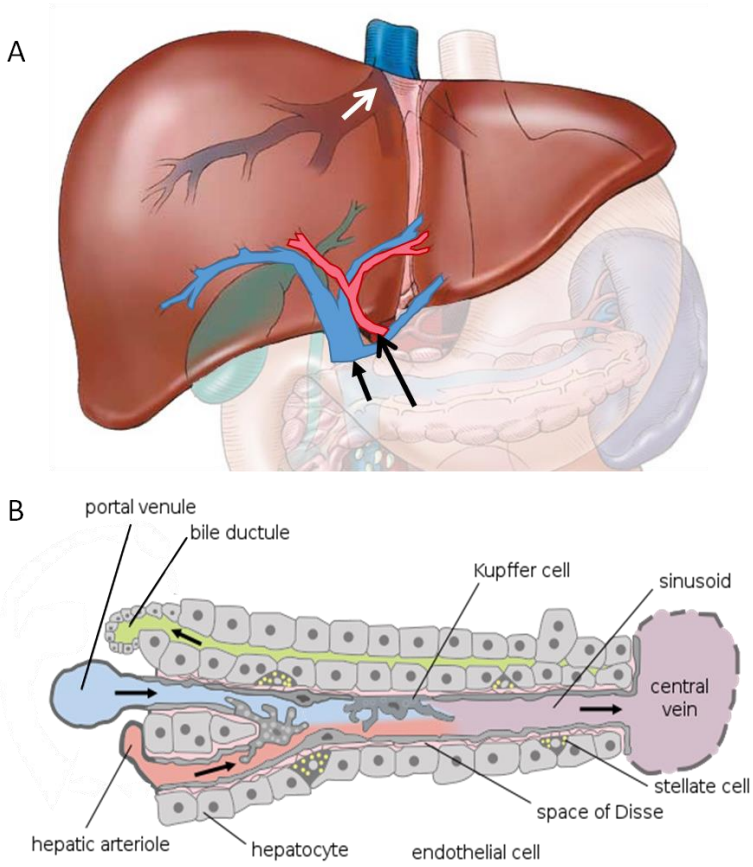

Figure 1.1: A human liver schematic (A), supplied by the portal vein (short black arrow) and the hepatic artery (long black arrow). The blood is processed through the liver and collected into the inferior vena cava (short white arrow) [image adapted from Netter (28)]. Process of liver filtration through a liver lobule (B): the blood flows from the portal venule and hepatic arteriole along liver sinusoids, and finally the filtered blood is collected in to the central vein. The central veins coalesce into hepatic veins, which drain into the inferior vena cava [image adapted from Frevert *et al*. (29)].

Small mammals such as mice and rats are often used in research due to their similar physiology to man. In addition, the mouse and rat liver has the same function and similar relative PV and HA contributions to humans (30) making them suitable for pre-clinical models of hepatic disease. The main difference between the human and rodent liver is the arrangement of the lobes – the human liver is divided into four lobes: right, left, quadrate and caudate. In comparison, the mouse and rat liver is commonly split in to six lobes: upper- and lower right, upper- and lower caudate, left lateral and median. The liver's microenvironment is comprised of lobules which pack together to form the lobes. The

lobules draw blood from the portal venules and hepatic arterioles (as well as bile from the bile ducts) and Kupfer cells break down and filter the blood within the liver sinusoids. The sinusoids are separated from the hepatocytes by the Space of Disse, which allows plasma and small molecular weight compounds to pass through. The filtered blood is collected in to the central vein which drains in to the inferior vena cava (IVC) via hepatic veins (Figure 1.1B). This multiple input, multiple compartment tissue results in complicated pharmacokinetic models to describe the liver (5, 31). In addition, these models often need to be adapted in disease situations as the lobules physiology will change.

1.1.4 Summary

From understanding the progression of hepatic disease and therapeutic changes on the pathophysiology, it is apparent that blood flow imaging offers potential diagnostic information. Perfusion imaging may provide vital biomarkers of tissue functionality, inform on risk-affected areas and monitor disease progression: the next section reviews liver perfusion imaging techniques. A brief summary of the existing techniques will be explored, followed by a review of the MRI methods of estimating perfusion.

1.2 Measurements of Liver Perfusion

1.2.1 Clinical Techniques

A large amount of clinical liver perfusion measurements have been undertaken using CT in combination with iodine-based contrast agents. From modelling of the uptake curves based on regions within the descending aorta and portal vein (32), the arterial and venous contributions to the liver parenchyma and disease nodules can be estimated. Hepatic CT has been successfully applied to measuring perfusion deficits in HCC, metastases, fibrosis and cirrhosis, and in addition detected changes in the HPI (32-34). However, the quantification of the contrast agent uptake is reliant on characterising the ‘arterial input function’, which requires high temporal resolution, and the imaging modality exposes patients to ionising radiation.

Doppler ultrasound can be used to measure blood flow in the major vasculature, and has been demonstrated to image portal hypertension (35), and estimates of bulk liver flow can be derived from velocity measurements. However, though this technique is fast, non-invasive and flow measurements showed a high sensitivity to the cirrhosis scores, there is an element of user-variability in this measurement. Ultrasound has also been combined with a microbubble contrast agent to measure regional liver and malignant tumour

perfusion, though the quantification and pharmacokinetics of the contrast agent has not been extensively explored (36).

1.2.2 Pre-clinical Techniques

Pre-clinically, the majority of invasive perfusion measurements have been performed in rats rather than mice due to the larger anatomy facilitating intricate surgery. A body of literature reports the use of fluorescent or radioactively-labelled microspheres to systemically embed in the capillary bed, and the tissues can then be evaluated for their concentration relative to a blood sample. This *ex vivo* technique is often considered a gold standard, and has been applied in mice (37) and rats (38), though is not a trivial experiment, as there are a number of complications within the procedure and quantification (20).

There are a number of *in vivo* techniques using clearance of a labelled contrast agents such as Indocyanine Green (ICG), galactose (39), ^{133}Xe (40), ^{85}Kr (41). These techniques are invasive, typically exposing the liver to a counter to then estimate a liver perfusion from the uptake of the contrast agent. These measurements, however, do not provide a regional measure of hepatic blood flow.

1.2.3 Liver Perfusion MRI

Anatomical liver imaging is a well-established method for MR; scans are commonly used to diagnose hepatocellular carcinoma (HCC), cirrhosis, metastases and hepatic lesions (42). Currently, dynamic contrast enhancement (DCE) MRI is the most common form of clinical liver perfusion imaging. DCE MRI utilises the T_1 shortening caused by a paramagnetic contrast agent, typically a chelated form of Gadolinium. The post-bolus signal enhancement is modelled, based closely on the enhancement models from dynamic CT, to generate estimates of physiological parameters. DCE-MRI has been successfully applied to hepatocellular carcinoma (HCC) (43) and patients with liver metastases undergoing various therapies (44). It is commonplace for DCE-MRI to be used for qualitative diagnostic evaluation to determine tissue malignancy from arterial, portal and equilibrium phases (45). In addition, hepatocyte-targeting contrast agents can give liver-specific contrast, which describe the late phase enhancement as ‘hepatobiliary’ phase. Kinetic modelling developed for contrast-CT has been adopted by DCE-MRI such as single- and dual-input and single- and dual-compartment models which respectively address the vascular supply and contrast distribution (46). However the choice of modelling of DCE-MRI has not yet been standardised, and the modelled parameters yield a challenging interpretation – a

commonly reported parameter is K_{trans}, which relates to the microvascular permeability, whereas a measurement of perfusion offers a more physiological assessment of the tissue.

Tissue	Approximate Perfusion Ranges (ml 100 g^{-1} min^{-1})
Cortex	110 – 180 (47, 48)
Myocardium	360 - 700 (49, 50)
Renal Cortex	400 – 750 (51, 52)
Total Hepatic	180 - 250 (53, 54)
Skeletal Muscle	17 – 60 (55)

Table 1.1: Typical ranges of mouse organ perfusion measured using ASL MRI and other invasive measurements.

Pre-clinical applications of DCE-MRI have been applied to rat models of liver fibrosis (56) and HCC (57); both of these studies were carried out in a clinical 1.5T system, and utilised the imaging acceleration techniques available on human imaging system. Hartono *et al* carried out a feasibility study measuring liver blood flow in mice on a pre-clinical 7T system; across five mice, a mean liver perfusion of approximately 2.5 ml g^{-1} min^{-1} was estimated, when normalised to a typical mouse liver mass (2g) (58). The temporal resolution (2s) of the DCE acquisition however was insufficient to differentiate between arterial and venous supply to the liver parenchyma. The predominant issue with pre-clinical liver DCE MRI is defining the first bolus of contrast-agent due to the rapid circulation, which makes separating the arterial and portal venous blood supply difficult in addition to quantifying the perfusion signal.

An alternative, non-contrast method of estimating bulk liver flow can be calculated from phase contrast (PC) angiography measurements in the portal vein. PC-MRI is well established on clinical scanners (59), and has been applied to rat liver dysfunction models (60), though pre-clinical development in this field is limited. Phase-contrast angiography is particularly useful for late stage liver dysfunction where reverse flow is possible. However bulk flow estimates based on input-vessel velocities do not provide localised measurements within the liver tissue and could not be directly applied to for example, metastases measurements, though velocity changes in the hepatic supply can be indicative of other gross hepatic dysfunction (61, 62).

Barash *et al.* utilised a 'functional-MRI' approach to infer liver perfusion dynamics by measuring changes in T_2*-weighted signal intensities in response to hyperoxia and hypercapnia (27). This technique reported a decrease in portal perfusion and increase in arterial perfusion following ligation of the portal vein, from the changes in signal intensities

under the two gas challenges relative to the normal liver. Edrei *et al.* also used this approach to measure a reduced perfusion within a model of colorectal liver metastases in mice (63). It was suggested that the signal intensity changes within the tumours were due to an increased arterial supply, as has been previously reported, though the interpretation of such signal changes is challenging, as this method does not a direct quantification of the tissue perfusion.

Arterial spin labelling (ASL) is a contrast-free MRI method to measure perfusion, initially and predominantly applied in the brain (64). The technique has been applied to image other organs such as the heart, kidneys and pre-clinical tumour xenografts (49, 65, 66). To my knowledge, at the time of writing, no previous examples of pre-clinical hepatic arterial spin labelling (ASL) have been published, though a few recent examples exist of clinical liver arterial spin labelling: Katada *et al* (67) measured the portal perfusion in a HCC patient study, and these data were quantified using a single-input, single-compartment model and evaluated against CT portography. The limited amount of research may be due to the relatively low and unstructured signal across the liver compared to other researched organs (Table 1.1), in addition to complications due to respiratory motion and quantifying the dual-blood supply. Bland-Altman analysis identified an overestimation in non HCC liver tissue, suggestive of a systematic error which was attributed to the blood/tissue T_1 ratio which was not taken into account by the single compartment modelling. The inversion profile was planned to avoid the aorta, and so the application to liver tumours may be limited as cancerous deposits have a tendency to draw from the arterial supply (68). Hoad *et al* (69) used a free-breathing FAIR sequence to measure total liver blood flow in healthy volunteers, this sequence has been later applied to monitoring post-prandial changes in cirrhosis patients (70). This research used dual-input, single compartment model which showed improved reproducibility between imaging sessions over DCE-MRI. Recently, a 'pseudo-continuous' ASL method to separate the arterial and venous contribution of the liver was demonstrated in normal volunteers and cirrhosis patients (71), which also measured post-prandial blood flow changes. This MRI technique is most promising, as a direct measure of arterial and venous perfusion in the liver can be achieved from separately labelling the vascular inputs, free of contrast agents and complex modelling of the perfusion quantification.

1.3 Arterial Spin Labelling

1.3.1 Introduction

This thesis focuses on perfusion imaging of the small animal liver; as there has been little published on hepatic arterial spin labelling (ASL), the following section introduces the technique and investigates developed pre-clinical and clinical ASL techniques. In addition, a focus will be made on previous kidney and cardiac perfusion imaging, as this may inform on the optimal methods of ASL preparation, perfusion quantification, and gated image acquisition, to counter respiratory motion of the liver.

Arterial spin labelling ASL is a perfusion-measuring MR technique, originally developed for imaging cerebral blood flow (CBF) in rats (64). The principle of ASL is to use water in the blood as an 'endogenous' tracer – the spins within the arterial blood are inverted so that the perfusion signal will come from a difference in relaxation as these 'tagged' spins travel to and exchange with the tissue under investigation. The success of brain perfusion imaging led to the technique being adapted to good effect in cardiac (72) and kidney (73) perfusion imaging. However, application of ASL to the liver has not been extensively undertaken.

The attractiveness of using ASL is that the technique can quantify blood flow without the need for invasive contrast agents or radio-chemicals, thus tissue perfusion can be utilised as a disease and regeneration biomarker. Though ASL suffers from a lower signal-to-noise ratio (SNR) than contrast-enhanced perfusion imaging, ASL will be better suited for longitudinal monitoring long term studies without potential discomfort from regular doses of contrast tracers or radiation exposure.

ASL can be considered in two modes of operation; continuous arterial spin labelling (CASL) and pulsed arterial spin labelling (PASL). CASL was the first mode of perfusion MRI proposed by Williams, Detre and Leigh (74) – application of a long-duration (~ approx. 2 s) RF pulse and a magnetic field gradient centred on the carotid arteries resulted in the blood magnetisation undergoing adiabatic inversion during transit toward the brain (75). However, the long-duration, off-resonance RF pulse induced magnetisation transfer (MT) effects, due to saturation of large macromolecules in the tissue exchanging with the free water, leading to an over-estimation of the perfusion.

However, due to the hardware demands and MT effects of CASL, the popularity of MR perfusion imaging moved to pulsed ASL. This format was first proposed around the same time by Kwong, Kim and Schwarzbauer (76) (77) (78), which uses a single inversion pulse to label the perfusing blood. This technique was far simpler to implement on standard MRI

scanners, and the single pulse removed the influence of MT saturation. Typical PASL sequences are “Flow-induced Alternating Inversion Recovery” (FAIR) and “Signal Targeting by Alternating Radiofrequency Pulses” (EPISTAR) (79) which orient the selective labelling pulse differently around the imaging slice to sensitise the images to perfusion. Though PASL has a reduced SNR relative to CASL, it is possible to tag closer to the imaging plane to optimise the perfusion signal, due to the reduced applied RF and gradients.

1.3.2 Flow-induced Alternating Inversion Recovery (FAIR) ASL

Arterial spin labelling estimates perfusion from signal subtraction, and the FAIR sequence achieves this by two signal preparations: a global and slice-selective inversion centred on the imaging slice. A T_1 map will be generated from the global inversion experiment, and the perfusion-weighting will arise from the slice-selective inversion: an apparent faster recovery of the inversion recovery curve will be measured as a result of fresh magnetisation from the blood pool arriving in to the imaging slice and exchanging with the tissue water. FAIR methods have been used to obtain perfusion maps of the brain and kidneys, and such a labelling approach is predominantly applied to measurements of myocardium perfusion due to the difficulty of labelling the supply vessels to this tissue.

1.3.3 Pseudo-Continuous ASL

Continuous ASL resurfaced with the advent of ‘pseudo-continuous’ ASL (pCASL) (80), which replaces the long duration labelling pulse with a train of closely-spaced, short RF pulses to give an effectively continuous pulse. As a result of the discretisation of the RF pulse, a larger gradient can be applied and further off-resonance RF pulses can be used which reduces the influence of magnetisation transfer produced in CASL (81). The development of pseudo-continuous ASL has facilitated vessel-selective labelling (81), (which can be achieved using intricate planning of the inversion slab in PASL (67)), which has been demonstrated to identify the cortical perfusion from the separate perfusing vessels (82).

1.3.4 Renal ASL

Both kidney and liver imaging employ similar gating strategies to overcome image artefacts from respiratory motion, thus renal ASL techniques offer useful information on the optimal approaches for perfusion measurements of the liver. Clinical examples of renal ASL have utilised EPI readouts for fast acquisition to overcome respiratory motion - however EPI may be difficult to implement within a mouse abdomen at high field due to susceptibility artefacts at air-tissue boundaries leading to image distortion. Clinical renal ASL have

employed controlled breathing strategies to acquire images (65), however, pre-clinical imaging is predominantly free breathing without invasive ventilating procedures.

Pre-clinical kidney perfusion imaging has recently been applied in mice using FAIR with a respiratory triggered, single shot SE-EPI at 7T (83). This study optimised the inversion efficiency for the ASL tagging by including the mouse heart within the transmit coil, however the coronal imaging plane did result in some unwanted labelling in the slice-selective inversion. Such unwanted labelling could be overcome by using a pseudo-continuous ASL (pCASL), as demonstrated in mice at 11.75T by Duhamel *et al* (84). This study compared a FAIR and a pCASL preparation and also investigated between a two-shot SE-EPI and a single shot Rapid Acquisition with Relaxation Enhancement (RARE) readout. ASL preparation was respiratory triggered, and images were synchronised with respiration in order to acquire in the quiescent phase. The pCASL module demonstrated a 20% increase in sensitivity over the FAIR technique, and additionally the RARE readout was less liable than EPI to susceptibility variations and motion artefacts when imaging coronally rather than axially. The pCASL preparation module was found to be limited to around 65% the tagging efficiency of the FAIR technique (calculated as the ratio of the renal perfusion values), which could be attributed to loss of flow driven adiabatic inversion in the aorta due to respiratory motion and pulsatile flow.

1.3.5 Myocardial ASL

There has been a considerable body of pre-clinical cardiac ASL and the techniques here may be instructive for applications to the liver. Belle *et al* (72) published one of the first quantitative *in vivo* measurements in rats, using an ECG gated, gradient echo sequence. The animals were ventilated and under sodium pentobarbital anaesthesia in this experiment, which is known to reduce heart and breathing rates – and the ventilation was paused during perfusion acquisition, which can be clinically translated as a voluntary breath-hold. Since this initial research, subsequent research has investigated the influence of isoflurane on myocardial perfusion and free–breathing strategies on myocardial perfusion imaging (85, 86). In 2012, Campbell-Washburn *et al* employed a free-breathing ECG gated FAIR Look-Locker sequence to study mouse myocardial perfusion at 9.4T (87). The Look-Locker technique shortened the acquisition time of multiple TIs post-inversion by regularly sampling the recovery curve with a small flip angle as to minimally perturb the magnetisation relaxation. As the inversion recovery period (approx. 6s) included a number of respirations, a retrospective algorithm was applied to discard corrupted images from recordings of the image acquisition and respiration cycles.

1.4 Summary

From reviewing the literature, it becomes apparent that avoiding motion and susceptibility artefacts is key when performing ASL MRI in the abdomen and, in particular, the liver (88). The choice of either a CASL or PASL labelling method for the liver will determine whether portal venous and hepatic arterial or total hepatic blood flow will be measured. As the total liver blood flow is expected to be approximately half of that of the kidney (1.8 ml g^{-1} min^{-1} to 5.1 ml g^{-1} min^{-1}, from microsphere data in mice (37)), a method to measure the total in-flow of blood to the liver, such as FAIR, in order to maximise the potential perfusion signal, will be ideal to initially assess the feasibility of liver ASL. In addition, this sequence is simple to implement whereas it may be technically difficult to implement a pCASL method in a pre-clinical liver setting.

Clinical liver ASL measurements have overcome breathing motion of the liver by timing the inversion and acquisition on free-breathing patient expiration (67, 69, 70), and also using breath-hold strategies (71). For pre-clinical measurements, a free-breathing approach will be implementable, though this will depend on stable physiology of the animal, which can vary and become more erratic over long experiment durations. Rajendran *et al.* imaged renal perfusion using a timing of the inversion and a single-shot EPI readout pulse, in a similar manner to the clinical liver examples above. Duhamel *et al*. acquired a single TI with a single-shot acquisition (EPI and RARE), by synchronising the readout with the respiration rate. This 'timing' method is reliant on rapid image acquisition, however, from initial experience, EPI of the mouse liver suffered from many artefacts. An alternative read-out method can employ retrospective gating of the data, in a manner demonstrated by Campbell-Washburn *et al*. in the mouse myocardium (87). Such a readout method offers promise in application to the liver, as the gradient-echo readout will not be as susceptible to distortions as EPI, and the efficient acquisition of multiple TIs will increase the accuracy of the perfusion estimate.

1.5 Thesis Structure

The aim of this thesis is to investigate the application of arterial spin labelling MRI to the mouse and rat liver. The remaining thesis is structured thus:

Chapter 2 provides the relevant theory for the following chapters, covering some basic aspects of MRI, as well as functional imaging techniques to measure perfusion, blood velocity and the B_0 field.

Chapters 3 to 5 report on the experimental results: Chapter 3 shows the development and optimisation of a T_1-mapping based quantification of liver perfusion using a Look-Locker acquisition and a FAIR-ASL approach. Methods to prospectively and retrospectively gate acquisition were investigated, and this was followed by a repeatability study to demonstrate the robustness of the technique.

Chapter 4 applies the optimised sequence to three pre-clinical liver models. First, the technique is used to measure perfusion differences between normal liver and two tumour cell lines in a mouse model of colorectal liver metastases. The perfusion changes within the tumours were then measured after administration of a vascular-disrupting therapy. Second, the sequence was applied to a rat model of cirrhosis, and compared to a phase-contrast MRI estimate of bulk liver flow. Finally, perfusion differences were measured between liver lobes in a rat model of selective portal ligation to stimulate rapid liver growth.

Chapter 5 investigates the feasibility of pCASL in the mouse liver, to separate the flow contributions of the portal vein and the hepatic artery. Measurements of the blood vessel's velocities and the B_0 shifts during respiration were taken in order to optimise and simulate the efficiency of the pCASL tagging. Abdominal EPI was tested with a pCASL preparation in the kidneys, before being applied to the mouse liver.

Finally, Chapter 6 summarises and discusses the work presented in this thesis.

References

1. Vollmar B, Menger MD. The hepatic microcirculation: mechanistic contributions and therapeutic targets in liver injury and repair. Physiol Rev 2009;89(4):1269-1339.

2. Williams R. Global challenges in liver disease. Hepatology 2006;44(3):521-526.

3. Fleming KM, Aithal GP, Solaymani-Dodaran M, Card TR, West J. Incidence and prevalence of cirrhosis in the United Kingdom, 1992-2001: a general population-based study. J Hepatol 2008;49(5):732-738.

4. Tsochatzis EA, Bosch J, Burroughs AK. Liver cirrhosis. Lancet 2014;383(9930):1749-1761.

5. Thng CH, Koh TS, Collins DJ, Koh DM. Perfusion magnetic resonance imaging of the liver. World J Gastroenterol 2010;16(13):1598-1609.

6. Merkel C, Montagnese S. Hepatic venous pressure gradient measurement in clinical hepatology. Dig Liver Dis 2011;43(10):762-767.

7. Pavlov CS, Casazza G, Nikolova D, Tsochatzis E, Burroughs AK, Ivashkin VT, Gluud C. Transient elastography for diagnosis of stages of hepatic fibrosis and cirrhosis in people with alcoholic liver disease. Cochrane Database Syst Rev 2015;1:CD010542.

8. Rouviere O, Yin M, Dresner MA, Rossman PJ, Burgart LJ, Fidler JL, Ehman RL. MR elastography of the liver: preliminary results. Radiology 2006;240(2):440-448.

9. Forner A, Llovet JM, Bruix J. Hepatocellular carcinoma. Lancet 2012;379(9822):1245-1255.

10. Duffy MJ. Carcinoembryonic antigen as a marker for colorectal cancer: is it clinically useful? Clin Chem 2001;47(4):624-630.

11. Schnitzbauer AA, Lang SA, Goessmann H, Nadalin S, Baumgart J, Farkas SA, Fichtner-Feigl S, Lorf T, Goralcyk A, Horbelt R, Kroemer A, Loss M, Rummele P, Scherer MN, Padberg W, Konigsrainer A, Lang H, Obed A, Schlitt HJ. Right portal vein ligation combined with in situ splitting induces rapid left lateral liver lobe hypertrophy enabling 2-staged extended right hepatic resection in small-for-size settings. Ann Surg 2012;255(3):405-414.

12. Hanahan D, Weinberg RA. The hallmarks of cancer. Cell 2000;100(1):57-70.

13. Bird NC, Mangnall D, Majeed AW. Biology of colorectal liver metastases: A review. J Surg Oncol 2006;94(1):68-80.

14. Chong G, Cunningham D. Improving long-term outcomes for patients with liver metastases from colorectal cancer. J Clin Oncol 2005;23(36):9063-9066.

15. Millikan KW, Staren ED, Doolas A. Invasive therapy of metastatic colorectal cancer to the liver. Surg Clin North Am 1997;77(1):27-48.

16. Van den Eynde M, Hendlisz A. Treatment of colorectal liver metastases: a review. Rev Recent Clin Trials 2009;4(1):56-62.

17. SCHENK WG, Jr., McDONALD JC, McDONALD K, DRAPANAS T. Direct measurement of hepatic blood flow in surgical patients: with related observations on hepatic flow dynamics in experimental animals. 156 ed. 1962. 463-471.

18. Lautt WW. Mechanism and role of intrinsic regulation of hepatic arterial blood flow: hepatic arterial buffer response. Am J Physiol 1985;249(5 Pt 1):G549-G556.

19. Ballantyne KC, Charnley RM, Perkins AC, Pye G, Whalley DR, Wastie ML, Hardcastle JD. Hepatic perfusion index in the diagnosis of overt metastatic colorectal cancer. Nucl Med Commun 1990;11(1):23-28.

20. Vollmar B, Menger MD. The hepatic microcirculation: mechanistic contributions and therapeutic targets in liver injury and repair. Physiol Rev 2009;89(4):1269-1339.

21. Richter S, Mucke I, Menger MD, Vollmar B. Impact of intrinsic blood flow regulation in cirrhosis: maintenance of hepatic arterial buffer response. Am J Physiol Gastrointest Liver Physiol 2000;279(2):G454-G462.

22. Van Beers BE, Leconte I, Materne R, Smith AM, Jamart J, Horsmans Y. Hepatic perfusion parameters in chronic liver disease: dynamic CT measurements correlated with disease severity. AJR Am J Roentgenol 2001;176(3):667-673.

23. Cox EF, Ghezzi A, Bennet A, Patel M, Jackson A, Harman D, Costigan C, Omar NF, James MW, Ryder SD, Gowland PA, Aithal GP, Guha IN, Francis ST. A novel MRI protocol to axamine haemodynamic compartments in compensated liver cirrhosis. Proc Intl Soc Mag Reson Med 2013;21:0276.

24. Schalkx HJ, van Stralen M, Peters NHGM, Veldhuis WB, van Leeuwen MS, Pluim JPW, Petersen ET, van den Bosch MAAJ. Pre- and postprandial arterial and portal venous liver perfusion using selective spin labeling MRI with Look-Locker read-out. Proc Intl Soc Magn Reson Med 2014;22:372.

25. Keys A. The Oxygen saturation of the venous blood in normal human subjects. Am J Physiol 1938;124(13).

26. Lee SP, Silva AC, Ugurbil K, Kim SG. Diffusion-weighted spin-echo fMRI at 9.4 T: microvascular/tissue contribution to BOLD signal changes. Magn Reson Med 1999;42(5):919-928.

27. Barash H, Gross E, Matot I, Edrei Y, Tsarfaty G, Spira G, Vlodavsky I, Galun E, Abramovitch R. Functional MR imaging during hypercapnia and hyperoxia: noninvasive tool for monitoring changes in liver perfusion and hemodynamics in a rat model. Radiology 2007;243(3):727-735.

28. Netter F. Atlas of Human Anatomy. 5th ed. Saunders; 2010.

29. Frevert U, Engelmann S, Zougbede S, Stange J, Ng B, Matuschewski K, Liebes L, Yee H. Intravital observation of Plasmodium berghei sporozoite infection of the liver. PLoS Biol 2005;3(6):e192.

30. Kogure K, Ishizaki M, Nemoto M, Kuwano H, Makuuchi M. A comparative study of the anatomy of rat and human livers. J Hepatobiliary Pancreat Surg 1999;6(2):171-175.

31. Sourbron SP, Buckley DL. On the scope and interpretation of the Tofts models for DCE-MRI. Magn Reson Med 2011;66(3):735-745.

32. Goetti R, Leschka S, Desbiolles L, Klotz E, Samaras P, von BL, Stenner F, Reiner C, Stolzmann P, Scheffel H, Knuth A, Marincek B, Alkadhi H. Quantitative computed tomography liver perfusion imaging using dynamic spiral scanning with variable pitch: feasibility and initial results in patients with cancer metastases. Invest Radiol 2010;45(7):419-426.

33. Zhong L, Wang WJ, Xu JR. Clinical application of hepatic CT perfusion. World J Gastroenterol 2009;15(8):907-911.

34. Kim SH, Kamaya A, Willmann JK. CT perfusion of the liver: principles and applications in oncology. Radiology 2014;272(2):322-344.

35. Zironi G, Gaiani S, Fenyves D, Rigamonti A, Bolondi L, Barbara L. Value of measurement of mean portal flow velocity by Doppler flowmetry in the diagnosis of portal hypertension. J Hepatol 1992;16(3):298-303.

36. Goetti R, Reiner CS, Knuth A, Klotz E, Stenner F, Samaras P, Alkadhi H. Quantitative perfusion analysis of malignant liver tumors: dynamic computed tomography and contrast-enhanced ultrasound. Invest Radiol 2012;47(1):18-24.

37. Sarin SK, Sabba C, Groszmann RJ. Splanchnic and systemic hemodynamics in mice using a radioactive microsphere technique. Am J Physiol 1990;258(3 Pt 1):G365-G369.

38. Groszmann RJ, Vorobioff J, Riley E. Splanchnic hemodynamics in portal-hypertensive rats: measurement with gamma-labeled microspheres. Am J Physiol 1982;242(2):G156-G160.

39. Pollack GM, Brouwer KL, Demby KB, Jones JA. Determination of hepatic blood flow in the rat using sequential infusions of indocyanine green or galactose. Drug Metab Dispos 1990;18(2):197-202.

40. Sherriff SB, Smart RC, Taylor I. Clinical study of liver blood flow in man measured by 133Xe clearance after portal vein injection. Gut 1977;18(12):1027-1031.

41. Rice GC, Leiberman DP, Mathie RT, Ryan CJ, Harper AM, Blumgart LH. Liver tissue blood flow measured by 85Kr clearance in the anaesthetized rat before and after partial hepatectomy. Br J Exp Pathol 1977;58(3):243-250.

42. Maniam S, Szklaruk J. Magnetic resonance imaging: Review of imaging techniques and overview of liver imaging. World J Radiol 2010;2(8):309-322.

43. Sahani DV, Holalkere NS, Mueller PR, Zhu AX. Advanced hepatocellular carcinoma: CT perfusion of liver and tumor tissue--initial experience. Radiology 2007;243(3):736-743.

44. Nathan P, Zweifel M, Padhani AR, Koh DM, Ng M, Collins DJ, Harris A, Carden C, Smythe J, Fisher N, Taylor NJ, Stirling JJ, Lu SP, Leach MO, Rustin GJ, Judson I. Phase I trial of combretastatin A4 phosphate (CA4P) in combination with bevacizumab in patients with advanced cancer. Clin Cancer Res 2012;18(12):3428-3439.

45. Maniam S, Szklaruk J. Magnetic resonance imaging: Review of imaging techniques and overview of liver imaging. World J Radiol 2010;2(8):309-322.

46. Thng CH, Koh TS, Collins DJ, Koh DM. Perfusion magnetic resonance imaging of the liver. World J Gastroenterol 2010;16(13):1598-1609.

47. Zheng B, Lee PT, Golay X. High-sensitivity cerebral perfusion mapping in mice by kbGRASE-FAIR at 9.4 T. NMR Biomed 2010;23(9):1061-1070.

48. Duhamel G, Callot V, Tachrount M, Alsop DC, Cozzone PJ. Pseudo-continuous arterial spin labeling at very high magnetic field (11.75 T) for high-resolution mouse brain perfusion imaging. Magn Reson Med 2012;67(5):1225-1236.

49. Belle V, Kahler E, Waller C, Rommel E, Voll S, Hiller KH, Bauer WR, Haase A. In vivo quantitative mapping of cardiac perfusion in rats using a noninvasive MR spin-labeling method. Jmri-Journal of Magnetic Resonance Imaging 1998;8(6):1240-1245.

50. Streif JU, Nahrendorf M, Hiller KH, Waller C, Wiesmann F, Rommel E, Haase A, Bauer WR. In vivo assessment of absolute perfusion and intracapillary blood volume in the murine myocardium by spin labeling magnetic resonance imaging. Magn Reson Med 2005;53(3):584-592.

51. Duhamel G, Prevost V, Girard OM, Callot V, Cozzone PJ. High-resolution mouse kidney perfusion imaging by pseudo-continuous arterial spin labeling at 11.75T. Magn Reson Med 2013.

52. Rajendran R, Lew SK, Yong CX, Tan J, Wang DJ, Chuang KH. Quantitative mouse renal perfusion using arterial spin labeling. NMR Biomed 2013;26(10):1225-1232.

53. Sarin SK, Sabba C, Groszmann RJ. Splanchnic and systemic hemodynamics in mice using a radioactive microsphere technique. Am J Physiol 1990;258(3 Pt 1):G365-G369.

54. Hartono S, Thng CH, Ng QS, Yong CX, Yang CT, Shi W, Chuang KH, Koh TS. High temporal resolution dynamic contrast-enhanced MRI at 7 Tesla: a feasibility study with mouse liver model. Conf Proc IEEE Eng Med Biol Soc 2011;2011:2788-2791.

55. Bertoldi D, Loureiro de SP, Fromes Y, Wary C, Carlier PG. Quantitative, dynamic and noninvasive determination of skeletal muscle perfusion in mouse leg by NMR arterial spin-labeled imaging. Magn Reson Imaging 2008;26(9):1259-1265.

56. Kubo H, Harada M, Ishikawa M, Nishitani H. Hemodynamic changes with liver fibrosis measured by dynamic contrast-enhanced MRI in the rat. Magn Reson Med Sci 2006;5(2):65-71.

57. Braren R, Curcic J, Remmele S, Altomonte J, Ebert O, Rummeny EJ, Steingoetter A. Free-breathing quantitative dynamic contrast-enhanced magnetic resonance

imaging in a rat liver tumor model using dynamic radial T(1) mapping. Invest Radiol 2011;46(10):624-631.

58. Jones LD, Nielsen MK, Britton RA. Genetic variation in liver mass, body mass, and liver:body mass in mice. J Anim Sci 1992;70(10):2999-3006.

59. Jajamovich GH, Dyvorne H, Donnerhack C, Taouli B. Quantitative liver MRI combining phase contrast imaging, elastography, and DWI: assessment of reproducibility and postprandial effect at 3.0 T. PLoS One 2014;9(5):e97355.

60. Chouhan, M., Ramasawmy, R., Campbell-Washburn, A. E., Bainbridge, A., Wells, J. A., Davies, N., Pedley, R. B., Mookerjee, R., Punwani, S., Taylor, S., Walker-Samuel, S., and Lythgoe, M. F. Measurement of Bulk Liver Perfusion: Initial Assessment of Agreement Between ASL and Phase-Contrast MRI at 9.4T [abstract]. In: Anonymous. 2013.

61. BRADLEY SE, INGELFINGER FJ, BRADLEY GP. Hepatic circulation in cirrhosis of the liver. Circulation 1952;5(3):419-429.

62. Kin Y, Nimura Y, Hayakawa N, Kamiya J, Kondo S, Nagino M, Miyachi M, Kanai M. Doppler analysis of hepatic blood flow predicts liver dysfunction after major hepatectomy. World J Surg 1994;18(1):143-149.

63. Edrei Y, Gross E, Corchia N, Tsarfaty G, Galun E, Pappo O, Abramovitch R. Vascular profile characterization of liver tumors by magnetic resonance imaging using hemodynamic response imaging in mice. Neoplasia 2011;13(3):244-253.

64. Golay X, Hendrikse J, Lim TC. Perfusion imaging using arterial spin labeling. Top Magn Reson Imaging 2004;15(1):10-27.

65. Karger N, Biederer J, Lusse S, Grimm J, Steffens J, Heller M, Gluer C. Quantitation of renal perfusion using arterial spin labeling with FAIR-UFLARE. Magn Reson Imaging 2000;18(6):641-647.

66. Schor-Bardach R, Alsop DC, Pedrosa I, Solazzo SA, Wang X, Marquis RP, Atkins MB, Regan M, Signoretti S, Lenkinski RE, Goldberg SN. Does arterial spin-labeling MR imaging-measured tumor perfusion correlate with renal cell cancer response to antiangiogenic therapy in a mouse model? Radiology 2009;251(3):731-742.

67. Katada Y, Shukuya T, Kawashima M, Nozaki M, Imai H, Natori T, Tamano M. A comparative study between arterial spin labeling and CT perfusion methods on hepatic portal venous flow. Jpn J Radiol 2012;30(10):863-869.

68. Breedis C, YOUNG G. The blood supply of neoplasms in the liver. Am J Pathol 1954;30(5):969-977.

69. Hoad C, Costigan C, Marciani L, Kaye P, Spiller R, Gowland P, Aithal G, Francis S. Quantifying Blood Flow and Perfusion in Liver Tissue using Phase Contrast Angiography and Arterial Spin Labelling. Proc Intl Soc Mag Reson Med 2011;19:794.

70. Cox, E. F., Ghezzi, A., Bennet, A., Patel, M., Jackson, A., Harman, D., Costigan, C., Omar, N. F., James, M. W., Ryder, S. D., Gowland, P. A., Aithal, G. P., Guha, I. N., and

Francis, S. T. A novel MRI protocol to examine haemodynamic compartments in compensated liver cirrhosis [abstract]. In: Anonymous. 2013.

71. Schalkx HJ, van Stralen M, Peters NHGM, Veldhuis WB, van Leeuwen MS, Pluim JPW, Petersen ET, van den Bosch MAAJ. Pre- and postprandial arterial and portal venous liver perfusion using selective spin labeling MRI with Look-Locker read-out. Proc Intl Soc Magn Reson Med 2014;22:372.

72. Belle V, Kahler E, Waller C, Rommel E, Voll S, Hiller KH, Bauer WR, Haase A. In vivo quantitative mapping of cardiac perfusion in rats using a noninvasive MR spin-labeling method. J Magn Reson Imaging 1998;8(6):1240-1245.

73. Karger N, Biederer J, L++sse S, Grimm J, Steffens JC, Heller M, Gl++er CC. Quantitation of renal perfusion using arterial spin labeling with FAIR-UFLARE. Magnetic Resonance Imaging 2000;18(6):641-647.

74. Williams DS, Detre JA, Leigh JS, Koretsky AP. Magnetic resonance imaging of perfusion using spin inversion of arterial water. Proc Natl Acad Sci U S A 1992;89(1):212-216.

75. Dixon WT, Du LN, Faul DD, Gado M, Rossnick S. Projection angiograms of blood labeled by adiabatic fast passage. Magn Reson Med 1986;3(3):454-462.

76. Kwong KK, Chesler DA, Weisskoff RM, Donahue KM, Davis TL, Ostergaard L, Campbell TA, Rosen BR. MR perfusion studies with T1-weighted echo planar imaging. Magn Reson Med 1995;34(6):878-887.

77. Kim SG. Quantification of relative cerebral blood flow change by flow-sensitive alternating inversion recovery (FAIR) technique: application to functional mapping. Magn Reson Med 1995;34(3):293-301.

78. Schwarzbauer C, Morrissey SP, Haase A. Quantitative magnetic resonance imaging of perfusion using magnetic labeling of water proton spins within the detection slice. Magn Reson Med 1996;35(4):540-546.

79. Edelman RR, Siewert B, Darby DG, Thangaraj V, Nobre AC, Mesulam MM, Warach S. Qualitative mapping of cerebral blood flow and functional localization with echo-planar MR imaging and signal targeting with alternating radio frequency. Radiology 1994;192(2):513-520.

80. Dai W, Garcia D, de BC, Alsop DC. Continuous flow-driven inversion for arterial spin labeling using pulsed radio frequency and gradient fields. Magn Reson Med 2008;60(6):1488-1497.

81. Wong EC. Vessel-encoded arterial spin-labeling using pseudocontinuous tagging. Magn Reson Med 2007;58(6):1086-1091.

82. Okell TW, Chappell MA, Woolrich MW, Gunther M, Feinberg DA, Jezzard P. Vessel-encoded dynamic magnetic resonance angiography using arterial spin labeling. Magn Reson Med 2010;64(2):430-438.

83. Rajendran R, Lew SK, Yong CX, Tan J, Wang DJ, Chuang KH. Quantitative mouse renal perfusion using arterial spin labeling. NMR Biomed 2013.

84. Duhamel G, Prevost V, Girard OM, Callot V, Cozzone PJ. High-resolution mouse kidney perfusion imaging by pseudo-continuous arterial spin labeling at 11.75T. Magn Reson Med 2013.

85. Streif JU, Nahrendorf M, Hiller KH, Waller C, Wiesmann F, Rommel E, Haase A, Bauer WR. In vivo assessment of absolute perfusion and intracapillary blood volume in the murine myocardium by spin labeling magnetic resonance imaging. Magn Reson Med 2005;53(3):584-592.

86. Kober F. High-Resolution Myocardial Perfusion Mapping in Small Animals in Vivo by Spin-Labelling Gradient-Echo Imaging. Magn Reson Med 2004;51:62-67.

87. Campbell-Washburn AE, Price AN, Wells JA, Thomas DL, Ordidge RJ, Lythgoe MF. Cardiac arterial spin labeling using segmented ECG-gated Look-Locker FAIR: variability and repeatability in preclinical studies. Magn Reson Med 2013;69(1):238-247.

88. Yang RK, Roth CG, Ward RJ, deJesus JO, Mitchell DG. Optimizing abdominal MR imaging: approaches to common problems. Radiographics 2010;30(1):185-199.

Chapter 2

Theory and Materials

This chapter presents an overview of the relevant theory prerequisite for the following chapters. MRI theory, including image relaxation and image acquisition will be introduced. The origin and quantification of the MRI perfusion measurement using arterial spin labelling, used in Chapters 3 - 5, will be covered. In addition, the theory of phase-contrast velocity measurements and field mapping will be covered as these techniques are used in Chapters 4 & 5. Finally, an overview of the hardware used in this thesis research will be presented.

2.1 The Principles of Magnetic Resonance Imaging

2.1.1 Origin of the MRI Signal

A brief overview of magnetic resonance imaging (MRI) will be presented in this chapter, explaining the derivation of the signal and the acquisition of an image. However, more detailed explanations can be found in the literature of Haacke, Bernstein and McRobbie (1-3).

The origin of the nuclear magnetic resonance (NMR) and MRI signal is founded in the quantum mechanical description of nuclei with non-integer spin. Nuclear spin is an intrinsic property of protons and neutrons, and nuclei formed of an uneven number will exhibit a discrete angular momentum. The predominant non-integer spin isotope used in MRI is ^{1}H – hydrogen, which is found in great abundance within organic tissue, in addition, MRI has been performed measuring ^{18}F – Fluorine, ^{23}Na Sodium ^{31}P – Phosphorus signal. The spin property manifests as a nuclear magnetic moment, which in the presence of a magnetic field, cause these nuclei to precess from the resultant torque. This mechanism is similar to the classical example of a gyroscope precessing in the Earth's gravitational field. Lamor described that the rate of precession will be proportional to the present magnetic field:

$$\omega = \gamma B. \qquad \text{Equation 2.1}$$

The gyromagnetic ratio γ will vary depending on the nuclei – for Hydrogen, γ_H = 42 MHz/T. Characterisation of the Lamor frequency is fundamental to the 'resonance' principle of MRI, and it is possible to build up an image with the use of additional magnetic field gradients, as will be explained later.

When present in a magnetic field (referred to as B_0), nuclei will align parallel or anti-parallel to the external field. The two states of alignment have an energy difference ΔE = $\hbar\omega$, where $\hbar$ is the reduced Planck's constant, which determines the detectable signal from the spins. From Equation 2.1, it is possible to observe that greater strength external fields will result in a larger energy difference. Most of the nuclei's angular momentum will cancel out due to the parallel/anti-parallel alignment, however, a small number will remain unopposed in the lower energy state, as determined by the Maxwell-Boltzmann distribution:

$$\frac{N_+}{N_-} = e^{\frac{\hbar\omega}{k_B T}}. \qquad \text{Equation 2.2}$$

N_+ represents the number of spins aligning parallel with B_0, N_- the number of anti-parallel spins, k_B – the Boltzmann constant and T is the temperature. This ratio is very small at room temperature (approximately 7 N+ per million N-, at room temperature and at 1T), however

due the number of spins present within tissue, the small ratio manifests as a tangible macroscopic magnetisation. The convention of MRI defines the B0 field in the z direction, thus the macroscopic magnetisation precesses around the z-axis at a frequency determined by Equation 2.1.

2.1.2 MRI Principles: Excitation

Common MRI field strengths between 1 – 9.4 T, equate to a resonant frequency approximately between 40 – 400 MHz for hydrogen nuclei, which is that of radiofrequency (RF). Using an electromagnetic pulse, the spins can be manipulated using the magnetic component of these waves.

It is often easier to comprehend the interactions of the applied pulses by switching to a rotating reference frame, spinning around the z-axis at the Lamor frequency (Figure 2.2A). In this frame, the magnetisation is fixed, and pointing along the z-axis. Application of a circularly-polarised RF pulse at the Lamor frequency results in a relatively small magnetisation vector B_1, in this example, along the y-axis (Figure 2.2B). The presence of this new external magnetic field will result in the magnetisation to precess around the y-axis.

Changes in the magnetisation $M(t)$ due to the magnetic field $B(t)$ are described by the Bloch equations, which are derived from the Lamor relation. Ignoring any spin relaxation:

$$\frac{d\vec{M}(t)}{dt} = \vec{M}(t) \times \gamma\vec{B}(t). \qquad \text{Equation 2.3}$$

From this equation, in the rotating frame, it is predicted that the magnetisation will precess around the y-axis at a slower rate than the Lamor frequency. In the laboratory frame, the magnetisation rotates around the effective magnetic field Beff, which is the vector sum of applied fields (Equation 2.4). This results in the magnetisation to precess at an angle to the z-direction. The spins are described as being in an excited state, as the magnetisation will have a component in the transverse plane, which can be detected within receiver coils by Faraday induction. Applying the B_1 field for ranges of durations and pulse powers will control the angle the magnetisation vector makes with the z-axis, known as the 'flip-angle' (Figure 2.2B). As the detectable signal within the receiver coils is determined by the transverse projection of the magnetisation vector, thus a maximal signal will follow a 90° pulse.

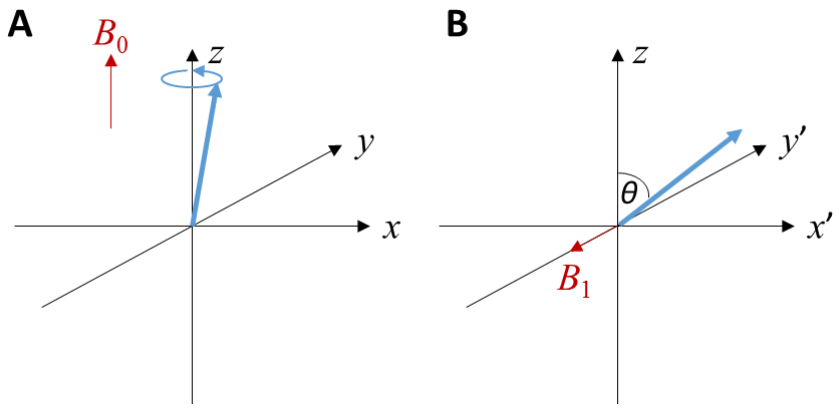

Figure 2.2: (A) A spin precessing around the B_0 field, applied in the z-direction. (B) A spin in the rotating frame during the application of an on-resonance RF pulse. In this example, the magnetic component of the circularly-polarised pulse is in the y-axis. Due to the presence of the new magnetic field B_1, the spin begins to precess around *y*-axis. The angle (θ) the spin makes with the z-axis is known as the flip angle, which will depend on the strength and duration of B_1.

$$\vec{B}_{eff} = B_1\hat{y} + B_0\hat{z}. \qquad \text{Equation 2.4}$$

2.1.3 MRI Principles: Relaxation

Two signal decay mechanisms of the MRI signal have been empirically observed; longitudinal (T_1) and transverse relaxation (T_2 & T_2*). T_1 relaxation is propagated by thermal interaction between the spins and the "lattice" – the environment the spins are in. The spin-lattice relaxation determines the rate at which the longitudinal component of the magnetisation M_z returns to the B_0 direction following excitation:

$$\frac{dM_z}{dt} = \frac{M_0 - M_z}{T_1}. \qquad \text{Equation 2.5}$$

Equation 2.5 describes that the rate of decay recedes as the spins approaches the equilibrium magnetisation M_0. Methods to quantify tissue T_1 properties are explored in Chapter 2.3.1.

Transverse relaxation describes the loss of the detected MRI signal due to incoherent precession of the excited spins. When the macroscopic magnetisation is tipped into the transverse plane, the spins are in phase and a maximal transverse magnetisation can be detected. However, due to the magnetic field of each spin perturbing neighbouring spins, the spins will dephase as a result of the different Lamor frequencies each will be precessing at. In the rotating frame, this will appear as magnetisation vectors fanning away from the *x*-axis, after a 90° flip angle excitation pulse. This results in the net transverse magnetisation $M_{x,y}$ decaying to zero, as characterised by the transverse rate T_2:

$$\frac{dM_{x,y}}{dt} = -\frac{M_{x,y}}{T_2}. \qquad \text{Equation 2.6}$$

Spin-spin propagated decay as described by Equation 2.6 is the behaviour of spins in a perfect system. However, local inhomogeneities of the magnetic field, caused by the sample creating susceptibility variations, increase the rate of dephasing. This acceleration of dephasing is characterised by T2*. Introducing a factor T2', which accounts for the field inhomogeneity, T_2* is defined:

$$\frac{1}{T_2^*} = \frac{1}{T_2} + \frac{1}{T_2'}. \qquad \text{Equation 2.7}$$

T_2* decay behaves as T_2 and is similarly described by Equation 2.6. It is generally observed that for the same tissue type, T_2* < T_2, and that transverse decay is much faster than the thermally-driven relaxation of T1. Methods to quantify tissue T_2/ T_2* properties are explored in Chapter 2.3.2. MRI acquires images using two techniques known as gradient echo and spin-echo imaging. The influence of the field inhomogeneities T_2' can be removed by the use of spin-echo MRI to characterise T_2, and gradient-echo MRI will include T_2* weighting; these sequences will be explained later in this chapter.

2.1.4 MRI Principles: Slice Selection

Consider a uniform sample in a uniform magnetic field; application of an on-resonance RF pulse will excite the entire volume, which obviously will not be medically relevant. However, applying a gradient G_z in the z-direction will facilitate a selective excitation:

$$B_z(z) = B_0 + G_z z. \qquad \text{Equation 2.8}$$

Using the Lamor relation, it is apparent that the sample's resonant frequency is spatially dependent on z. Applying an RF pulse at one frequency will thus only excite a 'slice' of the sample (Figure 2.3). However, a radiofrequency emission will contain a finite bandwidth of frequencies ($\Delta\omega$). Thus, a slice thickness (Δz) is defined by the slice-selection gradient (G_z) and the excitation bandwidth:

$$\Delta z = \frac{\Delta\omega}{\gamma G_z}. \qquad \text{Equation 2.9}$$

This relation assumes a uniform or 'box-car' excitation of the slice. The excitation profile is dependent on the Fourier Transform of the RF pulse shape, thus, for a box-car profile, a sinc RF pulse is required. As the ideal shape of a sinc pulse requires many 'side lobes', these pulses are often truncated, as a compromise between acquisition speed and idealised excitation profiles. Figure 2.3 also demonstrates how multiple slices can be excited using

the same slice-selection gradient: using successive RF pulses with resonant frequencies separated by their bandwidth; it is possible to excite contiguous slices for 2D MRI.

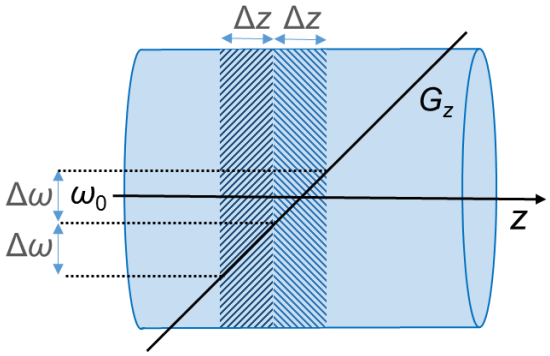

Figure 2.3: Schematic showing the prinicple of spatial frequency encoding and slice-selection. A gradient Gz is applied along the z-axis, leading to a z-dependence on the Lamor frequency within the sample. Application of a RF pulse, with frequency ω0 and bandwidth Δω, will lead to a discrete slab with thickness Δz. Application of a separate RF pulse at another frequency will lead to a subsequent slice to be excited with the same gradient, facilitating multi-slice acquisition.

2.1.5 MRI Principles: Frequency & Phase Encoding

Once the slice has been excited, the sample information is extracted using frequency and phase encoding. Frequency encoding works in the same manner as the slice selection: a linear gradient is applied in the frequency-encoding direction (orthogonal to the slice-selection), resulting in a spatial dependency of the frequencies. This gradient is also known as the read-out gradient (G_{RO}), as this is applied during the image acquisition. Considering a 1D example, with two samples at distinct positions – each sample will have a unique frequency during the application of G_{RO}. The detected signal in the receivers will be two exponentially decreasing (due to transverse relaxation) sinusoidal frequencies mixed together. As the data has been frequency-encoded, a Fourier Transform (FT) is required to return the data in to real-space. Using a Fourier transform, it is possible to identify the two frequencies and respective amplitude, and knowing the magnitude and duration of the frequency-encoding gradient, the position of the signal sources can be identified.

Phase-encoding extends this principle further by applying a phase-encoding gradient (G_{PE}), perpendicular to the read-out gradient (and to the slice-selection). Phase-encoding gradients are applied incrementally to 'comb' the sample for spatial frequencies, and will build up a 2D image in Fourier-space or k-space.

When acquiring the 2D k-space data, a single phase-encoding gradient is applied, alongside the read-out gradient (typically negative) to move the wave vector to the edge of the k-space. During the data acquisition, the read-out gradient is turned on, resulting in the wave

vector (k_{RO}) filling up this line of k-space. When the 2D k-space matrix is acquired, the largest signal is acquired when $G_{PE} = 0$, and the lowest signal is when G_{PE} is maximal (Figure 2.4A). K-space is digitised in to a number of matrix points, (typically 64 or 128), and commonly a square matrix is built up by using the same number of phase-encoding steps as the frequency matrix.

The receivers digitise the acquired signal using a demodulation process, which multiplies the acquired signal by a sine and cosine approximately at the B0 frequency. The resultant signals will be the sum of a low frequency and a high frequency signals – the high frequency component can be filtered out, and thus reduce required sampling frequency of the digitiser. The two resultant demodulated signals will then be digitised as the real and imaginary data, and recombined within the complex k-space.

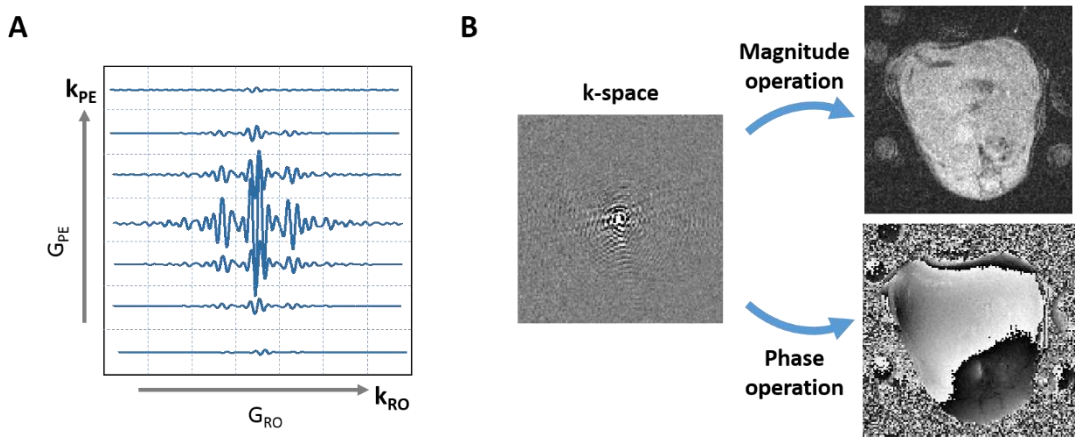

Figure 2.4: 2D image acquisition in k-space: (A) Schematic of k-space, application of phase-encoding and readout gradients move through k-space. The largest signal is acquired in the centre of k-space, the sustained readout gradient is applied alongside the receiver acquisition, so the signal is focussed in the middle of k_{ro}. The phase-encoding gradient is incremented per readout so that over the image acquisition, an analogous phase encode gradient is applied in the k_{pe} direction. Increasing the number of phase-encoding steps and receiver digitisation will increase the image resolution. (B) From the fourier transform (FT) of the complex k-space data, the images can be separated in to the magnitude and phase images. The majority of MRI analyses the magnitude data, but useful information can be encoded within the phase image.

A 2D Fourier transform of the k-space data will result in a complex, real-space dataset. The magnitude of this is the image form that is most prevalent in MRI, and the phase of the complex, real-space data can be used for velocity and field measurements (Figure 2.4B). The next sections look at the two forms of how the image is acquired: gradient- and spin-echo imaging.

2.2 Pulse Sequences

2.2.1 Gradient Echo Imaging

The gradient-echo (GE) technique is designed to acquire the radiofrequency signal using a reversal of the read-out gradient in order to locate the maximal magnetisation signal in the centre of k-space; the steps have been described in Figure 2.5. Figure 2.5A shows a schematic of a sequence diagram: the applied RF, gradients and expected signal are represented with respect to time. Step 1 is the slice-selective excitation: the RF pulse shape represents a truncated sinc function. The slice selective gradient G_{SS}, previously denoted as G_z, is applied and held on for the duration of the excitation pulse. A negative rephasing lobe is included to G_{SS} to balance any additional phase accrual caused by the presence of the slice-selection gradient. The gradients have all been represented with a trapezoidal shape, to represent the real-world limitation of ramp-time for the gradients to be switched on.

The signal refocusing is best understood in the rotating transverse plane, represented in Figure 2.5B: the magnetisation begins to dephase (step 2) following excitation, then the read-out gradient is applied negatively (step 3) which causes the spins to dephase faster. This negative lobe also moves the point in k-space to the edge of k_{RO}, and the application of the phase-encoding gradient also moves the point in k-space in the k_{PE} direction (red arrows Figure 2.5C). Two example trajectories have been shown for separate excitation and acquisitions; the application of different phase-encoding gradients will facilitate building up the k-space data. The time between successive excitation pulses is defined as the repetition time (TR).

The read-out gradient is then reversed, and at the same time the receivers are turned on. The reversal of the read-out gradient causes the magnetisation to rephase (step 4), eventually forming a coherent echo (step 5). The time between excitation and rephasing is known as the “echo-time” or *TE*. The readout gradient is left on until the other edge of k-space is reached, while the magnetisation continues to dephase (step 6).

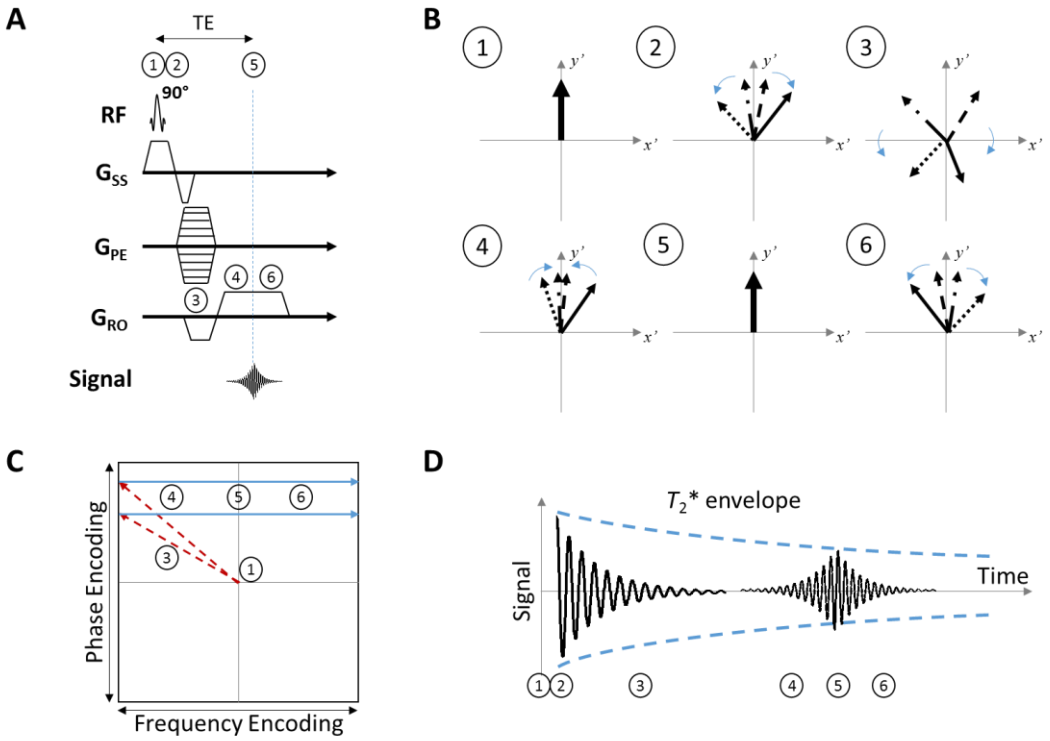

Figure 2.5: Gradient Echo (GE) sequence. (a) Sequence diagram (RF – radiofrequency pulses, G_{SS} – slice select gradient, G_{PE} – phase encoding gradient, G_{RO} – readout gradient, Signal – expected signal acquisition and receivers opened). (b) Schematic of the behaviour of four spins in the rotating transverse magnetisation frame. (c) K-space schematic showing the path traversed for two phase-encoding steps. (d) Representaion of the acquired signal if the receivers were on for the steps. Slice-selective excitation (1) followed by immeditate dephasing in the transverse rotating frame (2). Spatial encoding by application of phase-encoding and a negative readout gradients (3), the readout gradient is then reversed (4) which will cause the transverse magnetisation to rephase. A signal maximum occurs at the point the total readout gradient moment is equal to zero (5). The readout gradient is held on and the signal decreases as the magnetisation continues on to dephase (6).

Considering the signal acquired in the receiver coils (Figure 2.5D), a maximal signal is present immediately following excitation, and the presence of the read-out gradient accelerates the signal decay, which is recovered following the reversal of the gradient. The signal at the echo will be reduced by the T_2* decay present, due to field imperfections, thus, GE imaging is considered to be T_2*-weighted. This effect of T_2* decay can be removed by the use of spin-echo imaging, as will be explained in the next section.

2.2.2 Spin Echo Imaging

The spin-echo (SE) technique uses a second RF pulse to refocus the magnetisation in the transverse plane; the steps have been represented in Figure 2.6. The sequence diagram (Figure 2.6A) is similar to that of the gradient-echo technique, however, following excitation (step 1), a positive read-out gradient is applied alongside a phase-encoding gradient (step 2). In the transverse plane (Figure 2.6B) the spins dephase as a result of the applied

gradient and local inhomogeneity, and the position in the k-space matrix (Figure 2.6C) is taken at the right-hand side. A slice-selective 180° RF pulse is then applied on the *y*-axis, which results in the magnetisations being flipped around the y-axis (step 3), also manifesting as a reflection in the x-y direction within k-space (grey arrow, Figure 2.6B). The spins will consequently begin to refocus (step 4), as each magnetisation will have the same angle to sweep at the frequency it was travelling before. The echo (step 5) will occur at twice the time period between the 90° and 180° pulse, thus the readout gradients are switched on before the echo time (TE) and the receivers are turned on, and the magnetisation will continue to dephase after (step 6). Due to the 180° pulse, the effects of the T_2* are removed as the local dephasing is reversed to produce the signal echo, thus signal detected in the receivers is only reduced due to spin-spin interactions (Figure 2.6D).

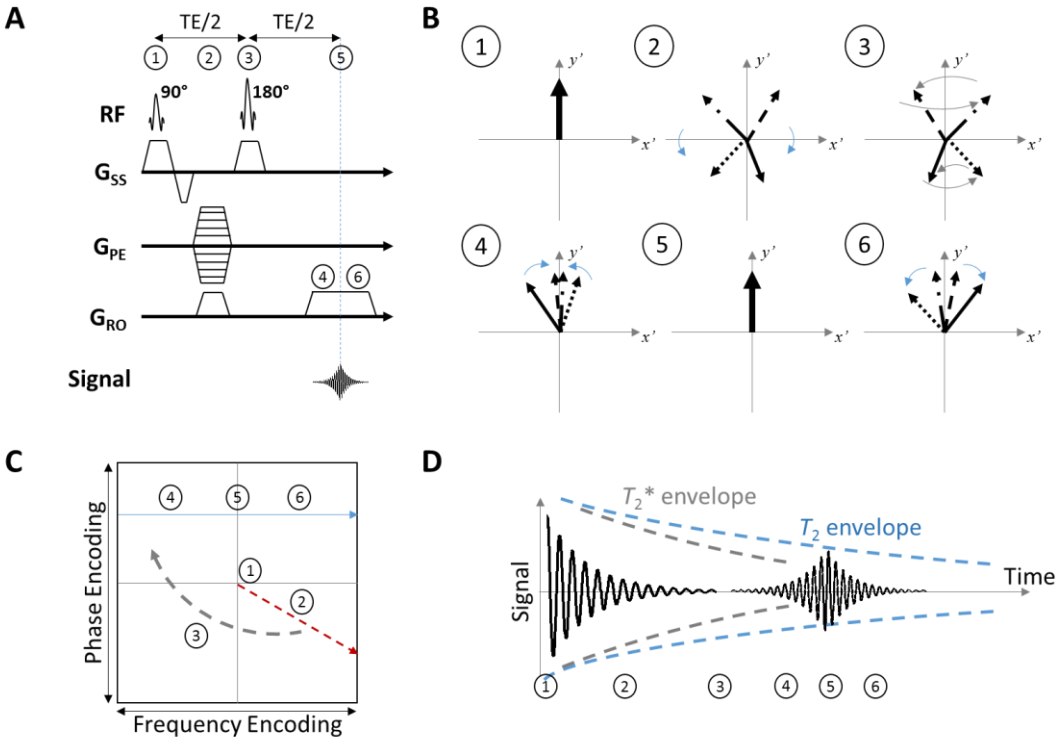

Figure 2.6: Spin Echo (SE) sequence. (a) Sequence diagram – the spin echo utilises an 180° pulse to refocus the spins. (b) Schematic of the behaviour of four spins in the rotating transverse magnetisation frame. (c) K-space schematic showing the path traversed for an example phase-encoding step. (d) Representation of the acquired signal if the receivers were on for the steps. Slice-selective excitation (1) followed by spatial encoding by application of phase-encoding and a readout gradient (2). An 180° pulse is applied alongside a slice selection gradient (3), causing the spins to flip around the y-axis. The pulse is followed by the readout gradient (4) which will cause maximal rephasing when the readout gradient areas before and after the 180 are equal (5). The readout gradient is held on and the signal decreases as the magnetisation continues to dephase (6).

2.2.3 Echo Planar Imaging

Echo planar imaging (EPI), was first presented in the early 1980s by Mansfield *et al.* (4) as a rapid imaging technique in which multiple lines of k-space are acquired in every TR, resulting in short scan durations <100 ms. This segmented acquisition uses fast oscillations of the readout gradients to move in positive and negative trajectories along the frequency encoding direction. A brief phase-encoding gradient is 'blipped' in order for the data to fill k-space. EPI can be used as a gradient or spin-echo acquisition (Figure 2.7A & C), the sequence premise is as above, but with the rapidly oscillating gradients applied afterwards. Using such an acquisition method, the k-space matrix can be filled following a single excitation, (known as a 'single-shot'). However, in many cases, a small number of interleaved 'shots' are used to systematically fill up k-space (Figure 2.7B). With its short acquisition time, EPI has found many applications in brain MRI, such as dynamically imaging functional MRI (fMRI), diffusion and perfusion imaging.

However, the rapid gradients used in EPI can lead to image distortions as the technique is dependent on large, fast, and well-shielded gradient coils. Alternate echoes are time-reversed before the Fourier Transform into the image domain, however residual differences between odd and even echoes due to eddy currents, gradient asymmetry and magnetic field inhomogeneity can lead to a reconstruction artefact known as a 'Nyquist ghost'. The effect of this ghost can be corrected using an EPI reference scan with no phase-encoding. In addition, the rapid bipolar gradients result in a small signal bandwidth in the phase-encoding direction, leading to large chemical shift artefacts, which can be minimised with suppression pulses. The small bandwidth means that perturbations in the magnetic field manifests as large image distortions in regions of high susceptibility, typically found at air-tissue boundaries. Using a multi-shot EPI acquisition can decrease the image distortions by effectively increasing the phase-encoding bandwidth per shot.

The techniques presented here and used in the remainder of this thesis use 'Cartesian' acquisition of k-space; the data is acquired along the frequency encoding direction. An alternative method to rapidly acquire images uses radial or spiral trajectories to cover k-space. Such regimes can quickly acquire images and suppress motion artefacts, however, these require well calibrated gradients to reconstruct the images.

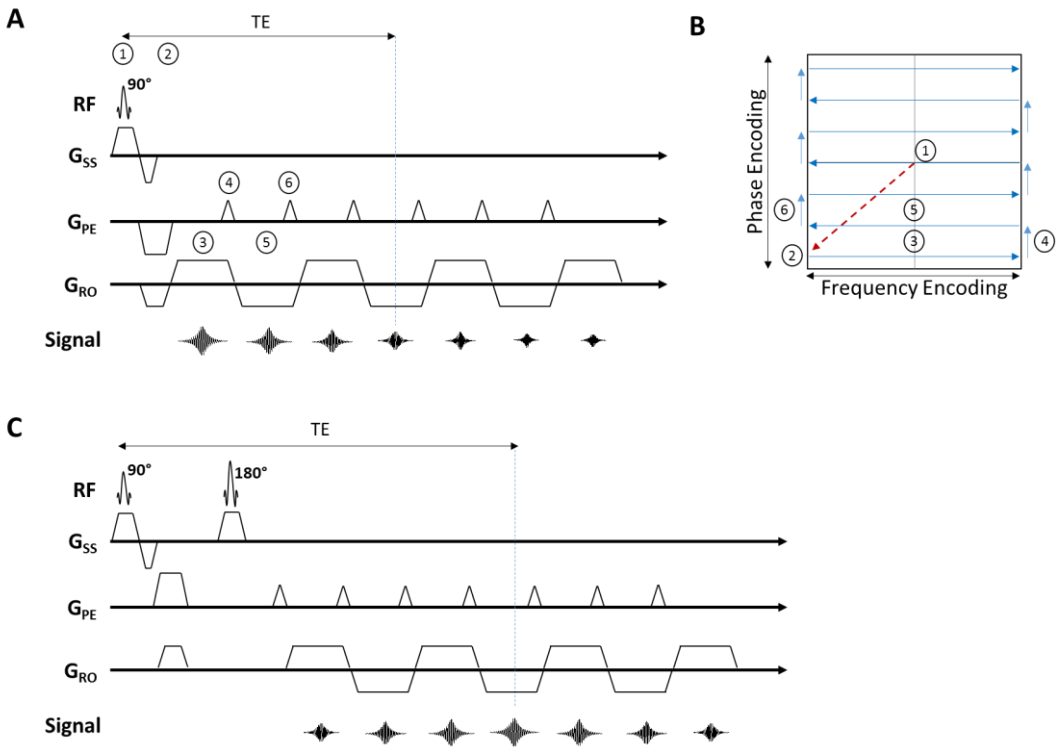

Figure 2.7: Echo Planar Imaging (EPI) sequence diagrams. (A) GE-EPI: The excitation steps (1-3) are the same as the GE technique. At the end of the readout gradient a phase-encoding gradient 'blip' is applied (4) to jump in up to the next phase-encoding step. The readout gradient is reversed, and the next echo is acquired (5) until the end of the readout gradient and the next blip (6). This process is continued until the end of the EPI acquisition; in this example, 7 lines of k-space are acquired per excitation, where usually this will much longer (up to 64 for a single-shot). (B) K-space trajectory for the GE-EPI example. (C) SE-EPI, which uses the same excitation as the standard SE-EPI, followed by the rapid gradient-switching.

2.3 Quantification of MRI Relaxation

2.3.1 Longitudinal Relaxation: T_1

The longitudinal relaxation times of tissues are quantified by inverting the magnetisation and characterising the signal evolution in a process known as 'inversion recovery'. Solving Equation 2.5, and using a perfect inversion, the magnetisation will relax back to equilibrium, passing through zero (Figure 2.8A). As MRI signal is magnitude data, the signal will follow the magnitude of this equation:

$$S(t) = S_0\left(1 - 2e^{-t/T_1}\right) \qquad \text{Equation 2.10}$$

Where S_0 is the equilibrium signal, and $S(t)$ is the measured time-dependent signal. The simplest MRI acquisition to characterise the signal recovery is shown in Figure 2.8B: an

inversion pulse is followed by an excitation and read-out (here shown as a gradient-echo). The time between inversion and excitation pulse is known as the inversion time or *TI*. The magnetisation is then left to recover back to equilibrium (typically around 5x the longest T_1) before the next inversion pulse. Multiple TI measurements facilitate a better fitting of the signal recovery and improves the T_1 estimation, and thus, this sequence is inefficient at characterising the signal recovery: one line of k-space of one TI is being acquired per inversion. Look and Locker (5) proposed a scheme to increase the efficiency of the sequence by including multiple, small flip-angle excitation pulses, separated by a regular inversion time ($TI_{Look\text{-}Locker}$) per inversion pulse (Figure 2.8C). This regime facilitates multi-TI acquisition per inversion, and the small flip-angle (<10°, (6)) sampling ensures that the inversion recovery is not disrupted.

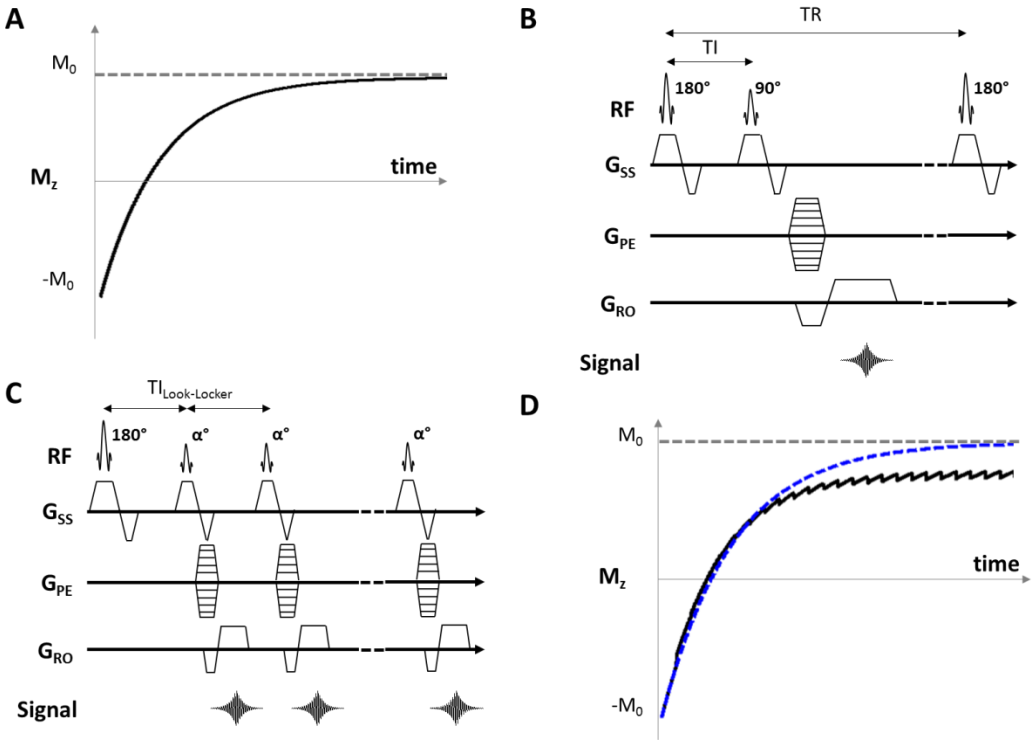

Figure 2.8: Quantification of T_1: (a) Schematic of magnetisation behaviour following a 180° pulse, this shape is known as inversion recovery (IR). (b) A IR-GE acquisition sequence diagram, the normal gradient echo acquisition is preceded by an inversion pulse. The inversion time (TI) is set to characterise the image signal along the IR curve, and the magnetisation is left to relax back to equilibrium before the subsequent 180° pulse set by the repitition time (TR). With this technique, a single line of a single TI is acquired per inversion pulse - increased TIs allow for better characterisation of the recovery curve. (c) Sequence diagram of a Look-Locker technique for efficient IR characterisation. The initial inversion is followed by regularly spaced (interval TILook-Locker) small flip-angle (α < 10°) pulses, allowing for multiple TIs to be acquired per inversion pulse to increase the efficiency of the T1 characterisation. (d) The regular pulses in the Look-Locker acquisition each impart a small deflection in the magnetisation (black curve), and this acrues to an eventual signal saturation and the equilibrium magnetisation does not recover fully to M_0 like the standard inversion recovery (blue dash).

However, the Look-Locker train will partially saturate the tissue signal, resulting in an apparent longitudinal relaxation time, T_1*, that is shorter than the true T_1 time (Figure 2.8D). If the sampling pulses with flip angle α is spaced at regular intervals $TR_{\text{Look-Locker}}$, T_1* will be given by:

$$T_1^* = \left\{ \frac{1}{T_1} - \frac{1}{TR_{Look-Locker}} \ln(\cos(\alpha)) \right\}^{-1}. \qquad \text{Equation 2.11}$$

However, it is difficult to calculate the T_1 from this equation because the exact value of α is impractical to estimate due to B_0 inhomogeneity and imperfections in the selective pulse. T1* can then estimated by fitting data to a three parameter model (Equation 2.12) (7).

$$S(t) = S_0(1 - \beta e^{-t/T_1^*}) \qquad \text{Equation 2.12}$$

The true T_1 can be estimated using Equation 2.13 (6), which factors the signal saturation, where β is the inversion efficiency from Equation 2.11, which assumes a perfect initial inversion.

$$T_1 = T_1^*(\beta - 1) \qquad \text{Equation 2.13}$$

2.3.2 Transverse Relaxation: T_2 & T_2*

Transverse relaxation rates can be measured by repeating gradient and spin-echo acquisitions at a range of echo times, respectively for T_2* and T_2 quantification. Solving Equation 2.6 shows that the transverse signal decays exponentially with the increased incoherence of the spins (Figure 2.9A):

$$S(t) = S_0 e^{-t/T_2} \qquad \text{Equation 2.14}$$

The estimation of transverse relaxation will be improved with an increased number of echoes, thus the efficiency of the T_2 and T_2* measurements can be improved by using multiple echoes per excitation – an example pulse sequence of a multi-echo, GE acquisition has been shown in Figure 2.9B. Transverse relaxation times are often reported as the inverse rates: R_2 and R_2*.

Spin echo measurements can be sped-up by using a fast spin echo (FSE) acquisition. The concept is similar to the multi-echo GE sequence; multiple 180° pulses and readouts follow the excitation pulse. As k-space is being filled following a single excitation, the image is

formed from a mix of echo times; therefore such a technique is not optimal for quantitative T_2 mapping, though efficient for anatomical imaging.

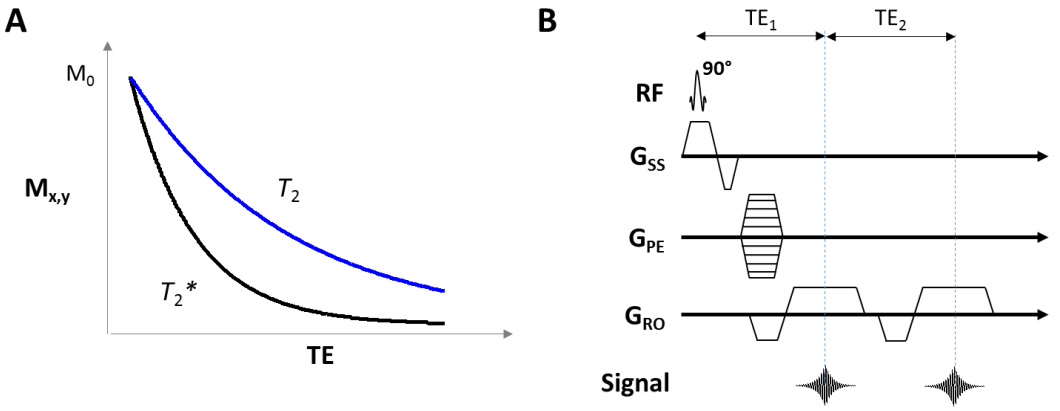

Figure 2.9: Quantification of the transverse relaxation: (A) Signal evolution of T_2 (blue) and T_2* (black) with echo time. Spin-echo experiments will give T_2 weighting and gradient-echo will give T_2* weighting. (B) Sequence diagram for a multi-echo gradient echo sequence for efficient T_2* characterisation.

2.4 Arterial Spin Labelling

2.4.1 The Modified Bloch Equations

Detre *et al.* first suggested using arterial blood to act as a endogenous tracer to measure tissue perfusion (8). The blood was labelled, via inversion, in transit within the carotid arteries. Following labelling, the blood will pass into the brain's capillary bed and exchange magnetisation with the tissue. The tissue magnetisation will decrease, and with the use of a control image, the signal differences can be attributed to perfusion. The control image was performed by placing the tag equidistant from the image plane but outside the body such that any magnetisation transfer effects caused by a long duration RF pulse would be removed in the image subtraction. The Bloch equation of longitudinal tissue magnetisation (M) was modified to include a blood flow (P) term:

$$\frac{dM(t)}{dt} = \frac{M_0 - M(t)}{T_1} - P\left(\frac{M(t)}{\lambda} - M_a(t)\right) \qquad \text{Equation 2.15}$$

Where λ is the blood-tissue partition coefficient, which determines the freedom of exchange between the tissue and blood supply, which for most applications of arterial spin labelling is between 0.8 – 1 g ml^{-1} (9-11). M_a is the time-dependent magnetisation of arterial blood. This model assumes a fast exchange of labelled blood in to the tissue, a single compartment and a steady state such that the outflowing magnetisation is equal to $M(t)/\lambda$. The solution to this modified Bloch equation, and thus the quantification of

perfusion is explored below. First, the two methods of blood labelling: continuous and pulsed ASL are explained.

2.4.2 Continuous ASL and Flow-driven Inversion

The technique of vessel-selective tagging introduced by Williams *et al*. used the flowing blood to promote the mechanism of adiabatic inversion. The method, known as adiabatic fast passage (12), applies a gradient in the direction of the blood flow (for example in the z-direction) at the same time as an off resonance RF pulse, resulting in a position dependent frequency offset. Given a time-dependent position for the moving spins, this results in the effective magnetic field (B_{eff}) in the rotating reference frame to have a time-dependence on the *z*-position. The polarity of B_{eff} will then invert as the moving spins pass through the centre of the gradient, and thus the magnetisation will invert as they follow B_{eff}, given the adiabatic condition:

$$\frac{1}{T_2} \ll \frac{Gv}{|\vec{B}_{eff}|} \ll \frac{\gamma|\vec{B}_{eff}|}{2\pi}. \qquad \text{Equation 2.16}$$

At low velocities, the T_2 relaxation of the blood will dominate, and at high velocities the change in B_{eff} is too rapid for the spins to follow. Thus, spins moving at the optimal velocities to be inverted before they exchange with the tissue under investigation. By placing a tag location outside of the brain for the control experiment, no blood would be labelled. In addition, the control tag was positioned such that effects of magnetisation transfer saturation, from the off-resonance pulse, would be matched in order to not overestimate the perfusion.

2.4.3 Pseudo-Continuous ASL

2.4.3.1 Tagging Mechanism

The hardware demands of long CASL pulse and gradient durations were circumvented by instead using a train of many short rectangular pulses (13), to create a 'pseudo' continuous labelling pulse. In addition, the short pulses dramatically reduce the effects of magnetisation transfer saturation. However, the Fourier transform of the rectangular pulse train creates a number of aliased tagging planes. This aliasing effect can be reduced by selecting an RF shape which has a smaller coefficient following the Fourier transformation, such as a Hanning pulse.

The tag selectivity can be further improved by making the tag gradient time-dependent. An increased gradient (G_{max}) is applied for the duration of the Hanning pulse, and the gradient

is reversed (Figure 2.10). Defining the average gradient (G_{ave}) over the RF spacing, aliased labelling planes can be avoided in the following condition:

$$\frac{G_{max}}{G_{ave}} \gg \frac{\Delta t_{RF}}{\delta_{RF}}. \qquad \text{Equation 2.17}$$

Where Δt_{RF} is the spacing between the pCASL tagging pulses with duration δ_{RF}. Thus, by maximising the ratio of G_{max}/G_{ave}, the spatial selectivity of the tagging pulse can be optimised. However, for this condition to produce an effective tag, G_{ave} should be of the same order as a CASL tagging gradient. The control experiments are performed in two manners; i) balanced, where the tag gradient waveform is repeated, and ii) unbalanced, where by alternating the gradient polarity, G_{ave} = 0. The control tag is applied in the same location, unlike the extra-corporeal location used in the original CASL experiment. In both control schemes, the phase between successive tagging pulses is shifted 180° (14), thus the B_{eff} is maintained parallel to the main field and the spins do not invert.

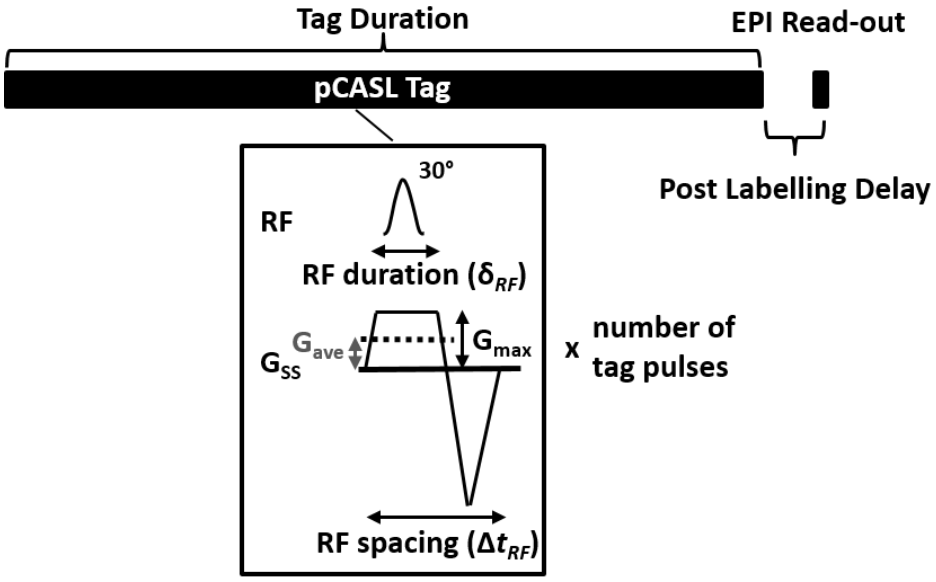

Figure 2.10: Pseudo-continuous arterial spin labelling (pCASL) sequence diagram. The tag is formed from many closely spaced Hanning-shaped RF pulses; these are applied at the same time as the tag gradient with amplitude G_{max}, applied in the blood vessel direction. In this balanced sequence, the tag gradient is rewound to maximise the ratio of the maximum gradient to the average gradient between pulses. This pulse block repeats for the tag duration, followed by a post labelling delay to allow the tagged spins to perfuse the organ. An image readout, for example EPI, follows this delay; the post labelling delay can be varied to assess perfusion dynamics.

2.4.3.2 Multi-phase pCASL Tag Optimisation

Though the pCASL method offers ease of implementation over CASL and an increased SNR over PASL techniques, the method is reliant on the phase evolution of the successive RF pulses following that of the moving spins. The tagging will experience a reduced efficiency

due to a number of factors including B_0 inhomogeneity and gradient and B_1 imperfections, leading to a potential underestimation of perfusion.

Jung *et al*. proposed a system to optimise the control and labelling *in situ*, which varies the phase offset between successive RF pulses (15). It was proposed that the generalised phase of the moving spins will be generated from the sum of two phases; the *track* and *offset* phases. The track phase is contributed by the tagging gradient G_{ave}, the pulse spacing Δt and the distance between the tag plane and the iso-centre z_0: this phase will increment for each pulse. An additional offset phase describes the tag and control RF trains; tagging is achieved by having a zero phase offset between successive pulses, therefore m = 0. A control pulse train will have a 180° phase shift between successive pulses, thus m = 1. However, as a result of field inhomogenities and hardware imperfections, the phase increment may be affected by a 'phase tracking error' ε, between successive pulses. The effect of the phase tracking error can be observed in Figure 2.11. The idealised case with no alias phases is represented with a circle; the tag pulse has a phase offset of 0°, the spins follow B_{eff} and an optimal inversion is achieved (Figure 2.11A). The control experiment has a phase offset of 180°, and the magnetisation remains at equilibrium. The case with a -45° tracking error is presented with a cross, the adiabatic condition is not fully met and the magnetisation is not maximally inverted – in this model the tracking error on the control tag does not significantly alter the magnetisation. The phase tracking error thus results in a reduced tagging efficiency (Figure 2.11B), calculated from the difference between the tag and control magnetisation normalised by the equilibrium magnetisation.

In order to negate the inefficiency of the intrinsic phase error, Jung *et al*. proposed to increment the tag/control offset phase across a 2π range:

$$\Delta\theta = \gamma G_{ave}\Delta t z_0 + 2\pi\frac{m}{M} \quad m = 0,1,\dots M-1. \qquad \text{Equation 2.18}$$

For example m is stepped 45° from 0° to 315°. Jung *et al*. proposed a method of perfusion quantification which models the shape of the tagging efficiency, an additional advantage being that different supply vessels may have variant levels of phase errors. The multi-phase technique can also be used to calibrate single vessel labelling in a more traditional tag-control pair experiment; the tag and control phases will be selected from the maximal difference in signal separated by 180°.

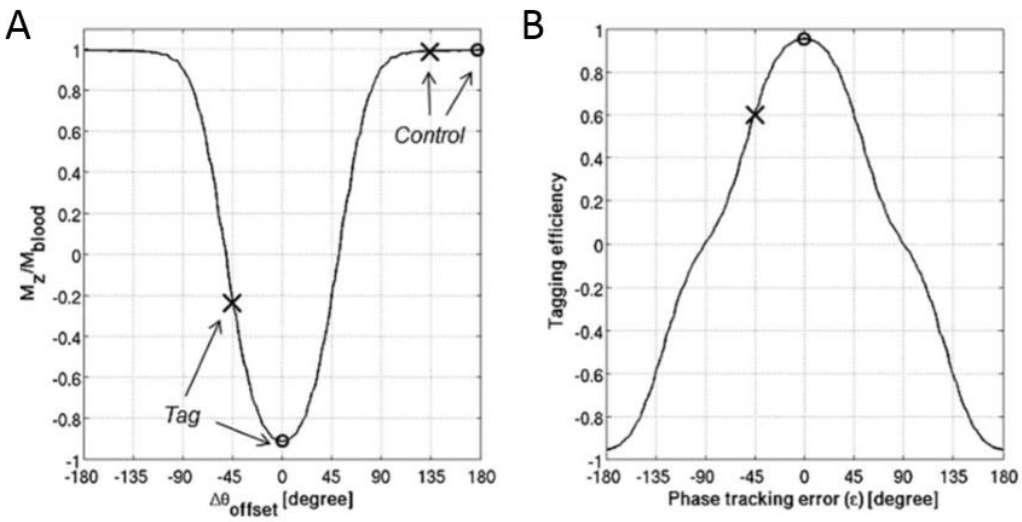

Figure 2.11: Phase tracking errors induced by system faults and field inhomogeneities will result in unwanted phase evolution between successive tagging pulses and thus the magnetisation will not be optimally inverted (a), equivalently this will reduce the tag efficiency (b). An ideal case with zero phase errors is marked with a circle, and a phase error of -45° has been marked with a cross [images taken from Jung *et al*.(15)].

2.4.4 FAIR ASL

Kwong, Kim, Schwarzbauer *et al*. proposed flow-sensitive alternating inversion recovery (FAIR) pulsed ASL around the same time (16-18). Rather than using a long continuous labelling module, FAIR employs two adiabatic inversion pulses to perfusion-sensitise images. The pulsed technique reduced the effects of magnetisation transfer and avoided complex labelling for organs such as the heart. The tag condition is created by a 'global' inversion pulse over the tissue, thus the blood arriving within the imaging slice is recovering longitudinally. The control condition is created by a narrow, 'slice-selective' inversion around the imaging slice; unlabelled blood then immediately flows into the slice, and as this magnetisation exchanges with the tissue, causes an apparent acceleration in the longitudinal tissue magnetisation (Figure 2.12). Pulsed ASL sequences typically employ hyperbolic secant adiabatic fast passage (19) inversion pulses for better slice selection profiles.

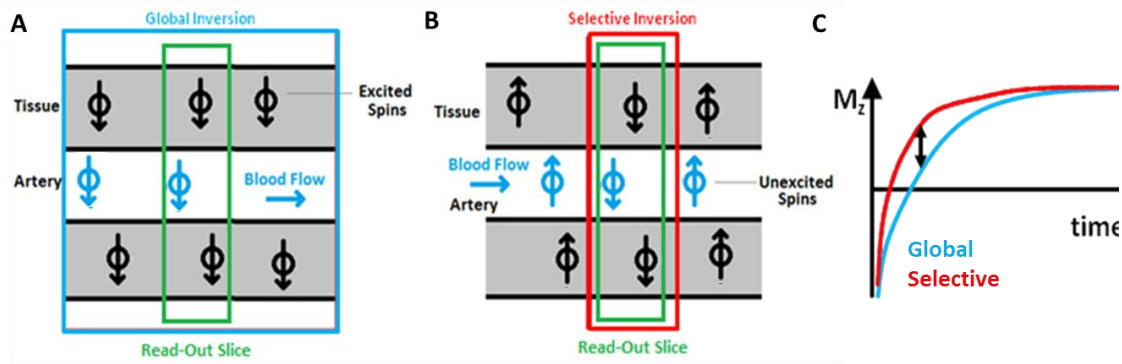

Figure 2.12: Schematic of the Flow-induced Alternating Inversion Recovery (FAIR) sequence: A global inversion of all the spins (a) provides a T1 measurement (blue curve, c) and a selective inversion around the read-out slice (b) will yield an accelerated T1 recovery (red curve, c) as un-inverted arterial magnetisation exchange with the tissue within the read-out slice. Perfusion can be estimated from the difference between the two T1 experiments.

2.4.5 Perfusion Quantification

2.4.5.1 General Model

A general model of perfusion was constructed by Buxton, *et al.* (20) which considers the magnetisation within a voxel after arterial blood tagging and incorporates transit delays from the tag plane to the imaging slice. Three functions are defined to explain the signal evolution of the magnetisation difference between tag and control $\Delta M(t)$: the delivery function $c(t)$, the residue function $r(t,t')$, the relaxation function $m(t)$. The delivery function describes the normalised concentration of arterial magnetisation arriving in the voxel. The residue function describes the fraction of tagged water molecules which arrived at time t' but within the voxel at time t. The magnetisation relaxation function describes the fraction of the original longitudinal tag carried by the water molecules that arrived at time t' and remains at time t.

The signal difference is constructed as a sum over of the delivery of tagged magnetisation to the tissue weighted by the fraction of the remaining magnetisation in the voxel. The amount delivered to a voxel between t' and dt' is $2\alpha M_0 P c(t')$, where α represents the inversion efficiency, and P is the blood flow. The fraction of the delivered magnetisation which remains at time t is then $r(t-t')m(t-t')$:

$$\Delta M(t) = 2M_0 P \int_0^t c(t')r(t-t')m(t-t')dt' \qquad \text{Equation 2.19}$$

This model is based on three assumptions of 'plug flow', single-compartment kinetics and complete extraction from the arterial blood and tissue. The plug flow assumption

essentially models that no labelled blood arrives until the arterial transit time δ, followed by uniform labelling for the tag duration τ, followed by no labelling: this describes the delivery function. The arterial transit time, or transit delay, is due to the gap between the labelling plane and imaging plane – for pulsed ASL techniques, this is generally shorter due to the narrow slice-selective profile around the imaging slice. The single-compartment kinetic assumption describes that potential sub-compartments within the tissue maintain the same concentration ratios due to a rapid exchange of water. In addition, a steady state is assumed that the ratio of the total tissue magnetisation to the venous magnetisation is equal to the blood/tissue partition coefficient: this assumption describes the residue function. The complete extraction assumption means that the labelled water is completely extracted from the vasculature as soon as it arrives within the tissue voxel. The magnetisation first relaxes at the rate of the arterial blood T_{1a}, and once it exchanges with the tissue, continues to relax at the tissue rate T_1: this assumption hence describes the relaxation function. These assumptions can be described mathematically:

$$\begin{aligned} c(t) &= 0 && 0 < t < \delta \\ c(t) &= \alpha e^{-t/T_{1a}} \quad \text{(continuous)} && \delta < t < \delta + \tau \\ c(t) &= \alpha e^{-\delta/T_{1a}} \quad \text{(pulsed)} && \delta < t < \delta + \tau \\ c(t) &= 0 && t > \delta + \tau \end{aligned} \qquad \text{Equation 2.20}$$

$$r(t) = e^{-Pt/\lambda}$$

$$m(t) = e^{-\frac{t}{T_1}}.$$

These equations can then be solved for both the pulsed and continuous labelling schemes. The equations are separated in to piecewise functions, separated by the arterial transit delay and tag duration.

2.4.5.2 Pulsed ASL Solution

The signal difference following pulsed labelling is as follows:

$$M(t) = \begin{cases} 0 & 0 < t < \delta \\ 2M_0 P(t-\delta)\alpha e^{-t/T_{1a}} q_p(t) & \delta < t < \delta + \tau \\ 2M_0 P\tau\alpha e^{-t/T_{1a}} q_p(t). & t > \delta + \tau \end{cases} \qquad \text{Equation 2.21}$$

With the following substitutions:

$$q_p(t) = \frac{e^{kt}(e^{-k\delta} - e^{-kt})}{k(t-\delta)} \qquad \delta < t < \delta + \tau$$

$$q_p(t) = \frac{e^{kt}(e^{-k\delta} - e^{-k(\delta+\tau)})}{k\tau} \qquad t > \delta + \tau$$

$$k = \frac{1}{T_1} - \frac{1}{T_1'}$$

$$\frac{1}{T_1'} = \frac{1}{T_1} + \frac{P}{\lambda}.$$

The signal difference is thus directly proportional to the level of perfusion, as well as a number of other factors. The substitution $q_p(t)$ allows for a number of factors to be collected in to a single, dimensionless term, which typically has a value close to 1. For FAIR the tag duration τ, is given by the volume coverage of the RF coil.

2.4.5.3 Continuous ASL Solution

Solving for the continuous labelling case:

$$M(t) = \begin{cases} 0 & 0 < t < \delta \\ 2M_0 P T_1' \alpha e^{-\delta/T_{1a}} q_c(t) & \delta < t < \delta + \tau \\ 2M_0 P T_1' \alpha e^{-\delta/T_{1a}} e^{-(t-\tau-\delta)/T_1'} q_c(t). & t > \delta + \tau \end{cases}$$

Equation 2.22

With the substitution:

$$q_c(t) = 1 - e^{-(t-\delta)/T_1'} \qquad \delta < t < \delta + \tau$$

$$q_c(t) = 1 - e^{-\frac{\tau}{T_1'}}. \qquad t > \delta + \tau$$

Similarly to PASL , the $q_c(t)$ term simplifies the equations and collect the terms which relate to the steady state of the continuous labelling; if t or τ are much longer than T_1', then q_c approaches 1. In this condition the theoretical advantage of CASL to PASL is derived; the CASL signal reaches a peak steady-state dependent on the flow, apparent relaxation and arterial transit time which is approximately a factor of *e* larger than PASL.

2.4.5.4 Belle Model

Belle et al. (21) suggested a two-compartment model in order to quantitatively study myocardial perfusion measured using FAIR. The two compartments under consideration were the intravascular capillary blood and the extra-vascular tissue; the arterial and venous magnetisation signals are neglected due to their small contribution in the heart. Each compartment has a characteristic longitudinal relaxation time, i.e. labelled blood relaxes with the longitudinal relaxation time of arterial blood, until it reaches and exchanges with the tissue. This implies a fast exchange condition that labelled spins are instantaneously pass from the intravascular volume to the tissue (22). This model, though not designed for

liver parenchyma, was chosen as a simple perfusion model to initially estimate liver perfusion with; the quantification of liver perfusion will be later explored Chapter 3.5.

Quantification of FAIR using the Belle model characterises the apparent acceleration of the longitudinal decay as un-inverted spins flow in to the imaging slice. The apparent T_1 decay following slice-selective inversion will be given by the same relation as above in the general kinetic model:

$$\frac{1}{T_{1,sel}} = \frac{1}{T_1} + \frac{P}{\lambda} \qquad \text{Equation 2.23}$$

The global inversion will depend on these factors:

$$\frac{1}{T_{1,global}} = \frac{\frac{1}{T_1} + \frac{P}{\lambda}}{1 + \frac{P \cdot T_{1,cap}}{\lambda}} \qquad \text{Equation 2.24}$$

$T_{1.cap}$ is the intravascular capillary blood longitudinal relaxation time which can be measured from global T_1 maps. Combining equations (4) and (6) will give:

$$P = \frac{\lambda}{T_{1,cap}} \left(\frac{T_{1,global}}{T_{1,selective}} - 1 \right) \qquad \text{Equation 2.25}$$

Equation 2.25 demonstrates that the perfusion may be estimated from the ratio of the slice-selective to the global T_1 values, thus this technique benefits from an optimised T_1 mapping sequence.

2.5 Phase Contrast

Phase contrast MRI (PC-MRI) uses a gradient-echo sequence with velocity-encoding gradients, applied in the direction of the flow, to proportion phase data to the rate of flow. Velocity encoding gradients take a bipolar form (Figure 2.13): stationary spins will accrue and lose phase so that at the end of the gradient module they will have a zero net phase, whereas moving spins will experience a changing gradient strength, and thus accumulate a non-zero net phase at the end of the velocity-encoding module. The sequence is repeated with the polarity of the bipolar gradients reversed in order to estimate the velocities from the phase difference of the two images.

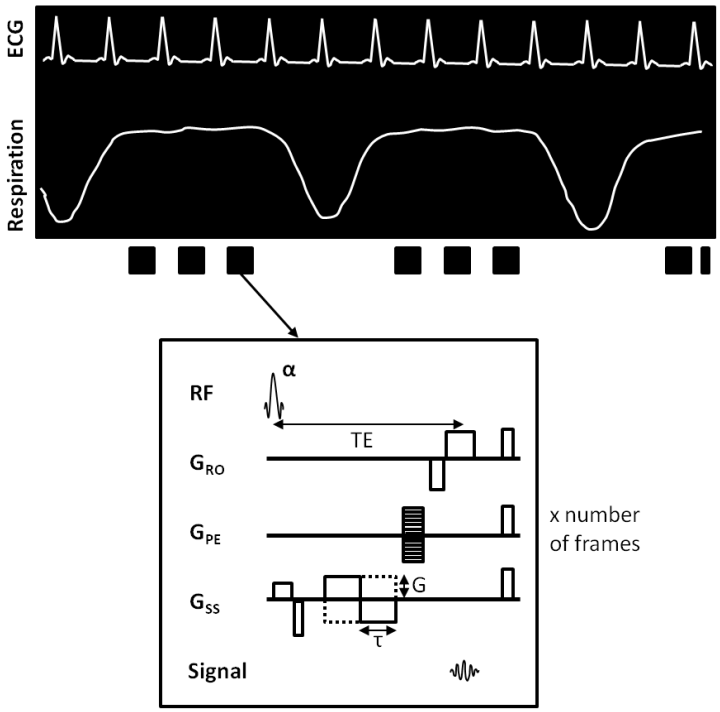

Figure 2.13: Pulse sequence diagram for a cardiac gated phase contrast sequence with flow encoding only in the slice-selective direction. This sequence was based from a cardiac cine sequence, in order to map flow variations in the cardiac cycle. The sequence continues to pulse during respiration, but does not acquire in order to maintain a steady state. The inclusion of bipolar gradients with amplitude *G* and duration *τ* will impart a phase to moving spins, and no phase to stationary spins.

The phase difference between two complex datasets Z_1 and Z_2 can be calculated using Equation 2.26, where the '*' represents the complex conjugate (2):

$$\Delta\phi = arctan\left(\frac{Im(Z_1 Z_2^*)}{Re(Z_1 Z_2^*)}\right). \qquad \text{Equation 2.26}$$

Application of a gradient will give rise to a series of gradient moments m_n. The bipolar nature of the gradients will remove the m_0 component for static spins, and the relatively small contributions of higher moments (i.e. accelerating spins) are ignored. A phase ϕ will be imparted due to the gradient moment m_1 on spins moving with velocity *v,* where γ represents the gyromagnetic ratio:

$$\phi = \gamma m_1 v. \qquad \text{Equation 2.27}$$

With a consecutive, rectangular, bipolar gradient with strength G, and lobe duration *τ,* this yields a gradient moment m_1 given by Equation 2.28:

$$m_1 = G\tau^2. \qquad \text{Equation 2.28}$$

Due to periodic nature of phase, the maximal encodable velocity (v_{enc}) will be limited by a final phase difference of π:

$$v_{enc} = \frac{\pi}{\gamma|\Delta m_1|}. \qquad \text{Equation 2.29}$$

Therefore the velocity as calculated from the phase difference image will be:

$$v = \frac{\Delta\phi}{2\gamma G\tau^2}. \qquad \text{Equation 2.30}$$

The voxel-wise velocity measurements (cm s^{-1}) can be subsequently used to estimate bulk flow to the tissue, by summing up the velocities over the cross-sectional area (cm^2) of the blood vessel, and normalising this to the total mass of the tissue (m_{tissue}). The factor of 60 is included to convert the bulk flow estimate to physiologically relevant units of ml g^{-1} min^{-1}:

$$P_{bulk} = \frac{60}{m_{tissue}} \int v\partial A. \qquad \text{Equation 2.31}$$

Generally, in pre-clinical measurements perfusion units of ml g^{-1} min^{-1} are used for mice (typical weight around 30g). For larger animals and humans, a scaled perfusion measure of ml 100 g^{-1} min^{-1} is more typical.

2.6 B_0 Mapping

Field mapping is performed using a GE acquisition over multiple echoes. The phase of the spins will evolve in the presence of the external magnetic field, and thus the differences in B_0 can be estimated from the evolution of the phase signal over different echo times (*TE*) (23):

$$\phi = -\gamma B_0 TE. \qquad \text{Equation 2.32}$$

The B_0 field can be estimated from a single echo, though the accuracy of the map is improved with including a number echoes. In the ideal case the longest *TE* will not have exceeded a phase of π, however unwrapping algorithms can be applied to overcome this. A requirement of the *TE* spacing is that the water-fat phase is kept constant; this increment can be determined using the Larmor equation (3):

$$\Delta TE = \frac{1}{\gamma B\sigma}. \qquad \text{Equation 2.33}$$

Where σ is the chemical shift, which for water-fat is approximately 3.5 ppm. For 9.4T, using a gyromagnetic ratio of 42.56 MHz T^{-1}, the echo spacing Δ*TE* is equal to 0.71ms.

2.7 Pre-Clinical MRI Equipment

2.7.1 Mouse set-up

All *in vivo* experiments were performed in accordance with the UK Home Office Animals Scientific Procedures Act, 1986. Mice scans were performed in a 9.4T Agilent VNMRS 20 cm horizontal-bore system (Figure 2.14A) with 1000 mT/m gradient inserts with an inner diameter of 60 mm (Agilent Technologies, *Santa Clara, US*). Chapters 3 & 4 used a 39 mm transmit/receive birdcage coil (Rapid Biomedical, *Rimpar*, Germany) (Figure 2.14B), and Chapter 5 used a 35 mm transmit/receive birdcage coil (Rapid Biomedical, *Rimpar*, Germany).

Both mice and rats were anaesthetised using 4% isoflurane (Abbot Laboratories, Illinois, USA) in 1 L O_2/min, and generally maintained between 1-2 % isoflurane in 1 L O_2/min within the MRI scanner, so that the breathing rates would be between 40 – 80 breaths per minute. Mice temperatures were monitored and maintained using heated water pipes and a temperature probe, and respiratory bellows were placed below the sternum for physiological monitoring (SA Instruments Inc., Stony Brook, NY) (Figure 2.14C). An example respiratory trace can be seen in Figure 2.14D, the white and red blocks (arrow) indicate where the gate has been set to. The starting point and the width of the respiratory gate can be adjusted by the user. For example, the trigger point can be set at inspiration or exhalation, and the gate can be further delayed after these triggers. However, the success of these blocks is dependent on the strength and consistency of the breathing. The majority of the experiments were performed without ECG probes, except for cardiac gating phase-contrast MRI measurements which used a three-lead ECG system (SA Instruments Inc., Stony Brook, NY).

The physiology recordings can be sent to a Power1401 data-logger and recorded in Spike2 v5 software (Cambridge Electronic Design, Cambridge, UK) (Figure 2.14E). In addition, a marker can be programmed in to the pulse sequence, typically placed to signal a RF emission. Thus, these markers can be compared against the physiology within the Spike2 software to check the timing of the data acquisition with the status of the respiration. These recordings are later used for retrospective analysis in Chapter 3.4. A gating simulator (SA instruments, NY, USA) (Figure 2.14F), which can generate cardiac traces, including respiration induced spikes to the waveform, was used to test triggering in phantom experiments for sequence development as well as for the prospective gating experiment in Chapter 3.3.

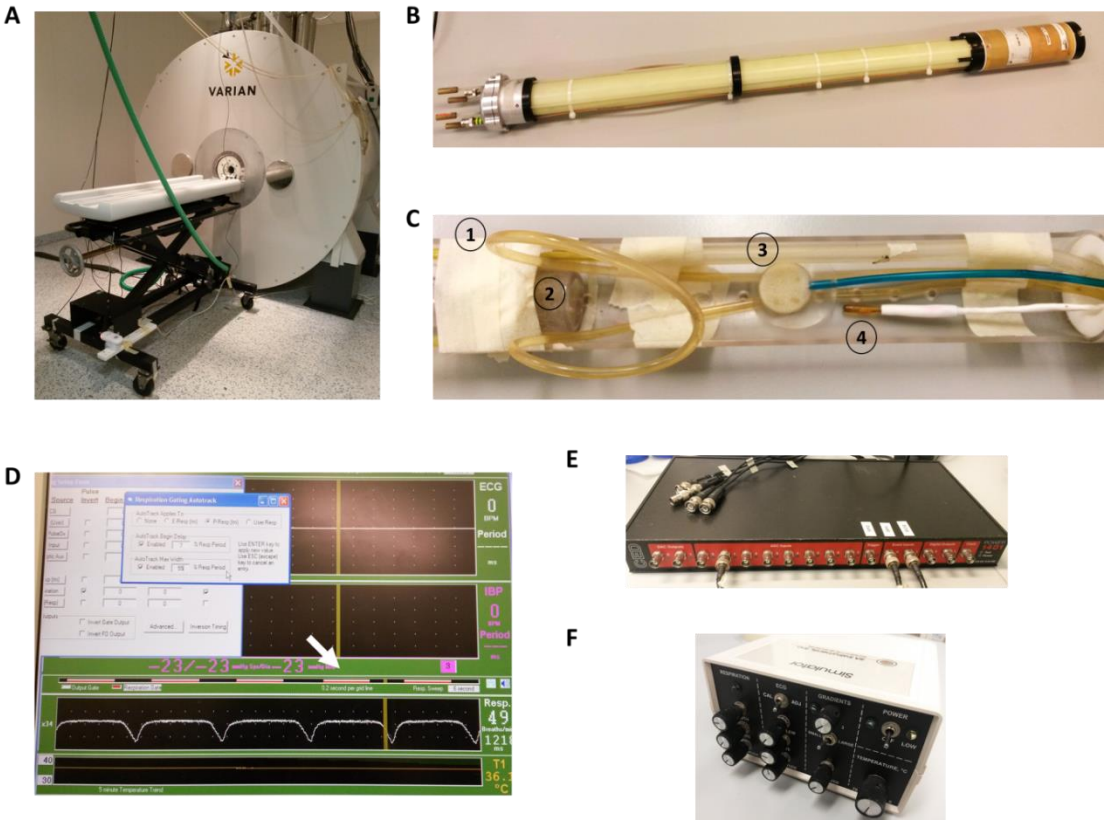

Figure 2.14: Photographs of the equipment used for the majority of the mice experiments. (A) The 9.4T MRI scanner, with the 60 mm gradient inserts. The mouse bed, including the monitoring system, anaesthetic and water pipes are fed in to this side of the scanner. (B) The 39 mm transmit/receive birdcage coil used for imaging; the coil is fed in to the rear of the magnet. (C) Mouse cradle: (1) heated water pipes, (2) nose cone for anaesthesia administration, (3) respiratory bellows (4) rectal temperature probe. (D) Screenshot of the animal monitoring software, reporting on the animal temperature and respiratory rate. The digital gating has been marked by an arrow, corresponding to the red and white block in the software, the position and duration of which is determined by the user. (E) Digital data-logger with inputs set up for recording RF pulse markers, ECG pulses, and digital respiratory gating (as seen in D). (F) Respiration and cardiac simulator box with adjustable amplitude and rate.

2.7.2 Rat set-up

Scans were performed on the 9.4T magnet, with 400 mT/m gradient inserts and an inner diameter of 120 mm (Agilent Technologies, *Santa Clara, US*), using a 72 mm transmit/receive birdcage coil (Rapid Biomedical, *Rimpar*, Germany). The rat bed is a larger analogue to the mouse set-up, with heated water pipes keeping the animal warm and the respiratory bellows and temperature probe used for monitoring the animal's physiology. In addition, all rat imaging was performed using the three-lead ECG system.

References

1. Haacke EM, Brown RW, Thompson MR, Venkatesan R. Magnetic Resonance Imaging: Physical Principles and Sequence Design. 1 ed. Wiley-Liss; 1999.

2. Bernstein M, King K, Zhou X. Handbook of MRI Pulse Sequences. Academic Press; 2004.

3. McRobbie DW, Moore EA, Graves MJ, Prince MR. MRI from Picture to Proton. Cambridge University Press; 2003.

4. Mansfield P. Real-time echo-planar imaging by NMR. Br Med Bull 1984;40(2):187-190.

5. Look D, Locker D. Time Saving in Measurement of NMR and EPR relaxation times. Rev Sci Instrum 1970;41:250-251.

6. Deichmann R, Haase A. Quantification of T1 Values by Snapshot-Flash NMR Imaging. Journal of Magnetic Resonance 1992;96(3):608-612.

7. Deichmann R HA. Quantification of T1 values by SNAPSHOT-FLASH NMR imaging. J Magn Reson 1992;96:608-612.

8. Detre JA, Zhang W, Roberts DA, Silva AC, Williams DS, Grandis DJ, Koretsky AP, Leigh JS. Tissue specific perfusion imaging using arterial spin labeling. NMR Biomed 1994;7(1-2):75-82.

9. Rajendran R, Lew SK, Yong CX, Tan J, Wang DJ, Chuang KH. Quantitative mouse renal perfusion using arterial spin labeling. NMR Biomed 2013;26(10):1225-1232.

10. Schor-Bardach R, Alsop DC, Pedrosa I, Solazzo SA, Wang X, Marquis RP, Atkins MB, Regan M, Signoretti S, Lenkinski RE, Goldberg SN. Does arterial spin-labeling MR imaging-measured tumor perfusion correlate with renal cell cancer response to antiangiogenic therapy in a mouse model? Radiology 2009;251(3):731-742.

11. Williams DS, Detre JA, Leigh JS, Koretsky AP. Magnetic resonance imaging of perfusion using spin inversion of arterial water. Proc Natl Acad Sci U S A 1992;89(1):212-216.

12. Dixon WT, Du LN, Faul DD, Gado M, Rossnick S. Projection angiograms of blood labeled by adiabatic fast passage. Magn Reson Med 1986;3(3):454-462.

13. Wong EC. Vessel-encoded arterial spin-labeling using pseudocontinuous tagging. Magn Reson Med 2007;58(6):1086-1091.

14. Wu WC, Fernandez-Seara M, Detre JA, Wehrli FW, Wang J. A theoretical and experimental investigation of the tagging efficiency of pseudocontinuous arterial spin labeling. Magn Reson Med 2007;58(5):1020-1027.

15. Jung Y, Wong EC, Liu TT. Multiphase pseudocontinuous arterial spin labeling (MP-PCASL) for robust quantification of cerebral blood flow. Magn Reson Med 2010;64(3):799-810.

16. Kwong KK, Chesler DA, Weisskoff RM, Donahue KM, Davis TL, Ostergaard L, Campbell TA, Rosen BR. MR perfusion studies with T1-weighted echo planar imaging. Magn Reson Med 1995;34(6):878-887.

17. Kim SG. Quantification of relative cerebral blood flow change by flow-sensitive alternating inversion recovery (FAIR) technique: application to functional mapping. Magn Reson Med 1995;34(3):293-301.

18. Schwarzbauer C, Morrissey SP, Haase A. Quantitative magnetic resonance imaging of perfusion using magnetic labeling of water proton spins within the detection slice. Magn Reson Med 1996;35(4):540-546.

19. Hardy CJ, Edelstein WA, Vatis D. Effecient adiabatic fast passage for NMR population inversion in the presence of radiofrequency field inhomogeneity and frequency offsets. Journal of Magnetic Resonance 1986;66(3):470-482.

20. Buxton RB, Frank LR, Wong EC, Siewert B, Warach S, Edelman RR. A general kinetic model for quantitative perfusion imaging with arterial spin labeling. Magn Reson Med 1998;40(3):383-396.

21. Belle V, Kahler E, Waller C, Rommel E, Voll S, Hiller KH, Bauer WR, Haase A. In vivo quantitative mapping of cardiac perfusion in rats using a noninvasive MR spin-labeling method. J Magn Reson Imaging 1998;8(6):1240-1245.

22. Williams DS, Detre JA, Leigh JS, Koretsky AP. Magnetic resonance imaging of perfusion using spin inversion of arterial water. Proc Natl Acad Sci U S A 1992;89(1):212-216.

23. Robinson S, Jovicich J. B0 mapping with multi-channel RF coils at high field. Magn Reson Med 2011;66(4):976-988.

Chapter 3

Feasibility of Pre-Clinical Liver Perfusion Measures using Arterial Spin Labelling

This chapter shows the progression and optimisation of hepatic perfusion estimates obtained using a Flow-sensitive Alternating Inversion Recovery (FAIR) ASL with a Look-Locker read-out. The sequence was initially applied to a mouse liver, and then optimised in a T_1-matched agarose phantom. Prospective and retrospective-gating techniques to remove image artefacts from respiration were implemented and compared. Once an imaging acquisition and analysis pipeline was established, the repeatability and reproducibility of this technique was tested in a cohort of mice. The Look-Locker read-out was further adapted to improve the acquisition efficiency, with additional testing in phantoms and *in-vivo* for possible sources of systematic errors.

The FAIR Look-Locker sequence was initially developed by Dr Adrienne E. Campbell-Washburn; its application has been previously published in the mouse heart. The prospective gating sequence was developed alongside Dr Simon Walker-Samuel. The retrospective data-logger based rejection was initially implemented by Dr A. E. Campbell-Washburn, though my own variant of the algorithm was applied to the data.

The work in this chapter has been published in *NMR in Biomedicine*; R. Ramasawmy, A. E. Campbell-Washburn, J.A. Wells, S.P. Johnson, R. B. Pedley, M. F Lythgoe and S. Walker-Samuel, *Hepatic Arterial Spin Labelling: An initial evaluation in mice*.

3.1 Initial Application to a Mouse Liver

An evaluation of liver perfusion measured by a FAIR ASL technique with a Look-Locker readout (FAIR-LL) was carried out in a wild-type mouse. This sequence was chosen as it had been previously established and tested in the mouse myocardium, thus would be an ideal platform to explore imaging and gating strategies in the liver. The mouse was anaesthetised and maintained using 1.5% isoflurane in 1L/min O_2. An initial pilot test applied a cardiac-gated cine sequence, typically used to capture the heart's movement through the cardiac cycle, to image any resultant liver motion due to the heart's adjacent location (data not shown). From these data, it was apparent that the superior liver was affected by cardiac motion, however the majority of the liver remained relatively static, so it was decided for initial testing a respiratory triggering would be sufficient.

3.1.1 Pulse Sequence

The scan parameters were as follows: an axial, single 2 mm slice, 128 x 128 matrix, FOV 30 x 30 mm^2, with 50 Look-Locker readouts spaced at $TI_{Look\text{-}Locker}$ 110 ms, and a sampling flip angle α of 10°. Inversions were interleaved between a slice selective inversion pulse (6 mm thick) and a global inversion (1), total acquisition time was around 15 minutes. Each inversion pulse was triggered post exhalation, followed by 50 segmented readout blocks (Figure 3.15), each containing four closely spaced sampling pulses (TR_{RF} 3.1 ms).

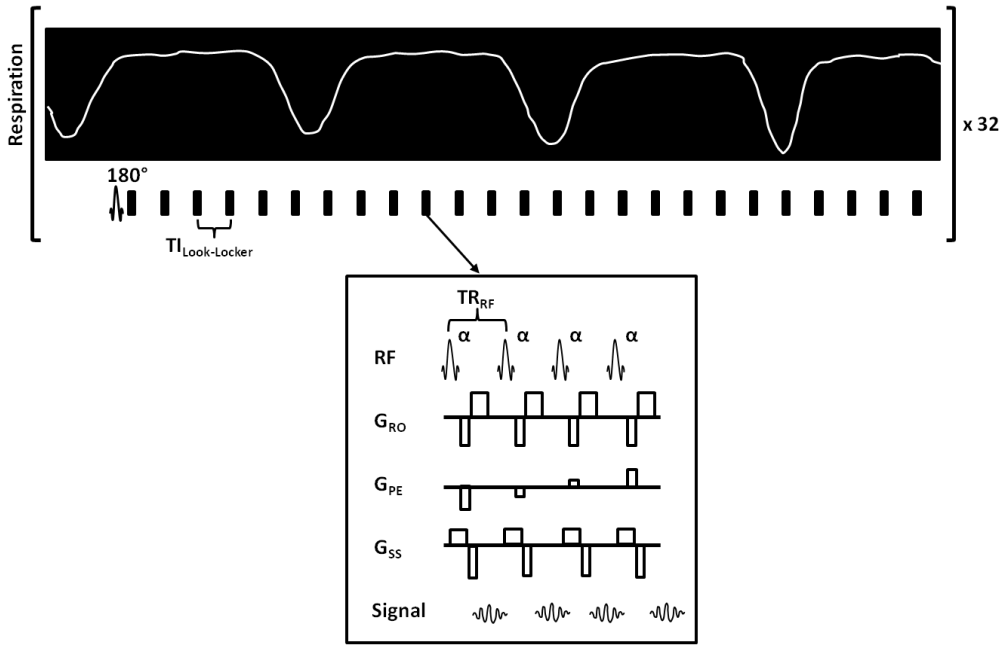

Figure 3.15: Pulse sequence diagram of the T_1-mapping acquisition using a Look-Locker technique. An adiabatic inversion is triggered post-exhalation followed by 50 sampling blocks, each separated by $TI_{Look\text{-}Locker}$. Each sampling block contains four closely-spaced sampling pulses given by TR_{RF}, which acquires four lines of k-space of each TI per inversion, which reduces the sequence duration. For a 128 phase-encode lines, 32 inversions are needed to acquire the image.

3.1.2 Perfusion Quantification

Total liver perfusion (P) maps were initially quantified using the Belle model (Section 2.4.6.4), which has been developed and previously demonstrated for measurements in the mouse myocardium (2). Liver perfusion estimates using the FAIR method will include both arterial and portal contributions, given by the difference in slice-selective ($T_{1,\ selective}$) and global ($T_{1,\ global}$) longitudinal relaxation measurements.

Prior to pixel-wise T_1-fitting, an edge-preserving filter (3) was applied to all data. Slice-selective and global T_1 maps were generated in MATLAB (MathWorks, Natick, MA, USA) using a non-linear least-squares parameter fit. The effects of the Look-Locker readout on the inversion recovery was corrected for by using the formula stated in Chapter 2.2.2. A blood-tissue partition coefficient λ = 0.95 $ml g^{-1}$ was taken from previously reported ^{85}Krypton gas clearance measurements (4). $T_{1,cap}$ is the intravascular capillary blood longitudinal relaxation time which has been measured in the ventricular blood pool in the mouse heart to have a value of 1.9 s at 9.4T (1).

3.1.3 Initial Evaluation: Results

As the first measure of liver perfusion in a mouse using arterial spin labelling (to our knowledge), this pilot experiment proved to be very encouraging. Figure 3.16A is an axial

fast-spin echo (FSE) image that acts as a structural reference: the liver has been indicated with the dashed ROI. Blood vessels, such as the inferior vena cava (IVC), appear hypo-intense. A homogeneous global T_1 map (mean T_1 = 1.46 s) can be seen across the liver parenchyma (Figure 3.16B); blood vessels are demarcated to their longer T_1. Figure 3.2C shows the resultant perfusion map across the liver. An area of perfusion signal loss is observable (star) which may be due to motion corruption-induced T_1 fitting errors. A high "perfusion" signal can be observed at the loci of the major vasculature, such as the IVC (arrow), though this does not represent classical perfusion (i.e. the delivery of blood to the capillary bed). A heterogeneous perfusion signal can be seen across the liver parenchyma, with the mean perfusion of the liver tissue (removing the blood vessels) estimated to be 0.8 $mlg^{-1}min^{-1}$. This is much lower than expected (5), and likely to be due to the large region of perfusion signal dropout. However, visual assessment of the large vessel-liver parenchyma contrast provided some encouragement that accurate mapping of mouse liver may be feasible with further methodological optimisation. Looking at the raw ASL data, it was possible to observe many images with motion-induced ghosting artefacts (Figure 3.16D).

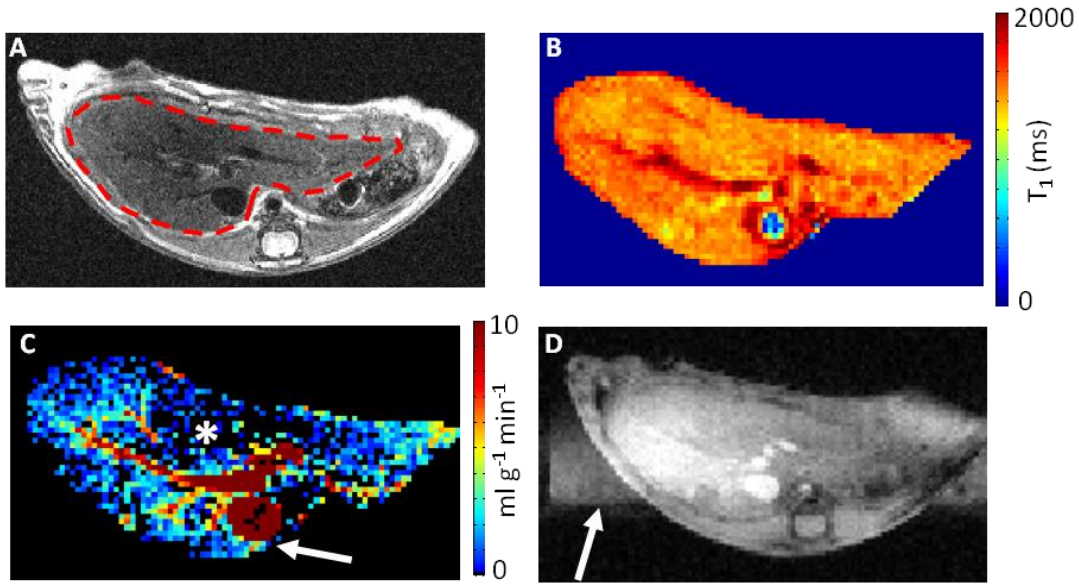

Figure 3.16: Initial mouse liver perfusion measurement using a Look-Locker FAIR protocol: (A) fast spin echo reference image, the liver has been outlined (dashed ROI). (B) Estimated global T_1 map (mean T_1 = 1.46 s) from the FAIR experiment. (C) Perfusion map – high, non-physiological perfusion can be seen at the location of the major vasculature, such as the inferior vena cava (arrow). The perfusion map shows area of low signal (star) – which could be a result of no strategy being applied to account for mouse respiration. (D) Example TI which has been corrupted by respiratory motion, as observed by ghosting artefacts (arrow).

From these initial measurements, it was decided to include a gated, high-resolution fast-spin echo sequence to the imaging protocol, in order to delineate tissue and vessel structures to aid understanding of the perfusion maps.

In addition several key iterative improvements to the pulse sequence were applied to optimise the T_1 mapping for liver perfusion estimates, including methods to remove the influence of respiratory motion from free-breathing acquisition strategies.

3.2 Sequence Optimisation

3.2.1 Phantom Experiments

A 1.5% agarose phantom doped with copper sulphate was created to approximately match the T_1 measured in a few mice livers (approximately 1200 ms). This phantom would be used to develop and optimise pulse sequences to minimise animal usage.

When reconstructing the Look-Locker phantom images, an artefact became apparent; a hypo-intense vertical line could be seen in the second TI, which then was visible for the next few images (Figure 3.17). Investigating the corresponding k-space images, a zipper-like artefact could be seen to one side of the central few lines (phase-encoding was in the left-right orientation). In addition, simulating the Fourier transform of a solid line at the location of the artefact in MATLAB showed that such a localised signal increase would correspond to the observed vertical line. Closely inspecting the *in-vivo* images showed that this artefact was also present, though not as apparent possibly due to physiological noise. This artefact is sub-optimal, as this will lead to localised errors in the T_1 measurement.

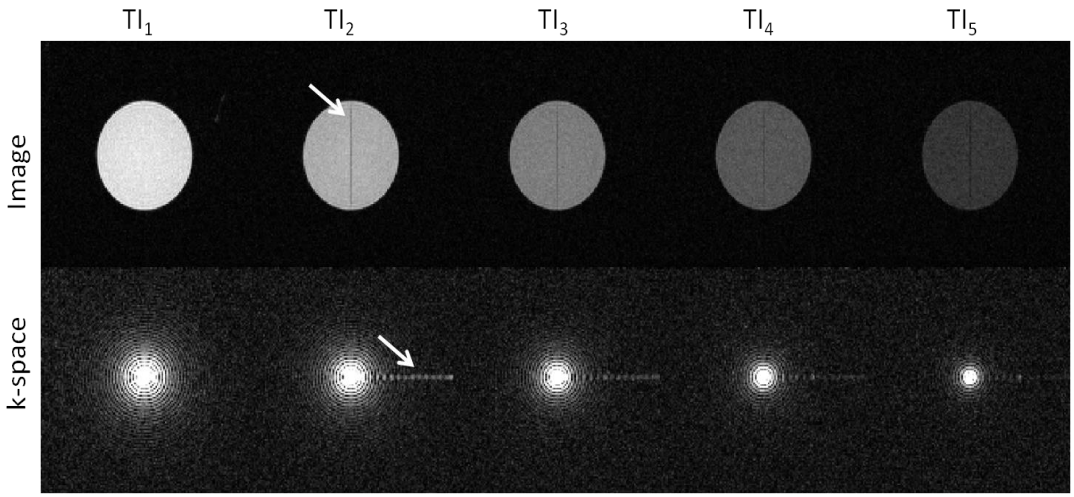

Figure 3.17: Observation of a line artefact (arrow) present from in the second image in both the global and slice-selective inversions. The line can be seen as a result of a zipper-like artefact present in the central lines of k-space (arrow). This artefact was present in the *in-vivo* images, but was obscured by physiological noise.

3.2.2 Spoiler Optimisation

It was hypothesized that this artefact was caused by stimulated echoes (6) as a result of the fast sampling, that were more apparent during low amplitude phase-encoding gradients as these would not effectively crush out the signal. These stimulated echoes were likely to be more apparent in the water-based phantom due to its T_2 of 94 ms being much longer than the mouse liver T_2 of 18 ms (data not shown).

To investigate this, an experiment was carried out incrementing the sampling flip angle (α) from 3 – 10°, which is the upper limit of the small angle approximation in the Look-Locker sampling technique (7). In addition sampling angles of 20° and 30° were used to emphasise any echo stimulation.

Selecting only the second TI, where the artefact is most prominent, flip angles less than 5° showed no evidence of the line artefact (Figure 3.18A). The line becomes more apparent at higher flip angles, and at the extreme higher sampling angles the artefact becomes hyper-intense and wider, most likely due to stimulated echoes producing measurable signal at higher phase-encoding gradients.

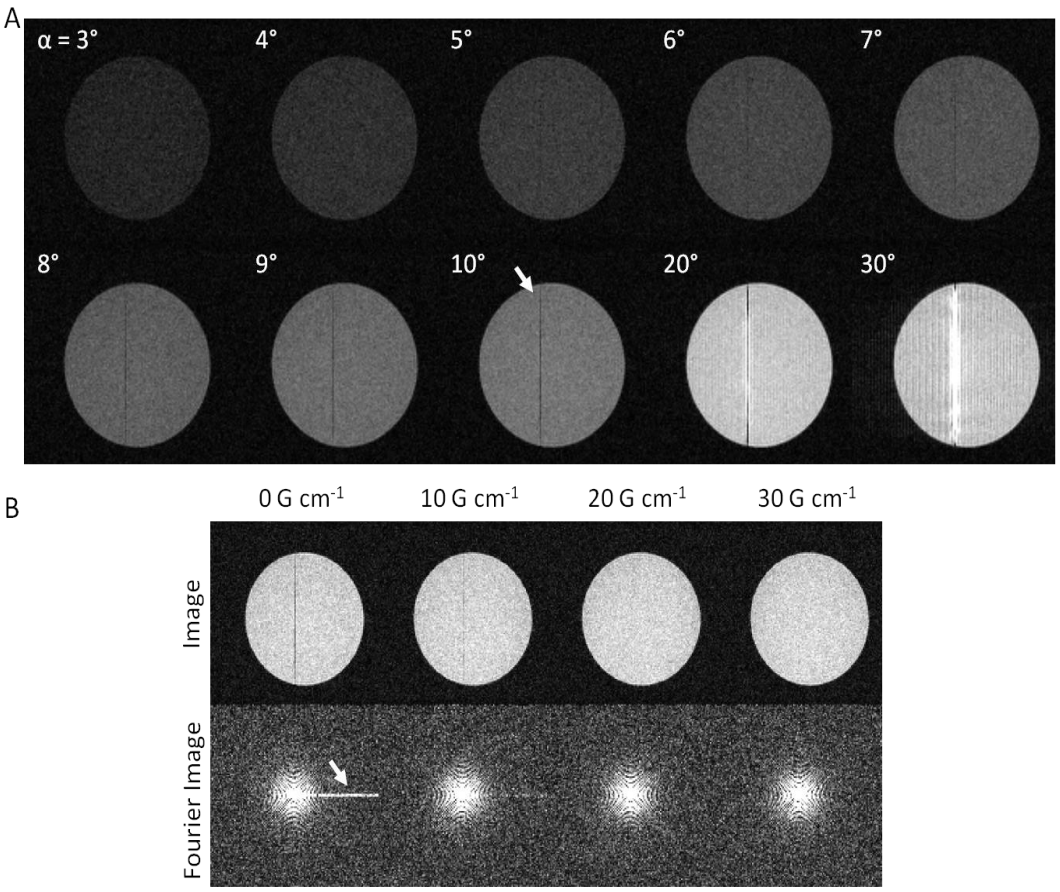

Figure 3.18: Investigating the line-artefact by increasing the sampling flip angle (A). Each image is the second TI from the slice-selective datasets. The artefact is not apparent at low flip angles (<5°) and becomes more pronounced at larger flip angles (arrow). Increased application of spoiler gradients (B) shows a successful removal of the artefact at a spoiler gradient strength of 20 G cm^{-1}. The source of the artefact can be understood from the Fourier image where a zipper-like artefact can be seen in the right hand side of k-space (arrow).

In order to null these echoes, spoiler gradients were added after each segmented read-out. A 1 ms duration spoiler, with increasing strengths of 0, 10, 20 and 30 G cm^{-1} were applied (Figure 3.18B) with the sampling angle set to the maximal 10°. It is apparent from these data that a spoiler of 20 G cm^{-1} is sufficient to remove the line artefact. Assessing the T_1 of the phantoms in a ROI not including the line artefact, there was no significant difference ($p > 0.05$, one-way ANOVA) between the spoiler strengths, and thus a spoiler of 20 G cm^{-1} was used in the following experiments.

3.2.3 Flip Angle Optimisation

The sampling angle of the Look-Locker readout will determine the SNR of the ASL data. Previous literature has stated the limitation of using a Look-Locker sampling technique is that the quantification is reliant on a small sampling angles (<10°) to not overly perturb the

inversion recovery (7). Incrementally increasing the flip angle in an agar phantom from 3 – 10°, the estimated T_1 and the SNR was assessed using:

$$SNR = \frac{\overline{S}}{0.7979 \cdot \overline{N}} \qquad \text{Equation 3.34}$$

Where $\overline{S}$ is the mean magnitude within the sample and $\overline{N}$ is the mean magnitude of a noise region. This equation accounts for low-signal Rician distribution of the noise (8). The SNR estimation was taken from the last TI of each data set.

It is possible to observe the benefit of using a higher flip angle in Figure 3.19A; the mean estimated global T_1 measurements do not display any dependence on flip angle, but the standard deviation of the T_1 values within an ROI reduces at increased sampling angles. However, as the background noise increases as well as a function of flip angle, the SNR estimates decreases with flip angle (Figure 3.19B).

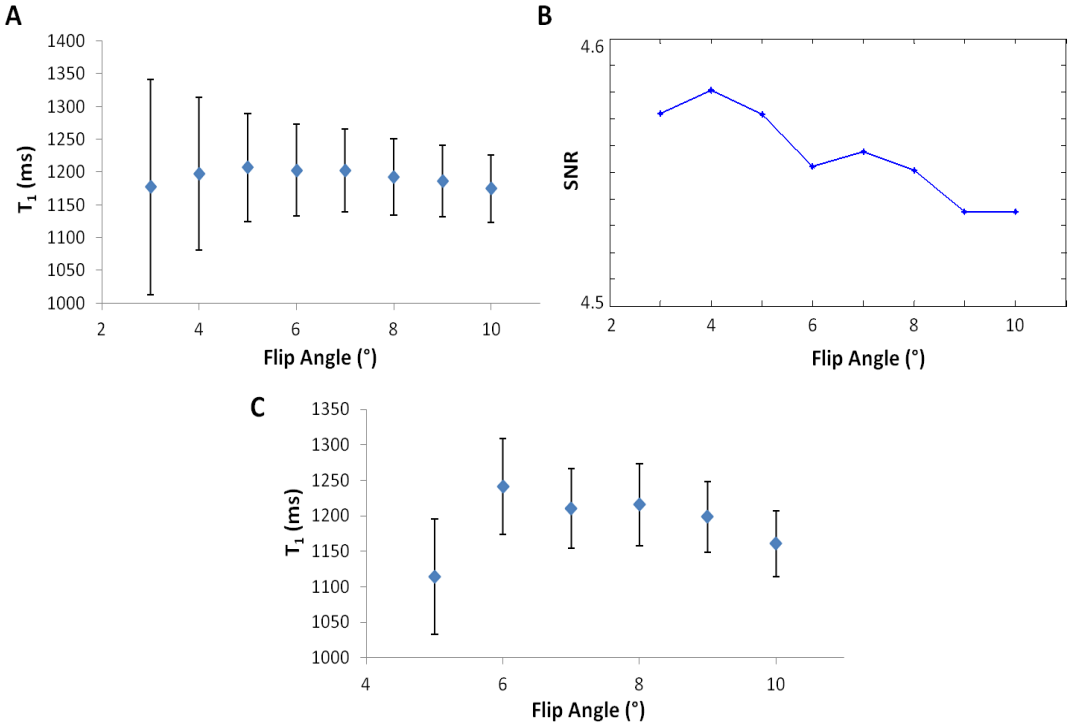

Figure 3.19: Increasing the sampling flip angle does not affect the measured T_1 in an agar phantom (A), but the standard deviation within a ROI decreases, as shown by the error bars. However, the signal-to-noise decreases slightly with increased flip angle (B). Testing the flip angle dependency *in-vivo* (C), the standard deviation of the T_1 estimate of a homogenous tissue region again decreases at higher flip angles.

The experiment was repeated *in-vivo*, increasing the sampling flip angle from 5 – 10°. A ROI was drawn in a uniform region of liver parenchyma; Figure 3.19C shows the sampling flip-angle dependency of mean T_1 and standard deviation within that ROI. There are no

significant differences between the measurements ($p > 0.05$, one-way ANOVA). From this data, a sampling flip angle of 8° was chosen, as a compromise of SNR and standard deviation of the estimated T_1 which will determine the uncertainty of the perfusion as estimated by the Belle model.

3.2.4 Inversion Ratio Optimisation

The width of the slice selective inversion is an important experimental parameter in pulsed ASL studies. Too narrow a width can lead to non-perfusion related signal differences between the images acquired following slice selective and global inversions due to slice profile effects (6). Too broad a width can lead to long arterial transit times which may violate assumptions of the perfusion quantification model. In this section I performed experiments to optimise the width of the slice selective inversion pulse within the FAIR-LL sequence applied to the mouse liver. The global inversion pulse was chosen to be 15-20 cm, larger than the typical length of a mouse.

The slice-selective inversion thickness was optimised *in-vivo* by increasing the inversion thickness around a 1 mm slice from 3 – 10 mm *in vivo*. The mean signal was measured from a ROI drawn in the portal vein to monitor the inflow of blood in to the slice. The assumption of the FAIR quantification is that the spins originally outside the slice-selective inversion immediately replenish the blood magnetisation and exchange with the tissue. Thus, the mean signal within a perfusing blood vessel following inversion would be time-independent as the inflowing spins are all at equilibrium magnetisation.

However, signal relaxation back to equilibrium was observed across all inversion thicknesses (Figure 3.20A). Regular 'dips' within the mean signal are due to respiration-induced signal loss. Assessing the early phase recovery (zoomed box), the larger inversion thicknesses (see key) have lower signal: the blood has not completely washed in due to the slow portal flow. This may produce an underestimation of the liver perfusion; this will be further discussed in section 3.7.1. Similar signal recovery was observed between thicknesses of 3 to 6 mm.

Quantifying the T_1 and ROI standard deviation of a uniform area of liver parenchyma (Figure 3.20B), there appears to be a slight trend up to 6 mm after which, it appears to plateau. From combining these results, a 6 mm slice-selective inversion thickness was chosen for future experiments.

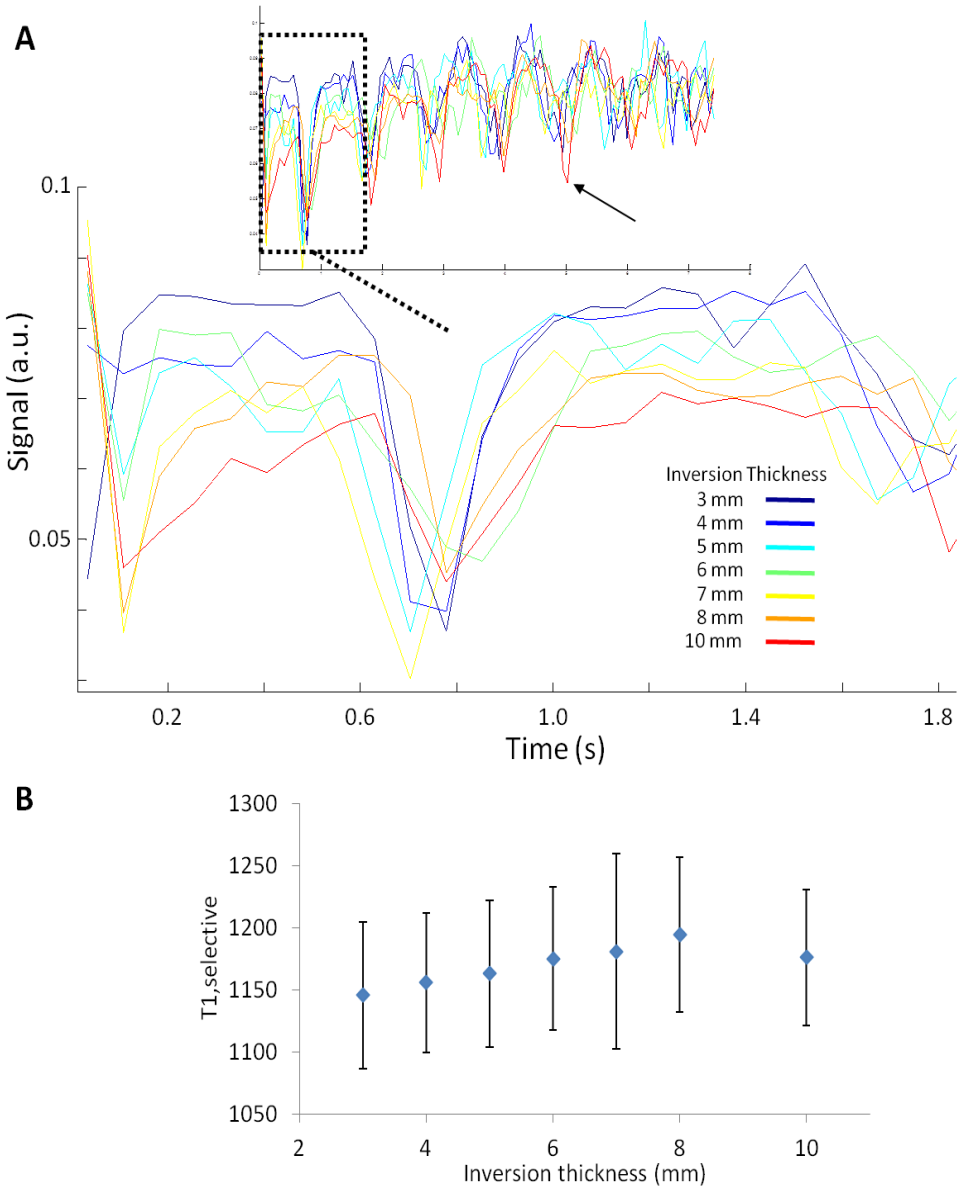

Figure 3.20: (A) Analysing the mean magnitude of a ROI within the portal vein following an increasing slice-selective inversion thickness from 3 to 10 mm (see key). Time in this plot is measured at the inversion times of the Look-Locker sequence (separated by 74 ms). The signal should stay constantly at the equilibrium magnetisation, however there is a slight recovery observable - the slow moving portal blood is not replenishing the blood in the slice immediately. The dips within the signal (arrow) represent where respiration has occurred and the ROI signal has been obscured by motion artefacts. Zooming in to the early phase of this measurement, there is a trend at larger thicknesses to have a reduced initial magnitude as the blood has further to travel in to the slice at the thicker inversions. (B) The mean T_1 and standard deviation of a uniform liver parenchyma ROI as a dependency on the slice-selective inversion.

These results formed an optimised protocol of the FAIR ASL technique for mice livers, as well as refinement of the Look-Locker readout for efficient T_1 mapping. The next section investigates gating strategies to remove the influence of respiratory motion artefacts in a free-breathing set-up.

3.3 Prospective respiratory gating

3.3.1 Respiratory-gated Look-Locker sampling

To characterise the T_1 recovery, a sampling period of approximately 6 seconds is used; this will contain a number of inhalations when imaging anaesthetised rodents (typical breathing rates are from 40 – 90 breaths per minute). The current quantification uses a 'brute-force' method; utilising the high number of sampling points along the recovery curve and assuming that this will allow a reasonably estimate of T_1. However, as the Belle model of perfusion quantification is reliant on T_1 differences, this approach may produce large errors in the perfusion estimates. In addition, alternative models of perfusion which rely on image subtraction, the influence of motion artefacts will greatly distort the model fitting.

A prospective gating strategy was proposed that would pause the Look-Locker sampling during inhalation Figure 3.21. This 'pausing' was chosen rather than a technique which would pulse continuously and acquire when appropriate, as natural variety in the breathing rate will lead to a number of images having an incomplete k-space due to the segmentation of the acquisition. The TIs with incomplete Fourier data could then be omitted retrospectively, but this does not present a distinct alternative to using the normal Look-Locker acquisition with retrospective gating. The advantage of prospective gating is that the all the images acquired can be used, which may improve the T_1 estimate.

The sequence was designed to 'check' the gating status, as set up on the physiological monitoring software (SA Instruments, NY, USA) and pause the sampling until the next quiescent respiratory phase, to ensure no image was corrupted by breathing motion.

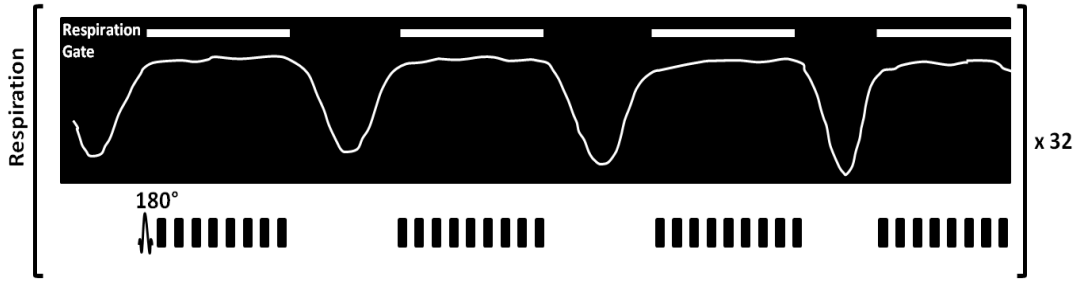

Figure 3.21: Pulse sequence schematic of the prospective respiratory-gated, Look-Locker acquisition. The black blocks represent the segmented sampling modules (see Figure 3.15), which are paused in this sequence as a result of the digital respiratory gate (white blocks) set up on the physiological monitoring.

However, 'pausing' the sequence will cause some complications for analysis: as stated in Chapter 2.2.2, Look-Locker quantification of T_1 is dependent on a regular spacing of the

small sampling pulses due to the steady magnetisation during the inversion recovery. However, the proposed 'pausing' would violate this clause. In addition, the second problem is the segmented structure of the sequence; if the animal is breathing irregularly, then neighbouring k-space lines of one image can potentially have a mixture of TIs; this will result in image reconstruction artefacts as well as T_1 quantification difficulties. The 'real-world' effects of these were explored in the next section.

Normal and gated sequences were carried out, with the sampling pulses and respiratory gates recorded using a digital data-logger (Cambridge Electronics, UK). An initial method of T_1 estimation using an average TI from all the gated timings was tested. Simulations were then created to estimate the discrepancies in quantification, and finally the sequence was repeated in phantoms using a gating simulator (SA instruments, NY, USA).

3.3.2 Assessment of Respiratory Gating

Figure 3.22A is an example image at a TI during a respiration using the standard Look-Locker readout and the same TI using the prospectively-gated sequence is shown in Figure 3.22B; it is clear that the gated sequence improves the quality of the raw image. In this dataset, no distinct image reconstruction artefacts were present in the prospectively-gated acquisition.

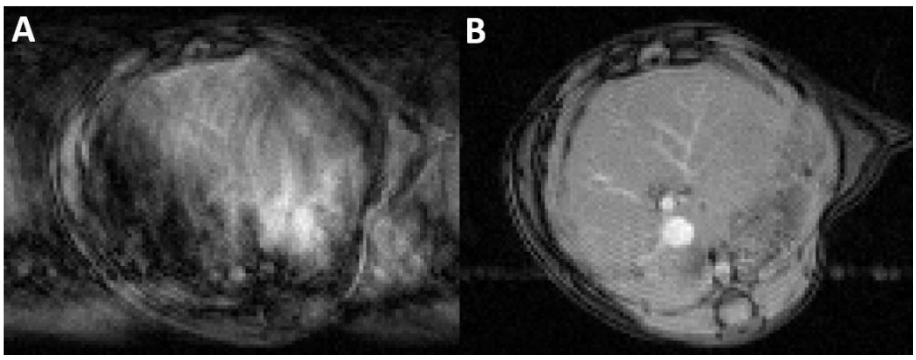

Figure 3.22: An image acquired during respiration with the Look-Locker sequence (A), and the same TI acquired using the gated technique (B); the gated sequence clearly improves the raw data with no obvious image artefacts.

For the prospective breathing method, the quantification of the T_1 recovery required each inversion and sampling timings recorded, as the animal's breathing may be inconsistent between the separate inversions. Such breathing irregularity has been visualised in Figure 3.23.

Figure 3.23A shows a normal, un-gated Look-Locker timing; in this sequence, with 4 lines acquired in one segment and 50 TIs per inversion, each 180° pulse will be followed by 200

sampling pulses. Time is along the x-axis, and the Look-Locker RF pulse number (LL RF index) is along the y-axis. A normal-mode Look-Locker sampling acquisition is observable: four pulses separated by TR_{RF} are then followed by the $TI_{Look\text{-}Locker}$, the TIs are regularly spaced.

An example timing graph of a gated Look-Locker acquisition after a single inversion can be seen in Figure 3.23B; the flat regions correspond to where the sequence is paused during respiration. Overlaying all the sampling timings from an entire FAIR experiment (i.e. 64 inversions, Figure 3.23C), it is possible to visually assess how varied the breathing was, by the 'band thickness'. For example, choosing a particular LL RF index, the band thickness is the spread of the timings for that TI; the bands become wider with time due to physiological drift in the respiratory rate. Two different examples of prospective gating are shown: a relatively consistent breathing (Figure 3.23C) over the duration of the Look-Locker sequence, and inconsistent breathing (Figure 3.23D) with a clear outlier. We can produce a simplified estimation of T_1 by averaging the sampling timings for each Look-Locker RF index.

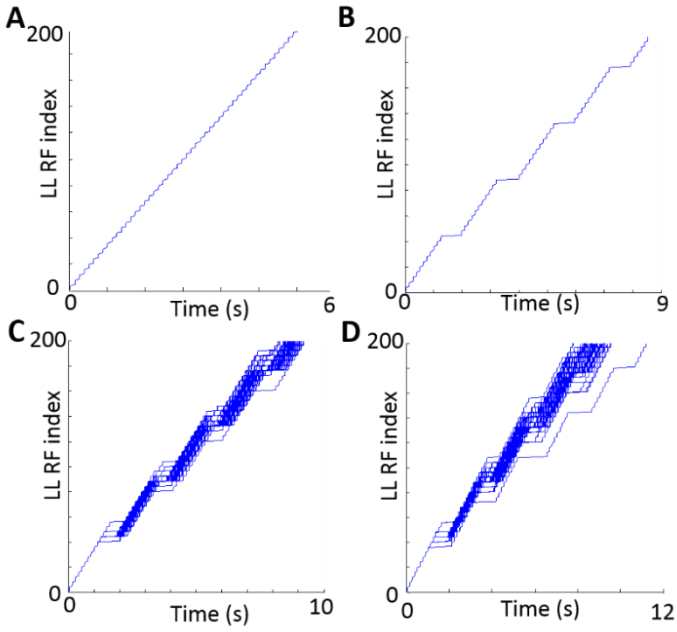

Figure 3.23: The Look-Locker acquisition was designed to partially sample 50 Tis per inversion, with 4 lines of each image acquired in quick succession; this will result in 200 RF pulses post-inversion. These graphs demonstrate the differences and difficulties in using a gated acquisition. A normal, un-gated acquisition (A); the pulses are regularly timed. An example gated acquisition following a single inversion (B); flat regions can be seen where the sequence is waiting for the breathing motion to stop. A whole experiment with all the recorded sequence timings overlaid, with a relatively consistent breathing rate (C) and more erratic breathing (D).

The potential benefits of gating can be seen in the T_1 maps (Figure 3.24A); the free-breathing map exhibits areas of where the T_1 fitting failed (arrow). A visual assessment between the two sequences shows a reasonable correspondence of T_1 values. Across both slice-selective and global T_1 maps, the prospective-gating sequence produced a mean 2.4% underestimate of T_1 values in a homogenous region of liver tissue. The differences in signal recovery from a ROI of liver tissue can be seen in (Figure 3.24B); the free-breathing signal (red) has signal deviations as a result of the respirations artefacts, which can result in an over-estimation of T_1. The gated signal (blue) doesn't display such reductions in signal, though the relaxation of the magnetisation during the sampling pauses causes some step increases in the signal. The perfusion map calculated from the free-breathing acquisition exhibits high perfusion and signal drop out (arrow, Figure 3.24C), whereas the liver parenchymal perfusion was much more even with the prospective gating- showing the necessity for strategies to overcome the influence of respiratory motion on the perfusion signal.

This experiment has demonstrated a method of perfusion acquisition which improves on the free-breathing technique, demonstrating the importance of removing the influence of respiratory motion. However, the quantification of the T_1 was carried out using a simplistic averaging of the LL RF indices. Though this performed well relative to free-breathing, the possible errors in this method were then investigated by using a gated Look-Locker simulation using the *in vivo* timing data and a phantom study with a physiology simulator.

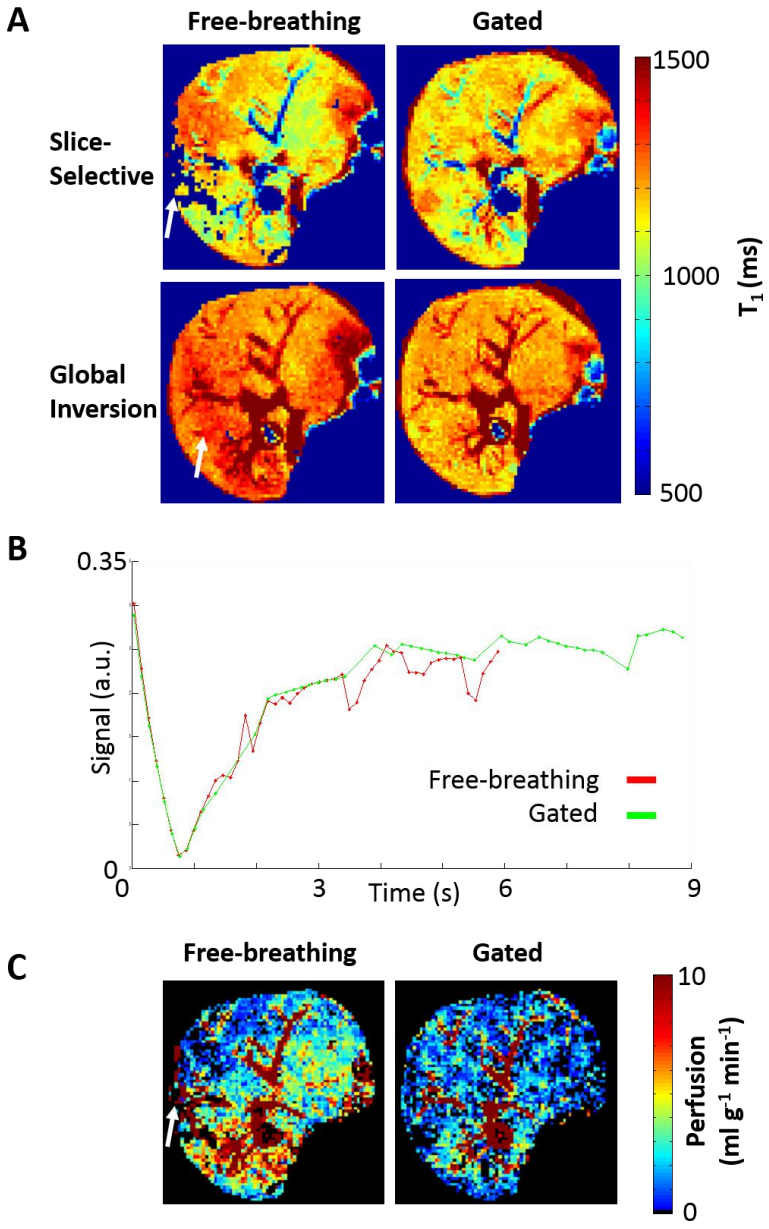

Figure 3.24: (A) Demonstration of T_1 mapping using a Look-Locker acquisition that has been triggered (normal) and the respiration gated (gated) sequence. In the normal slice selective data, signal dropout can be seen (arrow) where the inversion recovery was not successfully fitted; this problem was not present in the gated data. A band of increased T_1 (arrow) can be seen in the normal global inversion data, most likely due to a respiratory artefact present in the images; the gated sequence produces a much more homogenous T_1 map. The gated T_1 mapping was calculated using the mean inversion times from the segmented acquisition. (B) Assessing the normal signal (red) in a small ROI, the inversion recovery is disrupted as a result of the respirations artefacts, which can result in an over-estimation of T_1. The gated signal (green) doesn't display such large fluctuations, but sampling saturation and recovery is visible. (C) The resultant perfusion map from the free-breathing analysis (calculated using the Belle model) shows regions of spurious high perfusion, and signal dropout (arrow), whereas the gated acquisition produces a much more homogenous perfusion signal within the liver parenchyma.

3.3.3 Gated Look-Locker Simulation and Phantom Experiment

A simulation of the signal with a gated Look-Locker acquisition was carried out to compare potential estimation errors in the quantification. An algorithm was established that could model the magnetisation saturation caused by the progressive small angle sampling pulses. The model assumed a perfect inversion, and would subsequently calculate the deflection of the magnetisation after each pulse using a T_1 of 1.2s. Inputting the sequence timings recorded during the *in vivo* gated acquisition, the effects of disrupting the Look-Locker train could then be visualized.

The modelling was performed using two sampling flip angles of 5 and 10° (Figure 3.25A). The magnitude of the modelled magnetisation has been plotted to reflect the acquired MR signal (points), and a three parameter fit shows the simple approach to quantify the signal (line). The magnetisation can be seen to recover during the sampling pauses, followed by a signal saturation decrease due to the applied pulses, which is much more apparent at the larger flip angle. The three-parameter fit works reasonably well with the 5° flip angle, but is obviously inadequate to truly model the magnetisation, particularly at the larger flip angle. However, the percentage T_1 under-estimate was less than 1% for both a 5 and 10° flip angle in the simulation.

The gated sequence was then applied in a phantom using a physiology simulator. The advantage of using a phantom study to investigate the quantification effects of averaging the TIs is that a ground truth measurement can be made in the agarose without gating.

The physiological simulation box has modules for both respiration and cardiac traces. In order to simulate respiration, the ECG signal amplitude was minimised and the respiratory rate was set to approximately 60 breaths per minute. It was observed that the software did occasionally miss gates, though is not ideal, will add an element of variation in to the acquisition to potentially mimics the *in vivo* scenario.

The signal recovery of the gated sequence applied to the phantom using the physiology simulator, taken from the mean signal in a uniform ROI, can be seen in Figure 3.25B. The signal of the 10° flip angle is expectedly higher, though wasn't accounted for in the simulation. It is possible to observe that the 5° signal (points) and it's fitted (line) follows closer than the 10°, which exhibits large recovery and saturation periods, in accordance with the simulation. The fitting averages through these signal 'oscillations', which leads to a T_1 underestimation: the 5° and 10° estimated T_1s were respectively reduced to 93% and 87% of the estimated T_1 of a normal Look-Locker acquisition.

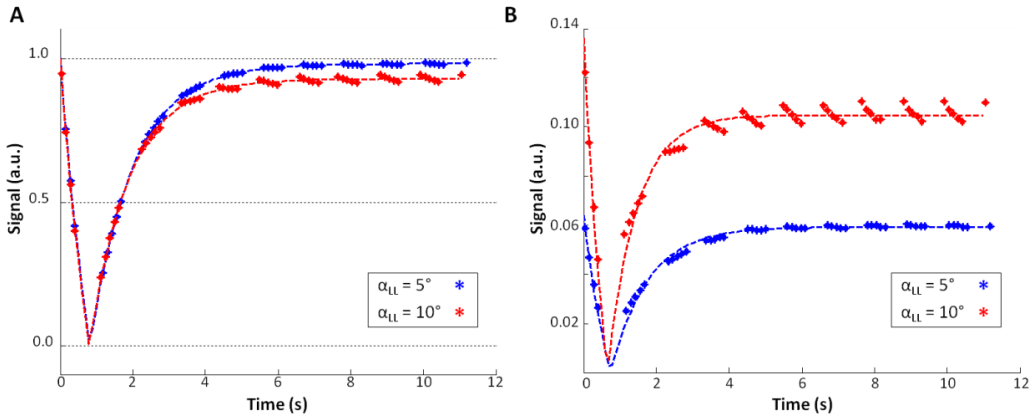

Figure 3.25: (A) Simulations of inversion recovery with a disrupted Look-Locker sampling train. Two different sampling flip angles have been used; 5° (blue) and 10° (red); the three-parameter fit of the data has been added. The effect of the sampling saturation and recovery during the pauses can be visualised in the 10° simulation – however, both flip angles estimated the simulated T_1 well. Prospectively-gated inversion recovery signal and fitting following a global inversion in an agar phantom for a 5° (blue) and 10° (red) sampling regimes, using a physiology simulator box.

3.3.4 Conclusion

Though the respiratory gated sequence performs well to eradicate motion artefacts from the raw data, the analysis is complex and introduces a systematic T_1 underestimation. The reconstruction of the images and quantification are overly reliant on stable physiology. The dataset shown in Figure 3.24 is from a more consistent breathing dataset – however large fluctuations in the pulse timings can have adverse effects on the 'averaged' TI based inversion recovery fitting.

To shorten the scan time to ideally minimise the amount physiological drift, fewer TIs could be captured: the last TI in the normal acquisition is around 6s, and approximately 10s for the gated scan. The pausing of the sequence causes the final image to be acquired later than the necessary 5 x $T_{1,liver}$ (approx. 6 s) allowed for magnetisation recovery. The phantom experiments showed that the gated sequence will produce underestimations of the longitudinal relaxation, though these measurements may be worsened by the variations in acquisition caused by the occasional missed gates, even from using a physiology simulator. Though the *in vivo* signal recovery did not seem as dramatically affected as the phantom, the T_1 underestimation and mixed sources of timings per data set mean that such a prospective gating strategy will have difficulties to estimate perfusion.

As cardiac imaging has successfully applied retrospective methods to analyse data and remove motion artefacts, three retrospective methods were then investigated to improve perfusion estimates.

3.4 Retrospective respiratory gating

3.4.1 Recorded Data-based rejection

This method has been previously reported in a Look-Locker acquisition in the mouse myocardium (1). The acquisition pulse timing and the respiration status are recorded, and the images can then be automatically rejected afterwards based on two criteria:

- Image rejection if at least 50% of k-space has been acquired during a respiration.
- Image rejection if one of the three central lines of k-space were acquired during respiration.

The threshold of 50% was chosen as a limit to the number of corrupted k-space lines in a TI, however the most apparent image artefacts occur when the any of the central three lines of k-space have been affected. The digital respiration gate was set using SA Instruments software, and this trace and the timing of the RF pulses were acquired in Spike2 (Cambridge Electronics, UK). The retrospective data conditioning programs were written in MATLAB.

3.4.2 Phase Encoded Noise-Based Image Rejection (PENIR)

The PENIR scheme was initially developed for retrospective gating where respiratory trace recordings for FAIR-LL perfusion imaging were not available. PENIR exploits the presence of "ghost" artefacts in the phase-encoded direction due to subject motion. PENIR highlights corrupted images by observing spikes in a user-determined ROI from the extra-corporeal space (Figure 3.26A). From this area the mean signal (Figure 3.26B, blue dotted line) will be expected to spike due to respiratory motion-induced ghosting. A threshold is generated from the mean noise signal plus one standard deviation in the remaining extra-corporeal field and is calculated every ten TIs. When the spikes significantly exceed the data-generated threshold (red solid line), images acquired at those inversion times will be then be attributed to respiratory induced artefacts and rejected from T_1-fitting. Typically, without the PENIR correction scheme, the signal within a liver parenchyma ROI will be reduced due to the motion artefact (solid diamonds, Figure 3.26C), which will result in an overestimation of T_1 and will hence affect the accuracy of perfusion estimation.

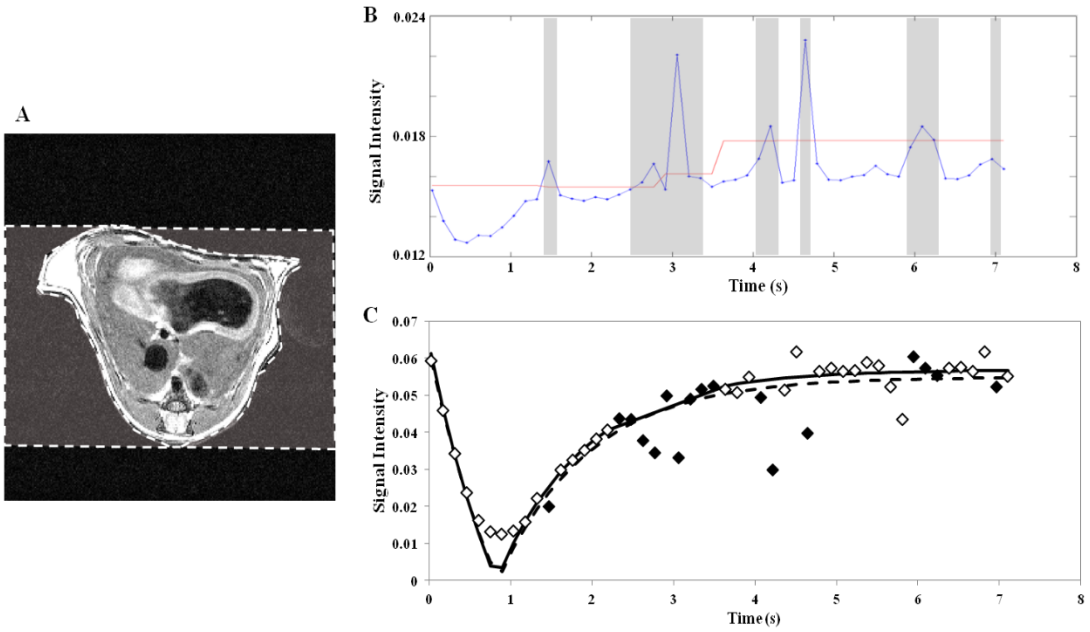

Figure 3.26: The Phase Encoded Noise-based Image Rejection (PENIR) scheme for retrospectively removing motion-corrupted data: Axial image of a mouse liver with an example user-determined ROI (dashed) in the phase-direction, extra-corporeal space (A). Significant increases in the mean noise signal (B) (point-line) above a signal-generated threshold (solid line) will result in image omission (greyed areas). Inversion recovery fitting (C) in a liver region will typically over-estimate T1 without correction (dashed line) compared to with rejection (solid line) due to reduced tissue signal from corrupted images (solid diamonds).

3.4.3 Assessment of Retrospective Gating Strategies

Ten mice underwent a series of perfusion measurements over two imaging sessions (Section 3.6) and four retrospective data conditioning modes were compared:

- No conditioning;
- Image rejection due to acquisition of any of the central three k-space lines during a breath as recorded by a digital data logger (1);
- Image rejection due to 50% or more of the lines in k-space being acquired during respiration as recorded by a digital data logger;
- Image rejection using the Phase Encoded Noise-based Image Rejection (PENIR) algorithm.

The differences in retrospective gating on T_1 mapping can be visualised in Figure 3.27: the dataset with no conditioning (mode i) exhibits areas of signal dropout (arrow) which corresponds to data that cannot successfully be fitted to the inversion profile due to motion artefact-induced signal deviations. The T_1 maps following gating using the data-logger (mode ii & mode iii) and PENIR (mode iv) successfully recover these areas.

For comparison across all the rejection modes, data from 19 of 20 data sets were evaluated as one session was untenable due to a data-logger malfunction. From the implemented

Look-Locker protocol, a total of 50 TIs are acquired and it is optimal to maximise the inversion recovery sampling points in order to minimise the uncertainty in the T_1 estimate. Conditioning with mode (ii) (data-logger rejection based on the central three k-space lines being corrupted) 34.2 ± 10.3% of the readout images remained post rejection, mode (iii) (data-logger rejection based on 50% of the k-space lines being acquired during respiration) 62.8 ± 4.9% and mode (iv) (PENIR) 54.3 ± 13.4%. Mode (ii) may be rejecting the data too harshly and mode (iii) may not be sufficiently rejecting the data; the PENIR scheme produced the smallest uncertainty in the T_1 fitting.

Perfusion estimates were calculated for each conditioning mode, using the Belle model as above. No rejection, mode (i), gave perfusion estimates that were non-significantly higher ($p > 0.2$, Tukey ANOVA) than the respiratory-corrected estimates (2.8 ± 0.4 $mlg^{-1}min^{-1}$ compared to the rejected average 2.3 ± 0.5 $mlg^{-1}min^{-1}$), which is consistent with the Campbell-Washburn's results (1). Averaged over the animals there was not a significant perfusion difference between data conditioning modes ($p = 0.21$, ANOVA with Tukey test) though there were 10 cases out of 18 (55%) where the Tukey analysis returned a significant difference ($p < 0.05$) between mode (i) and mode (ii), 9 cases (50%) between mode (i) and mode (iii), 8 cases (44%) between mode (i) and mode (iv). No significant difference in perfusion was measured between modes (ii), (iii) and (iv). This is suggestive of an error in the perfusion estimate without any conditioning, which is perhaps not surprising given the marked signal instability that is introduced by motion as previously demonstrated (e.g. Figure 3.8).

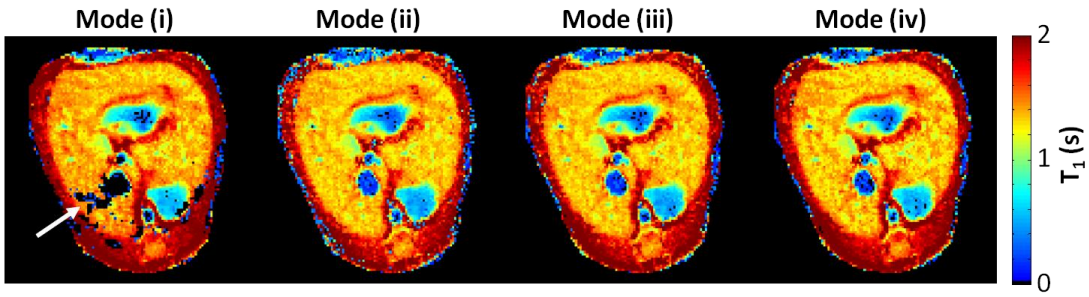

Figure 3.27: Comparison of T_1 maps following the different retrospective gating strategies: mode(i) no correction; mode(ii) data-logger based correction based on the central three lines of k-space; mode(iii) data-logger based correction based on the percentage of corrupted lines within an image; mode (iv) PENIR corrected. Without any gating, the T_1 map suffers from areas of poor fitting (arrow), this region is successfully recovered by all three conditioning modes. Representative data from a single mouse is shown.

3.4.4 Conclusion

Both prospective and retrospective respiratory gating of the Look-Locker readout have been explored. Where the prospective gating has the advantage of reduced respiratory motion in the raw data, the subsequent quantification of the T_1 is complex. Four retrospective conditioning modes were explored, and these showed a marked improvement on the uncertainty of the T_1 fitting.

The data logger-based and PENIR retrospective respirator gating algorithms can both be used to improve the T_1 and perfusion quantification when using the Look-Locker sequence: the advantage of acquiring many TIs allows images to be discarded whilst maintaining adequate sampling of the inversion recovery. Previous analysis of the data logger-based rejection favoured the rejection criteria if any of the central three lines of k-space were acquired during respiration (data not shown). The PENIR mode gave the smallest uncertainty in the T_1 measurements, showing the most promise for application to the liver. No significant differences were measured between the different retrospective approaches, thus the PENIR system does not seem to suffer from any apparent loss of accuracy. In addition the PENIR system does not require additional hardware to record the data, thus it is possible to retrospectively apply it to datasets that had not acquired the respiration and pulse timings.

For both image rejection schemes, both require steady animal physiology – variation in breathing rates will result in many TIs having been acquired during respiration, which will result in a large block of image rejection by all conditioning modes. A slower breathing rate will also result in fewer images being thrown away, though it has been suggested that slow rates of free-breathing can produce larger fluctuations in breathing (9). Generally, a larger

amount of ghosting can often be seen towards the later TIs (data not shown), as slight changes in breathing rates will be most apparent later, and the rejection of this late 'equilibrium' point can affect the T_1 quantification.

In the scenario of inconsistent breathing rates, the automated data-logger based rejection can throw away too many images to allow robust quantification, although it is possible to vary the 50% threshold. The PENIR system included a check of a minimum number of TIs (chosen to be 15 from visual analysis of fitting), where the noise threshold could be increased to allow more images to be included. A more iterative version of this thresholding may provide a better retrospective-gating strategy in the future.

A combination of the data-logger and PENIR conditioning modes could be an optimal method of image rejection; the PENIR system fails to reject images when the magnetisation passes through zero due to the low SNR, and the data logger system could assist this region.

From these data, PENIR was chosen to retrospectively respiratory gate the FAIR-LL data prior to T_1 quantification. Finally, to complete the perfusion imaging pipeline, two approaches to quantify liver perfusion were assessed.

3.5 Perfusion Quantification Model

With the FAIR preparation and gating strategy optimised, the quantification model was reassessed to determine the suitability of the Belle model. A large body of perfusion quantification uses the general kinetic models to fit the magnetisation post ASL preparation (10), however, the quantification for the mouse liver has not been explored: two cases of clinical liver perfusion estimates employed a general model (11, 12). Gunther *et al*. further developed the FAIR quantification model to account for the Look-Locker saturation of the magnetisation (13):

$$M(TI) = \begin{cases} 0 & 0 < t \leq \delta \\ \dfrac{-2M_0P}{\delta R} e^{-R_{1a}TI}\left(1 - e^{\delta R(TI-\delta)}\right) & \delta > t \end{cases} \qquad \text{Equation 3.34}$$

Where R_1 is $1/T_1$, $\delta R = R_{1a} - R_{1,app}$, R_{1a} is the relaxation rate of arterial blood. $R_{1,app}$ is defined by $R_{1,app} = R_1 + P/\lambda$ - ln(cos α)/TI_2, where α is the flip angle, and TI_2 is the time between the Look-Locker pulses. This dependency on flip angle requires Look-Locker acquisitions to have a robust B_1 spatial characterisation, however, the exact flip angle isn't required for calculating the perfusion as this can be extracted from fitting Equation 3.1. M_0 was taken from the last successful TI of the Look-Locker readout, as a parameter-matched equilibrium

image wasn't acquired for the preliminary tests, this saturated M_0 will cause the perfusion to be overestimated. $M(TI)$ was the pixel-wise PENIR retrospectively-gated signal. A two parameter fit was used to estimate perfusion, f, and arterial transit time.

FAIR datasets were analysed from three mice, and the PENIR scheme was applied to remove the motion-corrupted TIs. The perfusion map as estimated using the Gunther adaptation of the general kinetic model can be seen Figure 3.28A; a lower level of perfusion can observed across the liver parenchyma, $P_{Gunther}$ = 0.90 ± 0.26 ml g^{-1} min^{-1} (mean ± standard deviation), compared to Belle model estimate (Figure 3.28C), P_{Belle} = 2.09 ± 0.58 ml g^{-1} min^{-1}. The arterial transit time (ATT) map estimated from the fitting can be seen in Figure 3.28B – reduced transit times can be seen in the blood, and a homogenous ATT can be seen across the liver parenchyma (mean ATT 0.27 ± 0.01 s).

From these measurements, the perfusion estimated by the Belle model is closer to previous invasive microsphere measurements in mice livers, which measured a mean perfusion of 1.8 ± 0.3 ml $g^{-1}min^{-1}$ (14). In addition, the fitting success of the general model can be seen in Figure 3.28D. The blue points represent the difference in tissue signal post slice-selective and global inversion, and the red line shows the expected behaviour of the model. It is clear that the general kinetic model does not fit the data suitably, and further work is necessary to develop this. However, owing to the concordance of the Belle model to literature values, the following research will use this quantification approach. The Belle model is susceptible to producing high flow from fast inflowing blood, so care will have to be taken to remove the influence on non-liver perfusion levels – values over 10 ml g^{-1} min^{-1} were chosen to be excluded from the mean perfusion measurements.

The optimised FAIR-LL in combination with the PENIR algorithm now offers an imaging pipeline to estimate mouse liver perfusion, the repeatability and reproducibility of the technique was then tested in order to assess its suitability in application to therapy of hepatic disease.

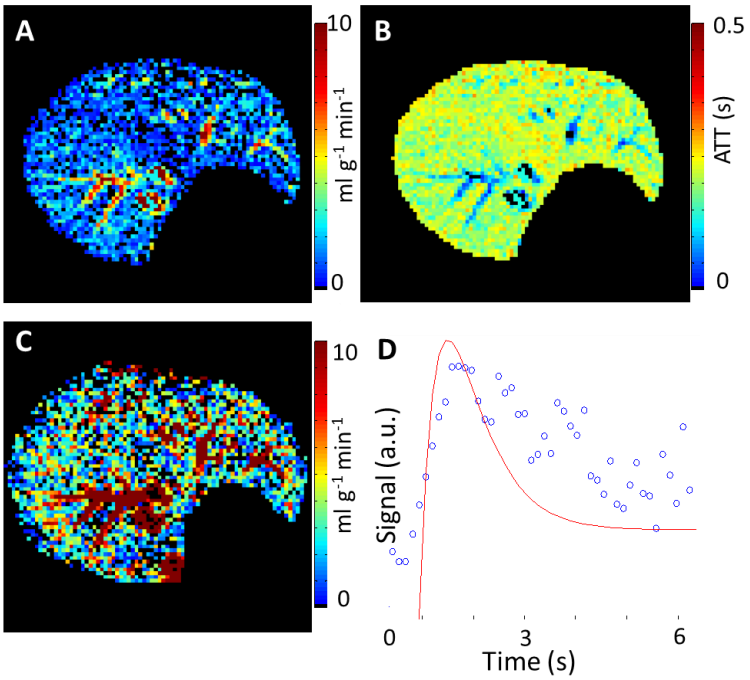

Figure 3.28: (A) Perfusion quantification using general kinetic model with Look-Locker correction. (B) Corresponding arterial transit time (ATT) map, reduced transit times can be seen at the location of the large vessels. (C) Perfusion map from the same dataset following Belle quantification, the perfusion is markedly increased. (D) – quantification fitting from general k model shows poor model fitting (red line) success to the data (blue points).

3.6 Repeatability and Reproducibility of Hepatic FAIR-LL ASL

3.6.1 Materials & Methods

3.6.1.1 Animal models

10 female BALB/C mice aged 6-8 weeks were anesthetised with isoflurane (3% in 1L O_2/min for induction) and placed in a supine position within the scanner bore, as this was found to be optimal for placing the respiratory bellows. Animals were maintained at a steady level of isoflurane (approx. 1.9% isoflurane in 1L O_2/min) during scanning. Animals had access to food and water *ad libitum* and were weighed immediately before being placed in the scanner.

3.6.1.2 Imaging Procedure

An axial, respiratory-triggered, high-resolution, T_2-weighted, multi-slice Fast Spin Echo sequence was used to determine a suitable and consistent slice for ASL measurements. Image parameters included: FOV = 30 x 30 mm^2, matrix size= 192 x 192, TR = 1500 ms, effective TE = 19 ms, three averages, whole liver coverage with 0.5 mm thick slices.

A single-slice, respiratory-triggered, segmented Look-Locker FAIR sequence with a spoiled gradient-echo readout was used to acquire the ASL data. Sequence parameters included: 1 mm thick slice, FOV = 25 x 25 mm, matrix size = 128 x 128, TE = 1.18 ms, inversion time spacing $TI_{Look\text{-}Locker}$ = 110 ms, repetition time between Look-Locker sampling pulses TR_{RF} = 2.3 ms, sampling flip angle α_{RF} = 8°. TR_I: 13 s, 50 inversion recovery readouts, 4 lines per segmented acquisition with 50 sampling points. A 6 mm localised selective inversion was followed by a global inversion, with the scan taking around 15 minutes. An adiabatic fast-passage inversion pulse with a length of 2 ms and bandwidth of 20 kHz was used for slice-selective and global preparations (15), and 500 µs Gaussian radiofrequency pulses were used for Look-Locker excitation. Datasets were retrospectively corrected for respiratory motion using the PENIR algorithm, prior to T_1 mapping and perfusion quantification.

3.6.1.3 Repeatability and Reproducibility Assessment

For the repeatability and reproducibility study, ten female Balb/C mice were scanned under the same protocol, one week apart. Each protocol contained a high-resolution, respiratory gated fast spin echo sequence which was used to determine the location of the porta hepatis, where both the hepatic artery and portal vein are visible. Four consecutive ASL scans were then performed, with the animal maintained at a constant level of anaesthesia and temperature.

3.6.1.4 Quantification

Mean perfusion was obtained by drawing an ROI within the liver parenchyma, avoiding the major blood vessels as they will contribute high (non-physiological) perfusion. In addition, spurious estimates of perfusion were removed by automatically thresholding the values above 20ml g^{-1} min^{-1} (2, 14), and noise-induced negative perfusion values were set to zero.

3.6.1.5 Statistical Analysis

The coefficient of variation (CV) (Eq. 4), a normalised measure of the data variability given by the ratio of the standard deviation σ to the mean µ, was used to compare measurements of liver perfusion.

$$CV = \frac{\sigma}{\mu} \times 100\% \qquad \text{Equation 3.35}$$

Three modes of variation were calculated: repeated measurements within an imaging session were used to assess the within-session CV (CV_{WS} ± standard error). The between-session CV was estimated from comparing index-matched scans between week 1 and week 2 for each mouse (i.e. week 1-scan 1 with week 2-scan 1). The between-animal variation,

CV_A, reflects the variability between perfusion estimates in different animals, was calculated from all ASL scans. Each coefficient was calculated from a region encompassing all the liver parenchyma within the slice. The inter-animal precision was obtained from the standard deviation of perfusion estimates between animals.

To determine the minimum detectable change in perfusion given by hepatic ASL, Bland-Altman repeatability coefficients (RC) (Eq. 5) were calculated. Bland-Altman RCs correspond to the 95% confidence interval given by two perfusion estimates; ΔP is the difference in perfusion estimates between time points, $\overline{P}$ is the mean perfusion, and n the sample size.

$$RC = \frac{1.96}{\overline{P}} \sqrt{\frac{\sum(\Delta P^2)}{n-1}} \times 100\% \qquad \text{Equation 3.36}$$

Repeatability coefficients were calculated from the first two scans within each session, for each week and averaged to produce RC_{WS}. The between session repeatability coefficient RC_{BS} was generated from averaging the RCs of number-matched scans between the weeks for all the animals.

3.6.2 Results

3.6.2.1 Hepatic Arterial Spin Labelling

The quantification of perfusion using the optimised T_1-difference method can be visualised in Figure 3.29. Taking the mean signal within a ROI of liver tissue, the different tissue relaxation can be observed following slice-selective (red) and global (blue) inversion (Figure 3.29A) – respiration-corrupted images have been omitted from the data. Applying the fitting pixel-wise, T1 maps following slice-selective (Figure 3.29B) and global (Figure 3.29C) inversions can be generated; the mean global T1 measured in the liver was 1.36 ± 0.06 s (mean ± standard deviation). An example fast spin echo image with the perfusion map overlaid on the liver parenchyma (Figure 3.29D); high non-physiological perfusion values are present within the major vasculature and there is a heterogeneous signal across the liver parenchyma. Mean perfusion measured across liver ROIs, inclusive of both repeat scans and including all animals, was 2.2 ± 0.3 mlg-1min^{-1} (mean ± standard deviation).

Again, this value agrees well with previous microsphere measurements in similar-weight mice measured a mean total hepatic perfusion of 1.8 ± 0.3 ml g^{-1}min^{-1} (14). This paper also measured a reference perfusion in the kidneys 5.1 ± 0.8 ml g^{-1}min^{-1}, which agrees well with a kidney ROI within the ASL data 5.3 ± 0.6 ml g^{-1}min^{-1}. Additionally, previous liver blood flow measurements in mice using DCE-MRI obtained 4.96 ± 1.87 ml min^{-1} (5) and a bulk

perfusion can be estimated as 2.48 ml $g^{-1}min^{-1}$ to match the ASL-estimated values, assuming an approximate mouse liver mass of 2g (16). In addition, the measured perfusion values agree well with previous literature measuring rat liver perfusion using ^{85}Krypton clearance (2.41 ± 0.50 ml g^{-1} min^{-1})(4), microspheres (1.9 ± 0.1 ml g^{-1} min^{-1})(17), and two clearance techniques using Indocyanine Green (2.03 ± 0.13 ml g^{-1} min^{-1}) and galactose (2.28 ± 0.49 ml g^{-1} min^{-1})(18). Although the majority of invasive liver blood flow measurements have been performed in rats, from analysis of renal ASL applied to the two species(19), we expect the physiology to be comparable to mice.

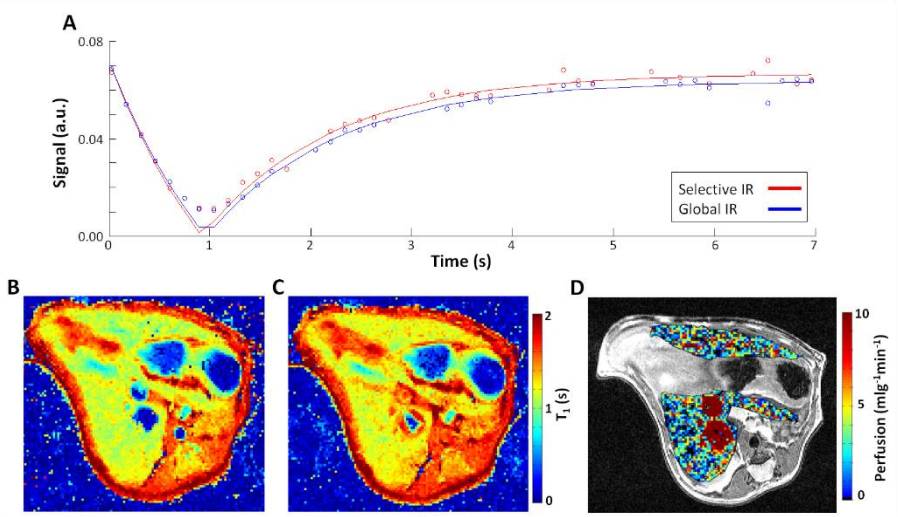

Figure 3.29: Quantifying perfusion from a hepatic FAIR-LL ASL dataset: The perfusion signal comes from the difference in longitudinal recovery (A) following slice selective (red) and global (blue) inversion. The inversion recovery plots were generated from the mean signal within a small ROI within liver tissue, and dataset had been retrospectively gated. Example T_1 map acquired after a slice selective inversion (B) and global inversion (C), T_1 values have been clipped at 2 seconds (mean liver T_1: 1.36 ± 0.06 s). The resultant perfusion map of liver parenchyma overlaid on high-resolution T2-weighted Fast Spin Echo (FSE) image (D). Non-physiologically high perfusion values can be seen within major blood vessels, perfusion values in this image have been limited at 10 $mlg^{-1}min^{-1}$.

3.6.2.2 Repeatability and Reproducibility of Liver Perfusion Estimates

A significant increase in animal mass was measured from week 1 (18.5 ± 0.6 g) and week 2 (18.9 ± 0.4 g) ($P < 0.05$, paired t-test). No significant difference in respiratory rate during scanning was observed between weeks 1 and 2 (49 ± 8 breaths/min in week 1 and 49 ± 9 breaths/min in week 2, $P > 0.3$). Furthermore, no significant correlation was measured between estimated liver perfusion and animal weight, breathing rate or isoflurane concentration, which was individually constant but varied from 1.7 to 2.2 % in 1L/min O_2 across the subjects. No influence of anaesthesia was expected as previous measurements

did not find a significant change in total liver blood flow over these relatively small differences in isoflurane concentration (20).

The variation within each perfusion imaging session across the cohort can be visualised in Figure 3.30A. From fitting each perfusion imaging session, a significant trend in perfusion was measured ($p < 0.01$, t-test) – though the mean perfusion change per scan (-0.05 $mlg^{-1}min^{-1}$) is within the uncertainty of the technique; this is also reflected in a non-significant paired t-test using the first and last perfusion estimate across the all the imaging sessions ($p > 0.2$). Additionally, there was no between-session perfusion trends observed when comparing scan-index matched perfusion estimates between week 1 and 2 estimates ($p > 0.4$, paired t-test).

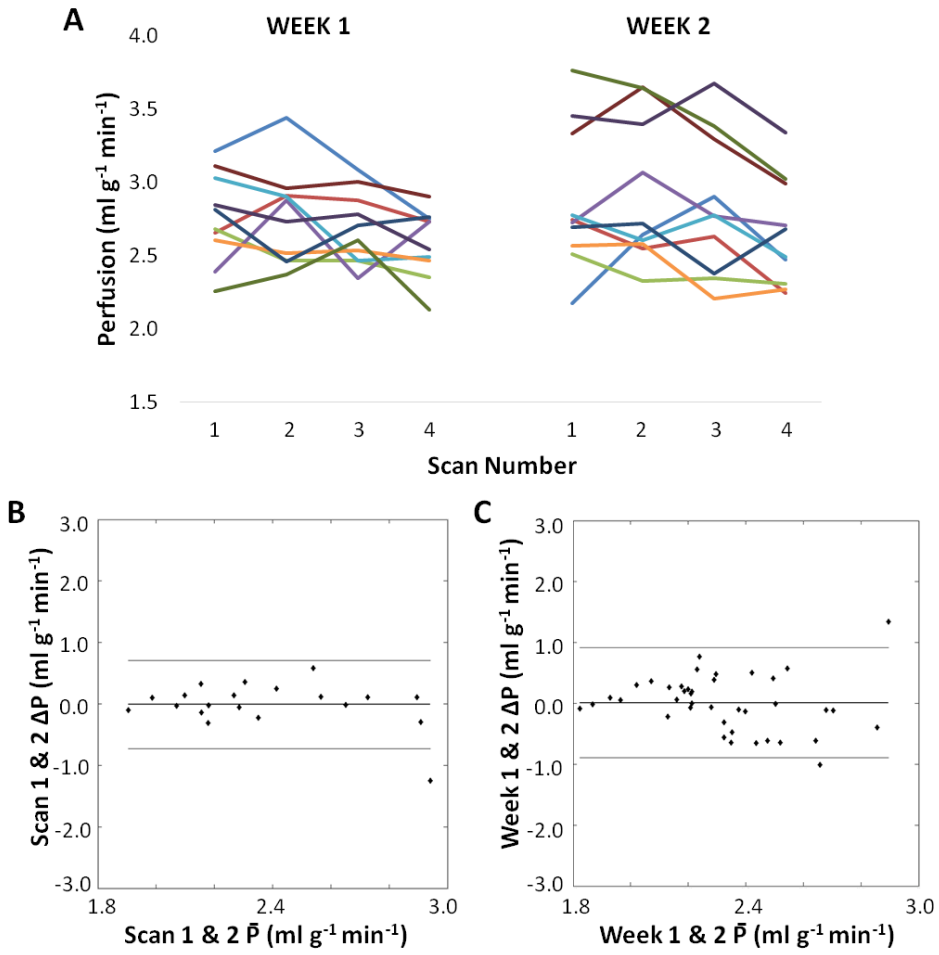

Figure 3.30: Repeatability and variability in mean liver perfusion, across all animals (shown in different colours) for both weeks (A). A significant negative perfusion trend was measured (-0.05 $mlg^{-1}min^{-1}$ per scan) within each session across the cohort, though this is within the uncertainty of the technique. No trends were observed between the imaging sessions. Bland-Altman plots showing the within-session variation in mean estimated liver perfusion from the first and second scan (B) and between-session mean perfusion repeatability plots (C) .The central, thick solid line represents the mean difference, and the two outer lines show the ± 1.96 x standard deviation. For all the plots, the mean difference measured was within the error of the technique, and no trends can be distinguished.

3.6.2.3 Coefficient of Variation

The within-session coefficient of variation $CV_{WS,}$ was 7 ± 1%, the between-session coefficient of variation CV_{BS} was 9 ± 1%. The between-animal CV_A was 15 ± 1%, The CVs between three data conditioning modes varied within 1%. The inter-animal precision was calculated to be ± 0.3 $mlg^{-1}min^{-1}$ across the whole liver.

3.6.2.4 Repeatability Coefficients

Figure 3.30B shows Bland-Altman plots to visualise the within-session differences by comparing perfusion estimates from repeated measurements. The plot is not suggestive of a magnitude dependence in perfusion estimates and has a mean difference of +0.01 ± 0.34

$mlg^{-1}min^{-1}$. Between-session Bland-Altman analysis is also free from any magnitude dependence and measured a mean difference of +0.01 ± 0.46 $mlg^{-1}min^{-1}$. The Bland-Altman repeatability coefficient provides an estimate of the percentage change required to measure a significant variation in a particular parameter estimate: the within session Bland-Altman repeatability coefficient RC_{WS} was 18% and the between session repeatability coefficient RC_{BS} was calculated to be 29%.

3.6.3 Discussion & Conclusion

This study tested the repeatability of the optimised liver ASL imaging pipeline. The variability in the within-session and between-session measurements were relatively small and comparable to previous myocardial perfusion variability using a similar technique (1). The repeatability coefficients give a measure of the required percentage change to observe a significant difference in perfusion measurements. The between session repeatability was larger than the within session changes, this was within expectations due to week-to-week changes. The minimum sensitivity for between session changes was 29%, which shows promise for application to disease and therapy monitoring: previously reported differences in perfusion between cirrhotic and normal patients have been approximately 30% (21) and DCE-MRI estimates of the perfusion related transfer constant K_{trans} have shown change a 40% change post vascular targeting therapy (22).

From the repeatability and reproducibility analysis, the largest variability was between animals, suggestive that subject variability was greater than that of the technique. However, it is difficult to isolate the precise source of variation, as the variability of the technique will contribute to the between animal variability measure. A slight downward trend was observed in the perfusion estimates over the imaging session, this may be due to dehydration during the experiment – the effects of this may have to be accounted for long duration scanning sessions, perhaps by using a saline infusion.

Between-session and between-animal perfusion variability has been previously attributed to variations in the level of administered anaesthesia. Isoflurane level has been previously reported to have a significant influence on myocardial perfusion measurements (23), although no such association was found in this study, which is agreement with previous liver studies (20). The influence of anaesthesia on perfusion can be seen from a FAIR-LL ASL experiment incrementing the level of administered isoflurane in two mice (Figure 3.31). No significant increases in perfusion were measured in the liver (blue) but were in the myocardium (red).

A further potential source of variability was the feeding status between animals, as animals were allowed to feed *ad libitum*. The portal vein draws blood from the intestines, and so the between animal variability observed may be exacerbated by differing dietary habits between the mice. Previous behavioural studies in mice reported a cyclic consumption of food approximately every 24 hours (24), though no trend in perfusion was correlated with the time of the day to suggest that an *ad libitum* diet may not be an influential factor to the variability in liver perfusion. Future studies may investigate the FAIR-LL technique's sensitivity to post-prandial liver perfusion changes following a controlled diet (25).

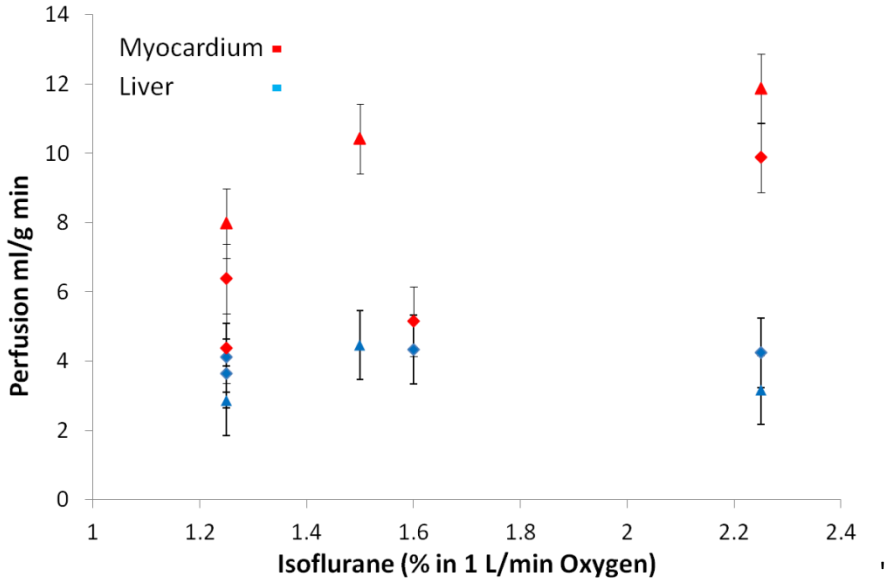

Figure 3.31: Physiological influence of anaesthesia on myocardial and hepatic perfusion in two subjects (diamond and triangle) with a liver (blue) and myocardial (red) ROI in a single slice. In this experiment the isoflurane was incrementally increased from 1.25 to 2.25% in 1L/min of Oxygen; a marked increase can be seen in the myocardial tissue (red) over the administrated range; where the liver perfusion values (blue) aren't affected. In addition, no trend was observed between liver perfusion and isoflurane.

This chapter has shown the development of a hepatic ASL technique, the repeatability analysis shows that it has promise in application to pre-clinical models of liver disease. Before such applications are explored, a few investigations were carried out to further explore the Look-Locker acquisition.

3.7 Further Optimisation of the Look-Locker Acquisition

3.7.1 Multi-slice FAIR-LL ASL

The FAIR-LL acquisition has thus far been single-slice; however by including more sampling pulses to the Look-Locker train, it is possible to acquire additional slices without increasing

the total acquisition time (Figure 3.32). This will allow for greater efficiency in coverage of the liver, which would be of particular use in application to pathology.

3.7.1.1 Methods: Pulse Sequence

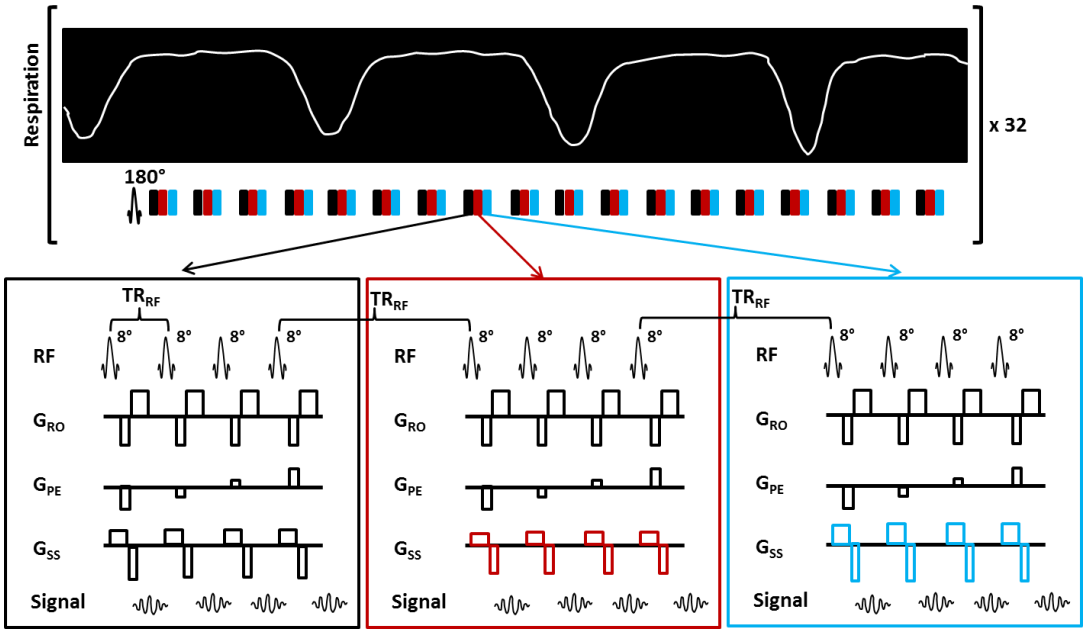

Figure 3.32: Multi-slice adaption to the Look-Locker sequence. This schematic shows a three slice acquisition; each single-slice readout block (black) has an additional two slices (red and blue) added in – each slice is acquired directly after the other at TRRF (3.1 ms). Using the method, it is possible to increase liver coverage and maintain the same scan duration.

Figure 3.32 demonstrates a three-slice example multi-slice adaptation of the Look-Locker acquisition; the new slices have been added in red and blue. By designing the sequence in such a manner and maintaining the $TI_{Look\text{-}Locker}$, the total acquisition time will not be altered.

With no gap between the three slices and each slice being 1 mm thick, the slice-selective thickness of 6 mm will be suitably wide enough to perfusion-weight all the slices. The effective slice-selective inversion thicknesses for each slice will be 4, 6 and 8 mm; from the optimisation of the inversion thickness (Figure 3.20), it possible to see that the slice furthest from the direction of flow may have some reduced perfusion as a result of the slow inflow of portal blood.

This inflow effect can be addressed using a blood-pool reference to inform a more complex model of perfusion developed by Campbell-Washburn *et al*. (26). The perfusion-modified Bloch equations are altered to factor in a time-dependent blood magnetisation, and thus the quantification requires a more complex numerical integration to estimate perfusion. Though this has been successfully implemented in the mouse myocardium, initial attempts to quantify the perfusion with this method was computationally expensive and returned

falsely high estimates of perfusion (Figure 3.33). This will need further work to refine this model for the liver, thus for the remainder of this chapter, the original Belle model will be used for perfusion quantification as before.

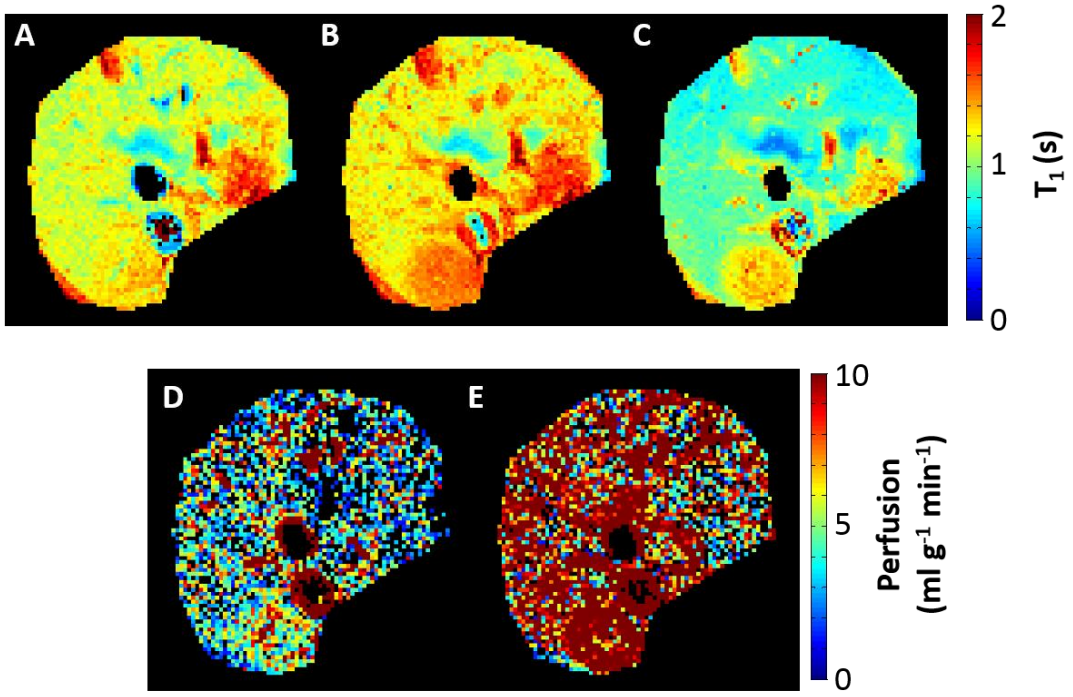

Figure 3.33: Preliminary investigations in to a blood-pool correction to the perfusion quantification: (A) slice-selective T_1 map (mean T_1 = 1.16 s), (B) global T_1 map (mean T_1 = 1.23 s), (C) tissue T_1 map (mean T_1 = 0.91 s) – derived from accounting for the blood relaxation taken from an ROI within the portal vein. The single-slice quantification method shows a perfusion map within physiological values (D) where the corrected quantification (E), exhibits high perfusion (mean standard perfusion was 1.9 ml g^{-1} min^{-1}, and the mean blood pool corrected perfusion was 7.4 ml g^{-1} min^{-1}).

3.7.1.2 Results: Comparison with Single Slice Measurement

The sequence was run in an agar phantom to measure if the increased pulses in the multi-slice sampling train affected the T_1 estimation compared to the single slice acquisition. No significant difference or bias (t-test, $p > 0.05$) was measured between the multi-slice and the single-slice measurements (Figure 3.34A). In addition, no significant differences were found in the T_1 measurements when using a gap of 0 or 0.2 mm between the slices, so continuous liver coverage is implementable.

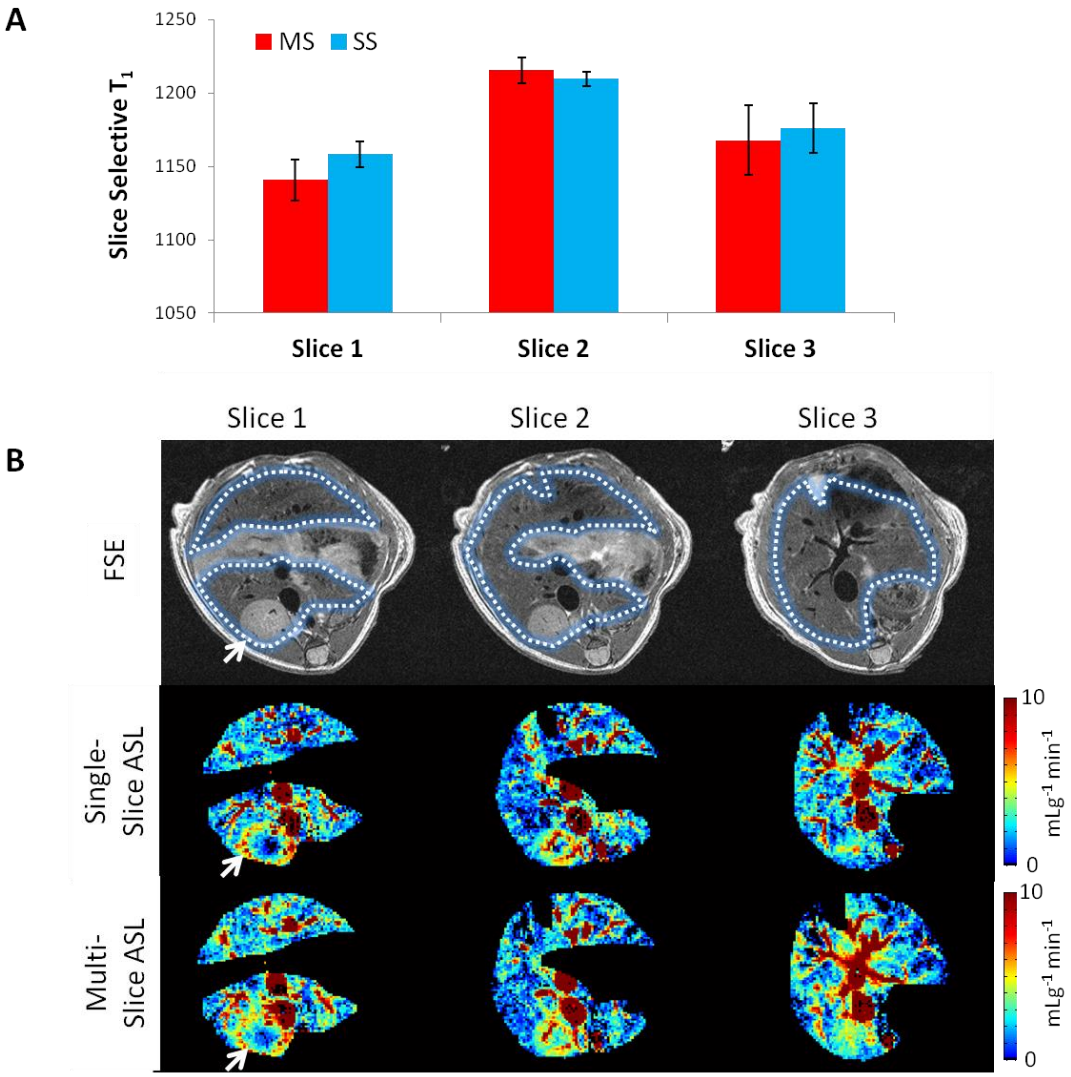

Figure 3.34: (A) Comparison of $T_{1,Selective}$ in three different slices as acquired by multi-slice (MS, red) and single-slice (SS, blue) FAIR-LL acquisition in an agar phantom – no significant differences were measured between the techniques. (B) Three T_2-weighted, fast spin echo images of a liver (ROI outlined) at the different slice positions (Row FSE) and the corresponding single-slice perfusion maps (Row Single-Slice ASL) and multi-slice perfusion maps (Row Multi-Slice ASL). Visual inspection indicates good correlation between the two techniques; high flow can be seen at major blood vessels and a ring of high perfusion can be observed in the renal cortex (arrow).

The multi- and single-slice sequences were then performed *in-vivo* in three mice to assess any perfusion differences. Visual assessment of the example perfusion maps in Figure 3.34B shows good correspondence between the multi- and single-slice FAIR-LL. The high regions of flow correspond to the locations of blood vessels which appear hypo-intense in the FSE anatomical images. The kidney has been included within the analysis ROI, which appears hyper-intense relative to the liver parenchyma on the FSE (arrow). In both sets of perfusion maps a 'ring' of raised perfusion can be seen within the renal cortex relative to the medulla (27). Across all three slices, the multi-slice under-estimates the perfusion 97.2 ± 16.3%, though this is non-significant (t-test; p >0.5) – the global T_1 was non-significantly

overestimated 107 ± 11% (t-test; p>0.05). By each slice; slice 1, which is closer to the portal vein, over-estimates perfusion: 118 ± 10%, slice 2 agrees well 99.7 ± 9.6 %, and slice 3 underestimates perfusion 74 ± 29%, though none of these were measured as significantly different (t-test, smallest p > 0.2), this is likely to be due to the slice positioning relative to the label plane as discussed above. This may be additionally related to the slice ordering during readout: due to the slice-selective inversion being centred about the first readout slice, the readout order is arranged such that the central slice was acquired first.

The quantification used for the multi-slice perfusion estimates has been the regular Belle model as used in the previous section. Figure 3.20 demonstrated the inflow of blood in the portal system isn't fast enough for the quantification assumptions to hold. However, this simplified approach to the multi-slice quantification visually compares well, but is likely to induce a systematic error. Further work will be required to investigate Campbell-Washburn modified Belle model: this method accounts for perfusion underestimation per slice by drawing a ROI within a blood vessel – however, this is difficult in more superior parts of the liver where the portal vein has branched in to small venules. In addition, this proposed method doesn't factor in the arterial contribution to the liver, as the hepatic artery is so small and its contribution to the total liver flow is much smaller than that of the portal vein.

Thus, due to the added complexities with multi-slice imaging, single-slice analysis will be used for the remainder of this thesis, though a multi-slice acquisition will be acquired so future development may retrospectively increase the available data.

3.7.2 Look-Locker Resolution & Segmentation

3.7.2.1 Pulse Sequences & Methods

Two adaptations to the Look-Locker acquisition were explored in this section: the acceleration of the sequence by increasing the segmentation of the sequence, and varying the number of TIs within the Look-Locker train.

The FAIR-LL sequence and retrospective gating is reliant on steady breathing in order to not induce too much physiological noise within the raw data. In order to improve this, an investigation was carried out in speeding-up the acquisition time in order to minimise possible physiological drift. The segmentation of each TI was increased from 4 to 8 samples, the additional sampling pulses can be seen in the schematic in red in Figure 3.35A.

Secondly, in order to possibly facilitate an alternative method of quantification using the subtraction of the magnetisation, the $TI_{Look\text{-}Locker}$ was decreased and thus more TIs could be

included. The original hypothesis was to improve the temporal resolution to improve alternative perfusion modelling and also enable the implementation a DCE-like dual-compartment analysis to be able to split the venous and arterial blood supply. DCE fitting is highly reliant on a high-temporal resolution to partition the blood contributions, and so the temporal resolution of the sequence was increased to 100 TIs with a $TI_{Look\text{-}Locker}$ 50 ms (Figure 3.35B). Alternatively, two normal acquisitions could be interleaved, however that would be less efficient than increasing the number of TIs.

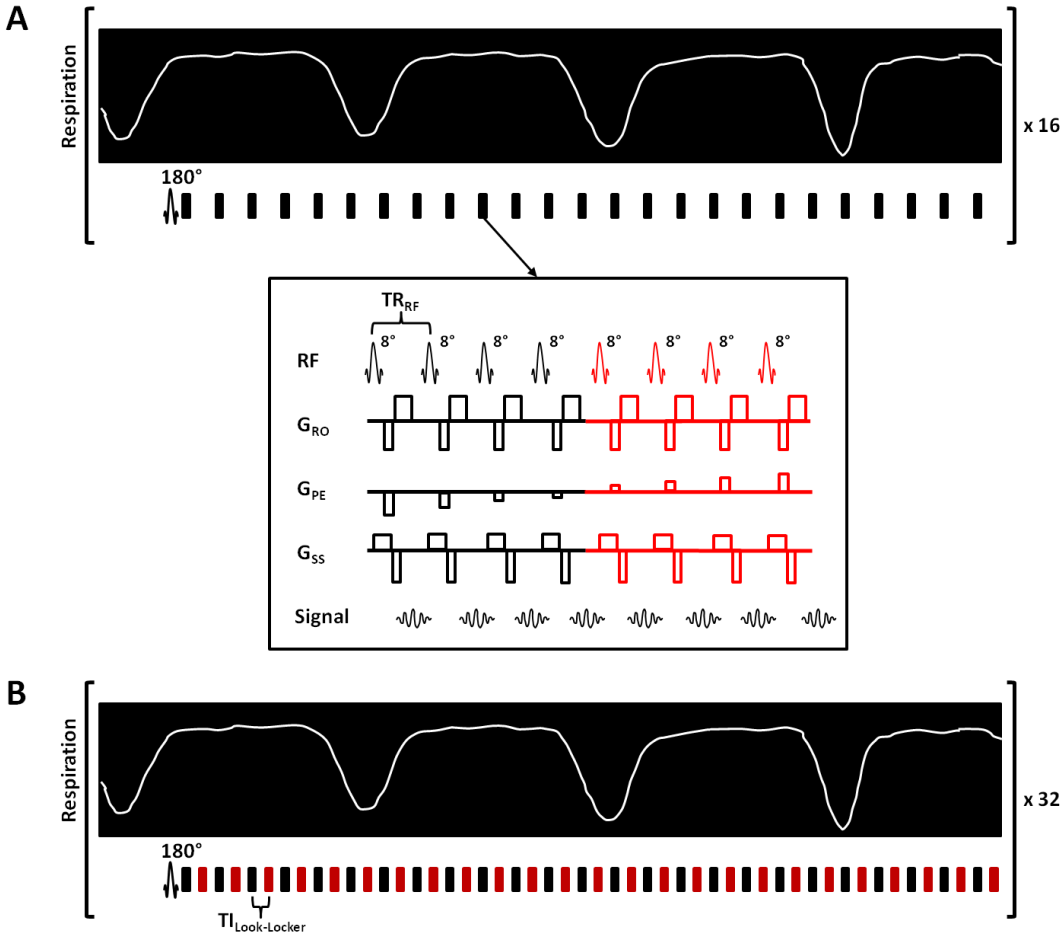

Figure 3.35: (A) Increasing the segmentation or speed-up factor (SF) of the Look-Locker acquisition. Each sampling block has four more sampling pulses added (red) to halve the acquisition time. (B) High temporal resolution adjustment to the Look-Locker sequence. Extra sampling blocks (red) have been added in to create a smaller $TI_{Look\text{-}Locker}$, and thus increase the temporal resolution of the sequence.

Four different Look-Locker sampling trains were then compared: acquiring 50 TIs with a speed-up factor (SF) of 4, acquiring 100 TIs with a SF of 4, acquiring 50 TIs with a SF of 8, and acquiring 100 TIs with a SF of 8. These acquisitions were first tested in an agar phantom to compare the T_1 estimations and then applied *in-vivo*.

Finally, Monte-Carlo (MC) simulations were carried out testing the influence of increasing the number of TIs to best characterise the T_1 value. A normally-distributed noise profile was added to the inversion simulation, with an SNR of 10, as measured from the *in-vivo* experiments in this section. The number of TIs were increased from 5 to 100, with the TIs evenly distributed across 7 seconds, and a simulated T_1 of 1.2 seconds. 100 repeats were carried out, and the error in the T_1 estimation as produced from MATLAB's *nlparci* 95% confidence interval was calculated for each number of TIs.

3.7.2.2 Results: Comparison of LL Acquisition Strategies

From ANOVA analysis in phantoms, no significant differences were measured across the read-out strategies (ANOVA; $p>0.8$). The *in-vivo* results can be seen in Figure 3.36A; no significant differences can be visualised between the different speed-up factors and TIs for both the $T_{1,global}$ and perfusion maps. Taking a liver parenchyma ROI, the effects of saturation can be visualised in the signal evolution plots (Figure 3.36B). The increased number of TIs (blue and green) causes a greater amount of signal saturation; however the T_1 maps still agree well due to the Look-Locker quantification accounting for the saturation. There are no obvious saturation differences for increasing the speed-up factor, which will allow faster acquisition.

The overlay of the MC simulations can be seen in Figure 3.36C, the error in the T_1 estimation can be seen to decrease with increased TIs – however there isn't such a large improvement between 50 and 100 TIs ($\Delta T_{1,TI=50} = 0.17s$, $\Delta T_{1,TI=100} = 0.12s$).

3.7.3 Conclusion

The sequence can be easily manipulated to acquire more slices, more images and in a shorter frame of time with no deterioration of image quality. The multi-slice acquisition, though visually looks promising when compared to a single-slice acquisition, will require further development to implement the blood pool correction factor to best estimate the T_1 and perfusion maps with the modified Belle model (28).

The high temporal resolution sequence will need further investigation with the general kinetic and dual compartment modelling. If the perfusion contributions from the arterial and venous supplies can be separated using a DCE-MRI type model, this will have potential application to liver disease models, where the ratio of the perfusion can vary. The increased segmentation does not seem to affect the T_1 and perfusion estimates, which halves the acquisition time and thus reduce the image sensitivity to breathing variation.

As no changes were observed by increasing segmentation and temporal resolution, it is recommended to use to help improve the liver ASL imaging using a Look-Locker readout, with a single-slice analysis. However, as the repeatability analysis was carried out using a speed-up factor of 4 with 50 TIs, Chapter 4 applies this single slice acquisition to pre-clinical models in response to therapy. AS Chapter 5 uses the FAIR-LL as a reference scan and T_1 map, the high-temporal resolution and increased segmentation sequence was used.

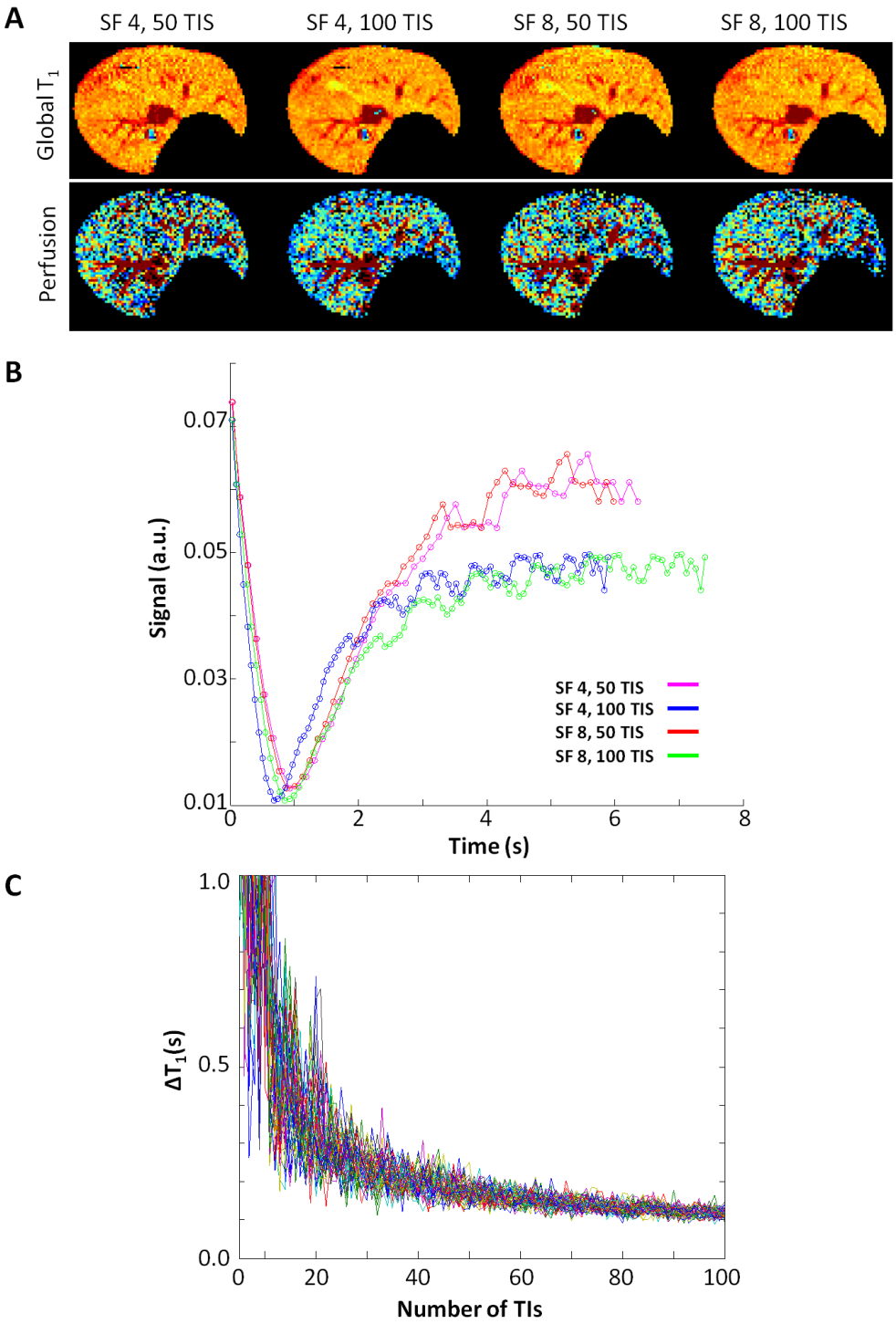

Figure 3.36: (A) Comparison of T_1 and perfusion maps using a combination of segmentation speed-up factors (SF) and number of TIs in the Look-Locker sampling train; the increased RF duty does not affect the longitudinal relaxation or perfusion maps. (B) Comparison of global inversions from the mean signal in a uniform region of liver tissue. The higher segmentation has an observable saturation difference, though from the T_1 values are recovered due to the inversion efficiency correction (Chapter 2, Eq 13). (C) Overlaid Monte-Carlo simulation of the error in the T_1 estimation (from 95% confidence interval) as a function of the number of TIs. The plots show that the larger number of TIs will aid better T_1 characterisation, however there is no significant change using TIs greater than 50.

3.8 Conclusions

3.8.1 Discussion and Conclusion

In this chapter, we have applied a Look-Locker FAIR arterial spin labelling MRI for the first time to measure liver perfusion in a pre-clinical setting. We have optimised the technique and investigated the technique's reproducibility and repeatability within and across imaging sessions. In addition, a method of retrospective gating (PENIR) was introduced that is wholly data-generated and was applied to reduce the perfusion estimate error.

The implemented FAIR-ASL preparation and T_1-based quantification is attractive due to its estimation of the total liver blood flow (i.e. both portal venous and arterial) independent from modelled parameters. The Belle model proved to be a more accurate measure of liver flow than the generalised perfusion model, when compared to previous invasive microsphere measurements.

A measurement of global liver perfusion changes may be a useful quantity when applied to models of cirrhosis and liver dysfunction (21). In addition, the parenchymal T_1 value has been reported to increase as a result of inflammation and fibrosis development (29) and cirrhosis onset (30) – a quantitative MRI parameter which is generated by the Look-Locker FAIR ASL acquisition.

The signal exhibited recovery in the portal vein following slice-selective inversion, even at the smallest inversion thickness. This means that the FAIR assumption isn't entirely valid, however the blood-pool quantification could be used here to account for any potential underestimation in perfusion.

The intrinsic low perfusion SNR of ASL experiments leads to the majority of methods employing the efficient EPI readout, however such a technique is particularly challenging in the rodent liver; the surrounding abdominal fat and air cavities in the stomach and lungs can make imaging prone to distortion and signal dropout. Hence a gradient echo acquisition was used, and to increase the efficiency of the ASL data set, a Look-Locker method was applied – however this employs a low sampling flip angle which can result in low SNR images leading to some noise in the perfusion maps. In an alternative set-up, this may be improved using a surface receiver coil, though we found a sub-optimal coverage of the liver using such an arrangement.

FAIR-LL ASL has been demonstrated in this chapter as a repeatable measure within the mouse liver. In the next chapter the technique will be applied to a number of hepatic

diseases. First, in tandem with a vascular targeting therapy of liver metastasis, then applied to rat model of cirrhosis. Finally, the perfusion of liver lobes will be measured in an experimental liver regeneration model in rats.

References

1. Campbell-Washburn AE, Price AN, Wells JA, Thomas DL, Ordidge RJ, Lythgoe MF. Cardiac arterial spin labeling using segmented ECG-gated Look-Locker FAIR: variability and repeatability in preclinical studies. Magn Reson Med 2013;69(1):238-247.

2. Belle V, Kahler E, Waller C, Rommel E, Voll S, Hiller KH, Bauer WR, Haase A. In vivo quantitative mapping of cardiac perfusion in rats using a noninvasive MR spin-labeling method. Jmri-Journal of Magnetic Resonance Imaging 1998;8(6):1240-1245.

3. Wells JA, Thomas DL, King MD, Connelly A, Lythgoe MF, Calamante F. Reduction of errors in ASL cerebral perfusion and arterial transit time maps using image de-noising. Magn Reson Med 2010;64(3):715-724.

4. Rice GC, Ryan CJ, Leiberman DP, Mathie RT, McGhee E, Harper AM, Blumgart LH. Measurement of liver blood flow in the rat using an 85Krypton clearance technique. Br J Exp Pathol 1977;58(3):236-242.

5. Hartono S, Thng CH, Ng QS, Yong CX, Yang CT, Shi W, Chuang KH, Koh TS. High temporal resolution dynamic contrast-enhanced MRI at 7 Tesla: a feasibility study with mouse liver model. Conf Proc IEEE Eng Med Biol Soc 2011;2011:2788-2791.

6. McRobbie DW, Moore EA, Graves MJ, Prince MR. MRI from Picture to Proton. Cambridge University Press; 2003.

7. Deichmann R, Haase A. Quantification of T1 Values by Snapshot-Flash NMR Imaging. Journal of Magnetic Resonance 1992;96(3):608-612.

8. Walker-Samuel S, Orton M, McPhail LD, Robinson SP. Robust estimation of the apparent diffusion coefficient (ADC) in heterogeneous solid tumors. Magn Reson Med 2009;62(2):420-429.

9. Duhamel G, Prevost V, Girard OM, Callot V, Cozzone PJ. High-resolution mouse kidney perfusion imaging by pseudo-continuous arterial spin labeling at 11.75T. Magn Reson Med 2013.

10. Buxton RB, Frank LR, Wong EC, Siewert B, Warach S, Edelman RR. A general kinetic model for quantitative perfusion imaging with arterial spin labeling. Magn Reson Med 1998;40(3):383-396.

11. Cox EF, Ghezzi A, Bennet A, Patel M, Jackson A, Harman D, Costigan C, Omar NF, James MW, Ryder SD, Gowland PA, Aithal GP, Guha IN, Francis ST. A novel MRI protocol to axamine haemodynamic compartments in compensated liver cirrhosis. Proc Intl Soc Mag Reson Med 2013;21:0276.

12. Schalkx HJ, van Stralen M, Peters NHGM, Veldhuis WB, van Leeuwen MS, Pluim JPW, Petersen ET, van den Bosch MAAJ. Pre- and postprandial arterial and portal venous liver perfusion using selective spin labeling MRI with Look-Locker read-out. Proc Intl Soc Magn Reson Med 2014;22:372.

13. Gunther M, Bock M, Schad LR. Arterial spin labeling in combination with a look-locker sampling strategy: inflow turbo-sampling EPI-FAIR (ITS-FAIR). Magn Reson Med 2001;46(5):974-984.

14. Sarin SK, Sabba C, Groszmann RJ. Splanchnic and systemic hemodynamics in mice using a radioactive microsphere technique. Am J Physiol 1990;258(3 Pt 1):G365-G369.

15. Wells JA, Siow B, Lythgoe MF, Thomas DL. The importance of RF bandwidth for effective tagging in pulsed arterial spin labeling MRI at 9.4T. NMR Biomed 2012;25(10):1139-1143.

16. Jones LD, Nielsen MK, Britton RA. Genetic variation in liver mass, body mass, and liver:body mass in mice. J Anim Sci 1992;70(10):2999-3006.

17. McDevitt DG, Nies AS. Simultaneous measurement of cardiac output and its distribution with microspheres in the rat. Cardiovasc Res 1976;10(4):494-498.

18. Pollack GM, Brouwer KL, Demby KB, Jones JA. Determination of hepatic blood flow in the rat using sequential infusions of indocyanine green or galactose. Drug Metab Dispos 1990;18(2):197-202.

19. Rajendran R, Lew SK, Yong CX, Tan J, Wang DJ, Chuang KH. Quantitative mouse renal perfusion using arterial spin labeling. NMR Biomed 2013;26(10):1225-1232.

20. Frink EJ, Jr., Morgan SE, Coetzee A, Conzen PF, Brown BR, Jr. The effects of sevoflurane, halothane, enflurane, and isoflurane on hepatic blood flow and oxygenation in chronically instrumented greyhound dogs. Anesthesiology 1992;76(1):85-90.

21. Van Beers BE, Leconte I, Materne R, Smith AM, Jamart J, Horsmans Y. Hepatic perfusion parameters in chronic liver disease: dynamic CT measurements correlated with disease severity. AJR Am J Roentgenol 2001;176(3):667-673.

22. Nathan P, Zweifel M, Padhani AR, Koh DM, Ng M, Collins DJ, Harris A, Carden C, Smythe J, Fisher N, Taylor NJ, Stirling JJ, Lu SP, Leach MO, Rustin GJ, Judson I. Phase I trial of combretastatin A4 phosphate (CA4P) in combination with bevacizumab in patients with advanced cancer. Clin Cancer Res 2012;18(12):3428-3439.

23. Kober F, Iltis I, Cozzone PJ, Bernard M. Myocardial blood flow mapping in mice using high-resolution spin labeling magnetic resonance imaging: influence of ketamine/xylazine and isoflurane anesthesia. Magn Reson Med 2005;53(3):601-606.

24. ANLIKER J, MAYER J. An operant conditioning technique for studying feeding-fasting patterns in normal and obese mice. J Appl Physiol 1956;8(6):667-670.

25. Schalkx HJ, van Stralen M, Peters NHGM, Veldhuis WB, van Leeuwen MS, Pluim JPW, Petersen ET, van den Bosch MAAJ. Pre- and postprandial arterial and portal venous liver perfusion using selective spin labeling MRI with Look-Locker read-out. Proc Intl Soc Magn Reson Med 2014;22:372.

26. Campbell-Washburn AE, Zhang H, Siow BM, Price AN, Lythgoe MF, Ordidge RJ, Thomas DL. Multislice cardiac arterial spin labeling using improved myocardial perfusion quantification with simultaneously measured blood pool input function. Magn Reson Med 2012.

27. Karger N, Biederer J, Lusse S, Grimm J, Steffens J, Heller M, Gluer C. Quantitation of renal perfusion using arterial spin labeling with FAIR-UFLARE. Magn Reson Imaging 2000;18(6):641-647.

28. Campbell-Washburn AE, Zhang H, Siow BM, Price AN, Lythgoe MF, Ordidge RJ, Thomas DL. Multislice cardiac arterial spin labeling using improved myocardial perfusion quantification with simultaneously measured blood pool input function. Magn Reson Med 2012.

29. Kim KA, Park MS, Kim IS, Kiefer B, Chung WS, Kim MJ, Kim KW. Quantitative evaluation of liver cirrhosis using T1 relaxation time with 3 tesla MRI before and after oxygen inhalation. J Magn Reson Imaging 2012;36(2):405-410.

30. Cox EF, Ghezzi A, Bennet A, Patel M, Jackson A, Harman D, Costigan C, James MW, Ryder SD, Gowland PA, Aithal GP, Guha IN, Francis ST. Liver T1 increases with fibrosis and is correlated with liver stiffness and ELF score. Proc Intl Soc Mag Reson Med 2013;21:4094.

Chapter 4

Application of Hepatic Arterial Spin Labelling to Pre-Clinical Liver Models

This chapter applies the developed FAIR-LL ASL pipeline to animal models of hepatic diseases. Initially we investigated the feasibility of ASL perfusion measurements in subcutaneous xenograft tumour models and subsequently applied it to an orthotopic model of colorectal liver metastasis. A vascular disruption agent therapy was then applied in situ to two lines of liver tumours, and the pre- and post-therapy perfusion was measured and compared to R_2*, a biomarker which has been trialled clinically. The FAIR-LL technique was then applied to a rat model of cirrhosis, to measure changes in perfusion with the onset of liver dysfunction. Finally perfusion changes were measured within a model of hepatic hyperplasia stimulation to image the lobe function in combination with high-resolution imaging of lobe growth.

The subcutaneous tumour and liver metastases research in this chapter was undertaken in collaboration with Dr Sean Peter Johnson, who cultivated the cells and implanted the mouse models. The histology and immunohistochemistry was performed by Uzma Qureshi and Professor Barbara Pedley. The vascular disrupting agent OXi4503 was developed by Oxigene, and procured by Professor Barbara Pedley. The acute, *in-situ* therapy monitoring with MRI was designed in collaboration with Dr Simon Walker-Samuel and Dr Sean Peter Johnson. The cardiac-gated phase contrast MRI sequence was developed by Thomas Roberts and Dr Simon Walker-Samuel. The subtractive phase-contrast MRI estimate of total liver blood flow was developed and validated by Dr Manil Chouhan. The liver cirrhosis research was led by Dr Manil Chouhan who designed the study, set up the model, and carried out the MRI- which was further assisted by Dr Alan Bainbridge. Details of the PC-MRI technique and validation can be found in his thesis. The liver ligation model was developed and performed by Dr Dipok Dhar, and the MRI and segmentation was performed in collaboration with Dr Manil Chouhan.

The application of a vascular disrupting agent to a mouse model of colorectal liver metastasis is currently in submission. The perfusion measurements in subcutaneous tumours contributed to Walker-Samuel, S., *et al.*, In vivo imaging of glucose uptake and metabolism in tumors. *Nat Med*. 2013 Aug;19(8):1067-72.

4.1 Introduction

4.1.1 Translational Research of Hepatic Disease and Therapy

Measurements of liver perfusion can have diagnostic value, and this chapter applies the previously optimised arterial spin labelling method to pre-clinical models of liver metastases, cirrhosis and lobe regeneration. As these diseases present differing flow dynamics to homeostasis, these will offer a validation of the sensitivity of the optimised ASL sequence.

Approximately 35,000 people are diagnosed with colorectal cancer in Britain per year (1), and about 40% of these will metastasise to the liver, in addition to a number of other primary tumour sites. Curative intervention is most critical at this stage, and a number of therapy options are available. Anti-cancer treatments such as vascular disrupting agents (VDAs) have shown promise to cause acute cessation of blood flow, and thus a method to directly measure perfusion changes following therapy would be of great utility. Furthermore, acute imaging following a VDA therapy can test the within-session sensitivity of the optimised liver FAIR ASL sequence.

In the UK, approximately 8000 new patients are diagnosed with cirrhosis each year (2). As cirrhosis develops, the liver becomes 'stiffer' and more resistant to flow due to deposition of collagenous fibres (3). Currently, there is no therapy available for cirrhosis, though surgical techniques such as hepatic resection and portal shunting have been used to assuage patient comfort (4). As there is an increased risk to patients associated to the Child-Pugh scoring of cirrhosis (5), accurate stratification of patient severity is key. A battery of blood tests are performed to diagnose cirrhosis, however, MRI offers the potential to localise any complications due to the disease. In addition to increases in tissue stiffness, perfusion has been shown to decrease as a result of cirrhosis, thus arterial spin labelling will have potential as a contrast-free method to characterise the level of liver dysfunction.

In patient cases of primary and widespread metastatic liver tumours, hepatic resection presents the best long term patient outcomes (6). Healthy livers are estimated to be functional with only 25% remaining; however for patients with hepatic dysfunction or damage due to chemotherapy, the advised future liver remnant (FLR) is around 40% (7). In some cases, such target liver volumes are difficult to achieve, thus there exist surgical techniques which promote lobe growth via selective portal occlusion or embolization. In particular, one recent procedure has shown a lot of promise which promotes the FLR to increase by 10-46% within 6-8 weeks (8). The insult due following selective ligation causes

neighbouring lobes to enlarge, and a further dissection along the falciform ligament can cause a rapid growth of the left lateral lobe. However, so far in this experimental procedure, little has been done to characterise the functionality of the enlarged liver lobes, asides from histological assessment from post-surgery biopsies. Arterial spin labelling may offer an assessment of liver function via liver perfusion, and in addition, contribute to the questions concerning the mechanism of the liver regeneration (9).

4.2 Methods: Cancer models

4.2.1 Cell lines: LS174T & SW1222

Two human colorectal cancer cell lines were used for the cancer research in this thesis, which exhibit different cellular and vascular structures. SW1222 tumours are well differentiated and have a well perfused vascular network, whereas LS174T tumours show poor differentiation and are comparatively less well vascularised and perfused, generally with larger hypoxic and necrotic regions (Figure 4.39F) (10, 11).

4.2.2 Subcutaneous Tumour Model

All *in vivo* tumour experiments were performed in accordance with the local regulations and the United Kingdom Coordinating Committee on Cancer Research (UKCCCR) guidelines (12).

The majority of cancer research has been performed in subcutaneous xenografts; the model is very reliable to establish and the tumour volume can be easily determined by callipers. The FAIR-LL sequence was first applied to a subcutaneous model to establish levels of perfusion within the solid tumours.

All cancer models were performed on immunocompromised mice (MF1 *nu*/*nu*, female, 6-8 weeks old, 25-30 g). Subcutaneous models were set-up using an established protocol: $5x10^6$ SW1222 cells were injected subcutaneously into the right flank of three mice using a 27G needle. Tumours were inspected visually and allowed to grow over 10–16 days.

4.2.3 Orthotopic Model of Liver Metastasis

Orthotopic models of cancer investigate tumours within a more clinically-relevant location compared to subcutaneous models. Metastasis models allow for tissue-specific environments and tumour heterogeneity, which has potential for translation to clinical patients.

Models were established using a previously published protocol. Mice were anaesthetised with isoflurane in O_2 at a concentration of 4% for induction, followed by 1.5% for maintenance. A subcutaneous injection of 0.1mg/kg buprenorphine (Vetergesic, Reckitt Benckiser, UK) was administered and the flank of the animal sterilised with clorhexidine solution. A laparotic incision of approximately 1cm was then made above the location of the spleen and the organ exteriorised for injection. Tumour cells were injected intrasplenically at a concentration of $1x10^6$ cells in 100µl in serum free media and allowed to wash through to the liver for 1 minute, followed by splenectomy to avoid the development of tumours at the site of injection (13). The laparotic incision was sutured (Ethicon, Johnson & Johnson, USA) and closed with wound clips (Autoclip system, Harvard Apparatus, UK).

For the models of colorectal liver metastases, SW1222 (n = 6) and LS174T (n = 6) cells were implanted using the protocol above. Tumour cells were transfected with luciferase so bioluminescent imaging could be used for early screening of model success. Solid tumour deposits which formed within the liver were monitored for cell engraftment using bioluminescent imaging (Photon Imager Optima, Biospace Lab, France) 1-3 weeks post-surgery. Mice that presented bioluminescent signal from the liver region were then promoted to T_2-weighted anatomical MRI at weeks 3-5 to observe tumour growth; perfusion MRI was performed in week 5.

4.2.4 Histology Methods

At the end of the MRI experiments, mice were intravenously injected (15 mg/kg) with the perfusion marker Hoechst 33342 (Cambridge Bioscience, UK) one minute before culling. Haematoxylin and eosin (H&E) staining for basic cell morphology was performed on 10µm thick slices on an AxioSkop bright-field microscope (Carl Zeiss, Germany). For Immunohistochemical (IHC) histology, livers were excised and snap frozen in isopentane/liquid nitrogen, before sectioning on a cryostat at 10µm thickness. Blood vessels were stained using the vascular endothelial marker CD31 (Abcam, UK), and dual biomarker images of blood vessels combined with the perfusion marker were taken on an AxioImager microscope (Carl Zeiss, Germany).

H&E and IHC histology was performed on untreated SW1222 and LS174T liver tumours, and further H&E staining was performed on the VDA-treated SW1222 metastases.

4.3 Application of FAIR-LL ASL to subcutaneous models

4.3.1 Subcutaneous MRI Protocol

Mice were anesthetised and then placed in the scanner so that the implanted tumour was upwards to facilitate maximising the tumour within a coronal field of view (FOV 20 x 20 mm^2). Dental paste (FlexiSil, Prevest DenPro, Germany) was applied to the tumour and flank region to restrict any movements due to respiratory motion. Thus, the FAIR acquisition and analysis was as before but without triggering or retrospective gating.

4.3.2 Results & Discussion

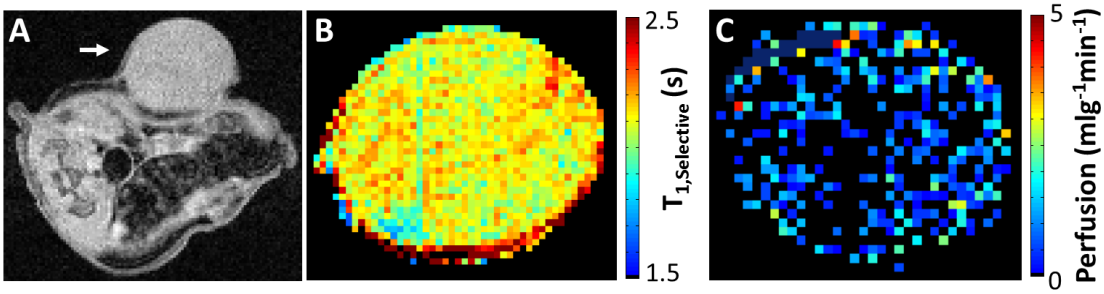

Figure 4.37: Application of FAIR-LL ASL to a SW1222 subcutaneous tumour model. (A) Axial GE image shows the tumour implantation marked by an arrow. (B) Slice-selective T_1 map shows a relatively homogenous structure within the tumour. (C) Resultant perfusion map within the tumour, the cell line presents low flow in the centre of the tumour and relatively higher flow around the tumour edge.

Subcutaneous tumours developed in all three mice, an example FAIR-LL dataset can be seen in Figure 4.37. An axial, *GE* image demonstrates the orientation of the tumour (arrow), the applied dental paste does not present any MR signal. The tumours are generally homogenous structures, though can exhibit necrotic regions, particularly in larger tumours. The T_1 maps reflected this unstructured phenotype (Figure 4.37B), with mean $T_{1,selective}$ 2.13 ± 0.07 s (mean ± std, n = 3). The perfusion maps presented very low levels of blood flow across the tumours (Figure 4.37C), mean perfusion was 0.19 ± 0.08 ml g^{-1} min^{-1}. A raised level of perfusion was measured at the periphery of the tumours, corresponding with vascular cast data (not shown) of these cell lines presenting large vessels chaotically networked around the tumour edge. Previous subcutaneous tumour FAIR measurements in three renal cancer cell lines measured similarly low perfusion levels, relative to other tissues: 0.801 ± 0.233 ml g^{-1} min^{-1} (A498), 0.751 ± 0.286 ml g^{-1} min^{-1} (786-0), and 0.102 ± 0.090 ml g^{-1} min^{-1} (Caki-1) (14) and 0.926 ± 0.429 ml g^{-1} min^{-1} (A498) (15).

Previous measurements have used twenty-four and forty averages to facilitate measuring the low perfusion. As the perfusion measurements presented low levels of tumour blood

flow, this will yield a low perfusion SNR, it is recommended that multiple averages of the FAIR-LL sequence are used to minimise quantification error from the T_1 differences. The hepatic ASL sequence was then applied to a mouse model of liver metastases to investigate any measurable level of perfusion within the tumours and differences between neoplasms to hepatic parenchyma.

4.4 Perfusion Measurements of Colorectal Liver Metastases

4.4.1 Liver Metastases MRI Protocol

Liver metastases successfully developed in 3 out of 6 LS174T models and 6 out of 6 SW1222 models. The hepatic ASL imaging pipeline used in Chapter 3.6 was applied to these two models of liver metastases.

Bioluminescent and high-resolution, T_2-weighted fast spin echo MRI (parameters as before in Chapter 3.4) were used to assess the success of tumour implantation over weeks 2 – 5 (Figure 4.38). The doubling time of liver metastases, estimated from volume estimations from manual segmentation, was 3.9 ± 0.6 days and 2.4 ± 0.6 days (mean ± standard error), for SW1222 and LS174T cells respectively. This is consistent with the range of doubling times observed in studies with other tumour cell lines: between 1.2 and approximate 4 days (16, 17). In addition, Kalber et al. measured a growth rate of approximately 2-3 days in LS174T liver metastases (18), which is in good agreement. These values reflect the variable growth rate in orthotopic tumours than traditional subcutaneous models, A similar rate of growth has been reported in subcutaneous models of SW1222 tumours; between 3 and 5 days (19, 20), though xenograft models will typically grow to larger volumes.

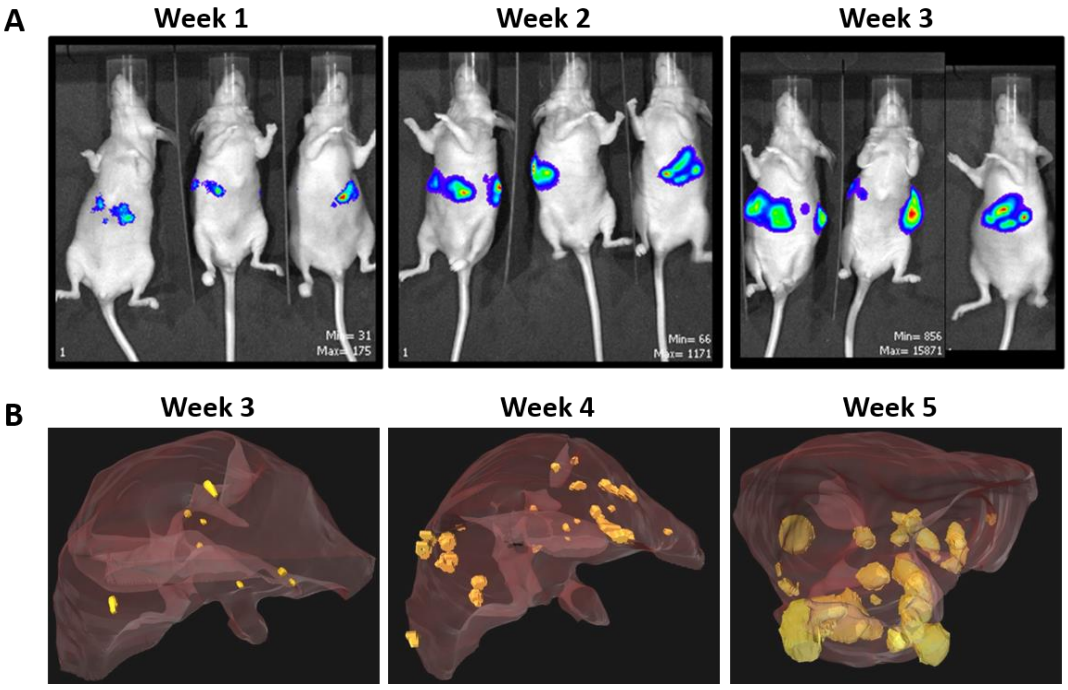

Figure 4.38: Monitoring the growth rate of a mouse model of liver metastases. (A) Bioluminescent images show light signal emitted from the site of the liver within a week of cell implantation. The signal intensity increases as the number of cells multiply over the weeks. (B) After three weeks, the tumours form solid tumours that can be visualised with a high-resolution T2-weighted imaging. In this series of manually segmented 3D visualisations, the liver appears semi-transparent red and the tumours as yellow. These tumours can be seen to increase in volume over three weeks.

The liver metastases appear hyper-intense (Figure 4.39, arrow) relative to the liver parenchyma (outlined) for both cell lines The FAIR-LL data was planned according to the anatomical images for a slice that contained a maximal number of tumours with a sufficiently large thickness and cross sectional area (0.7 mm^2, approximately 50 voxels), in order to avoid partial volume effects and to increase the number of tumour voxels for analysis. ROIs were drawn in the normal-appearing liver and tumours from the $T_{1,selective}$ map, and comparisons were assessed using Kruskal-Wallis ANOVAs.

4.4.2 Results

An example mapping from the SW1222 cohort has been shown in Figure 4.39B & C. The $T_{1,selective}$ maps (Figure 4.39B) were used to segment the metastases (arrow) as the tumour $T_{1,selective}$ was significantly raised ($p < 0.0001$, Kruskal-Wallis ANOVA) from the liver and vasculature for both cell lines: $T_{1,liver}$ 1.34 ± 0.07 s (mean ± std, both cell lines), $T_{1,Portal\ Vein}$ 0.29 ± 0.21 s (both cell lines), $T_{1,SW122}$ 2.15 ± 0.11 s (n = 6), $T_{1,LS174T}$ 2.49 ± 0.13 s (n = 3).

Observing the perfusion map in Figure 4.39C, low levels of perfusion are presented at the tumour locations relative to the liver parenchyma, and three metastases have been outlined which were sufficiently thick to avoid partial volume overestimation of perfusion.

A significant difference ($p < 0.05$, Kruskal Wallis ANOVA) was measured between the perfusion levels within the liver, SW1222 and LS174T metastases: P_{liver} 2.32 ± 0.34 ml g^{-1} min^{-1} (mean ± std), P_{SW1222} 1.03 ± 0.72 ml g^{-1} min^{-1}, P_{LS174T} 0.28 ± 0.16 ml g^{-1} min^{-1} (Figure 4.39D). This reduced level of perfusion is consistent with histology imaging (Figure 4.39E & F) of perfusion, as reported by the presence of Hoechst (blue), and blood vessel endothelial cells as marked by CD31 (red). The liver regions are marked by an arrow, which presents a well vascularised and perfused tissue. A marked reduction in perfusion and blood vessels can be seen in the SW1222 metastases region, (Figure 4.39E, star) and an even sparser tumour vascular environment is observed in the LS174T tumours (Figure 4.39F, star).

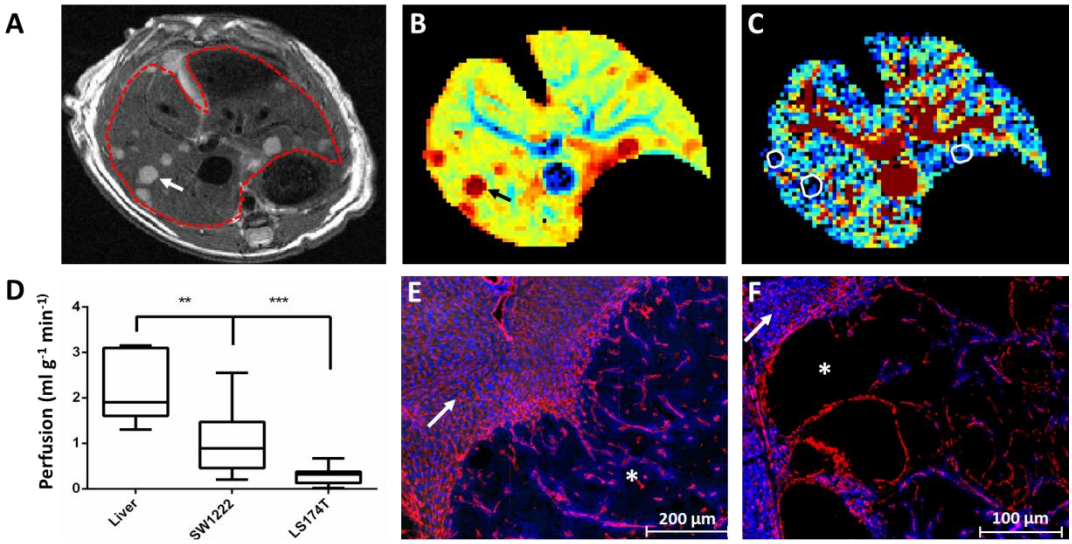

Figure 4.39: Application of FAIR-LL to a mouse model of colorectal liver metastasis. (A) Anatomical high-resolution T_2-weighted fast spin echo image shows an example liver with SW1222 tumour deposits (arrow) to be relatively brighter than the normal liver (red outline). (B) Corresponding T_1 map following slice-selective inversion; these maps were used to segment the tumours in the perfusion data as the tumour T_1 (arrow) was significantly higher than the liver, and additionally distinct from the vasculature. (C) In the perfusion map, the tumour regions (outlined) exhibit a reduced level of perfusion relative to the liver parenchyma. Flow estimates with non-physiologically high values can be seen at the location of the blood vessels. (D) A significant difference in perfusion was measured between the liver, SW1222 and LS174T liver metastases. This is concurrent with histological evaluation, which shows a marked reduction in perfusion (Hoechst, blue) and blood vessels (anti-CD31, red) between liver (arrow) and tumour (star) in the SW1222 metastases (E) and is even further reduced in the LS174T line (F).

These data demonstrate the FAIR-LL method's sensitivity to different levels of perfusion, and is a novel measurement of blood flow in mice liver metastases using an ASL method. The reduced perfusion of the metastases relative to the normal liver agrees with a number of previous invasive techniques; such as Hoechst measures of perfusion IHC in LS174T liver metastases (18) , 133Xe clearance imaging in rat a model of Walker-256 carcinoma metastases measured a perfusion within the liver as 0.84 ml g^{-1} min^{-1} and the tumours as

0.36 ml g^{-1} min^{-1} (21), microsphere measurements in a sarcoma rat model measured the tumour flow to be approximately 70% that of the liver (22). From these encouraging results, the hepatic ASL technique was then applied to monitor tumour perfusion following a vascular targeting therapy.

4.5 Monitoring Perfusion changes of Colorectal Liver Metastases following Vascular Disrupting Agent Therapy

4.5.1 Introduction: Vascular Disrupting Agents

Tumour vasculature is an attractive target for anti-cancer therapy, as the delivery of oxygen and nutrients from recruited blood vessels promote growth and malignant progression (23). The two main classes of chemotherapeutics to emerge from research targeting the tumour vasculature are anti-angiogenic compounds, that aim to stop any further vessel recruitment, and vascular disrupting agents (VDAs), that aim to destroy the existing tumour vascular network.

Anti-angiogenic compounds have been effectively applied to primary liver tumours in phase I & II clinical trials, however such therapy would be predominantly applied for early stage prevention of metastasis, rather than acute treatment (24). Little has been reported beyond phase I trials of vascular disrupting agents, due to toxicity or inefficacy (24). Vascular disrupting agents have an acute effect (typically within 24 hours of administration) (25), and do not cause a decrease in tumour volume due to a remnant surviving rim.

Therapeutic efficacy is commonly evaluated using the 'response evaluation criteria in solid tumours' (RECIST 1.1) (26), where response to therapy is assessed according to the apparent change in tumour size. This has been more recently amended with the modified-RECIST (mRECIST) (27) which accounts for the potential of derived parameters to assess tumours. However, as neo-adjuvant therapy was initiated for reducing tumour burden prior to resection, a strong emphasis of the mRECIST criteria remains on volumetric decrease. As VDAs have been shown to be effective at destroying the tumour vasculature, they have been used in combination with other therapies (28).

Changes in tumour pathophysiology have been assessed using MRI techniques such as dynamic contrast enhancement (DCE-MRI), intrinsic susceptibility (IS-MRI), and diffusion MRI (29). Though VDA treatment is succeeded by tumour regrowth from a surviving rim, there is still potential for use in combination therapy (30). However, due to the mechanism

and the acute nature of the drug action, there is potential for it to be used in conjunction with perfusion measurements from arterial spin labelling to inform on therapy efficacy.

4.5.2 Study Design

A study was performed in the two cell lines of colorectal liver metastases following administration of the vascular disrupting agent (VDA) OXi4503. This VDA has been trialled clinically (24), and though the therapy trials have recently subsided, the drug is known to be acutely effective (31), and hence will be a good candidate to mediate within-session, post-therapy perfusion changes. In addition to the perfusion measurements, the intrinsic susceptibility, given by R_2*, was measured to reflect a clinically-trialled biomarker following VDA treatment (29). The susceptibility is expected to rise following treatment, due to the increased presence of paramagnetic deoxyhaemoglobin within the tumour following vascular shut down.

As the perfusion within the LS174T tumours was low at baseline, and there was more uncertainty in the success of this tumour model, a control cohort was only established with SW1222 tumours (5 successful engraftments out of 6). The response to dosing study was performed 5 weeks following surgery in three groups: SW1222 with VDA treatment (n = 6), SW1222 with saline (n = 5) and LS174T with VDA treatment (n = 3). The main focus of this study was to assess the acute changes, however, in addition, a few mice were imaged over five days following the OXi4503 treatment.

4.5.3 *In-situ* VDA Response MRI Protocol

A primed intra-venous (i.v.) line was set up in the tail vein of the mouse, and secured in place for an in-situ administration of the vascular disrupting agent OXi4503. Baseline perfusion and previously optimised R_2* measurements were performed before administering 40mg/kg OXi4503 or saline via the i.v. line. R_2* imaging followed immediately up to 90 min post-dose, followed by an ASL acquisition at 90 minutes; this scan time had been determined due to the local limitations of small-animal imaging, so the animals may recover for potential longitudinal measurements. In addition, previous literature has reported a 50% reduction in blood flow within an hour following OXi4503 (31).

4.5.4 MRI Methods & Analysis

Values of the MRI transverse relaxation rate (R_2*) were estimated from a respiratory-gated multi-echo, multi-slice gradient echo sequence. Sequence parameters included: 8 echoes, TE_1 2ms, echo spacing 2 ms, TR = 280 ms; matrix size = 128 x 128, FOV = 30 x 30 mm^2, 15

slices, and slice thickness 1mm. R_2* was estimated using a maximum likelihood approach that took into account the Rician distribution of the data (32).

Paired t-tests (Wilcoxon) were performed on metastases and internal controls of normal-appearing liver, before and after *in-situ* dose for both perfusion and R_2* measurements. Longitudinal changes were analysed by normalising each tumour to its baseline value and differences between the days were assessed using Kruskal-Wallis analysis.

Liver and metastasis volumes were manually segmented using Amira 5.4 (FEI, Oregon, USA). Tumour locations were manually assessed on the high-resolution T_2 weighted images and divided into three categories: a) peripheral, b) near small, and c) near large vessels. The limit to the tumour's proximity to major vasculature was defined as 3-4 voxels (0.5 mm) for both small and large vessels. Venous and arterial blood vessels appear hypo-intense on the T_2-weighted image and small vessels were categorized by a cross sectional area less than 0.1 mm^2 (around 7-8 voxels). The perfusion and R_2* differences between the location categories were analysed using Kruskal-Wallis ANOVA comparisons.

Across the cohort of animals, for the SW1222 + VDA 18 metastases were evaluated from the single-slice ASL data and 34 metastases were assessed by IS-MRI data, 12 metastases were assessed for the LS174T + VDA by ASL and IS-MRI, and 10 metastases were assessed for the SW1222 + saline for both ASL and IS-MRI.

4.5.5 Results: Acute R_2* and Perfusion Changes

4.5.5.1 Response to OXi4503

Pre-treatment tumours showed variable baseline measurements of perfusion and R_2*; a heterogeneous response to OXi4503 was observed in both ASL and IS-MRI techniques as can be seen in an example SW1222 model in Figure 4.40. Baseline measurements for perfusion (top) and R_2* (bottom) have been overlaid on the T_2-weighted anatomical image. The highlighted tumour demonstrates the expected response post-treatment; the perfusion reduces and the R_2* increases due to an accrual of deoxyhaemoglobin.

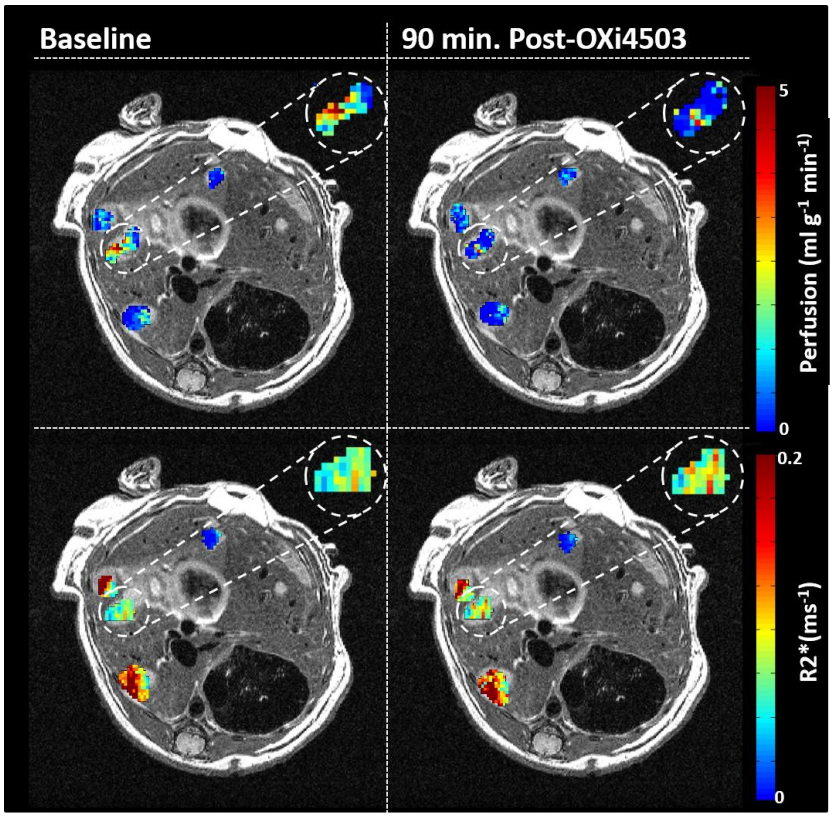

Figure 4.40: Image data showing the acute response at 90 minutes to 40 mg/kg of OXi4503, assessed using perfusion measured by hepatic arterial spin labelling (A) and intrinsic susceptibility MRI (via the R_2* parameter) (B). Images are overlaid on high resolution T_2-weighted axial anatomical data, in which tumour deposits appear hyperintense relative to liver parenchyma. A heterogenous response to OXi4503 therapy was observed across the metastases. One tumour has been highlighted to show the regional response.

The changes within the different groups as detected by ASL and IS-MRI can be seen in Table 4.2; the percentage changes for the liver have been included as an internal control. The results show that a significant decrease in perfusion was detected in SW1222 metastases for both treated and control groups, and a non-significant increase was measured in the treated LS174T tumours. In general, the liver perfusion decreased following the systemic administration, though non-significantly. A varied response was seen with the R_2* across all the groups, a significant change was measured with the VDA-treated LS174T tumours, and no significant changes were observed in the SW1222 tumours (treated and control) or the normal-appearing liver.

		SW1222 + OXi4503	LS174T + OXi4503	SW1222 + Saline
Perfusion	**Tumours**	-0.49 ± 0.44	0.04 ± 0.23	-0.17 ± 0.31
	%	-43 ± 33 % ***	61 ± 152 %	-16 ± 39 % *
	Liver	-0.35 ± 0.28	-0.14 ± 0.45	-0.54 ± 0.28
	%	-12 ± 12 %	-10 ± 27 %	-26 ± 15 %
R_2*	**Tumours**	0.005 ± 0.028	0.013 ± 0.012	0.011 ± 0.016
	%	0 ± 26 %	28 ± 25 % ***	6 ± 10 %
	Liver	0.012 ± 0.010	0.016 ± 0.010	0.008 ± 0.012
	%	9 ± 11 %	13 ± 11 %	5 ± 7 %

Table 4.2: Absolute (perfusion in ml g-1 min-1, R2* in ms-1) and percentage change (mean ± std) of SW1222 metastases treated with OXi4503 (n = 6), LS174T metastases treated with OXi4503 (n = 3) and SW1222 metastases given a saline control (n = 5). The internal control of the liver has been included for each group. Stars denote the significance determined by paired Wilcoxon t-tests (* $p < 0.05$, ** $p < 0.01$, *** $p < 0.001$).

4.5.5.2 Correlation of Perfusion and R_2* Changes with Baseline Measurements

Figure 4.41 shows the potential predictive nature of baseline perfusion measurements by ASL; acute changes for perfusion and R_2* taken 90 minutes post i.v. injection of OXi4503 can be observed relative to the baseline measurement for both SW1222 and LS174T tumours. A significant linear correlation (R^2 = 0.76, $p<0.001$ Pearson's R) for SW1222, though non-significant (R^2 = 0.18, $p >0.1$) for the LS174T was found between the baseline and the change in tumour perfusion after administration of the vascular disrupting agent (Figure 4.41, top row). However, no corresponding correlation was observed between baseline R_2* and subsequent change in intrinsic susceptibility after OXi4503 (Figure 4.41, row R2*). No significant correlation ($p > 0.1$) was measured between the changes in perfusion and the change in R_2* at 90 minutes following OXi4503 administration.

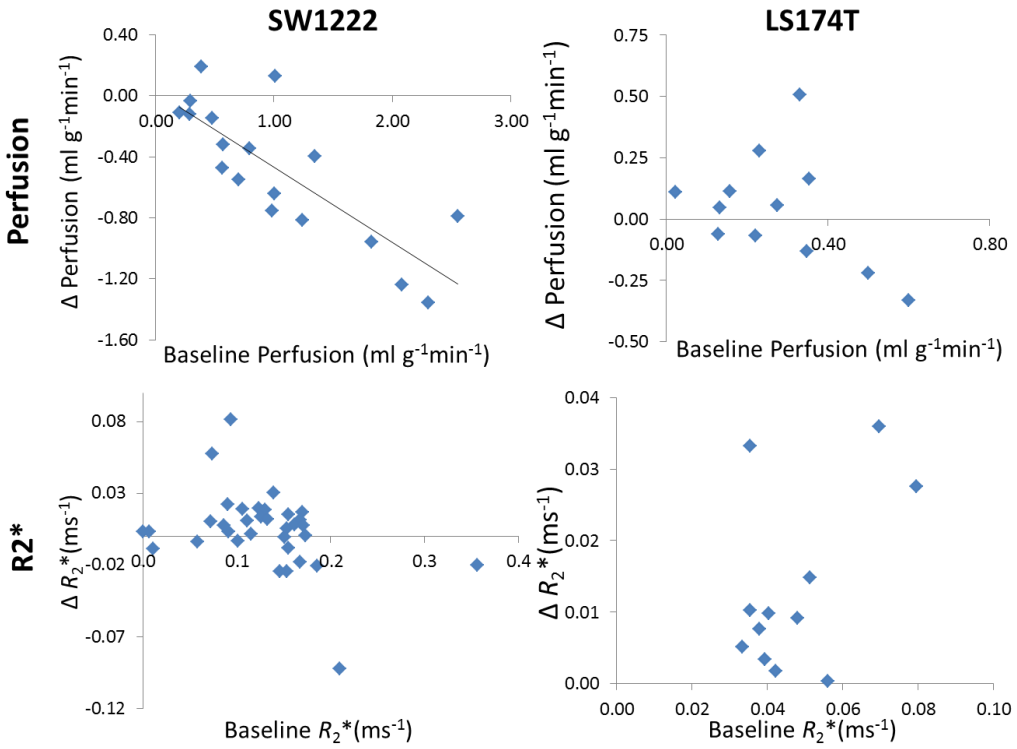

Figure 4.41: Graphs showing the relationship between pre-therapy perfusion and R_2* in SW1222 and LS174T liver metastases, and the subsequent change in each parameter at 90 minutes following administration of 40 mg/kg OXi4503. A significant, negative correlation was found between pre-therapy and post-therapy vascular perfusion (SW1222: R^2 = 0.76, p<0.001 Spearman's rho, LS174T: R^2 = 0.78, p<0.001 Spearman's rho), although no such correlation was found for R_2*. A graph of the change in R_2* against the change in perfusion (C) showed no significant correlation (p=0.19, Spearman's rho), however a suggestion of a negative trend can be discerned, in conjunction with the expected behaviour.

4.5.5.3 Relationship between response and tumour location

In Figure 4.42A, three example tumours have been outlined as classified by their proximity to large vessels (>8 voxels, red), small vessels (<8 voxels, green) and distal (>4 voxels, blue) to vasculature - typically located at the periphery of the liver lobe. Figure 4.42B shows a manually-segmented 3D rendering of an example mouse liver from T_2-weighted FSE MRI data, in which the liver parenchyma can be seen in transparent red, the major vasculature in purple, metastases in yellow and the tumours have been coloured according to their classification.

Figure 4.42C shows the percentage changes in SW1222 tumour perfusion (red, green and blue outline) and R_2* (solid red, green and blue) at 90 minutes post OXi4503 when liver metastases were grouped according to their location. This analysis was not performed in the LS174T tumours due to the low number of tumours.

Tumours close to major vasculature were better perfused at baseline ($p < 0.05$, Kruskal-Wallis ANOVA): 1.5 ± 0.8 $mlg^{-1}min^{-1}$ (mean ± standard deviation), 1.3 ± 0.7 $mlg^{-1}min^{-1}$, 0.6 ± 0.3 $mlg^{-1}min^{-1}$ for locations 1), 2) and 3) respectively. No significant differences in perfusion reduction were measured between the groups ($p > 0.1$, Kruskal-Wallis ANOVA), though the data suggests that the largest perfusion decreases can be observed in metastases proximal to vasculature. The most consistent mean decrease in perfusion was observed in metastases proximal to large vessels (-62% ± 19%, mean ± standard deviation), whereas a more varied decrease in blood flow was seen in tumours near smaller vessels (-36% ± 51%). Tumours in the periphery of the liver lobe displayed a smaller but largely variable response in perfusion (-32% ± 25%).

No significant differences ($p > 0.05$, Kruskal Wallis ANOVA) were measured between baseline R_2* measurements: 0.11 ± 0.05 ms^{-1}, 0.27 ± 0.14 ms^{-1}, 0.21 ± 0.11 ms^{-1} for locations 1), 2) and 3) respectively. No significant differences were measured in R_2* response post-OXi3403 as grouped by location ($p > 0.15$, Kruskal Wallis). Metastases in all locations behaved inconsistently for R_2* (large vessel 16% ± 26% (mean ± standard deviation), small vessels -13% ± 29%, and periphery -4% ± 20%).

This heterogeneous response to therapy has been observed in H&E histology (Figure 4.42D): a necrotic centre is observable in some tumours (arrows) where other metastases in the same lobe have seemingly not responded (stars). However, histology was not directly paired to the MRI data as it is difficult to follow single tumours from the MRI to the histology due to the malleable and lobular nature of the liver. As all animals were followed longitudinally, the results of which are reported below, the earliest histology was taken at 24 hours after VDA therapy.

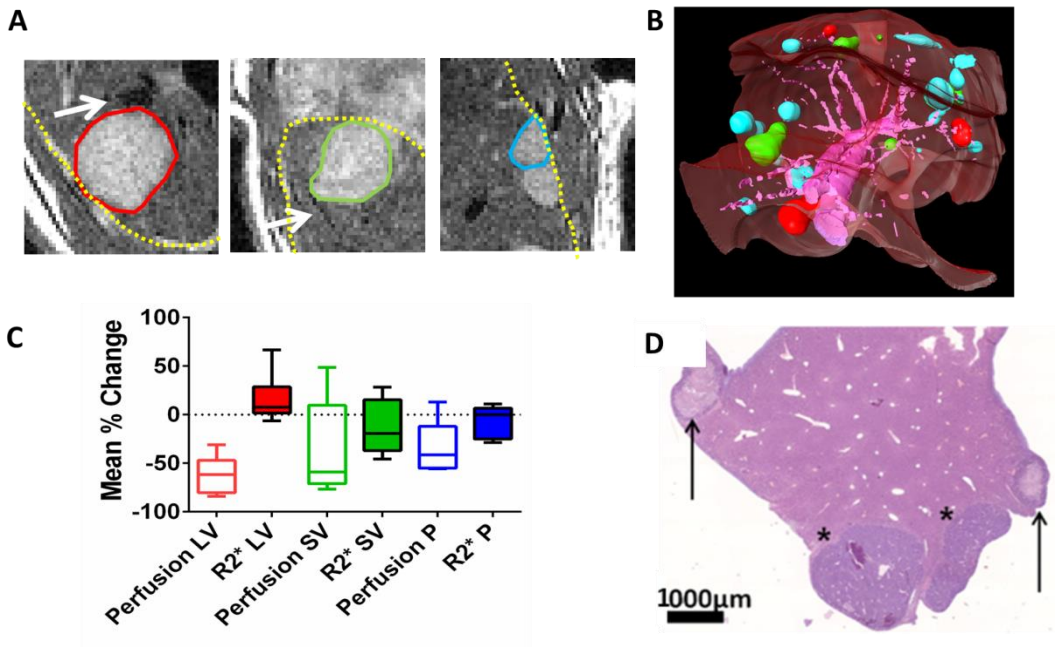

Figure 4.42: (A) Example determination of tumour location into three categories: proximal (< 0.5mm) to large vessels (> 0.1mm^2) (red), small vessel (green), and peripheral to vasculature (blue). Vasculature appears hypo-intense on T2-weighted images, and example vessels have been highlighted with an arrow. (B) A 3D visualisation of a manually-segmented mouse liver at week 5 post-implantation, showing liver parenchyma (transparent red), major vasculature (purple) and metastases have been coloured as classified by their location. (C) Percentage change in perfusion and R_2* at 90 minutes following administration of 40 mg/kg of OXi4503, categorised according to proximity to vessels and location within the liver (see colour bar). Large perfusion decreases were observed in metastases close to large and small blood vessels though tumours near smaller vessels demonstrated a more variable response. Peripheral metastases did not display a significant change in perfusion. No significant changes were measured in R_2* across the defined liver locations. (D) H&E histology at 24 hours shows a varied response of OXi4503 to a model of liver metastases – successful administration in tumours exhibit a necrotic core (arrows) and unaffected deposits have viable cells (stars).

4.5.6 Longitudinal Monitoring

The OXi4503-treated mice with metastases were monitored at 24 hours (n = 5 SW1222, n = 3 LS174T), 72 hours (n = 3 SW1222, n = 2 LS174T) and at 120 hours (n = 2 SW1222, n = 2 LS174T) post administration; the saline-SW1222 mice were not followed longitudinally. However, due to the single slice hepatic ASL acquisition and the flexible nature of the arrangement of the liver lobes, it was difficult to capture consistent tumours within a single acquisition. As a result, in combination with animals being taken for longitudinal assessment by histology, it was difficult to maintain the number of tumours for analysis for longitudinal monitoring. The changes in mean tumour perfusion and R_2* (with standard error), normalised to baseline, over 5 days can be seen for both SW1222 (Figure 4.43A) and LS174T (Figure 4.43B) cell lines. Visual inspection of the graphs suggest that both cell lines exhibit the expected decrease in tumour perfusion and increase in R_2* at 24 hours post

treatment, however, no significant differences were found between days in either cell line or either MRI derived quantity (SW1222 perfusion $p > 0.15$, SW1222 R_2*$p > 0.9$, LS174T perfusion $p > 0.5$, LS174T R_2* $p > 0.4$, Kruskal Wallis ANOVA). In addition, analysis of the SW1222 tumour cells and corresponding normal-appearing liver T_1 (Figure 4.43C) showed no significant changes over time in the liver (Kruskal-Wallis ANOVA $p > 0.1$), however, a significant reduction in tumour T_1 was found at 120 hours (Kruskal-Wallis ANOVA $p < 0.01$). This result is in accordance with previous pre-clinical research which observed a reduction in T_1 following therapy, hypothesised to reflect the number of remaining viable tumour cells (33).

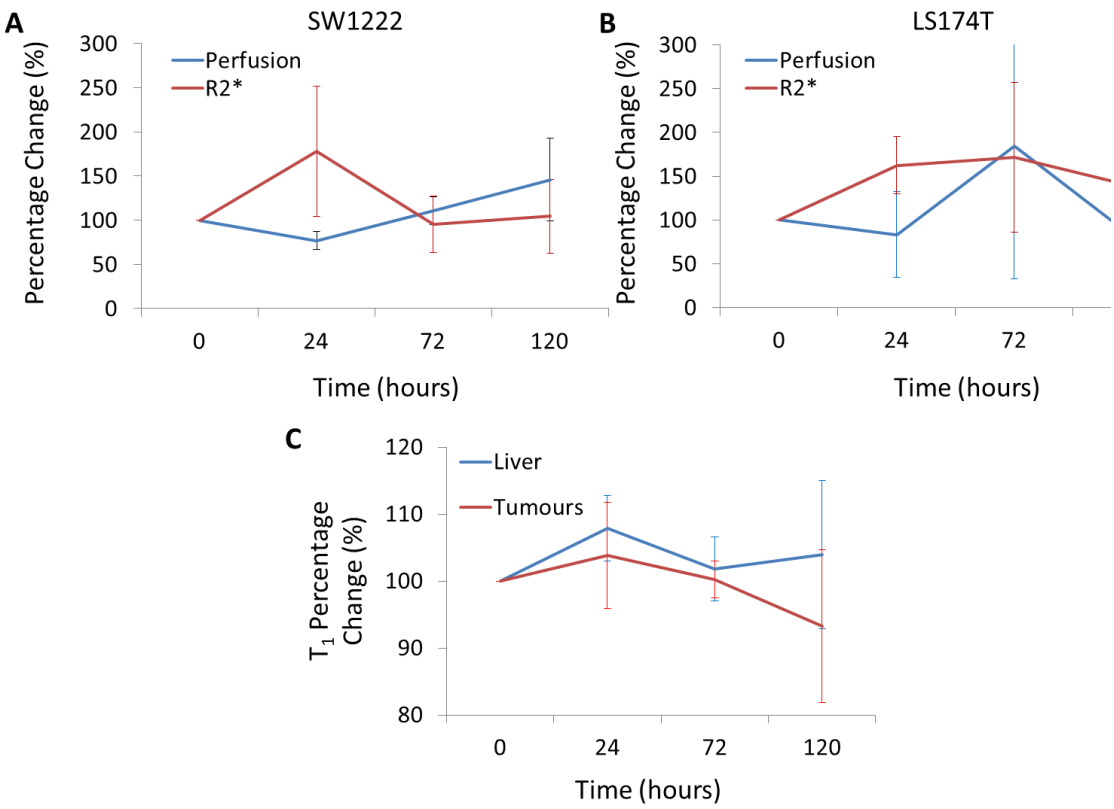

Figure 4.43: Normalised longitudinal changes of perfusion (blue) and R_2* (red) for SW1222 (A) LS174T (B) cells following OXi4503. No significant differences were found between baseline, 24 hours, 72 hours and 120 hours following therapy with either MRI-derived parameter. (C) A significant reduction was measured in SW1222 tumour longitudinal relaxation following OXi4503 treatment, though no changes were measured in the liver.

4.6 Discussion: Application of FAIR ASL to Liver Tumour Models

This was a novel measurement of perfusion within a model liver metastases using ASL MRI; blood flow differences between tumour and liver parenchyma were measured that reflected the histology. The correlation between baseline SW1222 perfusion measurements

and post-VDA response provides evidence towards the accuracy of the ASL measurement, in addition to the acute efficacy of the treatment. Thus FAIR-LL may offer a robust measure for clinical assessment of VDA therapy, furthermore, the correlation found suggests that a diagnostic perfusion measurement may inform on the therapy approach.

The FAIR sequence was first applied to a model of subcutaneous tumours, and a low level of perfusion was measured, as previous reports have shown, though in different cell lines [1] (21, 22). The low perfusion signal may be improved by increasing the averaging, by using a faster imaging readout such EPI (14). As the subcutaneous tumours are stationary, and are fixed in place by use of a dental fixative, the advantages of image rejection using a Look-Locker readout are potentially superfluous.

The significant decrease in saline-administrated SW1222 tumours and large, though non-significant, percentage increase VDA-treated LS174T perfusion is most likely due to variability in the low baseline perfusion measurements: 0.3 ± 0.2 ml g^{-1} min^{-1} (LS174T), 0.6 ± 0.5 ml g^{-1} min^{-1} (SW1222 + saline) and 1.0 ± 0.7 ml g^{-1} min^{-1} (SW1222 + VDA). From Chapter 3.5, the variability in perfusion was measured to be ± 0.3 ml g^{-1} min^{-1}, so the treated LS174T and saline SW1222 perfusion values are approaching the lower limit of the sensitivity of the technique, and percentage variations can be amplified. Excluding LS174T metastases which exhibit a perfusion less than this threshold, the percentage change is still non-significant, but reduced to 13 ± 89 %.

The measurement perfusion decrease of treated-SW1222 tumours did not correspond to an increase in R_2*, which has been previously reported, though not in SW1222 cell line (34). The LS174T tumours exhibited a slower baseline R_2* (0.047 ± 0.004 ms^{-1}) compared to VDA-treated SW1222 (0.132 ± 0.062 ms^{-1}) and saline-administrated SW1222 tumours (0.144 ± 0.017 ms^{-1}). A faster R_2* can be due to a number of factors, but suggests that there is a native raised susceptibility, possibly due to the content of deoxyhaemoglobin (34). However, as a hypoxic environment has been previously reported within the LS174T tumours, this result will need further investigation.

Bland Altman repeatability coefficients (35) calculated in the previous chapter for hepatic FAIR-LL determined the minimum percentage change for significance within the same session as 18% for the ASL technique. A separate test-retest dataset was carried out (data not shown) for the IS-MRI sequence, which estimated the within-session repeatability coefficient to be 17%. Using these values, a significant change in perfusion was detected in the OXi4503-treated SW1222 and LS174T tumours. However, the repeatability analysis may

have to be repeated in tumours, as they exhibit a reduced perfusion. The between-session repeatability measurement will be of particular interest for longitudinal monitoring following therapy.

A limitation of the tumour blood flow quantification is that it assumed the liver's blood-tissue partition coefficient – however previous ASL methods assumed a λ_T of 1 (14), and other invasive measurements vary from 0.46 – 0.96 (21, 22) which may induce a difference to the perfusion estimate. However measurements of the partition coefficients are highly invasive and not trivial.

The multi-parametric imaging approach used in this study showed that these complimentary measures can aid understanding of the tumour micro-environment: the R_2* values did not change where the perfusion decreased in the treated SW1222 tumours, and the R_2* did increase in the originally low-perfused LS174T tumours. The induced changes in perfusion and R_2* were not significantly correlated. This lack of correlation may be due to a complex pathophysiological relationship between changes in perfusion and changes in blood oxygen saturation following VDA therapy.

Further histological evaluation is necessary to determine the role of tumour and vessel proximity, according to our classifications. Previous anti-CEA targeted therapy reported a better uptake in large peripheral tumours rather than centrally located tumours, which are likely to be nearer large vessels (10). However this contrasting conclusion may be due to the larger tumours generally showing an increased uptake and the mechanism of targeting being different. A previous clinical trial of a combretastatin-based VDA reported heterogeneity in the treatment response but did not group the response by location in the liver (29).

This study showed a lot of promise of FAIR-LL ASL being applied to mice models of liver cancer, and the technique has the potential to be included in to future studies to assess the tumour viability though perfusion. The FAIR-LL sequence was then applied to a rat model of cirrhosis in order to detect the expected decreases in perfusion.

4.7 Application of FAIR-LL to a Rat Model of Liver Cirrhosis

4.7.1 Introduction

Reduced liver perfusion in patients with cirrhosis has been characterised by contrast CT measurements (36), as well as recent clinical liver ASL techniques (37, 38). These measurements of liver perfusion using ASL-MRI were additionally performed alongside portal flow measurements using phase-contrast (PC) MRI which characterised post-prandial blood-flow differences between cirrhotic and healthy livers. This next section investigates the application of the FAIR-LL sequence alongside phase-contrast MRI to a rat model of liver cirrhosis – pre-clinical liver perfusion measurements of cirrhosis using ASL has not been previously reported, and there are limited examples of flow quantification using DCE-MRI. First, the two techniques estimates of liver perfusion will be compared in healthy rat livers, following this, their sensitivity to reduced blood flow in liver dysfunction will be investigated.

4.7.2 Methods

4.7.2.1 Cirrhosis Model

Male Sprague-Dawley rats, weighing 250-300g, were randomised to bile-duct ligation (BDL) procedure (n = 12) or sham laparotomy (n = 13). BDL and sham surgery was conducted as described previously (39): a midline abdominal incision was made under 2% isoflurane and intraperitoneal levobupivacaine in both groups. For animals undergoing BDL procedure, the common bile duct was isolated, triply ligated with 3-0 silk and sectioned between the ligatures. After closure and recovery, BDL animals were maintained for 5 weeks to allow the development of portal hypertension and features of cirrhosis.

4.7.2.2 FAIR-LL ASL MRI

Rats were positioned prone within the bore of the scanner with physiological monitoring of the ECG, respiratory rate and temperature. A respiratory-gated, 2D, GE sequence was used to plan ASL and phase-contrast imaging. Perfusion was measured by the respiratory-triggered, segmented FAIR Look-Locker ASL sequence with the same Look-Locker readout parameters as in Chapter 3.6. Images were acquired with a 2 mm slice thickness, matrix 128 x 128, and FOV 65 x 65 mm^2. A 9 mm slice selective inversion was interleaved with global inversions to acquire the FAIR data. The PENIR algorithm was used to correct for motion artefacts and the Belle model was applied for quantification.

Mean perfusion of each subject was calculated from two users, blinded to the group, placing three circular ROIs on separate areas of the liver devoid of any blood vessels.

4.7.2.3 Phase Contrast MRI

A subtractive methodology had been previously validated in-house to estimate total liver bulk flow, and hepatic arterial fraction. Respiratory-gated 2D PC-cine sequence (Chapter 2.5) was carried out using the following methodology. Within the imaging software, three markers were positioned in the vessel lumen of axial images for automated planning of scanning slices to ensure slice othorgonality to the blood vessels (VnmrJ 3.2, Agilent, Oxford, UK). Two separate positions were imaged in order to estimate total liver perfusion; the inferior liver with both the portal vein (PV) and inferior vena cava (IVC) within the slice, and imaging the IVC at the superior liver, before it returns to the heart. The total liver blood flow (TLBF) was extracted from the difference in the IVC flows before and after the contributions of the liver outflow, assuming a steady state of flow within the liver. The portal venous contributions can be directly measured from the portal vein, and this value can be subtracted from the TLBF to estimate the contribution of the hepatic artery (HA) - as this vessel is generally too small for the applied resolution. The hepatic perfusion index (HPI) was estimated as the hepatic arterial flow normalised to the TLBF.

Phase contrast cine parameters: 2 mm slice thickness, TR 10 ms, TE 1.2 ms, 20° flip angle and a 128 x 128 acquisition matrix, minimum of ten frames throughout the cardiac cycle, 2 averages; one PC-MRI dataset took 10-15 minutes to acquire. Data were acquired using a v_{enc} settings of 33 cm/s for PV and inferior IVC flows, 66 cm/s for superior IVC flows. Bulk flow of each vessel was quantified integrating the velocities over the cardiac cycle, and estimations of PV, TLBF and HA bulk perfusion were normalised to explanted liver weight. Data were analysed using in-house developed MATLAB code. For comparison with the bulk flow estimates, ASL perfusion was calculated in units of ml 100 g^{-1} min^{-1}.

4.7.3 Results

4.7.3.1 Comparison of HASL to PCMRI estimates of liver perfusion

An example, mid-liver phase contrast MRI dataset can be seen in Figure 4.44A & B. From the gradient echo readout (Figure 4.44A), the major vasculature appears hyper-intense and has been labelled on the image. From the resultant phase-contrast data (Figure 4.44B), coherent signal can be seen at the location of the blood vessels – the descending aorta has a negative polarity due to the flow running anti-parallel to the IVC, PV and HA. An example hepatic ASL dataset is shown in Figure 4.44C & D; bright regions corresponding to the vasculature in the gradient-echo anatomical scan (Figure 4.44C) align with high, non-physiological regions of flow in the perfusion map (Figure 4.44D). A relatively homogeneous perfusion signal can be seen across the liver parenchyma.

Mean perfusion measured in the sham-operated rat with FAIR ASL was 317 ± 84 ml $100g^{-1}$ min^{-1} and total bulk flow estimated by the PC-MRI measured 444 ± 119 ml $100g^{-1}$ min^{-1}. Bland-Altman analysis (Figure 4.44E) comparing the bulk perfusion estimated by PC-MRI and the mean perfusion from the ASL exhibit no magnitude dependence, though a significant mean difference was measured of 127 ± 71 ml $100g^{-1}$ min^{-1}; $p < 0.01$ (paired t-test). Previous literature using invasive techniques has shown rat liver perfusion to be between 190 – 240 ml $100g^{-1}$ min^{-1} (40-42), suggestive that the PC-MRI is overestimating the total bulk flow. However, the limited optimisation of the FAIR technique in the rats may be influencing this discrepancy; this will be further discussed later. In addition, an outlier can be seen in Figure 4.44E, which can be caused by low perfusion measurements due to inconsistent respiration resulting in sub-optimal perfusion quantification.

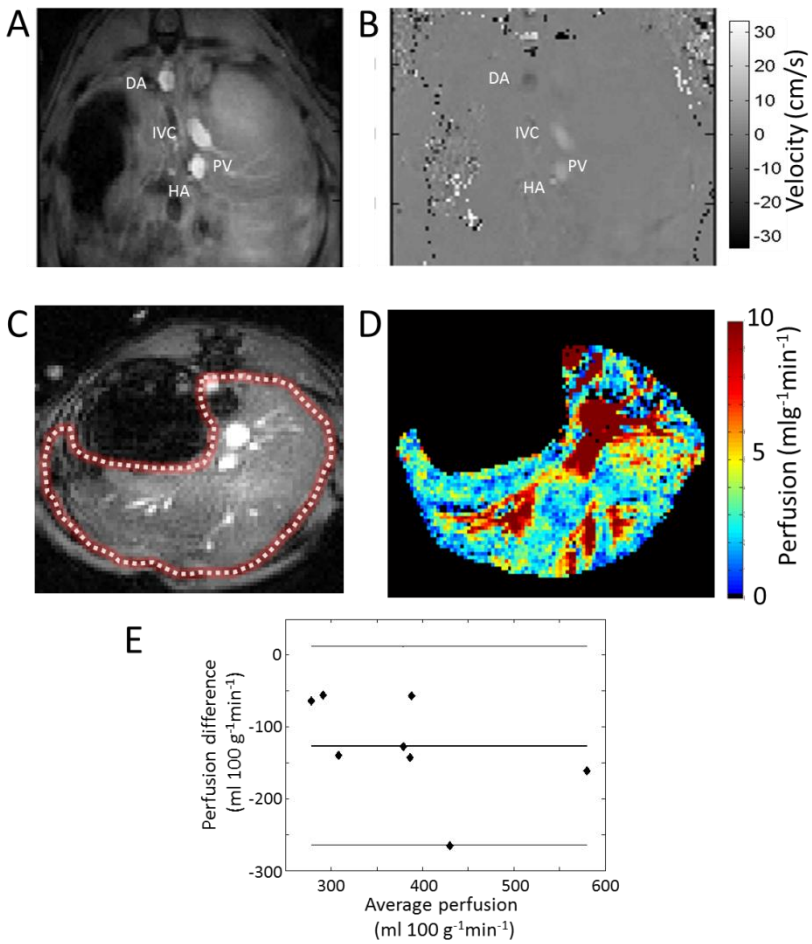

Figure 4.44: Comparison of phase contrast MRI and FAIR-LL ASL measurements applied to liver perfusion. (A) Example GE magnitude image of the PC-MRI. The vasculature appears bright, and the descending aorta (DA), inferior vena cava (IVC), portal vein (PV) and hepatic artery (HA) have been labelled. (B) In the corresponding phase contrast image coherent signal can be seen at the vessel loci; the HA is much more apparent as a smaller vessel next to the PV, and the DA is flowing in the opposite direction. (C) Reference GE image, the vasculature appears hyper-intense relative to the liver (outlined) and its corresponding perfusion map (D). As with the mice, a high flow can be seen at the location of the blood vessels, and a heterogeneous signal is apparent across the liver parenchyma. (E) Bland-Altman analysis comparing perfusion estimates shows no trend, a mean difference of -127 ± 71 ml $100g^{-1}$ min^{-1} was measured, suggestive of an over-estimation of the PC-MRI.

4.7.3.2 ASL and PC-MRI perfusion measurements of cirrhosis

Experiments were performed in sham operated (n = 11) and BDL (n = 11) rats. Four weeks post-surgery, mean BDL body weight (403 ± 14 g) was significantly lower than mean sham body weight (463 ± 7 g; $p < 0.001$). Conversely, mean BDL wet liver mass (30 ± 2 g) was significantly higher than mean sham wet liver mass (14 ± 1 g; $p < 0.0001$). Problems with prospective inversion triggering resulted in poor quality ASL data for two BDL and one sham operated subject. Final analysis was performed using data from ten sham operated and seven BDL rats.

The hepatic ASL technique did not measure any significant perfusion differences between sham (317 ± 84 ml $100g^{-1}$ min^{-1}) and cirrhotic (302 ± 64 ml $100g^{-1}$ min^{-1}) animals ($p > 0.7$, Mann Whitney-U), though the PC-MRI measured a significant decrease ($p < 0.005$, Mann Whitney-U) between sham (444 ± 119 ml $100g^{-1}$ min^{-1}) and cirrhotic bulk perfusion (211 ± 113 ml $100g^{-1}$ min^{-1}) (Figure 4.45A). There was no significant change (Mann Whitney U, $p > 0.3$) in the subtracted PC-MRI estimated arterial contributions: HPI_{sham} 38 ± 6 %, $HPI_{cirrhotic}$ 41 ± 8 %. From the PC-MRI estimates of portal venous flow, a reduced portal bulk flow was observed in the BDL group (114 ± 51 ml $100g^{-1}$ min^{-1}), compared to sham rats (273 ± 90 ml $100g^{-1}$ min^{-1}), indicative of portal hypertension.

Baseline T_1 measurements taken from the global inversion maps were compared in sham (n = 10) and BDL (n = 7) rats. Baseline mean hepatic parenchymal T_1 in BDL animals (1523 ± 43 ms) was significantly higher ($p < 0.001$, Mann Whitney-U) than in sham operated animals (1266 ± 17 ms) (Figure 4.45B).

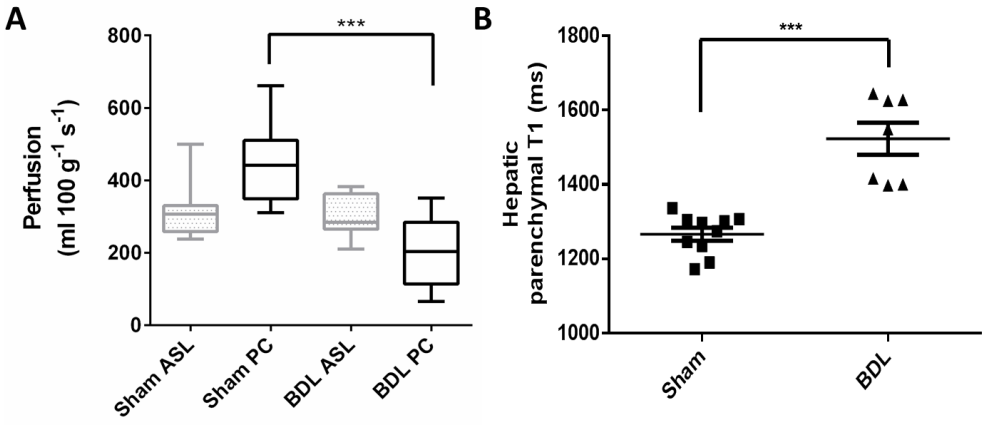

Figure 4.45: (A) Mean group-wise perfusion as estimated by ASL (grey) and PC-MRI (black); no significant differences were measured by ASL whereas PC-MRI measured a reduced perfusion in the cirrhotic animals. (B) Mean parenchymal T_1 as measured using the FAIR technique showed a good sensitivity to the onset of cirrhosis.

4.7.4 Discussion

This research compared a novel measurement of bulk liver perfusion from phase contrast measurements and total liver perfusion using FAIR-LL ASL in rats. A significant overestimation was measured in the PC-MRI measurement relative to ASL in healthy livers relative to previous literature using invasive techniques which has shown rat liver perfusion to be between 190 – 240 ml $100g^{-1}$ min^{-1} (40-42). However, the PC-MRI estimation of hepatic arterial fraction showed good correlation with the microsphere validation (data not

shown), suggestive that this technique may be producing a systematic overestimation in total liver bulk flow.

The PC-MRI method detected significantly lower TLBF in the cirrhotic animals; however, no such reduction was detected using ASL. This may be due to the large cirrhotic rats weighting limiting bandwidth of inversion pulse due to the coil loading. Thus the labelling efficiency may have been highly variably between animals, thus confounding accurate perfusion quantification using the ASL method. The typical inversion bandwidth used in this study was 4000 Hz. Whereas previous work on the same system showed that a bandwidth of >10,000 Hz was required for robust inversion at 9.4T (43). Furthermore, the resultant large inversion pulse and gradients often caused a pressure spike in the respiratory bellows, and would disrupt the gating.

Where the TLBF subtractive technique has shown its sensitivity to reduced flow in this disease state, the advantage of ASL is its potential ability to spatially map localised areas of dysfunction. In addition, as a by-product of the T_1 mapping in the FAIR sequence, the cirrhotic livers exhibited a significant increase in global longitudinal relaxation, due to raised tissue inflammation (44). Future work can include T_2* measurements to detect iron accumulation as this MRI parameter has been shown to alter in cases of fibrosis (45). In addition, as the presence of iron can reduce T_1, T_2* measurements could account for reduced potential longitudinal changes.

A large shortcoming of the FAIR-LL technique in rats was that the sequence parameters were not extensively optimised for the larger animal. The slice thickness was doubled to accommodate the larger anatomy and gain SNR in the readout, and the slice-selective inversion thickness was adjusted to 9 mm following some preliminary investigations (data not shown). In addition, alternative methods of perfusion quantification to the Belle model can be explored to improve on the values estimated here.

The phase-contrast technique had been previously validated against an invasive transit ultrasound technique and found a good correlation between the portal flow measurements, suggestive that the subtraction method of estimating TLBF may require further investigation. In addition, microsphere data showed a slight increase in HPI for the cirrhotic group, in correspondence to the phase-contrast MRI. Microsphere analysis wasn't extensively carried out to measure total liver blood flow, as such invasive experiments have many potential pitfalls for estimating perfusion such as aggregation leading to a poor mixing and distribution and complications of optical quantification (46).

Despite some disagreement with the PC-MRI and FAIR-LL in absolute blood flow, these two techniques could be used in the future to respectively estimate the contributions of the blood vessels in disease-state livers and regional maps of liver perfusion. The relation of vascular inputs in liver dysfunction can be further examined by altering the portal venous contribution by vasoconstrictors such as Terlipressin (47), and increased post-prandial flow; in the healthy liver, a reduced flow will be compensated by the hepatic arterial buffer response (HABR) (38, 48).

4.8 Application of FAIR-LL to a Model of Stimulated Liver Growth

4.8.1 Introduction

Hepatic resection candidates require only 25% of their functional liver, however for patients with hepatic dysfunction or damage due to chemotherapy, the advised future liver remnant (FLR) is around 40% (7), which may be unachievable. Recently, the FLR was reported to increase by 10-46% within 6-8 weeks following a selective portal venous ligation and dissection procedure (8). The insult due to the reduced perfusion and subsequent atrophy causes neighbouring lobes to enlarge, and a dissection along the falciform ligament has been demonstrated to cause a rapid growth of the left lateral lobe. However, so far in this experimental procedure, little has been done to characterise the functionality of the enlarged liver lobes, asides from histological assessment from post-surgery biopsies. Perfusion measurements may offer an assessment of liver functionality, and in addition, contribute to understanding the mechanism of the liver regeneration (9).

In this pilot study, MRI was used to assess a rat model of stimulated liver growth following selective ligation of two portal venous branches. As lobes downstream to the selective ligation would have reduced portal flow, the neighbouring lobes may have a resultant raised perfusion (9) which has been theorised to drive the subsequent hyperplasia. High resolution MRI was used to monitor the volumetric changes to the liver lobes, and in addition, hepatic arterial spin labelling was used to assess lobular changes in hepatic function as determined by liver perfusion.

4.8.2 Methods

4.8.2.1 Rat Model

A schematic of the surgery for the model can be seen in Figure 4.47A. Two male Sprague-Dawley rats (300 – 400g) were anesthetised and the portal vein branches to the left lateral lobe (LLL, red), left median lobe (LM, white) and right lobes (R, yellow) were selectively

ligated following a mid-line incision. This model was designed so that the neighbouring right median (RM, green) and caudate lobes (C, blue) would enlarge to account for the insult to the liver.

4.8.2.2 MRI Protocol

Surgery was performed on day 1, rats were imaged at day 2, day 5 and day 7. A high resolution, respiration gated, multi-slice Fast Spin Echo (FSE) sequence was used to image the whole liver. Sequence parameters: slice thickness 0.75 mm, FOV 65 x 65 mm^2, matrix size 192 x 192, effective TE = 19 ms, k_0 = 3, ETL 4, TR = 200.

For the superior slices nearer the heart, a separate FSE sequence which included cardiac gating was used. The improved effects of cardiac gating the superior slices can be seen in Figure 4.46; respiratory gating was insufficient to delineate the liver lobes and vessel structures (Figure 4.46A). Using a multi-slice, cardiac-triggered FSE, the motion artefacts are considerably reduced, though blurring was still visible using too long an echo train length (Figure 4.46B), an optimal imaging was found using an echo train length of 2, with an echo spacing of 7.5 ms, to maintain a similar contrast (Figure 4.46C).

Following the anatomical imaging, the FAIR-LL sequence (parameters the same as for the cirrhotic rats) was planned on a slice which contained the RM, C, R and LLL.

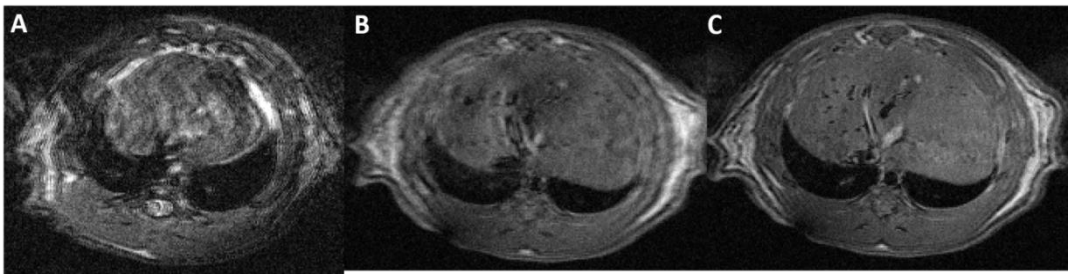

Figure 4.46: Effects of cardiac gating 2D FSE anatomical imaging of the superior liver. (A) Representative image with respiratory gating only, motion artefacts and signal loss are common due to cardiac motion. (B) Cardiac triggered image with an echo train length of 4 (echo spacing 7.5 ms); the image is more coherent but still presents some blurring. (C) Cardiac triggered FSE with an echo train length of 2 presents an optimal image clarity for delineating liver and blood vessel structures.

4.8.2.3 Data Analysis

Livers were segmented by two experienced pre-clinical liver MR imaging experts using Amira (FEI, Oregon, USA). Percentage volume changes of each lobe were calculated by normalising the segmented volumes to a weight-matched, control rat which underwent the same imaging protocol.

4.8.3 Results

It was observed while segmenting the FSE data that the ligated lobes exhibited a relatively hypo-intense signal to the non-ligated lobes (Figure 4.47B). This intrinsic contrast facilitated lobe delineation, and an example 3D visualisation of a segmented liver at day 2, 5 and 7 can be visualised in Figure 4.47C. The livers have been arranged in an axial orientation, from an inferior perspective. From visual inspections, a marked increase in right median (RM, green) and the caudate lobes (C, blue) can be observed alongside shrinkage of the left lateral lobe (LLL, red) and the right lobe (R, yellow). The portal vein ligation induced an expected atrophy in the LLL and R over the 7 days, while promoting hypertrophy in the RM and C (Figure 4.47D). A significant difference was measured between the ligated and non-ligated volume changes at day 7 ($p < 0.05$, Mann Whitney-U). Percentage volume changes relative to a weight-matched liver at day 7 were 95 ± 1 % (RM), -35% ± 16 % (LLL), 52 ± 4 % (C), -51 ± 15 % (R).

The corresponding perfusion map of the segmented lobes from Figure 4.47B can be seen at Figure 4.47E – a lower level of perfusion can be seen in the ligated lobes. No trend was shown in lobe perfusion (data not shown) over the week, however a significant ($p < 0.001$, Mann Whitney-U) mean perfusion deficit was observed in ligated lobes (1.6 ± 0.6 $mlg^{-1}min^{-1}$) relative to non-ligated lobes (2.8 ± 0.4 $mlg^{-1}min^{-1}$) averaged over the three time points (Figure 4.47F).

4.8.4 Discussion

In this pilot study, we have demonstrated FAIR-LL ASL applied to a model of selective portal ligation as means of determining viable liver tissue, as assessed by perfusion, in order to non-invasively improve on volumetric assessment of future liver remnant. We show in this model that the right median lobe almost doubled in volume 1 week post-surgery. This rapid regeneration will be greatly beneficial to resection patients by ensuring these patients have an adequate post-resection liver volume, in addition to reducing waiting time prior to hepatectomy.

Typically, the portal vein supplies around 75% of the blood to the liver (49); however an approximate 40% difference in perfusion was measured in lobes with a ligated portal supply, relative to the un-ligated lobes – this may be due to the hepatic arterial buffer response, which can accommodate reduction in portal venous flow[7]. Though the ligated lobes perfusion may be higher than expected, these results demonstrate that the FAIR-LL technique is sensitive to perfusion changes in rats. The PC-MRI estimated an approximate

50% reduction in bulk flow in the cirrhotic livers but, this was not detected with the FAIR ASL, thus further work is needed to validate the perfusion measurements. Phase-contrast MRI wasn't used in this study as the technique's estimation of bulk perfusion would not offer regional information on the blood flow in each lobe. Future work may explore the suitability of the perfusion as a measure of tissue viability by comparison to hepatocyte-targeting contrast agents which estimate liver function (50).

Previous clearance measurements of rat livers have measured lobe perfusion at 2.41 $mlg^{-1}min^{-1}$ (51): the hypertrophic lobes display a slight raised perfusion from this value and the atrophic lobes show an expected reduction of blood delivery. This may support the theory that an increased perfusion will drive the rapid hyperplasia (9), but further investigations will be needed to explore this. The level of perfusion within the atrophic lobes is potentially higher than expected following cessation of the portal supply. Previous 'functional-MRI' of rat livers following total portal ligation measured a 20% change in inferred arterial blood flow (52), though magnitude of change would not account for the 1.6 ± 0.6 $mlg^{-1}min^{-1}$ measured in the atrophic lobes. The role of ASL has been highlighted in this study in application to post-operation patients, as perfusion measurements may inform surgical success and highlight candidates likely in need of further support.

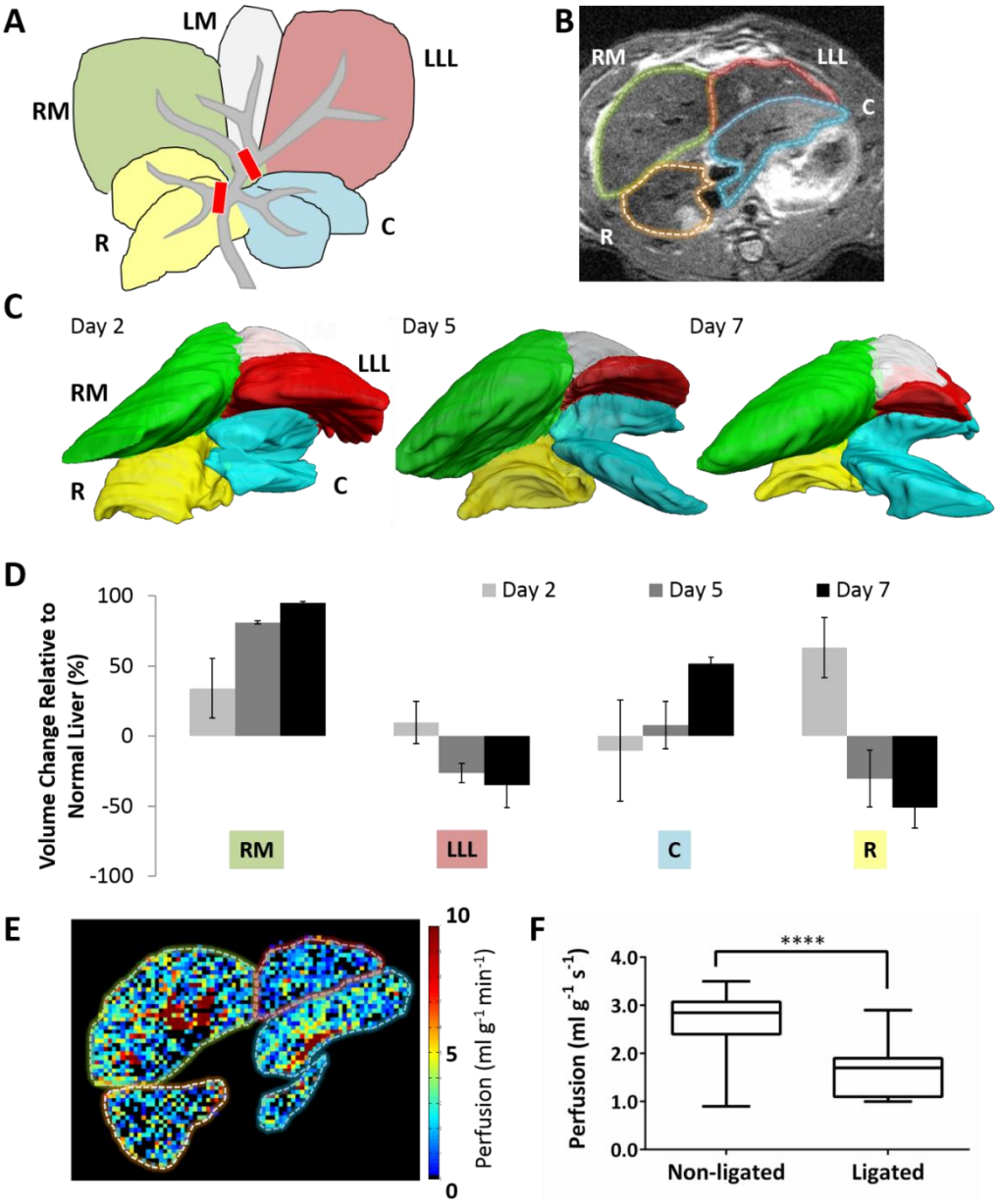

Figure 4.47: Stimulated growth and perfusion differences in a ligated liver: (A) Schematic of a rat liver shows the location of the selective ligation (red blocks) on the portal branches leading to the left lateral lobe (LLL, red) and the right lobe (R, yellow). This insult to the liver promotes growth in the right median (RM, green) and the caudate (C, blue) lobes. This colourscheme is maintained throughout this figure. (B) An example T_2-weighted FSE image of the rat liver, post-ligation lobe segmentation (lobes have been outlined and labelled) was facilitated by a relative hypo-intensity of the ligated lobes. (C) Example 3D visualisation of the lobe growth and shrinkage over one week and correspondng bar graph (D) of each lobe's respective volume changes. (E) Perfusion map corresponding to the FSE image; a reduced perfusion can be seen in the ligated lobes. (F) A significant reduction in perfusion was measured in the ligated lobes.

4.9 Conclusions

In this chapter the FAIR-LL sequence optimised in the Chapter 3 has been applied to two animal models of hepatic disease and a pilot study of hepatic intervention. We have combined intrinsic susceptibility (IS) MRI and arterial spin labelling (ASL) to produce a novel multi-parametric measurement of blood flow changes in liver metastases following vascular disrupting agent therapy. We found that hepatic ASL provided an assessment of response to OXi4503 that is more directly associated with the mechanism of action compared to IS-MRI, and showed a correlation in well-perfused tumours with pre-therapy perfusion and the subsequent change 90 minutes following administration of the drug. The hepatic ASL technique was then compared with a non-invasive estimate of bulk liver perfusion from blood velocity measurements from phase contrast MRI in application to a rat model of liver cirrhosis. Though the PC-MRI was suggestive of an overestimation of bulk perfusion, it was sensitive to a perfusion deficit in the cirrhotic animals, whereas the ASL was not. Finally, the FAIR-LL sequence was applied to a rat model of stimulated liver growth, and measured an expected perfusion difference between ligated and control lobes, whilst the anatomical MRI measured accelerated volume changes in the lobes.

The PC-MRI technique used in the cirrhotic rat study offered an insight in to separately measuring the respective contributions of the portal vein and hepatic artery, albeit using a subtractive method. The next chapter will investigate improving this measure of relative bulk arterial and portal perfusion estimates, by implementing a vessel-selective pseudo-continuous ASL sequence to the mouse liver. The advantage of such an ASL technique is that it offers a direct measure from each vessel and a voxel-wise map of the relative perfusion can be produced. As the hepatic vessels' contributions vary in disease and dysfunction, such a technique may be a useful tool for disease diagnosis and therapy monitoring.

References

1. Bird NC, Mangnall D, Majeed AW. Biology of colorectal liver metastases: A review. J Surg Oncol 2006;94(1):68-80.

2. Fleming KM, Aithal GP, Solaymani-Dodaran M, Card TR, West J. Incidence and prevalence of cirrhosis in the United Kingdom, 1992-2001: a general population-based study. J Hepatol 2008;49(5):732-738.

3. Thng CH, Koh TS, Collins DJ, Koh DM. Perfusion magnetic resonance imaging of the liver. World J Gastroenterol 2010;16(13):1598-1609.

4. Friedman LS, Maddrey WC. Surgery in the patient with liver disease. Med Clin North Am 1987;71(3):453-476.

5. Garrison RN, Cryer HM, Howard DA, Polk HC, Jr. Clarification of risk factors for abdominal operations in patients with hepatic cirrhosis. Ann Surg 1984;199(6):648-655.

6. Adam R, Laurent A, Azoulay D, Castaing D, Bismuth H. Two-stage hepatectomy: A planned strategy to treat irresectable liver tumors. Ann Surg 2000;232(6):777-785.

7. Schnitzbauer AA, Lang SA, Goessmann H, Nadalin S, Baumgart J, Farkas SA, Fichtner-Feigl S, Lorf T, Goralcyk A, Horbelt R, Kroemer A, Loss M, Rummele P, Scherer MN, Padberg W, Konigsrainer A, Lang H, Obed A, Schlitt HJ. Right portal vein ligation combined with in situ splitting induces rapid left lateral liver lobe hypertrophy enabling 2-staged extended right hepatic resection in small-for-size settings. Ann Surg 2012;255(3):405-414.

8. Vennarecci G, Laurenzi A, Santoro R, Colasanti M, Lepiane P, Ettorre GM. The ALPPS procedure: a surgical option for hepatocellular carcinoma with major vascular invasion. World J Surg 2014;38(6):1498-1503.

9. Abshagen K, Eipel C, Vollmar B. A critical appraisal of the hemodynamic signal driving liver regeneration. Langenbecks Arch Surg 2012;397(4):579-590.

10. Dearling JL, Flynn AA, Qureshi U, Whiting S, Boxer GM, Green A, Begent RH, Pedley RB. Localization of radiolabeled anti-CEA antibody in subcutaneous and intrahepatic colorectal xenografts: influence of tumor size and location within host organ on antibody uptake. Nucl Med Biol 2009;36(8):883-894.

11. El-Emir E, Boxer GM, Petrie IA, Boden RW, Dearling JL, Begent RH, Pedley RB. Tumour parameters affected by combretastatin A-4 phosphate therapy in a human colorectal xenograft model in nude mice. Eur J Cancer 2005;41(5):799-806.

12. Workman P, Aboagye EO, Balkwill F, Balmain A, Bruder G, Chaplin DJ, Double JA, Everitt J, Farningham DA, Glennie MJ, Kelland LR, Robinson V, Stratford IJ, Tozer GM, Watson S, Wedge SR, Eccles SA. Guidelines for the welfare and use of animals in cancer research. Br J Cancer 2010;102(11):1555-1577.

13. Fidarova EF, El-Emir E, Boxer GM, Qureshi U, Dearling JL, Robson MP, Begent RH, Trott KR, Pedley RB. Microdistribution of targeted, fluorescently labeled anti-carcinoembryonic antigen antibody in metastatic colorectal cancer: implications for radioimmunotherapy. Clin Cancer Res 2008;14(9):2639-2646.

14. Schor-Bardach R, Alsop DC, Pedrosa I, Solazzo SA, Wang X, Marquis RP, Atkins MB, Regan M, Signoretti S, Lenkinski RE, Goldberg SN. Does arterial spin-labeling MR imaging-measured tumor perfusion correlate with renal cell cancer response to antiangiogenic therapy in a mouse model? Radiology 2009;251(3):731-742.

15. Rajendran R, Huang W, Tang AM, Liang JM, Choo S, Reese T, Hentze H, van BS, Cliffe A, Rogers K, Henry B, Chuang KH. Early detection of antiangiogenic treatment responses in a mouse xenograft tumor model using quantitative perfusion MRI. Cancer Med 2014;3(1):47-60.

16. Graham KC, Wirtzfeld LA, MacKenzie LT, Postenka CO, Groom AC, Macdonald IC, Fenster A, Lacefield JC, Chambers AF. Three-dimensional high-frequency ultrasound imaging for longitudinal evaluation of liver metastases in preclinical models. Cancer Res 2005;65(12):5231-5237.

17. Paroo Z, Bollinger RA, Braasch DA, Richer E, Corey DR, Antich PP, Mason RP. Validating bioluminescence imaging as a high-throughput, quantitative modality for assessing tumor burden. Mol Imaging 2004;3(2):117-124.

18. Kalber TL, Waterton JC, Griffiths JR, Ryan AJ, Robinson SP. Longitudinal in vivo susceptibility contrast MRI measurements of LS174T colorectal liver metastasis in nude mice. J Magn Reson Imaging 2008;28(6):1451-1458.

19. El EE, Qureshi U, Dearling JL, Boxer GM, Clatworthy I, Folarin AA, Robson MP, Nagl S, Konerding MA, Pedley RB. Predicting response to radioimmunotherapy from the tumor microenvironment of colorectal carcinomas. Cancer Res 2007;67(24):11896-11905.

20. Popkov M, Jendreyko N, McGavern DB, Rader C, Barbas CF, III. Targeting tumor angiogenesis with adenovirus-delivered anti-Tie-2 intrabody. Cancer Res 2005;65(3):972-981.

21. Merkel C, Cagol PP, Da Pian PP, Bolognesi M, Sacerdoti D, Gatta A. Blood flow of experimental liver metastases in rat as evaluated by the locally injected 133-Xenon washout. Res Exp Med (Berl) 1985;185(3):207-215.

22. Flowerdew AD, Richards HK, Taylor I. Temporary blood flow stasis with degradable starch microspheres (DSM) for liver metastases in a rat model. Gut 1987;28(10):1201-1207.

23. Folkman J. What Is the Evidence That Tumors Are Angiogenesis Dependent? Journal of the National Cancer Institute 1990;82(1):4-7.

24. Lippert JW, III. Vascular disrupting agents. Bioorg Med Chem 2007;15(2):605-615.

25. O'Connor JP, Rose CJ, Jackson A, Watson Y, Cheung S, Maders F, Whitcher BJ, Roberts C, Buonaccorsi GA, Thompson G, Clamp AR, Jayson GC, Parker GJ. DCE-MRI

biomarkers of tumour heterogeneity predict CRC liver metastasis shrinkage following bevacizumab and FOLFOX-6. Br J Cancer 2011;105(1):139-145.

26. Eisenhauer EA, Therasse P, Bogaerts J, Schwartz LH, Sargent D, Ford R, Dancey J, Arbuck S, Gwyther S, Mooney M, Rubinstein L, Shankar L, Dodd L, Kaplan R, Lacombe D, Verweij J. New response evaluation criteria in solid tumours: Revised RECIST guideline (version 1.1). European Journal of Cancer 2009;45(2):228-247.

27. Lencioni R, Llovet JM. Modified RECIST (mRECIST) assessment for hepatocellular carcinoma. Semin Liver Dis 2010;30(1):52-60.

28. Siemann DW, Shi W. Dual targeting of tumor vasculature: combining Avastin and vascular disrupting agents (CA4P or OXi4503). Anticancer Res 2008;28(4B):2027-2031.

29. Nathan P, Zweifel M, Padhani AR, Koh DM, Ng M, Collins DJ, Harris A, Carden C, Smythe J, Fisher N, Taylor NJ, Stirling JJ, Lu SP, Leach MO, Rustin GJ, Judson I. Phase I trial of combretastatin A4 phosphate (CA4P) in combination with bevacizumab in patients with advanced cancer. Clin Cancer Res 2012;18(12):3428-3439.

30. Meyer T, Gaya AM, Dancey G, Stratford MR, Othman S, Sharma SK, Wellsted D, Taylor NJ, Stirling JJ, Poupard L, Folkes LK, Chan PS, Pedley RB, Chester KA, Owen K, Violet JA, Malaroda A, Green AJ, Buscombe J, Padhani AR, Rustin GJ, Begent RH. A phase I trial of radioimmunotherapy with 131I-A5B7 anti-CEA antibody in combination with combretastatin-A4-phosphate in advanced gastrointestinal carcinomas. Clin Cancer Res 2009;15(13):4484-4492.

31. Sheng Y, Hua J, Pinney KG, Garner CM, Kane RR, Prezioso JA, Chaplin DJ, Edvardsen K. Combretastatin family member OXI4503 induces tumor vascular collapse through the induction of endothelial apoptosis. Int J Cancer 2004;111(4):604-610.

32. Walker-Samuel S, Orton M, McPhail LD, Boult JK, Box G, Eccles SA, Robinson SP. Bayesian estimation of changes in transverse relaxation rates. Magn Reson Med 2010;64(3):914-921.

33. Weidensteiner C, Allegrini PR, Sticker-Jantscheff M, Romanet V, Ferretti S, McSheehy PM. Tumour T1 changes in vivo are highly predictive of response to chemotherapy and reflect the number of viable tumour cells--a preclinical MR study in mice. BMC Cancer 2014;14:88.

34. Robinson SP, Kalber TL, Howe FA, McIntyre DJ, Griffiths JR, Blakey DC, Whittaker L, Ryan AJ, Waterton JC. Acute tumor response to ZD6126 assessed by intrinsic susceptibility magnetic resonance imaging. Neoplasia 2005;7(5):466-474.

35. Campbell-Washburn AE, Price AN, Wells JA, Thomas DL, Ordidge RJ, Lythgoe MF. Cardiac arterial spin labeling using segmented ECG-gated Look-Locker FAIR: variability and repeatability in preclinical studies. Magn Reson Med 2013;69(1):238-247.

36. Van Beers BE, Leconte I, Materne R, Smith AM, Jamart J, Horsmans Y. Hepatic perfusion parameters in chronic liver disease: dynamic CT measurements correlated with disease severity. AJR Am J Roentgenol 2001;176(3):667-673.

37. Cox EF, Ghezzi A, Bennet A, Patel M, Jackson A, Harman D, Costigan C, Omar NF, James MW, Ryder SD, Gowland PA, Aithal GP, Guha IN, Francis ST. A novel MRI protocol to axamine haemodynamic compartments in compensated liver cirrhosis. Proc Intl Soc Mag Reson Med 2013;21:0276.

38. Schalkx HJ, van Stralen M, Peters NHGM, Veldhuis WB, van Leeuwen MS, Pluim JPW, Petersen ET, van den Bosch MAAJ. Pre- and postprandial arterial and portal venous liver perfusion using selective spin labeling MRI with Look-Locker read-out. Proc Intl Soc Magn Reson Med 2014;22:372.

39. Harry D, Anand R, Holt S, Davies S, Marley R, Fernando B, Goodier D, Moore K. Increased sensitivity to endotoxemia in the bile duct-ligated cirrhotic Rat. Hepatology 1999;30(5):1198-1205.

40. Rice GC, Ryan CJ, Leiberman DP, Mathie RT, McGhee E, Harper AM, Blumgart LH. Measurement of liver blood flow in the rat using an 85Krypton clearance technique. Br J Exp Pathol 1977;58(3):236-242.

41. McDevitt DG, Nies AS. Simultaneous measurement of cardiac output and its distribution with microspheres in the rat. Cardiovasc Res 1976;10(4):494-498.

42. Pollack GM, Brouwer KL, Demby KB, Jones JA. Determination of hepatic blood flow in the rat using sequential infusions of indocyanine green or galactose. Drug Metab Dispos 1990;18(2):197-202.

43. Wells JA, Siow B, Lythgoe MF, Thomas DL. The importance of RF bandwidth for effective tagging in pulsed arterial spin labeling MRI at 9.4T. NMR Biomed 2012;25(10):1139-1143.

44. Cox EF, Ghezzi A, Bennet A, Patel M, Jackson A, Harman D, Costigan C, James MW, Ryder SD, Gowland PA, Aithal GP, Guha IN, Francis ST. Liver T1 increases with fibrosis and is correlated with liver stiffness and ELF score. Proc Intl Soc Mag Reson Med 2013;21:4094.

45. Hoad CL, Palaniyappan N, Kaye P, Chernova Y, James MW, Costigan C, Austin A, Marciani L, Gowland PA, Guha IN, Francis ST, Aithal GP. A study of T(1) relaxation time as a measure of liver fibrosis and the influence of confounding histological factors. NMR Biomed 2015;28(6):706-714.

46. Prinzen FW, Bassingthwaighte JB. Blood flow distributions by microsphere deposition methods. Cardiovasc Res 2000;45(1):13-21.

47. Hansen EF, Strandberg C, Hojgaard L, Madsen J, Henriksen JH, Schroeder TV, Becker U, Bendtsen F. Splanchnic haemodynamics after intravenous terlipressin in anaesthetised healthy pigs. J Hepatol 1999;30(3):503-510.

48. Cox EF, Palaniyappan N, Aithal GP, Guha IN, Francis ST. Measuring dynamic changes in liver perfusion and blood flow following a meal challenge. Proc Intl Soc Mag Reson Med 2015;22:380.

49. Vollmar B, Menger MD. The hepatic microcirculation: mechanistic contributions and therapeutic targets in liver injury and repair. Physiol Rev 2009;89(4):1269-1339.

50. Van Beers BE, Pastor CM, Hussain HK. Primovist, Eovist: what to expect? J Hepatol 2012;57(2):421-429.

51. Rice GC, Leiberman DP, Mathie RT, Ryan CJ, Harper AM, Blumgart LH. Liver tissue blood flow measured by 85Kr clearance in the anaesthetized rat before and after partial hepatectomy. Br J Exp Pathol 1977;58(3):243-250.

52. Barash H, Gross E, Matot I, Edrei Y, Tsarfaty G, Spira G, Vlodavsky I, Galun E, Abramovitch R. Functional MR imaging during hypercapnia and hyperoxia: noninvasive tool for monitoring changes in liver perfusion and hemodynamics in a rat model. Radiology 2007;243(3):727-735.

Chapter 5

Feasibility of pre-clinical hepatic pseudo-Continuous ASL

This chapter reports on the development undertaken to establish a method of pseudo-continuous arterial spin labelling (pCASL) in the mouse liver. The potential advantage of such a technique would be the ability to selectively measure regional portal and arterial perfusion.

A pCASL-EPI sequence was first tested in an agar and then a water flow phantom. This was followed by an experiment applying pCASL-EPI to a mouse kidney, which included an optimisation of the acquisition protocol. A series of experiments were then undertaken to optimise the pCASL sequence for application to the liver. First, phase contrast MRI measurements were taken within the portal vein and descending aorta in order to optimise the tagging efficiency in these vessels. The portal venous perfusion was first optimised, as a larger perfusion signal would be available. The B_0 field within the portal vein was mapped through the respiration cycle in order to assess the possible reduction on the tagging efficiency due to inhalation. After these steps to optimise tag efficiency, the sequence was applied to the portal vein and descending aorta to successfully produce the first pre-clinical measurement of hepatic perfusion in mice using a pseudo-continuous ASL preparation. The pCASL-EPI estimates of hepatic arterial and portal venous perfusion were compared to the FAIR-ASL approach described in Chapter 3.

The pCASL-EPI pulse sequence was developed by Dr James Meakin whilst at Oxford University. The initial experiments were performed with Dr Jack Wells and Magda Sokolska. Magda Sokolska developed the simulation of pCASL efficiency and advised on calculating the effects of respiration on tag efficiency.

5.1 Introduction

In Chapter 4, estimates of total liver blood flow using a FAIR-ASL preparation were applied to disease models of liver metastases and cirrhosis. However, the insight that FAIR can provide about liver haemodynamics is restricted due to its non-selective labelling of in-flowing blood. As has been previously demonstrated using invasive techniques, the ratio of portal venous and hepatic arterial contributions may alter as a result of liver dysfunction (1, 2). A non-invasive MRI method, which doesn't use contrast agents, to separate the portal venous and hepatic arterial perfusion would be a useful tool to study disease and theraputic progression in both animal models and clinical applications. Pseudo-continuous ASL (pCASL) tags blood flowing through a defined plane (3) and has been applied to separate out blood vessel contributions to brain tissue (4), and thus the feasibility of this technique in the mouse liver will be investigated in this chapter.

The pCASL sequence was first tested in an agar and a flow phantom, to test the implementation of the sequence. The sequence was then applied to the kidneys *in vivo*, as pCASL has been implemented pre-clinically in this tissue (5), and informed on abdominal acquisition and gating strategies. As was mentioned in Chapter 2.4.3, the pCASL tag will be reduced in its efficacy due to B_0 inhomogeneity and the velocity profile of the flowing spins. The effects of field inhomogeneity are likely to be more pronounced at high field strengths (6), in particular the liver has many air-tissue boundaries that can induce high susceptibility. Thus a method to characterise the efficiency of the portal venous tag was investigated, as this would produce the larger of the perfusion signals, by mapping field changes during the respiratory cycle and measuring the velocity of blood in the target tagging vessels. The efficiency is estimated using a pCASL tagging simulator for a range of sequence parameters. Finally, the sequence was tested in the liver, for both arterial and venous blood supplies, and the efficiency of the portal-venous labelling estimated.

5.2 Phantom imaging

5.2.1 Saturation experiments

The pCASL-EPI experiment was initially tested for successful implementation using an agar phantom (described in Chapter 3.2). The pCASL sequence was tested using a five-shot, gradient-echo EPI: FOV 25 x 25 mm^2, matrix size 64 x 64, slice thickness 1 mm, effective TE 9.8 ms. The pCASL parameters: tag duration 1.4 s, post labelling delay 0.2 s, TR 1.8 s. In order to test the application of the tag in a stationary and unperfused object – the tag location was set to the readout slice – therefore in a multi-phase experiment (Chapter

2.4.3.2), the tag should impart a varied amount of saturation to the image, as demonstrated by Figure 5.48. Some ghosting artefacts can be seen within these images, potentially due to vibrations of the phantom within the coil. However, for the purposes of this experiment, varying saturation can still be visualised despite the ghosting. Future experiments testing different read-out strategies can use this set-up for quick *ex vivo* -testing.

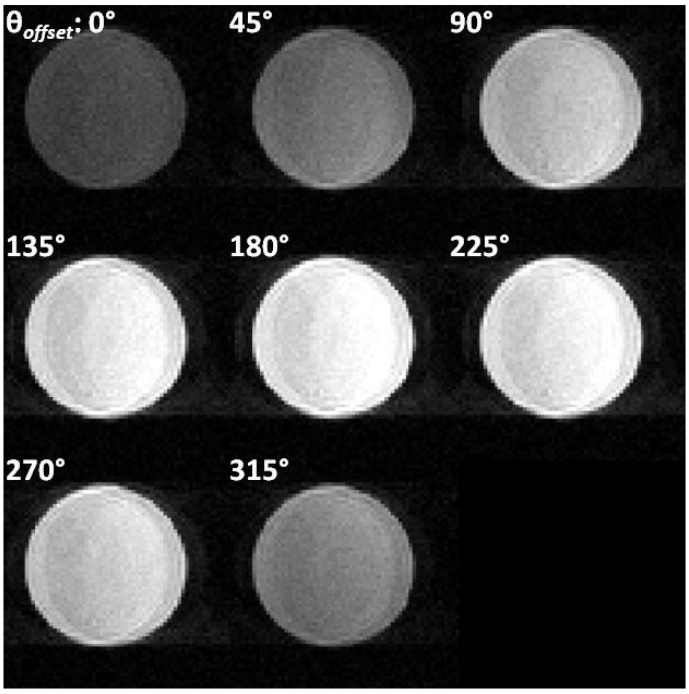

Figure 5.48: Multi-phase experiment performed on the image read-out slice for an agar phantom. A varying level of signal saturation can be visually assessed, in correspondence to the expected behaviour. Such an experiment will be useful when developing the sequence and image readouts.

5.2.2 Flow Phantom Experiment

Having established the pulse sequence in a non-flowing phantom, it was then tested in a water flow-phantom in order to investigate flow-driven inversion. A 50ml Falcon tube was loaded to a syringe driver, which pushed water through tubing (inner diameter of 1mm). The tubing was wound within the MRI bore in order to cover sufficient length for the inflowing water to align with B_0 field ($5*T_1*v$). The tubing then ran straight through the MRI scanner and in to a reservoir outside – the syringe driver could then be reversed to reload the water volume within the syringe after the experiment (Figure 5.49A). Two flow rates (3 ml/min and 6 ml/min) were used to test the phase contrast flow estimate, and the 3ml/min flow rate was used for the pCASL testing to minimise flow artefacts. The corresponding velocity of the water to the applied flow rates can be seen in Table 5.3. These flow rates

were chosen from empirical testing which allowed for a long enough time for sequence acquisition (≈ 8 min).

Flow velocities were estimated using the plug flow relation that the flow rate (Q) is determined by the product of the fluid velocity (v) and the pipe cross sectional area (A). The mean velocity can be estimated using a laminar flow approximation; which accounts for the flow profile down a pipe by halving the theoretical velocity (7):

$$v \approx \frac{1}{2}\frac{Q}{A}. \qquad \text{Equation 5.37}$$

The pCASL sequence was run with different values for G_{max}, the gradient applied simultaneously with the discretised tagging pulse (Chapter 2.4.3), which will control the average gradient over the tagging duration. The tagging efficiency of different velocities will depend on the G_{ave} parameter, and so the theoretical efficiency and measured efficiency will be tested for a single flow rate vs. G_{ave}. As G_{max} controls the average gradient in our sequence, the remainder of this chapter will adjust this variable for optimisation; the values of the average gradient (G_{ave}) corresponding to the maximum tagging gradient (G_{max}) are shown in Table 5.3.

G_{max} (G/cm)	G_{ave} (G/cm)
6.33	0.32
4.22	0.21
3.17	0.16
2.53	0.13

Table 5.3: G_{max} and the corresponding G_{ave} values.

5.2.3 pCASL Simulator

A pCASL simulation (8) was run inputting the measured flow velocities over an implementable range of G_{max} (2-7 G/cm). The simulator was implemented in MATLAB which solved the Bloch equations for a moving magnetisation and the effective magnetic field experienced, inclusive of longitudinal and transverse relaxation.

5.2.4 Flow Phantom Methods: Sequence Parameters

5.2.4.1 Phase Contrast MRI

Phase contrast MRI was introduced in the previous chapter as a method to non-invasively estimate the liver bulk perfusion. The flow measurement was used to validate the estimated flow from the apparatus, and thus ensure the scan planning for pCASL experiment was correct.

Phase contrast images were acquired using a gradient echo cine sequence; FOV 25 x 25 mm^2, matrix size 128 x 128, slice thickness 1 mm, TE/TR 1.8/5 ms. Velocity encoding gradients: G_{pc} 1.5 G/cm , τ_{pc} 2 ms; v_{enc} 11.1 cm/s. Phase contrast data were acquired for flow rates of 0, 3 and 6 ml/min. For the phantom experiment, no gating was used and 5 frames were acquired for averaging – scan time was 23 seconds.

5.2.4.2 pCASL EPI

The pCASL sequence was tested using a single-shot, gradient-echo EPI: FOV 25 x 25 mm^2, matrix size 64 x 64, slice thickness 2 mm, effective TE 5.3 ms. The pCASL parameters: tag duration 2.5 s, post labelling delay 0.3 s, TR 4 s, tag – readout distance = 1.5 cm at 3 ml/min.

A multi-phase experiment was run with 8 phases with a 45° spacing, to optimise the tag/control phase, followed by ten repeat acquisitions of the selected tag and control pair. This experiment was repeated with G_{max} set at 2.5, 3.2, 4.2 and 6.3 G/cm. This experiment was used to investigate signal saturation as an approximate measure of tag efficiency. The saturation was calculated as the mean percentage signal difference between the tag and control image from a ROI within the pipe.

5.2.5 Flow Phantom Results

Phase contrast MRI measurements of the mean velocity across the tubing corresponded well with predicted velocities (Table 5.4). A laminar flow profile can be observed across the pipe at both flow rates (Figure 5.49B), a reference, zero-flow image has been included. The underestimation of the speed at 6 ml/min compared to the theoretical velocity is a result of the v_{enc} parameter being set too low; without appropriate unwrapping post-processing, an erroneous value is measured at the centre of the pipe (star). In addition, an underestimation of flow may be induced due to the connectors between the syringe and tubing; however such 'real-world' effects do not seem to drastically affect the flow at 3 ml/min.

Flow rate (ml/min)	0	3	6
Theoretical velocity (cm/s)	0.0	3.2	6.4
Mean velocity (cm/s)	0.1	3.1	5.9

Table 5.4: Applied flow rates, predicted velocities (using Equation 5.37) and magnitude of the measured velocities using phase-contrast MRI. A good correspondence can be seen between the theoretical and measured velocities.

Using a velocity of 3 cm/s, the tag efficiency is predicted to increase with a larger G_{max} (Figure 5.49C). Testing this out in the flow phantom, a larger degree of saturation can be

seen in at higher flow rates Figure 5.49D. As the tag efficiency is predicted to be around 0.5, this will produce an effective null of the water signal, thus estimating the efficiency from the difference in signal will approach a maximum. The increased saturation and plateau with G_{max} and may be indicative of experimental factors that further reduce the simulated efficiency. This experiment proved a successful application of the pseudo-continuous flow driven inversion on the MRI scanner as well as a demonstration of the simulator.

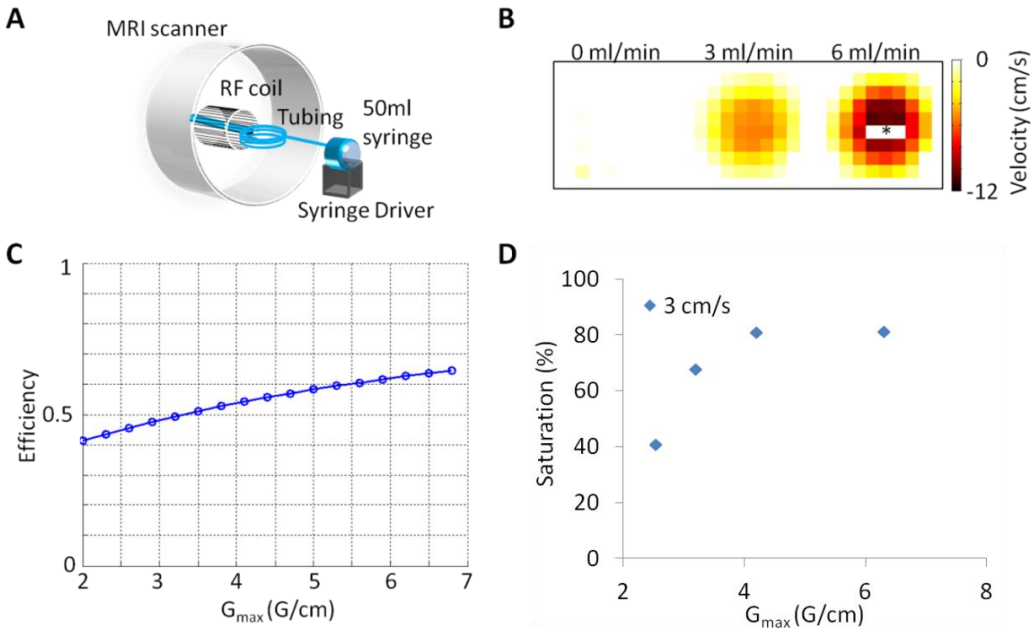

Figure 5.49: (A) Schematic of flow phantom set-up: a 50 ml phantom was loaded on a syringe driver which pushed water through tubing with a 1 mm inner diameter. The tubing was wound within the scanner bore to allow for the water to align with the static field, and passed through the coil to a reservoir outside of the MRI scanner. (B) Phase contrast MRI acquired velocity maps at flow rates of 0, 3 and 6 ml/min. The v_{enc} was set at 11.1 cm/s for all the scans, however at 6 ml/min this was inadequate for some phase wrapped erroneous velocities have been calculated (star). (C) Tag efficiency simulations for a flow rates of 3 cm/s; a better inversion can be achieved by increasing G_{max}. (D) Signal saturation differences from ten tag/control repeats within a flow phantom across four values of G_{max} for a flow rate of 3 ml/min. Higher G_{max} produced a larger expected amount of signal reduction, as a result of the water being tagged more effectively.

5.2.6 Conclusions

The series of phantom experiments has shown an effective implementation of the pCASL sequence on the system, and investigated systematic methods to optimise tagging. The sequence was then applied to wild-type mouse kidneys in order to establish *in vivo* methodology and quantification.

5.3 Implementation of Renal pCASL

5.3.1 Renal pCASL

In vivo murine renal pCASL was implemented as a methodological step between sequence validation using a phantom and eventual application *in vivo* to the liver. This was chosen because i) a previous study has reported murine renal perfusion using both FAIR-ASL and pCASL enabling a degree of comparison to earlier work performed under similar experimental conditions, ii) kidney perfusion is greater than liver perfusion and will yield increased SNR in the perfusion weighted measurements, iii) the extent of movement due to respiration is reduced in comparison to the liver, and gating approaches can be investigated.

5.3.2 Pulse Sequence MRI parameters

Five male C57/Black mice (approximate weight 25g) were anaesthetised and maintained at 1.75% isoflurane in 1L oxygen/min. Mice were positioned so that the top of the kidneys were positioned at the iso-centre of the magnet, this allowed for both the imaging plane and the tag location to be proximal to the iso-centre in order to yield optimal quality EPI and labelling. The descending aorta was labelled, placing the centre of the tag location between 6 – 10 mm away from the imaging slice, typically in the middle of the liver, where the descending aorta runs straightest.

The pCASL sequence parameters as described by Duhamel *et al.* (5) were used as a guideline for this section. A 3-shot spin-echo (SE) EPI readout (FOV 30 x 30 mm^2, matrix size 64 x 64, slice thickness 1 mm, k_0 11, effective TE 14.9 ms) followed a balanced pCASL preparation (10 control-tag pairs, two averages per image, tag duration 3s, post-labelling delay 0.3s, G_{max}/G_{ave} = 2.53/0.13 G cm^{-1}, Hanning duration/spacing 0.6 ms/ 1.2 ms, effective velocity range 17–48 cm s^{-1}, minimum tag gap 2mm). For kidney imaging, a three-shot EPI acquisition was chosen as a compromise between SNR time efficiency, echo time and image distortion.

The scan protocol was as follows: a single average, multi-phase pCASL experiment (Chapter 2.4.3.2) was performed to optimise tagging efficiency (8 phases at 45° steps, acquisition time 4 minutes); the biggest difference in signal intensity separated by a 180° phase was then chosen for the tag and control. Ten repeats of tag-control pairs were used for the perfusion imaging (acquisition time around 10 minutes). The FAIR-LL sequence was run for T_1 mapping and as a reference perfusion scan, in a matched position to the EPI readout; the acquisition parameters and quantification were as described in the Chapter 3.6.

5.3.3 Perfusion Quantification

Perfusion quantification was taken from the Duhamel *et al.* paper which used the general kinetic model (9) for when the image time (TI), (or post labelling delay) is greater than the arterial transit time δ (TI > δ). The paper was comparing a FAIR and pCASL preparation, and utilised the T_1 maps generated in the FAIR acquisition to aid quantification.

In the study, the arterial transit time was set to δ = 0.2 s, taken from brain perfusion data. The difference in magnetisation between the control and tag images would be given by:

$$\Delta M^{pCASL} = 2\frac{M^0}{\lambda} RBF \cdot \alpha \cdot T_{1,app} e^{-\frac{\delta}{T_{1a}}} e^{-\frac{TI-\delta}{T_{1,app}}} \left(1 - e^{-\frac{\tau}{T_{1,app}}}\right). \quad \text{Equation 5.38}$$

Where λ is the partition coefficient, set to 0.9 ml g^{-1}, M^0 is a reference equilibrium magnetisation image (i.e. no labelling), renal blood flow (*RBF*) in units of ml g^{-1} min^{-1}, α is the inversion efficiency, $T_{1,app}$ is the apparent T_1 as estimated from the slice-selective FAIR data, T_{1a} is the arterial blood T_1 and τ is the tag duration. The arterial blood relaxation time T_{1a} was set to 1.9 s, taken from the previous measurements at 9.4T (10). The inversion efficiency α was set to 0.65 as reported by Duhamel *et al.,* which was estimated from a ratio of the pCASL to FAIR perfusion values. The FAIR acquisitions will be quantified using the Belle model as an initial test, as with the previous chapter but using a partition coefficient of 0.9 ml g^{-1}.

5.3.4 Respiratory Synchronisation Simulation

The pCASL images acquired by Duhamel *et al*. was synchronised with the respiratory cycle (Figure 5.50A) – given a range of breathing rates, the pCASL tag train (green block) would be respiratory triggered so that the image acquisition (blue block) would finish in a period without breathing. The group reported that they found an optimal breathing rate was around 90 breaths min^{-1}, however from our own early *in vivo* experiments it was seen that small changes in high breathing rates could often lead to images being acquired during respiration.

A brief simulation was thus established that tested for successful image acquisition for a fixed tag duration and post labelling delay, as used in the kidney pCASL experiment (3 seconds and 0.3 seconds respectively), for a range of physiological breathing rates (30 – 100 breaths min^{-1}). An inhalation window was assumed to be 0.4 s, which has been empirically observed in mice. A successful image was defined as one acquired in between breaths,

assuming an instantaneous acquisition. The pCASL train started post-exhalation, as this would reflect the set-up in the triggering software.

In Figure 5.50B, a successful image is equal to one and unsuccessful image equal to zero – it is apparent that lower rates of respiration have wider 'windows' of image success, thus there may be a benefit of imaging at slower breathing rates as some variation will inevitably occur. Applying this simulation for a range of tag durations from 1.5 – 3.5 s and for a fixed post labelling delay of 0.3 s (Figure 5.50C), it is then possible to select the tagging duration when planning pCASL experiments based on the animal's breathing rates. In this plot, white and black squares respectively represent successful/unsuccessful image acquisition. Alternatively, if a series of experiments have started using a particular tagging duration, a delay can be placed within the gating software which will shift the beginning of the tagging pulses and avoid capturing respiration motion, and this simulation can aid in planning that.

With a tag duration of 3 s and a post label delay of 0.3 s, the plot suggests a breathing rate around 55 breaths min^{-1} would be optimal. Duhamel *et al*. may have suggested higher breathing rates as they may have found that the most physiologically stable with their choice of animal strain (C57B1/6J around 25g) and anaesthetic (isoflurane at 1.5% in .29 L min^{-1}). A wide image-success window is available using a short tag duration with low respiration rates, however the potential of reduced labelled bolus at such tag durations will need to be investigated.

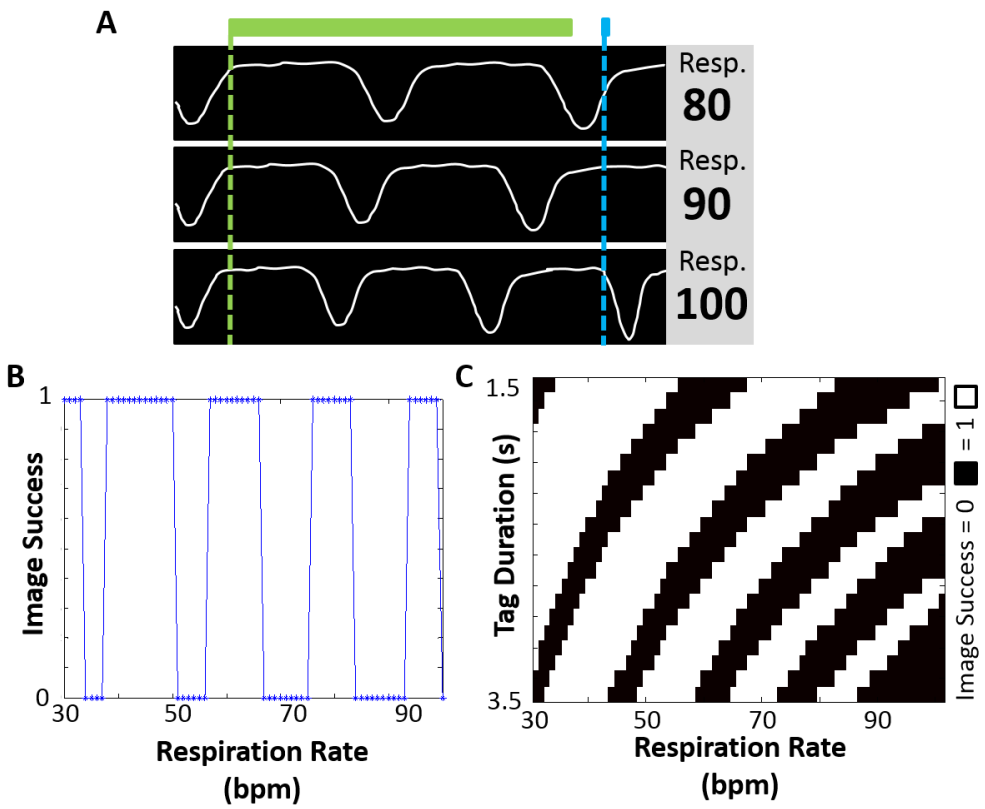

Figure 5.50: (A) Schematic demonstrating the concept of synchronised acquisition- the pCASL tag (green block) is triggered post-exhalation, and runs for its chosen duration. After the post labelling delay, the EPI image is acquired (blue block) – however there will be a unique set of respiration rates that the image can be successfully acquired at. [adapted from Duhamel *et al.* (5)] (B) Simulation of image success over a range of physiological respiration rates, with a tag duration of 3 s and a post labelling delay of 0.3 s. It is apparent that the 'windows' of image success are wider at slower breathing rates. (C) The image success simulation was run with a variety of tag durations for a fixed post labelling delay of 0.3 s. In this plot, an image success of one is a white square - it is possible to visualise the appropriate pCASL parameters a given breathing rate.

5.3.5 Results

A SE-EPI readout has been previously successfully applied to the kidneys, and an example EPI image at 9.4T can be seen in Figure 5.51B, compared to a high-resolution FSE image in Figure 5.51A. The EPI image does not suffer from gross deformations, though the fat-saturation has not been completely successful, the kidneys do not seem to be obscured by any artefacts. The perfusion-weighted image (PWI) following the tag-control subtraction and averaged over the ten pairs can be seen in Figure 5.51C: A ring-shaped signal can be seen at the location of the renal cortex, showing successful pCASL tagging of the arterial blood. For quantification using Equation 5.38, the apparent T_1 is taken from the slice-selective FAIR experiment (Figure 5.51D); mean $T_{1S,\,FAIR}$ was measured at 1.39 ± 0.29 s within the cortex.

Visual assessment of the perfusion over the kidney as estimated by pCASL-EPI (Figure 5.51E) and FAIR-LL (Figure 5.51F) shows good correspondence. The pCASL-EPI technique measured a mean renal cortex perfusion of 5.3 ± 0.3 ml $g^{-1}min^{-1}$ (mean ± standard error) and the FAIR-LL measured a mean perfusion 5.0 ± 0.2 ml $g^{-1}min^{-1}$. As expected, a reduced mean perfusion was estimated in the renal medulla: 1.1 ± 0.2 ml $g^{-1}min^{-1}$ measured with pCASL-EPI and 0.8 ± 0.1 ml $g^{-1}min^{-1}$ measured with FAIR-LL. The perfusion as estimated by both techniques across the five mice can be seen in Figure 5.51G, a significant difference was measured between the techniques ($p < 0.05$, paired t-test). This is indicative of a slight underestimation of the pCASL perfusion, though the FAIR parameters were not optimised for the kidneys.

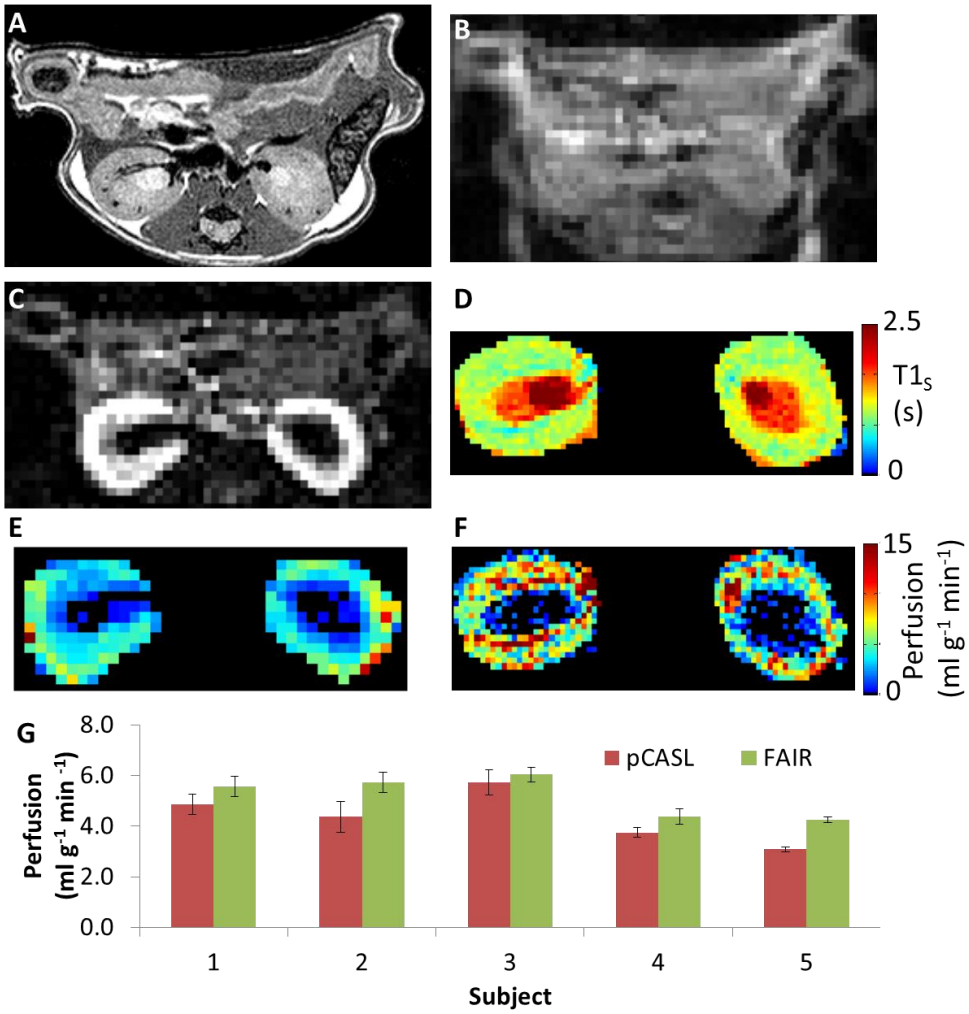

Figure 5.51: Estimation of renal perfusion using ASL. (A) Axial high-resolution fast spin echo (FSE) reference image, showing excellent contrast between the kidneys, muscle, spleen, liver and intestines. (B) Corresponding spin-echo EPI image (M_0 reference). (C) pCASL-generated perfusion weighted image (PWI), showing a bright ring-like signal at the location of the renal cortex. (D) Slice selective T_1 map, as estimated from the FAIR acquisition, the renal cortex and medulla are clearly distinguishable. Perfusion maps as calculated by pCASL (E) and FAIR (F) ASL, in both maps a bright ring of perfusion can be seen in the renal cortex. (G) Comparison of pCASL (red) and FAIR-ASL (green) perfusion values (mean + ste) across the five animals, a significant difference was measured ($p < 0.5$, paired t-test).

5.3.6 Discussion and Conclusion

The perfusion values compare well with previous measurements of kidney perfusion measured with ASL; the mean cortex perfusion was measured in the range of 5.5 – 7.5 ml $g^{-1}min^{-1}$ by Duhamel et al. in mice at 11.75T (5) and the mean medulla perfusion was measured in the range of 1.40 – 2.30 ml $g^{-1}min^{-1}$. Rajendran *et al*. (11) used a FAIR SE-EPI method at 7T in mice and measured a mean cortex perfusion of 3.97 ± 0.36 ml $g^{-1}min^{-1}$ (mean ± standard deviation), and a mean medulla perfusion of medulla 1.66 ± 0.41 ml $g^{-1}min^{-1}$. Though a significant difference was measured between the FAIR-LL and pCASL-EPI estimates of renal perfusion, the mean difference (0.4 ml $g^{-1}min^{-1}$) was not larger than the

variation over the group. The FAIR-LL quantification was not optimised for mice kidneys: the 6 mm slice-selective inversion in the FAIR experiment was larger than previous studies (4 mm (11)), and the Belle model was used for quantification as an initial look-see. The mean $T_{1S,\ FAIR}$ was measured at 1.39 ± 0.29 s within the renal cortex, this is in within reasonable agreement with previous reported values, though at different field strengths; 1.48 ± 0.08 s at 11.75T (5) and 1.57 ± 0.16 s at 7T (11). For those two papers, the longitudinal relaxation time of blood was respectively 2.1 s and 2.2 s, though the latter measurement was taken *ex vivo*.

Duhamel *et al*. compared readout schemes between an EPI and FSE acquisition. It was reported that the FSE acquisition was much more favourable in the coronal plane with their imaging system. However, implementation of a FSE readout resulted in poor perfusion signal for both phantom and *in vivo* experiments (data not shown). This can be further investigated as the FSE readout may prove favourable over EPI acquisition for liver imaging due to its reduced sensitivity to susceptibility-induced artefacts.

This study used the optimised FAIR acquisition from Chapter 3, which meant that there was a resolution difference between the LL and EPI acquisition. Future work may include reducing the resolution of the LL sequence, though this will quicken the scan, aligning the images using the same resolution is not necessarily straight-forward as the EPI image is susceptible to image distortions. Conversely, increasing the EPI matrix size will decrease the already small phase encoding bandwidth, and thus image distortions may be exacerbated due to B_0 imperfections.

This study successfully implemented the pCASL sequence within the mouse abdomen. This study was carried out as pre-cursor to liver imaging, to gain experience with respiratory gating and quantification. The ring-like PWI signal seen in the renal cortex gives perfusion imaging of the kidney a distinct advantage as the tagging success can be quickly visually assessed. The liver may not have such a distinct perfusion pattern, but it is encouraging that with these pCASL settings it was possible to tag the blood in the descending aorta superior to the kidneys. The next section will investigate optimising the tagging of the portal vein, as this will present the largest perfusion signal within the liver.

5.4 Optimisation of hepatic pCASL

5.4.1 Introduction

Having established the pCASL sequence successfully *in vivo* within the mouse abdomen, using a 'synchronised' EPI readout, the method has potential to be applied to the liver. However, the liver has a unique dual blood supply, and the slow flow within the portal vein may have a poor tagging efficiency, which may be further reduced due to respiratory motion.

This section investigated methods to optimise the pCASL pulse sequence for application to the liver. A phase contrast MRI sequence was used to measure the flow in the hepatic vessels, these values were then applied to the pCASL simulation to analyse the optimal tagging gradients. Following this the portal vein was imaged through the respiratory cycle to determine if there would be any resultant B_0 shifts and examine if these would inhibit pCASL tagging. Finally, a gradient-echo Look-Locker and EPI readout were compared in the kidney to optimise the perfusion estimation.

5.4.2 Velocity Measurements in the Hepatic Vasculature

5.4.2.1 Selecting the Dual Supply of the Liver

Separating the liver's blood vessels for selective tagging is potentially difficult due to the proximal nature of the hepatic artery (HA) to the portal vein (PV) (Figure 5.52A). The hepatic artery branches from the descending aorta (DA) towards the inferior end of the liver from the celiac trunk. Though Wong *et al*. have shown a method of distinguishing the perfusion from closely positioned blood vessels using transverse gradients (12), we aim to separate out the perfusion contribution in a two-tag approach as can be seen in the schematic in Figure 5.52B (13). This two-tag approach will aim to separate venous and arterial perfusion by sequential tagging of the portal vein and the descending aorta. We aim to tag the portal vein at a location before the celiac trunk and thus only sensitise the perfusion weighting to the venous blood (PV tag). With the DA tag is placed at the top of the liver, some of the blood flowing down the descending aorta will then enter the liver via the HA. A cardiac-gated phase contrast MRI was applied to measure the blood velocity of the DA and PV In order to optimise tagging of these two vessels. From these measurements of blood velocities within the vessels, the pCASL simulator will estimate the potential tagging efficiency over a range of G_{max}.

5.4.2.2 Methods: PC-MRI

Three male C57/Black mice (mean weight 25g) were anesthetised under isoflurane and three ECG leads were used to monitor the cardiac pulse (SA Instruments). The phase contrast sequence was as described in Chapter 4.7.2.3. As the portal vein and descending aorta run fairly axially, the slices were placed thus and the velocity encoding gradient applied along the z-axis. Two positions of the slice was used, to match the proposed tagging regions: one at the region of the celiac trunk to measure the PV (and IVC) flow, and the second at the top of the liver to measure the DA flow. The MRI scan parameters are FOV 30 x 30 mm^2, matrix 128 x 128, TE/TR 1.16/5 ms, 20 frames within the cardiac cycle, $V_{ENC,\ PV}$ 45 cm/s, $V_{ENC,\ DA}$ 82 cm/s (14).

5.4.2.3 Results: Velocity Measurement of the Hepatic Vasculature

An example phase-contrast MRI measurement with the portal vein (PV), inferior vena cava (IVC) and descending aorta (DA) ROI overlaid on a T_2-weighted anatomical image is shown in Figure 5.52C. The DA flow can be seen to be opposite in direction to that of the PV and IVC. An example velocity profile of the blood vessels through the cardiac cycle as estimated by the PC-MRI (Figure 5.52D) shows that the descending aorta, as expected, has a large velocity peak post-systole, whereas the IVC has a much more broader cardiac dynamic. The portal vein has a constant flow over the cardiac cycle, such behaviour is expected as this blood vessel is drawing the venous blood from the mesenteries (15, 16). The mean velocity measured in the portal vein was 8.1 ± 0.4 cm/s (mean ± standard error), and the mean DA speed 17.8 ± 0.5 cm/s. There is little literature reporting on the portal vein in mice, however a previous phase contrast MRI measurement reported a mean supra-renal aortic flow of 17.2 (14.8–19.5) cm/s in 18 wild-type C57BL/6J mice, which corresponds well with the value measured in the descending aorta (14).

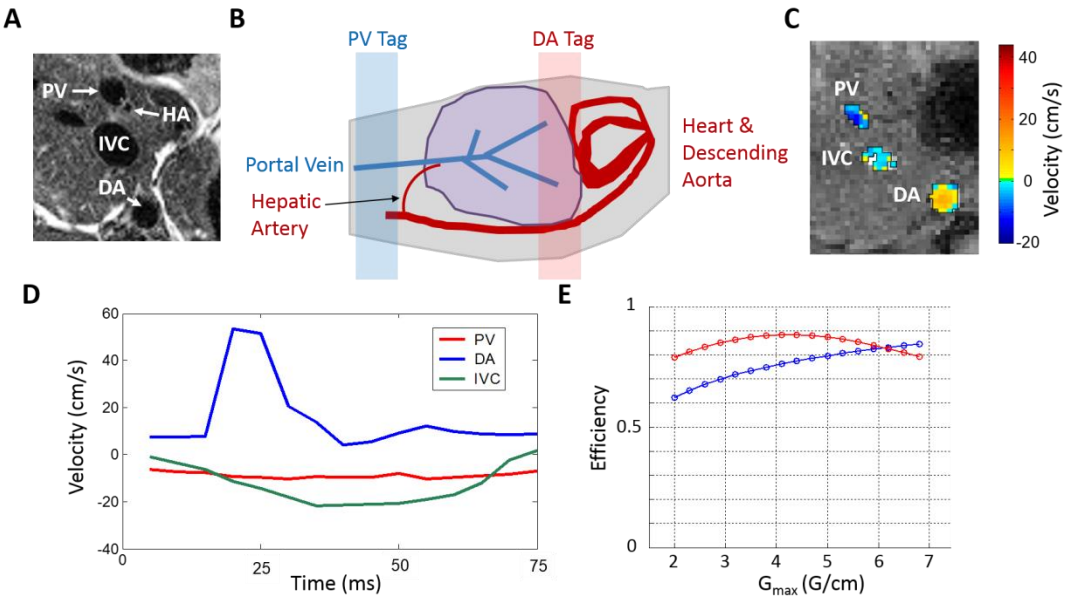

Figure 5.52: (A) High resolution, axial FSE image of the major hepatic vasculature, at a location superior to the celiac trunk. The vasculature appears hypo-intense relative to the dark liver tissue; the portal vein (PV), and much smaller hepatic artery (HA) perfuse the liver. The blood travels throught the liver sinusoids and eventually collects in to the inferior vena cava (IVC) which returns the blood to the heart. The descending aorta has its primary branch at the celiac trunk, from which the hepatic artery enters the liver. (B) The perfusing vessels can be visualised in this sagittal schematic. As the hepatic artery is small and proximal to the portal vein, a system of tagging the portal vein inferior to the celiac trunk (PV Tag) and the superior part of the descending aorta (DA Tag) may allow for the perfusion contributions to be separated. (C) Single frame within the PC-MRI overlaid on the magnitude data, as expected the PV and IVC are flowing in the opposite direction to the DA. (D) Plot of the blood velocity throughout the cardiac cycle – a large peak can be seen in the DA (blue) post-systole. The IVC (green) has a more spread peak over the cardiac cycle, and the PV (red) exhibits a steady flow. (E) Simulations of tag efficiency for the measured velocities within the portal vein (blue) and descending aorta (red) as determined by phase-contrast MRI.

5.4.2.4 Simulations of Tagging Efficiency

The optimal pCASL tagging parameters were determined by running the pCASL simulation with the measured velocities over a range of G_{max} (Figure 5.52E). From these simulations, the slower flow in the portal vein (blue line) will benefit from a larger G_{max} and the descending aorta (red line) should have an optimal tagging regime around 4 G/cm.

5.4.3 B_0 mapping of the Respiratory Cycle

5.4.3.1 B_0 mapping

As described in Chapter 2.4.3, the pCASL sequence is particularly sensitive to B_0 inhomogeneity, which can lead to an inefficient inversion. It was then of interest to investigate what changes to the static field may occur during respiration, and to determine what effects that would have on the tag efficiency. This section focuses on estimating the effects of the tagging efficiency in the portal vein.

B_0 mapping is a common sequence in static organs such as the brain (6, 17), the technique acquires gradient echo images at multiple echoes, and the phase increments are attributed to local changes to the static field. The technique of B_0 mapping has been used for field corrections within the heart (18), as well as EPI image correction within the brain (19). B_0 differences between the tagging and imaging plane will also contribute to tagging inefficiency, the total B_0 effects will then by the sum of the "static" field differences between the planes plus any shifts induced from respiration.

5.4.3.2 Pulse Sequence & Methods

In order to map through the respiratory cycle, a cine sequence was utilised to rapidly acquire an image throughout inhalation and exhalation (Figure 5.53). Cine sequences are used in cardiac imaging due to the rapid and regular motion of the heart. Generally, prospective gating is used to trigger a segmented acquisition of frames within the cardiac cycle, profiting from the regular motion of the heart to build up a 'movie' of the heart's motion. This concept will be utilised to image the breathing cycle, assuming a regular respiratory motion – which can be expected for anesthetised mice with stable physiology.

The trigger was set to the earliest point in the inspiration phase the physiology monitoring software could detect, this triggered the sampling pulse train, spaced at TR_{CINE} to capture the breathing motion up to quiescence. Each sampling pulse was followed by a spoiled gradient-echo read out, with one line of k-space sampled at each point. The 'resp-cine' sequence assumes a regular respiration motion for the duration of the experiment, as well as the gating to be consistent. This assumption is usually valid for cardiac cine imaging as the heart exhibits regular motion and the ECG trigger generated from the QRS complex is well defined.

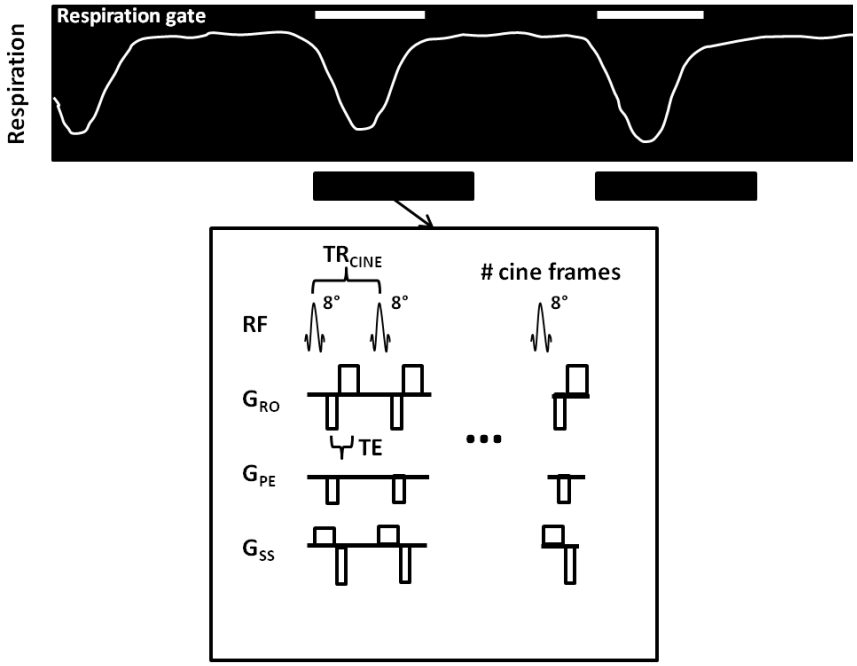

Figure 5.53: Pulse sequence diagram of the segmented resp-cine: the frame train is triggered at the inspiration phase and then collects a single line and single echo for each excitation pulse. The number of frames is set in order to capture the breathing motion as well as the rest-phase.

The resp-cine sequence was repeated at different TEs in order to calculate the B_0 field. A requirement of the TE spacing is that the water-fat phase is kept constant; this increment can be determined using the Larmor equation (20):

$$\Delta TE = \frac{1}{\gamma B \sigma}. \qquad \text{Equation 5.39}$$

Where σ is the chemical shift, which for water-fat is approximately 3.5 ppm (1.36 kHz at 9.4T (21)). For 9.4T, using a gyromagnetic ratio of 42.56 MHz T^{-1}, the echo spacing ΔTE is equal to 0.71 ms.

B_0 mapping was performed in 3 male C57/Black mice (mean weight 25g), FOV 30 x 30 mm^2, matrix 128 x 128, number of frames 20, and TR_{CINE} 15 ms. A series of axial and sagittal images were acquired to plan a single imaging slice which captured the majority of the portal vein. Such an orientation would be optimal for observing field changes along and within the portal vein and liver tissue with respect to the respiratory cycle. The respiration-cine was run for three echoes TE = 1.2, 1.91 and 2.62 ms; each acquisition took approximately 5 minutes.

5.4.3.3 Quantification

Using a multi-echo approach, the ΔB_0 value can be estimated from a linear fit of the phase relationship with the echo (6):

$$\Delta\phi = -\gamma\Delta B_0 TE. \qquad \text{Equation 5.40}$$

The fitting function was written in MATLAB, which adopted a built-in, one-dimensional unwrap function to temporally correct aliased phases to estimate the ΔB_0.

5.4.3.4 Results: Simulations of Tagging Efficiency

An example resp-cine at one TE (Figure 5.54A) shows the respiration and rest phases of the breathing cycle. The images are acquired in an oblique plane, approximately coronally in order to capture the portal vein within the slice. The lungs appear hypo-intense towards the top of the frame (the head of the animal is towards the top of the frame in this orientation) and it is possible to observe them expanding and contracting. The portal vein in these images appears hyper-intense relative to the liver tissue, and has been segmented out on one frame in red. From this dataset it is possible to visually assess that the breathing has been steady throughout the duration of the acquisition: there are no obvious artefacts present within the images. Combining this dataset with the other two TE resp-cines, it is possible to calculate the B_0 map through the respiratory cycle (Figure 5.54B). This is the first measurement of a field map in the mouse liver during respiration; the portal vein has a unique offset frequency from the liver. A large B_0 change is present in the top-left hand of the liver adjacent to the lung as a result of the inspiration, though no large changes are seen across the remaining of the liver.

The mean maximal shift was calculated by taking a ROI within the portal vein - drawn for each frame to ensure no liver tissue was being included, an example of which can be seen in Figure 5.54C. The shift was calculated from the baseline frequency of each mouse measured during the respiratory quiescence phase at the end of the cine. A peak in the static field shift can be seen at the point of maximal inhalation, followed by a plateau period during the rest phase (star). The mean maximal shift this was measured at 152 ± 25 Hz (mean ± standard error) within the portal vein and 114 ± 7 Hz for a liver region.

From a line profile covering 40 pixels (approximately 9 mm) within the liver, the mean maximal difference between tagging and imaging plane was measured to be 327 ± 311 Hz. This result is heavily skewed by one liver with a particularly bad shim; excluding this dataset, the mean maximal difference reduces to 147 ± 1 Hz.

In order to assess how this shift may affect the tagging efficiency, the pCASL simulation was run with a series of B_0 offsets (from 0 - 250 Hz in 10 Hz increments) and a range of G_{max} (Figure 5.54D). The simulation demonstrates the technique's sensitivity to a B_0 offset, an oscillatory pattern is produced as the control and tag magnetisation invert relative to each

other. The B_0 offset acts as a phase increment similar to section 5.2.4. Visual assessment determined the mean width of the B_0 shift during the respiratory cycle to be 155 ± 9 ms. An time-efficiency vector was then created for a tagging train with duration of 3 s and a breathing rate of 55 bpm; this would result in three breaths occurring during labelling. The time-efficiency vector was set to the idealised efficiency estimated by the simulator for the portal vein, except for the periods of respiration, which were adjusted for the estimated efficiency change due the frequency shift. The time-efficiency vector was averaged to produce a respiration-corrected efficiency (Table 5.5).

G_{max} (G/cm)	2.5	3.2	4.2	6.3
Simulated Efficiency	0.66	0.71	0.76	0.83
Respiration Efficiency	0.57	0.61	0.65	0.71

Table 5.5: Simulated and respiration induced B_0 shift-corrected efficiency calculated for a portal vein tagging regime with pCASL over a range of G_{max}.

The respiration-corrected efficiencies are expectedly lower than the ideal simulated efficiencies, on average by 86% for the assumed respiration rate and shape. This gives a good indication of the effects of the respiration on the tag efficiency, and additionally suggests that methods to minimise the number of breaths occurring during labelling (i.e. a slower breathing rate or shorter tagging duration) would produce favourable tagging efficiencies. Selecting G_{max} at 6.3 G/cm, the resultant estimated tagging efficiency is 0.71, which should be sufficient to produce a successful tag - previous measurements of pCASL efficiency around this number: Duhamel *et al*. reported a tagging efficiency of 0.61 and 0.65 in mice kidneys. Furthermore, this paper measured a $\Delta M/M_0$ (indicative of the perfusion signal) between 8 – 20%, as kidney perfusion is expected to be approximately double that of the liver, this suggests a measurable level of liver perfusion can be expected.

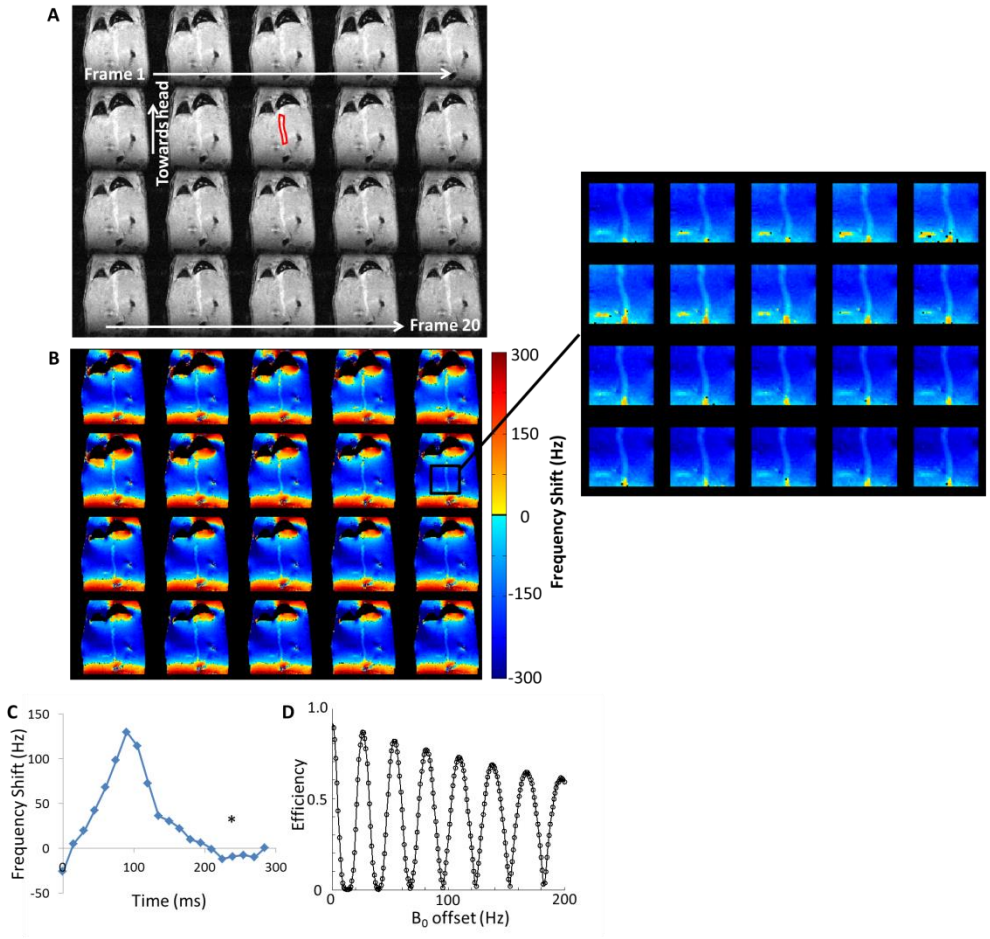

Figure 5.54: (A) Magnitude images of the respiration-cine. The images are acquired in an oblique angle, the head towards the top of the image, in order to capture the portal vein which appears hyper-intense compared to the liver (red ROI). The lungs can be seen as two areas of hypo-intensity at the top of the image, these can be seen expanding and contracting over the first ten frames. (B) Corresponding B0 maps, with a zoom on the portal vein inserted. A relatively small amount of changes can be seen across the liver during the respiration – the regions adjacent to the lungs can be seen to have a large amount of static field shift, as may be expected. (C) Example frequency shift profile of the portal vein during the breathing cycle. The region of respiratory quiescence has been marked with a star, and the mean maximal shift was measured around 150Hz. (D) Simulations of efficiency for increasing increments of B_0 shift, the efficiency modulates as a result of the tagging phase differences between the tag and control magnetisation.

5.4.4 Comparison of pCASL Readout Strategies

5.4.4.1 Readout Strategies

The EPI readout is popular for techniques such as ASL due to its high SNR efficiency. The FAIR acquisition was combined with the Look-Locker (LL) readout in Chapter 3 due to the known difficulties of EPI imaging within the liver at high field strengths. Recent work has shown the advantages of LL imaging within the liver for better efficiency of multi-TI perfusion quantification (13, 22). The advantage of the Look-Locker readout following pCASL preparation is that the increased TIs improve perfusion quantification, as well as its reduced sensitivity to susceptibility artefacts and image distortion.

5.4.4.2 Methods

Three different perfusion-sensitive sequences were compared: pCASL preparation with an EPI readout in one mouse, pCASL preparation with a Look-Locker readout and a FAIR preparation with a Look-Locker readout. For pCASL preparation, the parameters as used in section 5.3 were used (10 control-tag pairs, two averages per image, tag duration 3s, post-labelling delay 0.3s, G_{max}/G_{ave} = 2.53/0.13 G cm^{-1}). Single-shot gradient echo pCASL-EPI sequence parameters were: FOV 30 x 30 mm^2, matrix size 64 x 64, slice thickness 1 mm, k_0 7, effective TE 7 ms. The Look Locker readout following the pCASL tag had the following parameters: FOV 30 x 30 mm^2, matrix size 64 x 64, slice thickness 1 mm, TR 4 s, TE = 2.3 ms; $TR_{Look\text{-}Locker}$ 3.1 ms, 8 segments per TI, $TI_{Look\text{-}Locker}$ 75 ms, 50 TIs – acquisition time 3 minutes. A FAIR acquisition was additionally included as a reference (scan parameters: FOV 30 x 30 mm^2, matrix size 128 x 128, slice thickness 1 mm, TR 4 s, TE = 2.3 ms; $TR_{Look\text{-}Locker}$ 3.1 ms, 8 segments per TI, $TI_{Look\text{-}Locker}$ 25 ms, 100 TIs). The SNR of the perfusion weighted images was estimated from a ROI drawn in the kidneys and noise regions, and was calculated as SNR = 0.66 * mean(signal)/std(noise); the 0.66 is a product of a Rician noise correction (20). Perfusion of both pCASL-EPI and pCASL-LL data was quantified using Equation 5.38, and the FAIR-LL data was quantified using the Belle model.

5.4.4.3 Results

Figure 5.55 shows the differences between the EPI and the LL readouts (Image row); visual assessment shows that, as before, EPI imaging has not suffered from any gross distortions in the kidneys. The perfusion weighted signal-to-noise (PWI row) is much higher in the single PLD EPI acquisition (from the 2 averages built in to the acquisition mode) than in both the Look-Locker readouts. The Look-Locker PWIs was taken from the image subtraction at a TI around 0.3 s in order to match the pCASL-EPI acquisition. A comparison of the PWI SNR can be seen in Table 5.6. The LL readout exhibits a reduced SNR partly due to the low flip angle used in the acquisition. The FAIR-LL acquisition measured a larger PWI SNR than the pCASL-LL, which is unexpected for a pulsed ASL technique and a higher resolution.

	pCASL-EPI	**pCASL-LL**	**FAIR-LL**
Perfusion (ml $g^{-1}min^{-1}$)	6.7	5.2	6.8
PWI SNR	5.9	1.3	2.9

Table 5.6: Perfusion estimated from pCASL preparation with both an EPI and Look-Locker (LL) readout. A reference FAIR-LL acquisition was taken, and the perfusion value agrees well with that estimated by pCASL-EPI. An SNR calculation of the perfusion weighted images using. The EPI readout, has the optimal SNR in the PWI, followed by the FAIR-LL.

The perfusion model as described in Equation 5.38 was used to initially estimate the perfusion using the Look-Locker readout following a pCASL preparation, the resultant perfusion maps can be seen in Figure 5.55 (Perfusion row). All three perfusion maps display the expected ring of renal cortex perfusion and reduced perfusion within the medulla. The signal within a renal cortex voxel is suitably described by this model post PENIR correction, (Figure 5.55B) despite no correction for the magnetisation saturation as generated by the Look-Locker read-out (23), however this simplified model may account for the apparent under-estimation of the pCASL-LL perfusion (Table 5.6).

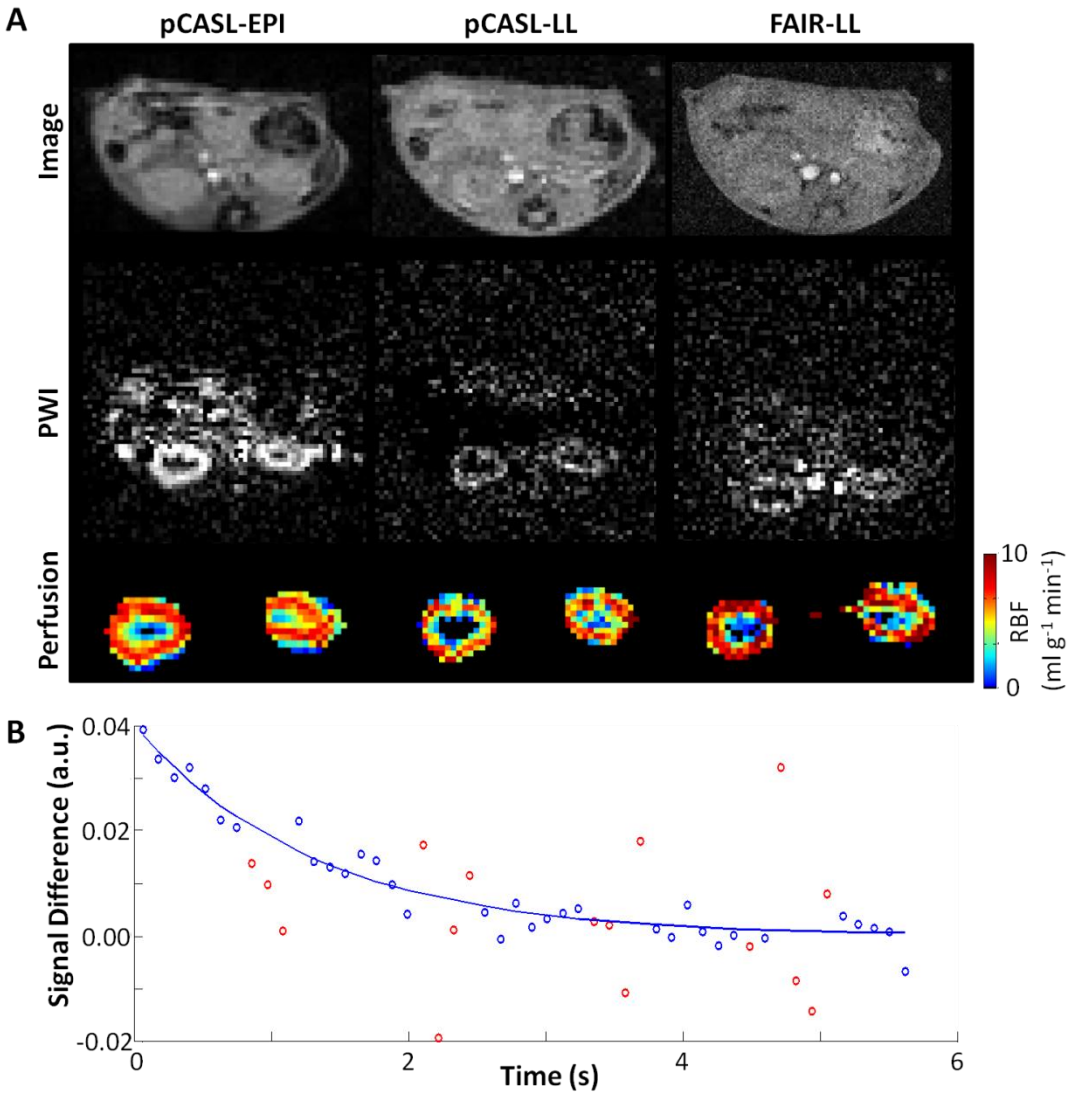

Figure 5.55: (A) A comparison of the pCASL preparation with an EPI readout and a Look-Locker readout, anda further comparison with a FAIR Look-Locker acquisition (n = 1). A single-shot gradient echo EPI image was used; however this acquisition does take two averages, as a reference image. The Look-Locker images were acquired with a 64 x 64 matrix for the pCASL preparation, and a 128 x 128 matrix for the FAIR Look-Locker acquisition. Below are the perfusion weighted images (PWI) for the three acquisitions, it is observable that the EPI image has a favourable PWI SNR, but a bright ring-like signal can be seen in all images. Finally, the perfusion maps as generated from each perfusion-weighting and readout; a similar level of perfusion can be observed between all techniques. (B) A simple model (using Equation 5.38) fitting for the Look-Locker acquisition. Using the PENIR algorithm, it was possible to remove the sginal acquired during respiration (red) and produce a robust fit.

5.4.5 Optimisation of Hepatic pCASL: Discussion and Conclusions

5.4.5.1 Phase Contrast MRI

Blood velocity measurements, obtained using a non-invasive phase-contrast MRI technique, measured the flow within the portal vein and descending aorta, so the pCASL sequence can be designed to optimally label these vessels. These measurements were particularly useful as the portal vein velocity measurements are not widely reported in mice. The estimations of flow in the descending aorta (17.8 ± 0.5 cm/s) showed a good correspondence with previously reported phase contrast MRI data in mice in the same location. For tagging the portal vein blood, the simulations suggest that the G_{max} parameter should be maximised in order to achieve the best inversion efficiency. The renal pCASL experiment showed a good perfusion signal using an aortic tag with a G_{max} of 2.5 G/cm, however the simulation from the descending aorta measurements suggest a G_{max} around 4 G/cm will further improve this. This relative inefficiency could account for the reduced kidney perfusion signal measured by pCASL compared to FAIR in the section above. The PC-MRI sequence may be further used as a comparative estimator of liver perfusion from bulk flow calculations taken from the portal vein. The subtractive measure of total and hepatic arterial flow (Chapter 4.7.2.3) could additionally be measured (24), though the subtraction introduces larger errors and two-position IVC flow measurements will require cardiac triggering and lengthen the experiment, whereas the portal venous flow is constant (Figure 5.52D) and will only require respiration gating.

5.4.5.2 B_0 Mapping of the Portal Vein

As far as the author is aware, this was the first application of a B_0 mapping technique applied to a mouse liver, and the first example of mapping the field changes over the respiratory cycle. The quantification assumed that the resp-cines, with the TEs acquired sequentially, aligned due to a regular breathing motion and prospective triggering. Generally for abdominal imaging, respiratory gating is set to acquire in the quiescent phase between breaths, thus there is some flexibility in where the trigger starts within these static periods. However, in order to capture a consistent trigger point, the resp-cine is dependent on a regular breathing rate and motion to aid the physiology software to detect the 'falling-edge' at inhalation. The data did not present any obvious image artefacts to indicate the potential effects of breathing irregularities, thus the sequential imaging and prospective gating method has been successful. This could be further improved by increasing the segmentation of the resp-cine to quicken the acquisition time and reduce the possibility of any variation in the animal's physiology. Future B_0 mapping in the liver will not necessarily

investigate the respiratory influence, so a standard gated, multi-slice, multi-echo GE acquisition will speed up the imaging time.

The measured frequency shift across the breathing cycle (150 Hz) is of larger magnitude to previous clinical literature: Robinson *et al*. (6) measured an approximate 80 Hz shift across the brain at 4T. Hernando *et al*. (25) applied a B_0 mapping technique to estimate iron content in the liver and measured frequency variations at 3T in the range of -20 to 80Hz. In these images, it was also possible to see intrinsic B_0 differences in the portal vein to the liver parenchyma. Bolan *et al*. (26) measured a maximum difference of 70 Hz in the breast at 4T between images acquired at max inspiration/expiration. Shah *et al*. (27) used a 2-echo cine combined with parallel imaging to measure changes within the range of 20 – 60 Hz across cardiac cycle at 1.5T in the heart. This difference in magnitude is likely to be due to the liver's compression within the respiratory cycle, and in addition, may be due to the higher magnetic field used in the pre-clinical system, and also potentially due to the manual shimming routine which does not flatten the field in a regional manner.

The resp-cine pulse sequence, which maps motion due to breathing, could be applied to a number of pre-clinical techniques to assess the effects of respiratory motion in different anatomical positions. A series of resp-cines could allow a 4D map of the liver's motion during respiration – which could help retrospective analysis as well as modelling image artefacts (28).

The simulation of tag efficiency which accounted for periods of poor inversion due to respiration-induced B_0 shifts showed that while the tag duration is much greater than the total period of respiration, an effective tag should be possible. The period of respiratory quiescence was assumed to not contribute to any B_0 shift, as verified by a minimal frequency change in the period 200-300 ms in 9C. A method of real-time shimming (17) based on the respiratory bellows signal could be a method to account for respiratory effects to maximise tag efficiency, however this will require complex hardware adjustments, which were found to be incompatible with Agilent's sequence programming design.

5.4.5.3 Readout Strategies

Recent improvement in the Agilent software and EPI sequences has improved the quality of abdominal EPI imaging. As seen in the kidney data in Section 5.4, both the PWI and perfusion map have a good SNR for a single post labelling delay. This study showed that, though the Look-Locker readout allows for an accurate pixel-wise modelling of the

perfusion, the intrinsic low signal-to-noise from using a small flip angle proves prohibitive in this application. The Look-Locker acquisition will include a number of breaths, and though the corrupted images can be discarded using the PENIR algorithm, the sequence is still very reliant on steady breathing. Any variations in breathing over the segmented acquisition make it difficult to distinguish the low perfusion signal. Future work can apply this investigation to more animals and the Look-Locker readout may find utility in the liver pCASL measurement, as the readout is not reliant on specific respiration rates for image 'synchronisation'. The Look-Locker technique may provide an efficient method of investigating the post labelling kinetics, however with the reduced PWI SNR, it may be very difficult to detect perfusion signal as liver: total hepatic perfusion is approximately half of that of the kidney (29), and less perfusion signal will be available after separately labelling the blood vessels. Thus, the EPI readout was chosen as the optimal readout for application of pCASL to the liver, though this technique may be difficult to implement in the anatomy due to possible increases in B_0 inhomogeneities.

5.5 Initial Measurements of Hepatic pCASL

5.5.1 Portal Vein pCASL Methods

The preceding experiments have considered optimisation and feasibility of application of a pCASL technique to measure the portal venous perfusion in a mouse liver. From these experiments, the following parameters were used to test the PV-pCASL *in vivo*.

Eight C57/Black mice (approximate weight 25g) were positioned so that the imaging plane and the tag location were both proximal to the magnet iso-centre. Two modes of EPI were tested; a single shot gradient-echo (GE-EPI) and a three-shot spin-echo (SE-EPI). Imaging parameters were FOV 30 x 30mm^2, matrix size 64 x 64, TE_{GE}/TE_{SE} = 6/12 ms. The GE-EPI was tested initially in each mouse, as this would provide the quickest acquisition. However, if the imaging quality appeared poor, the SE-EPI readout was used instead for pCASL experiments.

The pCASL sequence parameters: the tag duration was switched between 2.5 and 3 s dependent on respiration rates, post-labelling delay 0.3s, G_{max}/G_{ave} = 2.53/0.13 G cm^{-1}, Hanning duration/ spacing 0.6 ms/ 1.2 ms, TR 4 s.

As before in the kidney experiments, a multi-phase experiment was performed to optimise tagging efficiency[10], followed by ten tag-control pairs (acquisition time for the single-shot GE-EPI was 3 minutes, while 10 minutes for the three-shot SE-EPI). With the reduced

acquisition time, the single-shot GE-EPI additionally has the advantage of a potentially more stable physiology which should aid the synchronisation of imaging with respiration.

No retrospective gating was applied to the initial pCASL images. A liver ROI was drawn in the EPI image guided by a down-sampled $T_{1,selective}$ map, from which mean perfusion values were taken. Perfusion maps were calculated using the kidney pCASL quantification in Chapter 5.3.

5.5.2 Results: Comparison of EPI Readouts for PV pCASL

A comparison of GE and SE-EPI of the liver can be observed in Figure 5.56 (Anatomical row); a reference image of a T_2-weighted FSE acquisition has been included. For all 8 animals, the single-shot GE-EPI acquisition was used, and in two animals a SE-EPI acquisition was taken for comparison. A good visual correspondence can be seen between the FSE and the SE-EPI image, though some chemical-shift artefacts are apparent. The single-shot gradient echo image does not present any large deformations, though there is some visible signal dropout towards the top of the image, possibly due to cardiac motion. These images reflect the improvement in EPI software and hardware that have aided pre-clinical imaging. EPI in the liver is still quite challenging, particularly as shimming is performed over the imaging plane as well as the tagging vessel, which covers a large area of high susceptibility within the abdomen.

Both readouts produce coherent signal within the liver parenchyma in the perfusion weighted images (PWI row), a region of hypo-intense signal can be seen at the location of the gall bladder (appearing hyper-intense on the T_2-weighted anatomical image), particularly on the SE-EPI image. The perfusion maps (Perfusion Map row) visually correspond and match the perfusion map as estimated using the FAIR-LL sequence. Despite the drop-out in signal of the raw GE-EPI images, the perfusion map in this region is not affected. No significant difference in the liver perfusion estimate was observed between SE- and GE-EPI acquisition (3.1 ± 0.6 ml $g^{-1}min^{-1}$ (mean ± std) and 3.1 ± 0.2 ml $g^{-1}min^{-1}$ respectively, n = 2). The GE-EPI readout was chosen for further liver imaging, though the image quality is reduced, the speed of the acquisition will allow for quicker feedback when optimising tagging and the reduced scan time will benefit from a reduced likelihood of physiological drift.

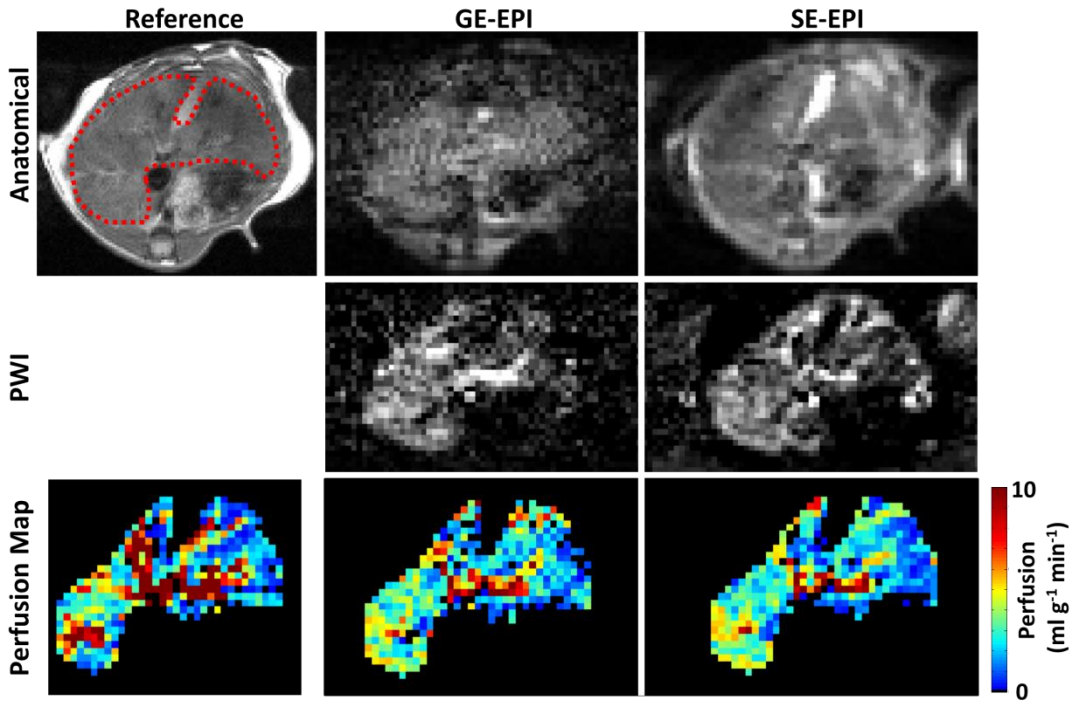

Figure 5.56: Estimation of portal venous perfusion using pCASL. A reference anatomical, axial FSE image (liver outlined in red) is shown next to example gradient echo and spin echo EPI readouts (top row, Anatomical). Perfusion weighted image (PWI), within the liver for both readouts (middle row, PWI). Perfusion maps (bottom row) as calculated by a reference LL-FAIR, and a single PLD pCASL using both spin echo and gradient echo EPI. A good visual agreement can be seen between both pCASL readouts, and the perfusion levels are similar to the reference FAIR acquisition.

5.5.3 Application of PENIR to pCASL data

The above data (Figure 5.56) demonstrated an acquisition where the physiology remained sufficiently stable so that the synchronised methodology (Chapter 5.3.4) was successful. However, in most cases there may be small variations in respiratory rate during the imaging period, so the PENIR algorithm (Chapter 3.4.2) was adapted for these datasets in order to remove motion-affected images.

The PENIR system had considerably less images to generate a threshold with compared to the LL images to which it was previously applied, so a dual-condition was implemented which required both an increase in the phase-encoded, extra-corporeal space as well as a decrease in signal within the body ROI, with respect to the average signal over tag and control images. This dual-condition system ensured that images weren't rejected too sensitively. Following rejection, the tag and control images were separately averaged, and then subtracted from each other to form the PWI.

The implementation of the PENIR system to the data can be seen in an example dataset in Figure 5.57. The individual tag and control images are displayed on the left hand side; three

of these images have been acquired during a respiration. These exhibit poor image quality and a reduced signal, an example corrupted image is highlighted with an arrow. These images erroneously influence subtraction by propagating the magnitude image in to PWI signal. In Figure 5.57A, a large area of signal dropout is visible (long arrow) within the liver parenchyma and also a bright signal can be seen in the back muscle (short arrow). The PENIR corrected dataset successfully removed the respiration-corrupted images, and the resulting PWI displays a more coherent signal within the liver parenchyma and the erroneous back muscle perfusion signal has been removed. The portal vein perfusion maps as calculated following no correction and PENIR correction can be seen in Figure 5.57B – the ROI in these perfusion maps does not include the muscle tissue around the liver. The uncorrected PWI results in a large area of perfusion dropout and an overestimation of the perfusion signal when compared to the FAIR-LL perfusion map. The PENIR corrected perfusion map visually corresponds well with that as estimated by FAIR-LL. The PENIR system will then be applied to all the pCASL data sets in order to remove any image artefacts.

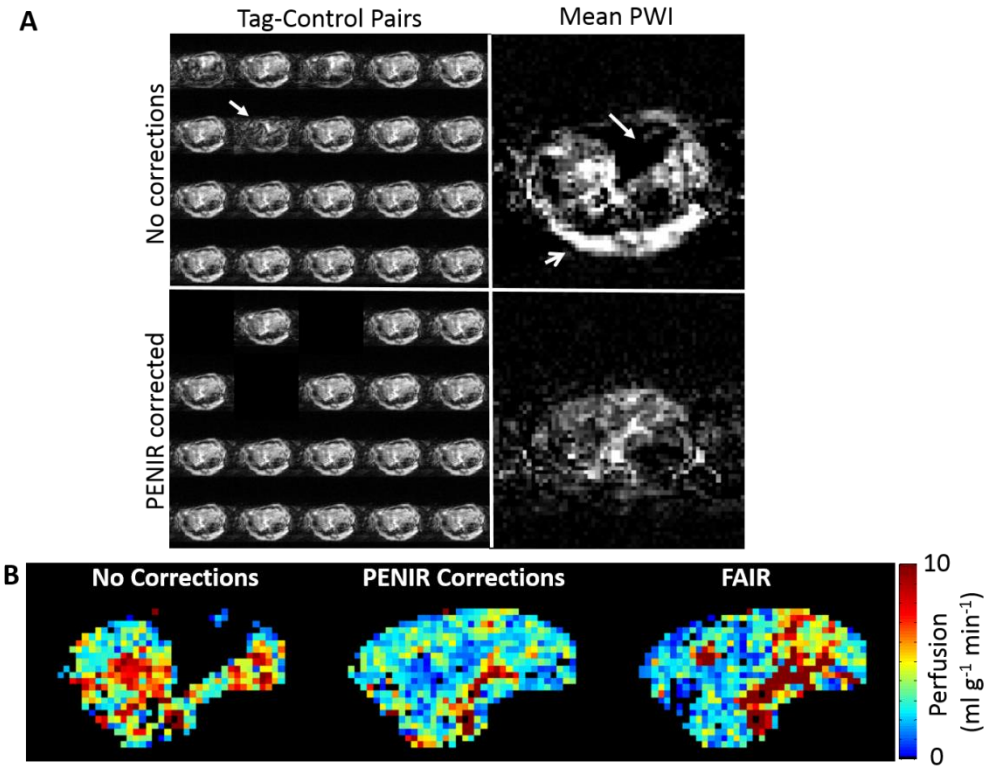

Figure 5.57: Application of the PENIR system to pCASL data. (A) Ten repeats of tag-control pairs, three images were acquired during respiration (arrow). These corrupted images will resultantly influence the perfusion weighted signal when the data is subtracted, the arrows in the uncorrected PWI show a region of hypoitensity due to respiration artefacts, and an erroneous bright perfusion weighed signal in the back muscle due to image subtraction. In the PENIR corrected datasets, these three images have been successfully removed and this yields an improved PWI – no perfusion signal is seen in the muscle. (B) Perfusion maps calculated without correction, following PENIR and a reference PENIR corrected LL-FAIR perfusion map. The uncorrected perfusion map shows an raised level of perfusion as well as a large drop out in perfusion signal. The corrected perfusion map matches the reference FAIR data very well.

5.5.4 Results: Portal Venous Perfusion using pCASL-EPI

The perfusion measured across 8 animals showed a mean pCASL perfusion 3.0 ± 0.3 ml $g^{-1}min^{-1}$ (mean ± standard error), and mean FAIR perfusion 3.4 ± 0.7 ml $g^{-1}min^{-1}$. An ex-vivo experiment was additionally carried out in two animals, which measured a perfusion decrease from 3.9 ± 1.4 ml $g^{-1}min^{-1}$ (mean ± std) to 0.3 ± 0.1 ml $g^{-1}min^{-1}$.

The perfusion estimated by the pCASL was expected to be approximately 75% of that of the FAIR-ASL's estimate of total liver blood flow, whereas the ratio was measured at 93%. This over-estimation in the perfusion may be as a result of the kidney-based quantification equation used earlier (Equation 5.38), which sets the inversion efficiency factor $\alpha = 0.65$. This 'real-world' value was used rather than the simulated inversion efficiency calculated in Chapter 5.4.3.4 as there may be factors which affect the overall efficiency. The simulation was carried out to assess the theoretical efficiency of the pCASL sequence in the mouse

liver; the next section investigates measuring the *in vivo* tagging efficiency of the portal vein.

5.5.5 *In vivo* Tagging Efficiency Estimation

The tagging efficiency of a pCASL experiment may depend on a number of factors such the B_0 field, scanner hardware (30), resonance offset, and the RF pulse flip angle (31). The theoretical method to calculated efficiency α is by the difference in control (M_T^0) and tag (M_T^0) magnetisation immediately following inversion:

$$\alpha = \frac{\mathrm{M}_C^0 - \mathrm{M}_T^0}{2\mathrm{M}^0}. \qquad \text{Equation 5.41}$$

The difference is normalised by the equilibrium magnetisation M^0. However as MRI signal is measures only the magnitude of the magnetisation, this equation was then adapted, assuming that the magnetisation of tagged spins passed through the null point (i.e. efficiency > 0.5). From the earlier efficiency simulations of the sequence, this assumption of the inversion seems valid:

$$\beta = \frac{S_C + S_T}{2S_0}. \qquad \text{Equation 5.42}$$

This approximate inversion efficiency β, is calculated from a very short post labelling delay and measures the blood vessel signal in the control (S_C) and tagged (S_T) images, as well as the reference S_0.

The PV-pCASL sequence was applied to three mice, and the G_{max} parameter was increased whilst maintaining the tag location plane relative to the iso-centre. A post labelling delay of 10 ms was used for this experiment, with ten repeated tag-control pairs following a multi-phase experiment. A reference M_0 EPI image was acquired in order to calculate the efficiency according to Equation 5.42.

G_{max}	**2.5**	**3.2**	**4.2**	**6.2**
Sim. Resp. Efficiency	0.57	0.62	0.65	0.71
***In vivo* Efficiency**	0.67 ± 0.15	0.67 ± 0.15	0.72 ± 0.15	0.73 ± 0.15

Table 5.7: *In vivo* measurements of portal vein pCASL tag efficiency as a function of the tag-gradient parameter G_{max} (mean ± std, n = 3). The simulated efficiencies, corrected for respiration B_0 shifts have been also included for comparison.

The calculated efficiencies are significantly higher than the respiration-corrected simulated efficiencies ($p < 0.05$, paired t-test). This indicates that the effects of respiration on labelling efficiency may be overestimated in the earlier simulation. As predicted, the measured *in vivo* efficiency shows an improved tag at the higher values of G_{max}. Including this measured

efficiency into the perfusion quantification may introduce an approximate 12% reduction to the portal venous blood flow estimate, however the resultant perfusion will still be overestimated compared to the FAIR perfusion.

5.5.6 Methods: Initial Measurements of Hepatic Arterial pCASL

There had been some difficulty in producing successful perfusion images tagging the descending aorta. This has been due to challenging EPI imaging and shimming over the descending aorta and imaging plane, as well as unstable physiology on the experiment days. The perfusion signal expected from the arterial supply is a third of that of the portal vein, and the small signal changes is often difficult to spot when running the multi-phase calibration experiment, and may require a number of averages to be more apparent. However, five data sets have proved very promising, using the pCASL GE-EPI methods used above, with G_{max} = 4.2 and a tag gap of 3 mm.

5.5.7 Results: Hepatic Arterial Perfusion using pCASL-EPI

The results of the DA tag placed at the top of the liver as can be seen in Figure 5.58. A reference FSE image (Figure 5.58A) delineates the liver parenchyma and blood vessels from the bowels and stomach. The single-shot GE-EPI (Figure 5.58B) presents a deformation on the right-hand side of the image. The perfusion weighted image (Figure 5.58C), post-PENIR correction to the pCASL data, shows a relatively homogenous signal within the liver parenchyma, with a bright region within the intestines. The T_{1app} values for the quantification are taken from the slice-selective T_1 mapping experiment within the FAIR method (Figure 5.58D). A relatively homogenous T_1 is measured across the liver parenchyma; the gut and the major blood vessel stand out with a reduced longitudinal relaxation. The resultant perfusion map following tagging of the descending aorta (Figure 5.58E) shows a markedly reduced perfusion compared to the total blood flow as measured by FAIR (Figure 5.58F); a potentially spurious high perfusion signal can be seen at the location of some intestines within the slice.

The perfusion measured across 5 animals showed a mean pCASL estimate of arterial perfusion 1.0 ± 0.5 ml $g^{-1}min^{-1}$ (mean ± standard error), and mean FAIR perfusion 2.2 ± 0.5 ml $g^{-1}min^{-1}$. The hepatic artery's perfusion estimated by the pCASL was overestimated (44%) compared to the expected 25% of the total liver blood flow measured by FAIR-ASL.

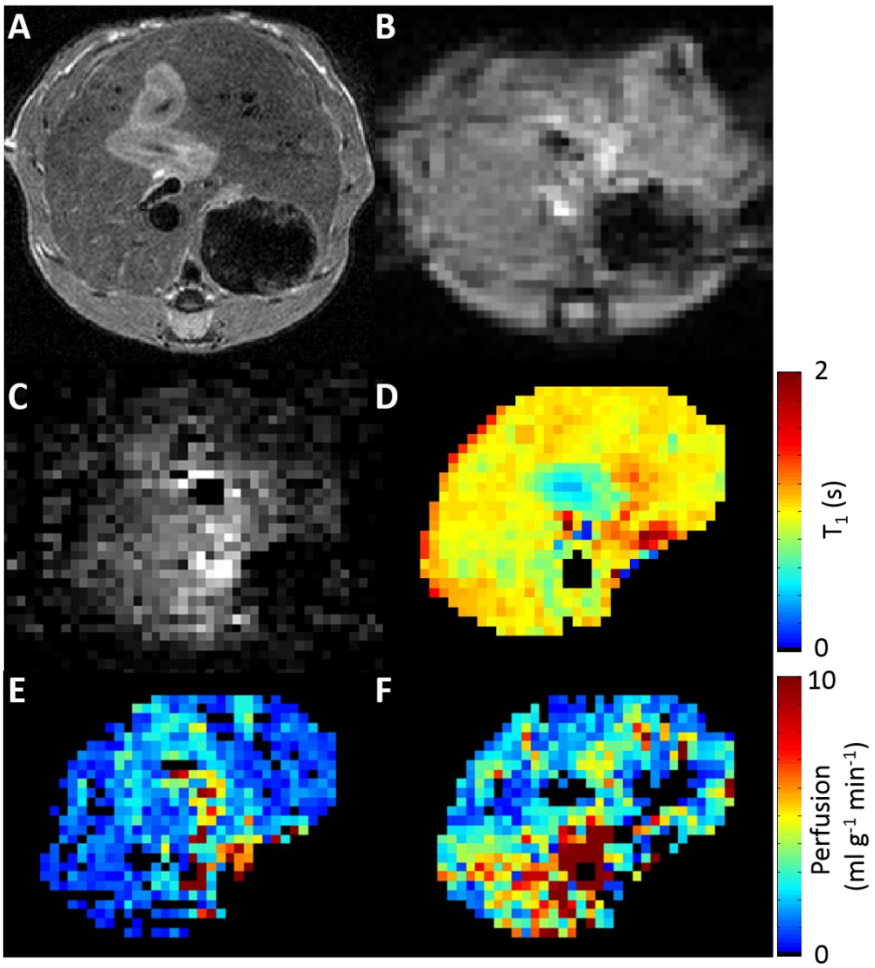

Figure 5.58: Estimation of hepatic arterial perfusion using pCASL from a single mouse. (A) Axial high-resolution fast spin echo (FSE) reference image. (B) Corresponding spin-echo EPI image (M_0 reference). (C) Perfusion weighted image (PWI), showing a bright signal at the location of the blood vessels. (D) Slice selective T_1 map, as estimated from the FAIR acquisition. Perfusion maps as calculated by DA-pCASL (E) and FAIR (F) – the FAIR perfusion data is higher, as expected, as it reflects the total liver blood flow.

The ratio of the pCASL mean estimated hepatic arterial to the sum of arterial and portal venous perfusion was 25 ± 49%, which is in agreement with previous literature, and indicates that the pCASL technique may be successful. However, further investigations in to its quantification are necessary so it can be compared to FAIR-LL.

5.5.8 Discussion: Initial Measurements of Hepatic pCASL

This section reports on the first successful application of pCASL techniques to separate the portal venous and hepatic arterial perfusion in the mouse liver. Though the PV and DA pCASL-EPI perfusion were overestimated compared to the FAIR-LL measurements, the mean HA to the PV perfusion was found to be around 25%, though this value was not estimated from relative contributions of the same liver. This agrees well with the known relative bulk flow to the liver from these feeding vessels (15) and provides encouragement

that this technique was able to accurately distinguish PV and HA flow contributions for the first time.

The PENIR algorithm was adapted for the tag-control pair pCASL-EPI data, and successfully performed data-driven retrospective gating. A data-logger based rejection mode could be easily implemented to the EPI data, which is likely to perform retrospective gating on single-shot data more reliably. However, this will require acquiring the physiology and pulse timing data for each experiment, and so the PENIR system provides a data-efficient method of retrospective gating. A prospective system had been tested which used a 'flag' system within the sequence to check on the respiration status at the time of acquisition – and then repeat that tag and acquisition if necessary. However, it was more time-efficient to use a 'brute-force' approach which entails prospectively triggering the start of the pCASL pulse train. The start-point of the trigger could be adjusted manually so that the EPI acquisition will occur between breaths, and when physiological variations occurred, PENIR analysis was applied to remove erroneous images.

One of most difficult aspects of this work is rapid imaging using the EPI sequence. Though the single-shot imaging produces a time and SNR efficient acquisition, the sequence is sensitive to many factors *in vivo*, and the liver is particularly challenging with its many air-tissue boundaries and motion which can produce distortions and image artefacts. A robust shim is essential over the imaging plane, though for efficient tagging, a homogenous field over the tagging vessel is also vital. This will potentially be made even more difficult if an experiment tagging the PV and DA in the same liver, as this will cover a large volume within the magnet. A dual-shim approach was tested, which switched the shim settings for tag and imaging phase, however, the VNMRJ software could only operate with one shim setting for a scan.

In addition, measuring the arterial perfusion from the descending aorta labelling was challenging. The multi-phase experiment produced very small changes in tissue signal, due to small perfusion signal available from the arterial perfusion. More recently, we proposed a method which tested the success of labelling the descending aorta with the pCASL sequence within a slice including a kidney, as the perfusion differences are much more apparent and can be quickly assessed in real-time.

From experimental experience, a thick shim voxel (around 5-6 times the slice thickness) was selected, and shimming was focussed on this region. From analysis of a separate test volume placed within the blood vessel, this shimming method would often produce a

robust shim within the imaging plane and labelling vessel. The thick shim voxel will also benefit a multi-slice readout, which can be easily implemented in to this sequence and facilitate whole liver coverage. However, EPI over the whole liver may exhibit image distortions due to high-susceptibility regions around the liver, in addition to signal loss due to cardiac motion.

A limitation of the pCASL investigation is that the PV-tag and the DA-tag were not applied in the same liver. With the current approach this will require repositioning of the animal in order to minimise the imaging and tagging distance to the iso-centre (5), this is sub-optimal as the animal will have to be re-shimmed, and the imaging slice may be difficult to align. A future investigation can be carried out with the imaging slice placed at the iso-centre, testing the tag efficacy of a separate DA and PV tag. In order to minimise the imaging and labelling regions, a vessel-encoded pCASL approach (4) may be able to separate the hepatic artery from the portal vein. Such a tagging scheme would aid whole-liver coverage, as the positioning of descending aorta tag currently saturates the superior liver tissue, though a located around the celiac trunk will produce a similar saturation of the inferior liver. In any case, such a technique will not be trivial to implement, as the hepatic artery does not have an extensive straight run from the celiac trunk to the liver.

Particularly in the PV perfusion maps, there is a large PWI signal within the blood vessels at a post-labelling delay of 0.3 s. This is indicative of an insufficient post-labelling delay, and which may cause an underestimation of the perfusion. Further work should apply multiple post-label delays to observe the perfusion kinetics, and in addition, potentially include a micro-vascular component to the perfusion model for the highly vascularised liver tissue, as the blood volume may dominate the perfusion signal (32).

One potential issue is that during the long pCASL tag duration (> 2.5 s), the blood will have time to circulate through the body and thus the PV and DA tagging may detect mixture of liver perfusion signals. It was assumed that the transit time for circulating blood will be sufficiently long that labelled water will have relaxed back to equilibrium. From in-house DCE-MRI experiments in rats, the contrast bolus was observed to arrive 1-2 seconds in the portal vein after the aorta, and this is likely to be shorter in the mouse. However, as the $P_{DA\text{-}pCASL}/P_{PV\text{-}pCASL}$ was calculated to be similar to the expected 25% ratio (15), this suggests re-circulating blood may not be influential on the perfusion signal. Re-circulation may be avoided in the clinical situation, as from DCE experiments the portal venous arrival time is approximately 15 seconds after the peak arterial phase (33).

The quantification may require a more liver-specific model of the complex hepatic kinetics, as is often employed in the DCE-estimated liver perfusion. One obvious limitation of this current quantification is the arterial transit time value of 0.2 s, taken from the kidney perfusion quantification by Duhamel *et al*. - though this was borrowed from brain measurements. This value is likely to be different for the liver, as the pCASL tagging has proved successful in both the portal vein and descending aorta, a Look-Locker readout may offer an efficient method to better observe the perfusion kinetics. A further advantage of the gradient-echo Look-Locker readout is that the images will better match the $T_{1,app}$ map generated as part of the FAIR-LL experiment used for the perfusion quantification. Currently, some image distortions produced by the EPI image may induce some errors in the perfusion quantification. The possible inadequacy of the model used for liver blood flow quantification may account for the slight discrepancy between perfusion estimates using FAIR and pCASL labelling schemes that was observed in this work.

5.6 Conclusions and Further Work

This chapter reported on the methodological development, theoretical and implemented optimisation of a novel measurement of pCASL in the mouse liver. This work demonstrated a successful implementation to separate both the portal vein and the hepatic artery's contribution to hepatic perfusion. The arterial and venous perfusion estimates were over-estimated, though within reasonable agreement with the FAIR-LL sequence that was optimised and assessed in the chapter 3.

Future tests of the pCASL sequence can modulate the contributions of the portal vein; hypercapnia can induce dilation of the portal vein (34) though the change in blood deoxyhaemoglobin content can induce susceptibility changes, which may affect the EPI readout. The hepatic contributions can be further investigated using pCASL tagging with induced portal blood flow changes post-prandium (13, 22), vasoconstriction (35) or invasive vessel ligation.

The sequential PV and DA-tag pCASL method can be further applied to hepatic diseases; the hepatic perfusion index (HPI) has been shown to increase in cancerous and cirrhotic tissue (1, 2). Though the perfusion in pathological states may be expected to be lower, as the arterial PWI showed a reasonable SNR, this work suggests that the pCASL technique has potential application to pre-clinical models of hepatic disease.

References

1. Ballantyne KC, Charnley RM, Perkins AC, Pye G, Whalley DR, Wastie ML, Hardcastle JD. Hepatic perfusion index in the diagnosis of overt metastatic colorectal cancer. Nucl Med Commun 1990;11(1):23-28.

2. Koranda P, Myslivecek M, Erban J, Seidlova V, Husak V. Hepatic perfusion changes in patients with cirrhosis indices of hepatic arterial blood flow. Clin Nucl Med 1999;24(7):507-510.

3. Dai W, Garcia D, de BC, Alsop DC. Continuous flow-driven inversion for arterial spin labeling using pulsed radio frequency and gradient fields. Magn Reson Med 2008;60(6):1488-1497.

4. Wong EC. Vessel-encoded arterial spin-labeling using pseudocontinuous tagging. Magn Reson Med 2007;58(6):1086-1091.

5. Duhamel G, Prevost V, Girard OM, Callot V, Cozzone PJ. High-resolution mouse kidney perfusion imaging by pseudo-continuous arterial spin labeling at 11.75T. Magn Reson Med 2013.

6. Robinson S, Jovicich J. B0 mapping with multi-channel RF coils at high field. Magn Reson Med 2011;66(4):976-988.

7. Batchelor GK. An Introduction to Fluid Dynamics. Cambridge Mathematical Library; 2000.

8. Sokolska M, Golay X, Thomas D. Perfusion Quantification Using Pseudo-Continuous Arterial Spin Labelling: The Impact of Labelling Efficiency Estimation. Proc Intl Soc Mag Reson Med 2013;(21):2177.

9. Buxton RB, Frank LR, Wong EC, Siewert B, Warach S, Edelman RR. A general kinetic model for quantitative perfusion imaging with arterial spin labeling. Magn Reson Med 1998;40(3):383-396.

10. Campbell-Washburn AE, Price AN, Wells JA, Thomas DL, Ordidge RJ, Lythgoe MF. Cardiac arterial spin labeling using segmented ECG-gated Look-Locker FAIR: variability and repeatability in preclinical studies. Magn Reson Med 2013;69(1):238-247.

11. Rajendran R, Lew SK, Yong CX, Tan J, Wang DJ, Chuang KH. Quantitative mouse renal perfusion using arterial spin labeling. NMR Biomed 2013.

12. Wong EC. Vessel-encoded arterial spin-labeling using pseudocontinuous tagging. Magn Reson Med 2007;58(6):1086-1091.

13. Schalkx HJ, van Stralen M, Peters NHGM, Veldhuis WB, van Leeuwen MS, Pluim JPW, Petersen ET, van den Bosch MAAJ. Pre- and postprandial arterial and portal venous liver perfusion using selective spin labeling MRI with Look-Locker read-out. Proc Intl Soc Magn Reson Med 2014;22:372.

14. Amirbekian S, Long RC, Jr., Consolini MA, Suo J, Willett NJ, Fielden SW, Giddens DP, Taylor WR, Oshinski JN. In vivo assessment of blood flow patterns in abdominal aorta of mice with MRI: implications for AAA localization. Am J Physiol Heart Circ Physiol 2009;297(4):H1290-H1295.

15. Vollmar B, Menger MD. The hepatic microcirculation: mechanistic contributions and therapeutic targets in liver injury and repair. Physiol Rev 2009;89(4):1269-1339.

16. Wood MM, Romine LE, Lee YK, Richman KM, O'Boyle MK, Paz DA, Chu PK, Pretorius DH. Spectral Doppler signature waveforms in ultrasonography: a review of normal and abnormal waveforms. Ultrasound Q 2010;26(2):83-99.

17. van GP, de Zwart JA, Starewicz P, Hinks RS, Duyn JH. Real-time shimming to compensate for respiration-induced B0 fluctuations. Magn Reson Med 2007;57(2):362-368.

18. Schar M, Vonken EJ, Stuber M. Simultaneous B(0)- and B(1)+-map acquisition for fast localized shim, frequency, and RF power determination in the heart at 3 T. Magn Reson Med 2010;63(2):419-426.

19. Jezzard P, Balaban RS. Correction for geometric distortion in echo planar images from B0 field variations. Magn Reson Med 1995;34(1):65-73.

20. McRobbie DW, Moore EA, Graves MJ, Prince MR. MRI from Picture to Proton. Cambridge University Press; 2003.

21. Yang Y, Smith DL, Jr., Hu HH, Zhai G, Nagy TR. Chemical-shift water-fat MRI of white adipose depots: inability to resolve cell size differences. Int J Body Compos Res 2013;11(1):9-16.

22. Cox EF, Palaniyappan N, Aithal GP, Guha IN, Francis ST. Measuring dynamic changes in liver perfusion and blood flow following a meal challenge. Proc Intl Soc Magn Reson Med 2014;22:380.

23. Gunther M, Bock M, Schad LR. Arterial spin labeling in combination with a look-locker sampling strategy: inflow turbo-sampling EPI-FAIR (ITS-FAIR). Magn Reson Med 2001;46(5):974-984.

24. Chouhan M, Ramasawmy R, Campbell-Washburn AE, Bainbridge A, Wells JA, Davies N, Pedley RB, Mookerjee R, Punwani S, Taylor S, Walker-Samuel S, Lythgoe MF. Measurement of Bulk Liver Perfusion: Initial Assessment of Agreement Between ASL and Phase-Contrast MRI at 9.4T. Proc Intl Soc Magn Reson Med 2013;21:2190.

25. Hernando D, Cook RJ, Diamond C, Reeder SB. Magnetic susceptibility as a B field strength independent MRI biomarker of liver iron overload. Magn Reson Med 2013.

26. Bolan PJ, Henry PG, Baker EH, Meisamy S, Garwood M. Measurement and correction of respiration-induced B0 variations in breast 1H MRS at 4 Tesla. Magn Reson Med 2004;52(6):1239-1245.

27. Shah S, Kellman P, Greiser A, Weale PJ, Zuehlsdorff S, Jerecic R. Rapid Fieldmap Estimation for Cardiac Shimming. Proc Intl Soc Magn Reson Med 2009;17:565.

28. Blackall JM, Ahmad S, Miquel ME, McClelland JR, Landau DB, Hawkes DJ. MRI-based measurements of respiratory motion variability and assessment of imaging strategies for radiotherapy planning. Phys Med Biol 2006;51(17):4147-4169.

29. Miller ED, Jr., Kistner JR, Epstein RM. Whole-body distribution of radioactively labelled microspheres in the rat during anesthesia with halothane, enflurane, or ketamine. Anesthesiology 1980;52(4):296-302.

30. Jung Y, Wong EC, Liu TT. Multiphase pseudocontinuous arterial spin labeling (MP-PCASL) for robust quantification of cerebral blood flow. Magn Reson Med 2010;64(3):799-810.

31. Wu WC, Fernandez-Seara M, Detre JA, Wehrli FW, Wang J. A theoretical and experimental investigation of the tagging efficiency of pseudocontinuous arterial spin labeling. Magn Reson Med 2007;58(5):1020-1027.

32. Alsop DC, Detre JA. Reduced transit-time sensitivity in noninvasive magnetic resonance imaging of human cerebral blood flow. J Cereb Blood Flow Metab 1996;16(6):1236-1249.

33. Bultman EM, Brodsky EK, Horng DE, Irarrazaval P, Schelman WR, Block WF, Reeder SB. Quantitative hepatic perfusion modeling using DCE-MRI with sequential breathholds. J Magn Reson Imaging 2014;39(4):853-865.

34. Cheng HL. Effect of hyperoxia and hypercapnia on tissue oxygen and perfusion response in the normal liver and kidney. PLoS One 2012;7(7):e40485.

35. Hansen EF, Strandberg C, Hojgaard L, Madsen J, Henriksen JH, Schroeder TV, Becker U, Bendtsen F. Splanchnic haemodynamics after intravenous terlipressin in anaesthetised healthy pigs. J Hepatol 1999;30(3):503-510.

Chapter 6

Conclusions

6.1 Summary and Future Work

The primary aim of this thesis was to investigate into the feasibility of utilising arterial spin labelling (ASL) MRI techniques in application to the liver, which was a limited field at the beginning of this research (1, 2), which has since grown moderately (3-6). This work demonstrated the development and first application of two arterial spin labelling methods to mice and rat livers. The techniques were applied to a number of hepatic disease and therapy models, and will continue to be applied in future liver work within the laboratory.

In Chapter 3, a 'pulsed', FAIR-ASL technique used in combination with a Look-Locker readout was optimised to investigate a measure of total liver blood flow in mice. The initial focus was to remove the influence of respiratory motion-induced artefacts that may reduce the image quality and perfusion signal. An algorithm which exploited the many images acquired with the Look-Locker readout was used to retrospectively condition the data for improved T_1 fitting. This 'PENIR' system proved to be more suitable for the image analysis than a previously established data-logger method (7), though both methods are reliant on a steady breathing regime when the data is acquired. Both these methods reduced the T_1 uncertainties compared to a non-corrected fitting.

After initial measurements of liver perfusion within mice, a repeatability study was carried out to estimate the technique's sensitivity to variations in liver perfusion; the within-session repeatability of the technique comparable to previous myocardial measurements (7). However, relatively large variations were measured between sessions, and this may be partly due the single slice acquisition used for the repeatability study. The mice were not controlled for diet variation as they were left to eat *ad libitum*, however, no trends were observed across the cohort to suggest that imaging time in the day was influential.

The Belle model (8) was used to quantify the perfusion maps, though there is scope for further investigations in to estimating liver blood flow. Preliminary work in to the blood-pool correction based quantification (9), based on a multi-slice correction for myocardial perfusion estimates, resulted in non-physiologically high estimations of perfusion. A general kinetic model (10) produced low estimates of liver perfusion in comparison with the literature. However, the body of clinical research in to liver ASL uses the general perfusion model (3, 5), rather than the Belle model, thus optimising the model for the pre-clinical liver can be further investigated. In addition, the complex blood flow of the liver has been extensively modelled from dynamic contrast measurements taken with MRI and CT (11,

12), and these kinetic models potentially can be appropriated to quantifying the ASL tagging.

Having established an ASL method of liver perfusion, the technique was applied to a model of liver metastases to test its ability to detect localised deficits within tumours. Perfusion differences were measured between normal liver and two cell lines exhibiting different vascular structures. The FAIR ASL sequence was sensitive to acute (90 minutes) changes in well-perfused tumours following the application of a vascular disrupting agent. However, further work is necessary to characterise the repeatability of the HASL technique in a tumour environment, particularly for longitudinal observations of therapy, as tumours have been characterised to re-develop after VDA treatment (13).

The FAIR ASL method was then applied to two rat models. First, it was applied to a rat model of cirrhosis, and compared to a subtractive method to estimate total liver blood flow using phase-contrast MRI, as an alternative, non-invasive and contrast-free technique. The FAIR estimates of perfusion agreed well with previous invasive measurements of the rat liver (14-16), however a significant difference was observed between FAIR and PC-MRI estimates of perfusion. However, PC-MRI was sensitive to the expected blood flow reduction in the cirrhotic livers (17), though the FAIR ASL was not. The FAIR sequence additionally measured a T_1 increase corresponding to an increase in fibrosis (18), demonstrating the model success. The PC-MRI indirectly measured an increase in the hepatic arterial fraction in the cirrhotic livers, corresponding to microsphere experiments, though a microsphere measure of total blood flow wasn't taken. The measured bias between the perfusion estimates of PC-MRI and FAIR ASL may be further investigated by applying both sequences to mouse models.

Secondly, the FAIR method was used to investigate liver functionality by assessment of its perfusion in a rat model of stimulated liver growth following selective portal ligation. High-resolution fast spin echo images were acquired to assess the volumetric changes between the liver lobes, showing successful model development. A perfusion deficit was measured between ligated and control liver lobes, indicative that the FAIR-LL sequence was sensitive to perfusion changes in rats, though a ligation model will drastically reduce the perfusion compared to liver dysfunction.

Finally, inspired by the estimates of the relative arterial and venous contributions by the phase contrast MRI, the feasibility of pseudo-continuous ASL (pCASL) in the mouse liver was investigated. A simulation of the pCASL tagging was run which used blood flow

measurements within the portal vein and descending aorta. The simulation was also adapted to estimate the effects of changes in the B_0 field due to respiratory motion, and found that the predicted tagging efficiency was comparable to previously measured renal perfusion in mice (19). The vessel selective, pCASL-EPI sequence was then successfully applied to separately tag the portal vein and hepatic artery via the descending aorta. This result requires further validation of the relative tagging efficiencies, though the pulsatile flow within the descending aorta will complicate such a measurement. The relative mean portal venous and hepatic arterial perfusion were consistent with the literature (20), though the combined total perfusion was greater than the FAIR measurement. The ability to separate the two blood supplies to the liver will aid diagnosis, as the relationship of the contributions alters in most hepatic diseases. A direct measure of relative perfusions using pCASL may improve on dynamic modelling post-administration of contrast agents, which is reliant on characterising the arterial input function (11), and thus will have application to the disease models explored in this thesis as well as in the clinic (5). Furthermore, the pCASL sequence has been used within the laboratory by Eoin Finnerty to measure the changes in portal venous blood flow to aid understanding of the susceptibility changes within the liver and vasculature in response to different inhaled gases.

6.2 Final Conclusions

The aim of this thesis was to investigate in to the feasibility of hepatic ASL in mice for eventual assessment of liver disease models. The techniques optimised here offer a novel use of non-invasive MRI techniques to spatially assess liver perfusion *in-vivo*, which can inform on disease onset and therapy efficacy in a number of clinically-relevant animal models of hepatic disease.

References

1. Gach HM, Li T, Lopez-Talavera JC, Kam AW. Liver Perfusion MRI using Arterial Spin Labelling. Proc Intl Soc Mag Reson Med 2002;10:1939.

2. Hoad C, Costigan C, Marciani L, Kaye P, Spiller R, Gowland P, Aithal G, Francis S. Quantifying Blood Flow and Perfusion in Liver Tissue using Phase Contrast Angiography and Arterial Spin Labelling. Proc Intl Soc Mag Reson Med 2011;19:794.

3. Cox EF, Ghezzi A, Bennet A, Patel M, Jackson A, Harman D, Costigan C, Omar NF, James MW, Ryder SD, Gowland PA, Aithal GP, Guha IN, Francis ST. A novel MRI protocol to axamine haemodynamic compartments in compensated liver cirrhosis. Proc Intl Soc Mag Reson Med 2013;21:0276.

4. Katada Y, Shukuya T, Kawashima M, Nozaki M, Imai H, Natori T, Tamano M. A comparative study between arterial spin labeling and CT perfusion methods on hepatic portal venous flow. Jpn J Radiol 2012;30(10):863-869.

5. Schalkx HJ, van Stralen M, Peters NHGM, Veldhuis WB, van Leeuwen MS, Pluim JPW, Petersen ET, van den Bosch MAAJ. Pre- and postprandial arterial and portal venous liver perfusion using selective spin labeling MRI with Look-Locker read-out. Proc Intl Soc Magn Reson Med 2014;22:372.

6. Cox EF, Palaniyappan N, Aithal GP, Guha IN, Francis ST. Measuring dynamic changes in liver perfusion and blood flow following a meal challenge. Proc Intl Soc Mag Reson Med 2015;22:380.

7. Campbell-Washburn AE, Price AN, Wells JA, Thomas DL, Ordidge RJ, Lythgoe MF. Cardiac arterial spin labeling using segmented ECG-gated Look-Locker FAIR: variability and repeatability in preclinical studies. Magn Reson Med 2013;69(1):238-247.

8. Belle V, Kahler E, Waller C, Rommel E, Voll S, Hiller KH, Bauer WR, Haase A. In vivo quantitative mapping of cardiac perfusion in rats using a noninvasive MR spin-labeling method. J Magn Reson Imaging 1998;8(6):1240-1245.

9. Campbell-Washburn AE, Zhang H, Siow BM, Price AN, Lythgoe MF, Ordidge RJ, Thomas DL. Multislice cardiac arterial spin labeling using improved myocardial perfusion quantification with simultaneously measured blood pool input function. Magn Reson Med 2012.

10. Buxton RB, Frank LR, Wong EC, Siewert B, Warach S, Edelman RR. A general kinetic model for quantitative perfusion imaging with arterial spin labeling. Magn Reson Med 1998;40(3):383-396.

11. Thng CH, Koh TS, Collins DJ, Koh DM. Perfusion magnetic resonance imaging of the liver. World J Gastroenterol 2010;16(13):1598-1609.

12. Sourbron SP, Buckley DL. On the scope and interpretation of the Tofts models for DCE-MRI. Magn Reson Med 2011;66(3):735-745.

13. Lippert JW, III. Vascular disrupting agents. Bioorg Med Chem 2007;15(2):605-615.

14. Rice GC, Ryan CJ, Leiberman DP, Mathie RT, McGhee E, Harper AM, Blumgart LH. Measurement of liver blood flow in the rat using an 85Krypton clearance technique. Br J Exp Pathol 1977;58(3):236-242.

15. McDevitt DG, Nies AS. Simultaneous measurement of cardiac output and its distribution with microspheres in the rat. Cardiovasc Res 1976;10(4):494-498.

16. Ballantyne KC, Charnley RM, Perkins AC, Pye G, Whalley DR, Wastie ML, Hardcastle JD. Hepatic perfusion index in the diagnosis of overt metastatic colorectal cancer. Nucl Med Commun 1990;11(1):23-28.

17. Van Beers BE, Leconte I, Materne R, Smith AM, Jamart J, Horsmans Y. Hepatic perfusion parameters in chronic liver disease: dynamic CT measurements correlated with disease severity. AJR Am J Roentgenol 2001;176(3):667-673.

18. Cox EF, Ghezzi A, Bennet A, Patel M, Jackson A, Harman D, Costigan C, James MW, Ryder SD, Gowland PA, Aithal GP, Guha IN, Francis ST. Liver T1 increases with fibrosis and is correlated with liver stiffness and ELF score. Proc Intl Soc Mag Reson Med 2013;21:4094.

19. Duhamel G, Prevost V, Girard OM, Callot V, Cozzone PJ. High-resolution mouse kidney perfusion imaging by pseudo-continuous arterial spin labeling at 11.75T. Magn Reson Med 2013.

20. Vollmar B, Menger MD. The hepatic microcirculation: mechanistic contributions and therapeutic targets in liver injury and repair. Physiol Rev 2009;89(4):1269-1339.